



Democratic and Popular Republic of Algeria
Ministry of Higher Education and Scientific Research
University Mohamed Khider of BISKRA
Faculty of Exact Sciences Natural and Life Sciences



Department of Material Sciences

THESIS

Presented by:

Hanna TOUHAMI

To obtain the degree of:

DOCTORATE

Title:

Experimental and DFT study on the physical properties of p-type semiconductors oxides for thermoelectric applications.

Board of Examiners:

Mr. Toufik TIBERMACHINE	Professor	University of Biskra	President
Mr. Said LAKEL	Professor	University of Biskra	Supervisor
Mme. Kenza ALMI	MCA	University of Biskra	Co-Supervisor
Mr. Miloud IBRIR	Professor	University of M'sila	Examiner
Mr. Said BENRAMACHE	Professor	University of Biskra	Examiner

Academic Year: 2023-2024

بِسْمِ اللَّهِ الرَّحْمَنِ الرَّحِيمِ

Acknowledgements

First and foremost, I am grateful to Allah Ta'ala, whose Grace has allowed me to carry out this work and overcome every obstacle. God blessings and peace upon our Prophet Mohammed (peace and blessings of Allah be upon him), who encourages us to pursue knowledge and science.

*I would like to express my sincere gratitude to my supervisor **Prof. Saïd LAKEËL** for his guidance and support. I express my deepest and heart felt gratitude to him for the valuable guidance, timely suggestions, moral support and encouragement given by him during the course of the research work.*

*My sincere thanks go also to my co-supervisor **Prof. Kenza ALMI** for guiding me throughout achieving this work.*

*Besides, I owe my sincere thanks to the **Prof. Toufik TIBERMACHINE.**, **Prof. Miloud IBRIR** and **Prof. Saïd BENRAMACHE** for their acceptance to judge this modest work.*

My sincere thanks also go to my parents for their infinite patience and for providing me with an ideal working environment. This project was made possible thanks to their support.

Finally, I would like to express my deepest thanks to all the academic and administrative staff of the Physics department at Mohamed Khider University - Biskra.

Hanna TOUHAMI



Dedication

*I dedicate this modest work to:
My incredibly supportive parents
who have supported me through
my entire education*

To my husband and my little son Moadh

*To my brothers, Hakim and Moussa,
and my little sister Lina*

To all of my supportive friends.

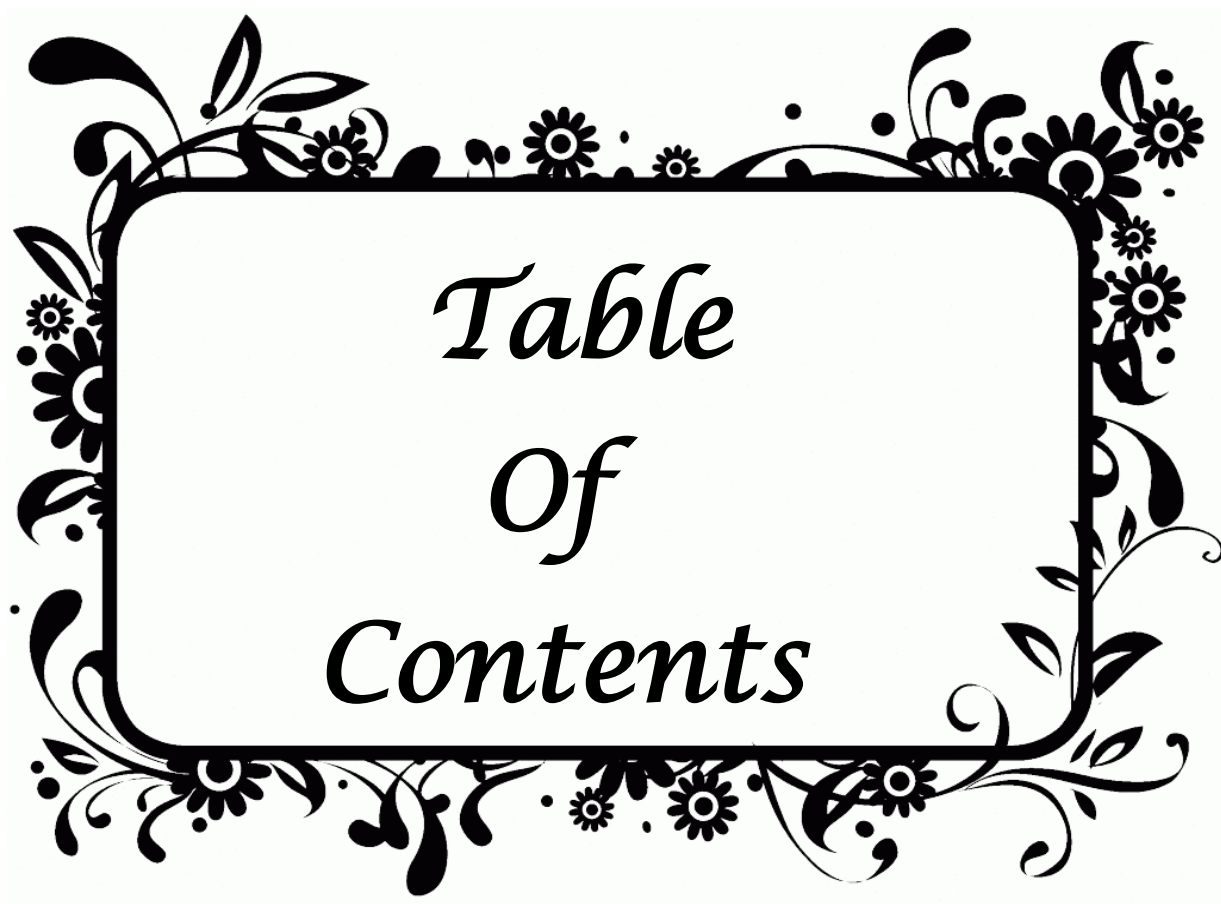


*Table
Of
Contents*

Contents

Acknowledgements	
Dedication	
Contents	
List of figures	vii
List of tables	x
General introduction	1
<i>Chapter I: Literature Revue</i>	
I.1.	Introduction 8
I.2.	The concept of semiconductor 8
I.3.	Electrical conductivity in semiconductors 8
I.4.	Types of semiconductors 10
I.4.1.	Intrinsic semiconductors 10
I.4.2.	Extrinsic semiconductors 10
I.4.2.1.	n-type semiconductors 10
I.4.2.2.	p-type semiconductors 10
I.5.	Classification of semiconductors 11
I.5.1.	Elementary semiconductors 11
I.5.2.	II - VI semiconductors 11
I.5.3.	Transparent metal oxides (TCOs) 11
I.5.3.1.	n-type TCOs 11
I.5.3.2.	p-type TCOs 12
I.6.	Nickel oxide (NiO) 12
I.6.1.	NiO properties 13
I.6.1.1.	NiO crystallographic properties 13
I.6.1.2.	Electronic properties of NiO 14
I.6.1.3.	Thermal oxidation of nickel 17
I.6.1.4.	Optical properties of NiO 17
I.6.1.5.	Electrical properties of NiO 19
I.6.1.6.	Magnetic properties 20
I.6.2.	NiO applications 21
I.6.2.1.	Photo-voltaic cells 21
I.6.2.2.	Protective films 21
I.6.2.3.	Antimicrobial activity 22
I.6.2.4.	Gas sensors 22
I.6.2.5.	Superconductors 22
I.6.2.6.	Batteries 23
I.7.	Earlier works done on alkali doped NiO based thin film: A Review 23
References	26

Chapter II: Experimental and Theoretical Backgrounds

II.1.	Experimental approach	33
II.1.1.	Introduction	33
II.1.2.	Physical deposition methods	33
II.1.2.1.	Pulsed Laser Deposition	33
II.1.2.2.	RF Sputtering	33
II.1.2.3.	Thermal evaporation	34
II.1.3.	Chemical deposition methods	34
II.1.3.1	Electrodeposition	35
II.1.3.2.	Chemical bath deposition	35
II.1.3.3.	Chemical Vapor Deposition (CVD)	36
II.1.3.4.	Spray pyrolysis technique	36
II.1.3.5.	Sol-gel technique	36
II.1.3.5. 1.	Reaction mechanisms	38
II.1.3.5. 2.	Sol-gel Transition	40
II.1.3.5.3.	Drying of the gel	40
II.1.3.5.4.	Thin films elaboration via sol-gel method	41
II.1.3.5.4. 1.	Dip-coating	41
II.1.3.5.4. 2.	Spin-coating	42
II.1.4.	Characterization techniques of NiO thin films	43
II.1.4.1.	Structural characterization	43
II.1.4.1.1.	Crystallite size calculation	44
II.1.4.1.2.	Lattice parameters calculation	44
II.1.4.1.3.	Stress-Strain calculation	44
II.1.4.2.	Optical Characterization	45
II.1.4.2. 1.	UV-visible spectroscopy	46
II.1.4.2. 2.	Measurement of optical properties	46
II.1.4.2. 2.3.	Measurement of thickness	46
II.1.4.2. 2.4.	Determination of the absorption coefficient	47
II.1.4.2. 2.5.	Band gap and Urbach energy determination	48
II.1.4.3.	Electrical properties measurements	50
II.1.4.3.1.	Resistivity measurements	51

II.1.4.3. 2.	Conductivity measurements	52
II.2.	Theoretical Approach	52
II.2.1.	Introduction	52
II.2.2.	The Many Body Problem	53
II.2.3.	Born Oppenheimer approximation	53
II.2.4.	Hartree approximation	54
II.2.5.	Hartree-Fock Approximation.	55
II.2.6.	Density Functional Theory (DFT)	56
II.2.6.1.	The Hohenberg-Kohn Theorem	57
II.2.6.2.	Kohn-Sham Equations	57
II.2.6.3.	Exchange-correlation energy	58
II.2.6.4.	Local density approximation (LDA)	58
II.2.6.5.	Local spin density approximation (LSDA)	59
II.2.6.6.	Generalized Gradient Approximation (GGA)	60
II.2.6.7.	DFT+U Approximation	61
II.2.7.	CASTEP	62
References		64

Chapter III: Results and Discussion

III.1.	Introduction	68
III.2.	Experimental part	68
III.2.1.	Experimental procedure and characterization techniques	68
III.2.2.	Results and discussion	69
III.2.2.1.	Structural properties	69
III.2.2.1.1.	Structural properties of Pure and Alkali doped NiO: $Ni_{1-x}A_xO$ (A=Li, Na and K)	69
III.2.2.1.2.	Structural properties of co-doped NiO $Ni_{1-2x}A_xLa_xO$ A= (Li, Na, K), (x=0.03, 0.06)	78
III.2.2.2.	Optical properties	80
III.2.2.2.1.	Optical properties of Pure and Alkali doped NiO ($Ni_{1-x}A_xO$) (A=Li, Na and K)	80
III.2.2.2.2.	Optical properties of co-doped NiO $Ni_{1-2x}A_xLa_xO$ A= (Li, Na, K), (x=0.03, 0.06)	91

III.2.2.3.	Electrical properties	95
III.2.2.3.1.	Electrical properties of Pure and Alkali doped NiO ($\text{Ni}_{1-x}\text{A}_x\text{O}$) (A=Li, Na and K)	95
III.2.2.3.2.	Electrical properties of co-doped NiO $\text{Ni}_{1-2x}\text{A}_x\text{La}_x\text{O}$ A=(Li, Na, K), (x=0.03, 0.06)	98
III.3.	Theoretical results	100
III.3.1.	Computational methods	100
III.3.2.	Structural properties	101
III.3.2.1.	Structural properties of pure and $\text{Ni}_{1-x}\text{A}_x\text{O}$ (A=Li, Na and K)	101
III.3.2.2.	Structural properties of $\text{Ni}_{1-2x}\text{A}_x\text{La}_x\text{O}$ (A=Li, Na and K)	104
III.3.3.	Electronic properties	105
III.3.3.1.	Introduction	105
III.3.3.2.	Electronic properties of pure and $\text{Ni}_{1-x}\text{A}_x\text{O}$ (A=Li, Na and K)	106
III.3.3.2.1.	Band structures of pure and $\text{Ni}_{1-x}\text{A}_x\text{O}$ (A=Li, Na and K)	106
III.3.3.2.2.	Density of states of pure and $\text{Ni}_{1-x}\text{A}_x\text{O}$ (A=Li, Na and K)	110
III.3.3.3.	Electronic properties of $\text{Ni}_{1-2x}\text{A}_x\text{La}_x\text{O}$ (A=Li, Na and K)	115
III.3.3.3.1.	Band structures	115
III.3.3.3.2.	Density of states	116
III.3.4.	Optical properties	119
III.3.4.1.	Optical Constants	119
III.3.4.2.	The dielectric function $\varepsilon(\omega)$	120
III.3.4.2.1.	The dielectric function $\varepsilon(\omega)$ of pure and $\text{Ni}_{1-x}\text{A}_x\text{O}$ (A=Li, Na and K)	120
III.3.4.2.2.	The dielectric function $\varepsilon(\omega)$ of $\text{Ni}_{1-2x}\text{A}_x\text{La}_x\text{O}$ (A=Li, Na and K)	123
III.3.4.3.	Refractive index $n(\omega)$	125
III.3.4.3.1.	Refractive index $n(\omega)$ of pure and $\text{Ni}_{1-x}\text{A}_x\text{O}$ (A=Li, Na and K)	125
III.3.4.3.2.	Refractive index $n(\omega)$ of $\text{Ni}_{1-2x}\text{A}_x\text{La}_x\text{O}$ (A=Li, Na and K)	126
III.3.4.4.	The extinction coefficient $k(\omega)$	127
III.3.4.4.1.	The extinction coefficient $k(\omega)$ of pure and $\text{Ni}_{1-x}\text{A}_x\text{O}$ (A=Li, Na and K)	127
III.3.4.4.2.	The extinction coefficient $k(\omega)$ of $\text{Ni}_{1-2x}\text{A}_x\text{La}_x\text{O}$ (A=Li, Na and K)	128
III.3.4.5.	Absorption coefficient $\alpha(\omega)$	129
III.3.4.5.1.	Absorption coefficient $\alpha(\omega)$ of pure and $\text{Ni}_{1-x}\text{A}_x\text{O}$ (A=Li, Na and K)	129
III.3.4.5.2.	Absorption coefficient $\alpha(\omega)$ of $\text{Ni}_{1-2x}\text{A}_x\text{La}_x\text{O}$ (A=Li, Na and K)	130

III.3.4.6.	Reflectivity $R(\omega)$	131
III.3.4.6.1.	Reflectivity $R(\omega)$ of pure and $\text{Ni}_{1-x}\text{A}_x\text{O}$ (A=Li, Na and K)	131
III.3.4.6.	Reflectivity $R(\omega)$ of $\text{Ni}_{1-2x}\text{A}_x\text{La}_x\text{O}$ (A=Li, Na and K)	132
III.3.4.6.	Energy loss function $L(\omega)$	133
III.3.4.6.1.	Energy loss function $L(\omega)$ of pure and $\text{Ni}_{1-x}\text{A}_x\text{O}$ (A=Li, Na and K)	133
III.3.4.6.2.	Energy loss function $L(\omega)$ of $\text{Ni}_{1-2x}\text{A}_x\text{La}_x\text{O}$ (A=Li, Na and K)	134
III.3.5.	Elastic properties	135
III.3.5.1.	Introduction	135
III.3.5.2.	Elastic constants calculation	136
III.3.5.2.1.	Elastic constants calculation of pure and $\text{Ni}_{1-x}\text{A}_x\text{O}$ (A=Li, Na and K)	136
III.3.5.2.2.	Elastic constants calculation of $\text{Ni}_{1-2x}\text{A}_x\text{La}_x\text{O}$ (A=Li, Na and K)	139
III.3.5.3.	Elasticity modulus	141
III.3.5.3.1.	Elasticity modulus of pure and $\text{Ni}_{1-x}\text{A}_x\text{O}$ (A=Li, Na and K)	141
III.3.5.3.1.1.	Bulk modulus	141
III.3.5.3.1.2.	Shear modulus	141
III.3.5.3.1.3.	Young's modulus	141
III.3.5.3.1.4.	Poisson's ratio	141
III.3.5.3.1.5.	Debye temperature	142
III.3.5.3.2.	Elasticity modulus of $\text{Ni}_{1-2x}\text{A}_x\text{La}_x\text{O}$ (A=Li, Na and K)	147
References		148

A decorative border in black ink, featuring stylized flowers, leaves, and swirling lines that frame the central text.

List of Figures

*List of Figures**Chapter I*

Figure.I.1.	Electrical conductivity at room temperature of some types of materials	9
Figure I.2.	The crystallographic structure and DRX spectrum of NiO.	12
FigureI.3.	Representation of the NiO energy levels.	14
Figure.I.4.	Schematic representation of the molecular structure of NiO in its ground state (Ni atom and O orbital)	14
Figure I.5.	Gibbs free energy versus temperature in nickel oxidation for the formation of NiO.	17
Figure I.6.	NiO transmittance specter.	18
Figure I.7.	A schematic of pure non-stoichiometric NiO crystal.	20

Chapter II

Figure II.1.	Schematic summary of the sol-gel process.	37
Figure II.2.	Dip coating principe.	41
Figure II.3.	Spin coating principe.	42
Figure II.4.	<i>BRUKER-AXS type D8</i> Diffractometer.	44
Figure II.5.	Schematic representation of UV-Visible spectrometer.	46
Figure.II.6.	Typical transmittance spectra of a pure NiO thin film prepared by spin coating.	47
Figure II.7.	Energy states distribution function of a crystallized semiconductor.	49
Figure II.8.	Function of distribution of energy states in bands: Encroachment of tails in the bands.	49
Figure II.9.	Energy gap determination of a nickel oxide thin film	50
Figure II.10.	Schematic of four points probe configuration	52

Chapter III

Figure III.1.	X-ray diffraction patterns of pure and Ni _{1-x} Li _x O (x=3%, 6%, 9%, 12%, 25%)	70
Figure III.2.	Variation of crystallite size and mean strain of NiO thin films as a function of Li concentration	72
Figure III.3.	X-ray diffraction patterns of pure and Ni _{1-x} Na _x O (x=3%, 6%, 9%, 12%, 25%)	73
Figure III.4.	Variation of crystallite size and mean strain of NiO thin films as a function of Na concentration	75
Figure III.5.	X-ray diffraction patterns of pure and Ni _{1-x} K _x O (x=3%, 6%, 9%, 12%, 25%)	76
Figure III.6.	Variation of crystallite size and mean strain of NiO thin films as a function of K concentration	78
Figure III.7.	X-ray diffraction patterns of co-doped NiO Ni _{1-2x} A _x La _x O A= (Li, Na, K), (x=0.03, 0.06)	79
Figure III.8:	Variation of crystallite size and mean strain size of co-doped NiO thin	80

	films.	
Figure III.9.	Transmittance spectra of undoped and Li-doped NiO	81
Figure III.10.	Reflectance spectra of undoped and Li-doped NiO	82
Figure III.11.	$(\alpha hv)^2$ vs. (hv) of undoped and Li doped NiO	82
Figure III.12.	Estimation of Urbach energy of undoped and Li-doped NiO thin films	84
Figure III.13.	Transmittance spectra of undoped and Na-doped NiO	85
Figure III.14.	Reflectance spectra of undoped and Na-doped NiO	85
Figure III.15.	$(\alpha hv)^2$ vs. (hv) of undoped and Li doped NiO	86
Figure III.16.	Estimation of Urbach energy of undoped and Na-doped NiO thin films	87
Figure III.17.	Transmittance spectra of undoped and K-doped NiO	88
Figure III.18.	Reflectance spectra of undoped and Na-doped NiO	89
Figure III.19.	$(\alpha hv)^2$ vs. (hv) of undoped and K doped NiO	90
Figure III.20.	Estimation of Urbach energy of undoped and Na-doped NiO thin films	91
Figure III.21.	Transmittance spectra of co-doped NiO	92
Figure III.22.	Reflectance spectra of co-doped NiO	92
Figure III.23.	$(\alpha hv)^2$ vs. (hv) co-doped NiO	93
Figure III.24.	Estimation of Urbach energy of co-doped NiO thin films	94
Figure III.25.	Variation of the resistivity of NiO thin films as a function of Li concentration	96
Figure III.26.	Variation of the resistivity of NiO thin films as a function of Na concentration	97
Figure III.27.	Variation of the resistivity of NiO thin films as a function of K concentration	98
Figure III.28.	Variation of the resistivity of co-doped NiO thin films	99
Figure III.29.	(a) $1 \times 1 \times 1$ NiO supercell (b) $2 \times 2 \times 2$ NiO supercell; O atoms are in red, Ni atoms are in blue, Yellow atom represents the dopant atom $x = \text{Li, Na, K, La}$.	101
Figure.III.30.	Evolution of lattice parameter and volume as a function of concentration x for pure and $\text{Ni}_{1-x}\text{A}_x\text{O}$ ($A = \text{Li, Na and K}$) structures	103
Figure.III.31.	Evolution of lattice parameter and volume as a function of concentration x for pure and $\text{Ni}_{1-x}\text{A}_x\text{O}$ ($A = \text{Li, Na and K}$) structures	105
Figure III.32.	Electronic band structure of undoped NiO	107
Figure III.33.	Electronic band structure of $\text{Ni}_{1-x}\text{Li}_x\text{O}$	107
Figure III.34.	Electronic band structure of $\text{Ni}_{1-x}\text{Na}_x\text{O}$	108
Figure III.35.	Electronic band structure of $\text{Ni}_{1-x}\text{K}_x\text{O}$	109
Figure III.36.	Total and partial electronic density of states of undoped NiO	111
Figure III.37.	Total and partial electronic density of states of $\text{Ni}_{1-x}\text{Li}_x\text{O}$	112
Figure III.38.	Total and partial electronic density of states of $\text{Ni}_{1-x}\text{Na}_x\text{O}$	113
Figure III.39.	Total and partial electronic density of states of $\text{Ni}_{1-x}\text{K}_x\text{O}$	114
Figure III.40.	Electronic band structure of co-doped NiO $\text{Ni}_{1-2x}\text{A}_x\text{La}_x\text{O}$ $A = (\text{Li, Na, K})$, ($x = 0.03, 0.06$)	116
Figure III.41.	Total and partial density of states of co-doped NiO $\text{Ni}_{1-2x}\text{A}_x\text{La}_x\text{O}$ $A = (\text{Li, Na, K})$, ($x = 0.03, 0.06$)	118
Figure III.42.	The imaginary part of the dielectric function of $\text{Ni}_{1-x}\text{A}_x\text{O}$ ($A = \text{Li, Na, K}$).	122

Figure III.43.	The real part of the dielectric function of $\text{Ni}_{1-x}\text{A}_x\text{O}$ (A=Li, Na, K).	123
Figure III.44.	The imaginary part of the dielectric function of co-doped NiO $\text{Ni}_{1-2x}\text{A}_x\text{La}_x\text{O}$ A= (Li, Na, K)	124
Figure III.45.	The real part of the dielectric function of co-doped NiO $\text{Ni}_{1-2x}\text{A}_x\text{La}_x\text{O}$ A= (Li, Na, K)	125
Figure III.46.	The refractive index of $\text{Ni}_{1-x}\text{A}_x\text{O}$ (A=Li, Na, K).	126
Figure III.47.	The refractive index of co-doped NiO $\text{Ni}_{1-2x}\text{A}_x\text{La}_x\text{O}$ A= (Li, Na, K).	127
Figure III.48.	The extinction coefficient of $\text{Ni}_{1-x}\text{A}_x\text{O}$ (A=Li, Na, K).	128
Figure III.49.	The extinction coefficient of co-doped NiO $\text{Ni}_{1-2x}\text{A}_x\text{La}_x\text{O}$ A= (Li, Na, K).	129
Figure III.50.	The absorption coefficient of $\text{Ni}_{1-x}\text{A}_x\text{O}$ A= (Li, Na, K).	130
Figure III.51.	The absorption coefficient of co-doped NiO $\text{Ni}_{1-2x}\text{A}_x\text{La}_x\text{O}$ A= (Li, Na, K).	131
Figure III.52.	Reflectivity of $\text{Ni}_{1-x}\text{A}_x\text{O}$ (A=Li, Na, K).	132
Figure III.53.	Reflectivity of co-doped NiO $\text{Ni}_{1-2x}\text{A}_x\text{La}_x\text{O}$ A= (Li, Na, K).	133
Figure III.54.	Loss functions of $\text{Ni}_{1-x}\text{A}_x\text{O}$ (A=Li, Na, K).	134
Figure III.55.	Loss functions of co-doped NiO $\text{Ni}_{1-2x}\text{A}_x\text{La}_x\text{O}$ A= (Li, Na, K).	155
Figure III.56.	Variation of elastic constants of $\text{Ni}_{1-x}\text{A}_x\text{O}$ (A=Li, Na, K) as function of the concentration x.	139
Figure III.57.	Variation of elastic constants co-doped NiO $\text{Ni}_{1-2x}\text{A}_x\text{La}_x\text{O}$ A= (Li, Na, K) as function of the concentration x.	140
Figure III.58.	Evolution of bulk modulus (B), shear modulus (G) and Young modulus of $\text{Ni}_{1-x}\text{A}_x\text{O}$ (A=Li, Na, K) as function of the concentration x.	146
Figure III.59.	Evolution of bulk modulus (B), shear modulus (G) and Young modulus of $\text{Ni}_{1-2x}\text{A}_x\text{La}_x\text{O}$ (A=Li, Na and K) as function of the concentration x.	148



List of Tables

List of Tables

Chapter I

Table I.1.	Crystallographic properties of NiO	12
Table I.2.	NiO energy band gap calculated using various methods	15
Table I.3.	Standard thermodynamic properties of nickel and NiO	16
Table I.4.	Experimental NiO energy band gap.	18
Table I.5.	Some electrical properties of NiO	19

Chapter III

Table III.1.	Values of Bragg angle 2θ , lattice constants a , crystallite size D , mean strain ϵ and dislocation density δ of NiO thin films as a function to the lithium concentration.	67
Table III.2.	Values of Bragg angle 2θ , lattice constants a , crystallite size D , mean strain ϵ and dislocation density δ of NiO thin films as a function of sodium concentration.	69
Table III.3.	Values of Bragg angle 2θ , lattice constants a , crystallite size D , mean strain ϵ and dislocation density δ of NiO thin films as a function of potassium concentration.	72
Table III.4.	Values of Bragg angle 2θ , lattice constants a , crystallite size D , mean strain ϵ and dislocation density δ of co-doped NiO thin films $\text{Ni}_{1-2x}\text{A}_x\text{La}_x\text{O}$ $\text{A} = (\text{Li}, \text{Na}, \text{K})$, ($x=0.03, 0.06$)	74
Table III.5.	Values of optical band gap energy E_g (eV), Urbach energy E_u (meV) and resistivity, of NiO thin films as a function of Li concentration.	77
Table III.6.	Values of optical band gap energy E_g (eV), Urbach energy E_u (meV) and resistivity, of NiO thin films as a function of Na concentration.	80
Table III.7.	Values of optical band gap energy E_g (eV), Urbach energy E_u (meV) and resistivity, of NiO thin films as a function of K concentration.	84
Table III.8.	Values of optical band gap energy E_g (eV), Urbach energy E_u (meV), resistivity, and dislocation density of co-doped NiO thin films $\text{Ni}_{1-2x}\text{A}_x\text{La}_x\text{O}$ $\text{A} = (\text{Li}, \text{Na}, \text{K})$, ($x=0.03, 0.06$).	87
Table III.9.	Structural parameters of $\text{Ni}_{1-x}\text{Li}_x\text{O}$ (lattice parameter and cell volume)	95
Table III.10.	Structural parameters of $\text{Ni}_{1-x}\text{Na}_x\text{O}$ (lattice parameter and cell volume)	95
Table III.11.	Structural parameters of $\text{Ni}_{1-x}\text{K}_x\text{O}$ (lattice parameter and cell volume)	96
Table III.12.	Structural parameters of $\text{Ni}_{1-2x}\text{A}_x\text{La}_x\text{O}$ ($\text{A} = \text{Li}, \text{Na}$ and K) ($x=0.0321, 0.0625$) (lattice parameter and cell volume)	97
Table III.13.	Theoretical and experimental band gap energy values of $\text{Ni}_{1-x}\text{Li}_x\text{O}$	102

Table.III.14.	Theoretical and experimental band gap energy values of $\text{Ni}_{1-x}\text{Na}_x\text{O}$	102
Table.III.15.	Theoretical and experimental band gap energy values of $\text{Ni}_{1-x}\text{K}_x\text{O}$	103
Table.III.16.	Theoretical and experimental band gap energy values of co-doped NiO thin films $\text{Ni}_{1-2x}\text{A}_x\text{La}_x\text{O}$ $\text{A}=(\text{Li}, \text{Na}, \text{K})$, ($x=0.03, 0.06$).	109
Table III.17.	Elastic constants of $\text{Ni}_{1-x}\text{Li}_x\text{O}$ as a function of the concentration x .	130
Table III.18.	Elastic constants of $\text{Ni}_{1-x}\text{Na}_x\text{O}$ as a function of the concentration x .	130
Table III.19.	Elastic constants of $\text{Ni}_{1-x}\text{K}_x\text{O}$ as a function of the concentration x .	130
Table III.20.	Elastic constants of $\text{Ni}_{1-2x}\text{A}_x\text{La}_x\text{O}$ ($\text{A}=\text{Li}, \text{Na}$ and K) as a function of the concentration x .	132
Table III.21.	Variation of the elastic modules and the Debye temperature θ_D of $\text{Ni}_{1-x}\text{Li}_x\text{O}$ as a function of the concentration x .	135
Table III.22.	Variation of the elastic modules and the Debye temperature θ_D of $\text{Ni}_{1-x}\text{Na}_x\text{O}$ as a function of the concentration x .	136
Table III.23.	Variation of the elastic modules and the Debye temperature θ_D of $\text{Ni}_{1-x}\text{K}_x\text{O}$ as a function of the concentration x .	136
Table III.24.	Variation of the elastic modules and the Debye temperature θ_D of $\text{Ni}_{1-2x}\text{A}_x\text{La}_x\text{O}$ ($\text{A}=\text{Li}, \text{Na}$ and K) as a function of the concentration x .	138



*General
Introduction*

General Introduction

Although it is an old project, the field of thin films has undergone significant changes and has sparked significant research efforts in recent years across several technological domains in order to address a collective need that are growing more and more.

Transparent and conductive oxides (TCOs) in thin films are important materials for their dual properties of electrical conductivity and transparency in the visible wave range [1]. Also semiconducting metal oxide compounds, such TiO₂, CuO, ZnO, and NiO, have garnered significant attention from both the academic and industrial communities and have been the focus of extensive research efforts in recent years. When compared to their equivalent micro and macro forms, these materials show an interesting shift in their characteristics at the nanoscale form. In addition to their uses as protective coatings or intelligent catalyst beds, TCOs are found in several kinds of solar cells [2]. They are employed as transparent electrodes and can be used in any kind of cell by employing polymers as active couches (active junctions) [3].

Nickel oxide (NiO) is a wide band gap semiconductor material ($E_g=4.00\text{eV}$) that belongs to the OCT p-family. Nickel oxide thin films have garnered more attention recently due to their high chemical stability, non-toxicity [4], its electrical, magnetic, and optical properties [5] additionally, because to their prospective applications in solar cells[6], full cells[6], electrochemical capacitors[7,8], gas sensors[9] and electrical devices [10].

Many methods can be used to prepare nickel oxide thin films, including spray pyrolysis [12] RF sputtering [11], pulsed laser deposition [13], and the sol gel spin coating process, which is one of the most popular techniques; it stands out for a variety of reasons, such as its low cost, environmental friendliness, and adjustability, safety, simple deposition equipment on a large-area films with uniform thickness. [14].

The ab initio methods [15] have been widely used for more than a decade. The majority of these methods require continuous updates to adapt to the speed and memory capacity of the calculator. Ab-initio calculations are powerful tools for predicting and studying new materials under various circumstances where the experience is nearly impossible to have, possibly even dangerous, harmful, or polluting.

Nickel oxide presents an important challenge for theoretical studies although being very simple to prepare experimentally due to its incomplete d shell, which creates a strong interatomic correlation and poses difficulties to DFT theory which bases on simplifying the many body problem into non-interacting one particle problem by that the valence electrons are delocalized, and neglects the interatomic correlation caused by the ionic core, thus the DFT theory predicts metallic characteristics for NiO [15]. To overcome this limitation, there are numerous theories, including GW approximation [16, 17], hybrid density functional like B3LYP [19], Hartree-Fock (HF) [20], self-interaction corrections (SIC) [18] and DFT+U [20], Have been developed. By incorporating on-site Coulomb repulsion and exchange interactions between 3d electrons into the DFT Hamiltonian [21].

Nickel oxide is one of the few p-type oxides with a band gap of 3.6–4 eV [22]. Its stoichiometric form has an insulating property with a resistivity of 10^{13} ohm.cm [23]. The non-stoichiometric p-type conductivity is caused by Ni^{2+} vacancies and oxygen interstitials [24]. Doping with alkaline atoms (Li, Na, and K) is an effective method for reducing NiO resistivity by introducing more charge carriers (holes). In recent years, doping NiO with alkaline atoms (Li [25-26]), (Na [27]), and (K [28-29]) has been extensively studied; however, all of these studies have focused on the dopant concentration effect, however the effect of dopant type on the physical properties of nickel oxide has not been undergone substantial research.

La-doped NiO has attracted a lot of attention recently because of its interesting uses La-doped NiO nanofibers produced using the electrospinning technique may be used as electrode materials in high-performance supercapacitors. [30]. Likewise, Han et al. [31] obtained La-doped NiO microspheres with porous structure using a hydrothermal method followed by calcination process for supercapacitor applications. Dakhel et al. [32] mentioned Li and La co-doped NiO ceramics displaying an enormous dielectric permittivity at low frequencies. In fact, Yan et al. [33] found that fuel cells using methane perform better and are more stable when La is added to the NiO anode. The same authors discovered that lanthanum oxide (La_2O_3) and a small quantity of NiO react to generate a secondary phase of lanthanum nickelate (La_2NiO_4).

The objective of this work was to deposit pure NiO, Alkali-doped NiO and La-Alkali co-doped NiO thin films on glass substrates using the Sol-Gel spin coating method. Then, the

effect of the Alkali doping concentration on the structural, optical and electronic properties of the elaborated films, was investigated. On the other hand, the first-principles method based on DFT-GGA with the semi-empirical Hubbard U model (DFT-GGA+U), as implemented in the CASTEP code, has been applied to calculate the structural, electronic, optical, and elastic properties of Alkali-doped, La-Alkali co-doped NiO and undoped NiO cubic materials, in order to improve especially the underestimation of the experimental energy band gap. Thus, the calculated results were compared with other experimental and theoretical results available in the literature.

The thesis is composed of three chapters, organized as follows; starting with the general introduction, the chapter 1 will give an overview of the technical and theoretical background of semiconductors, types, importance, basic properties and applications. This chapter also provides the state of the art of nickel oxide (NiO) thin films, its different chemical and physical properties and applications of the current research status. Furthermore, review of works done by many researchers is selected field on Alkali doped NiO thin films have been carried out in this chapter.

The second chapter covers various synthesis techniques for thin films with a general description of the sol-gel process, describing the experimental spin coating technique used to prepare thin films, as well as the principles of characterization for studying their physical properties. The second section of this chapter focuses on calculation methods. It describes the theoretical framework for our work. We present the basic principles of density functional theory (DFT). This section includes information on how CASTEP (Cambridge Serial Total Energy Package: Commercialized by Accelrys) was implemented in the current calculations.

The third chapter is divided into two sections and is devoted to presenting and discussing the results that were obtained:

The first part focused on the presentation of results obtained from characterization by various techniques of pure NiO and Alkali-doped and La-Alkali co-doped NiO oxide thin films (Li, Na and K) x ($x = 3\%$, 6% , 9% , 12% and 25%). The structural, optical and electrical properties of NiO thin films are then discussed.

In order to linking of experimental results with theory, usually separated in the literature, DFT-GGA approach was used to predict structural and elastic properties of pure NiO and Alkali-doped and La-Alkali co-doped NiO cubic structures, which were compared,

wherever possible, with their corresponding measured values. For band structure and density of states calculations the Hubbard U correction was introduced. These were to be the subject of the second part of the third chapter.

Finally, a brief summary of the main conclusions obtained either from simulation of pure NiO and Alkali-doped and La-Alkali co-doped NiO cubic structures or various characterizations of the prepared thin films, is given.

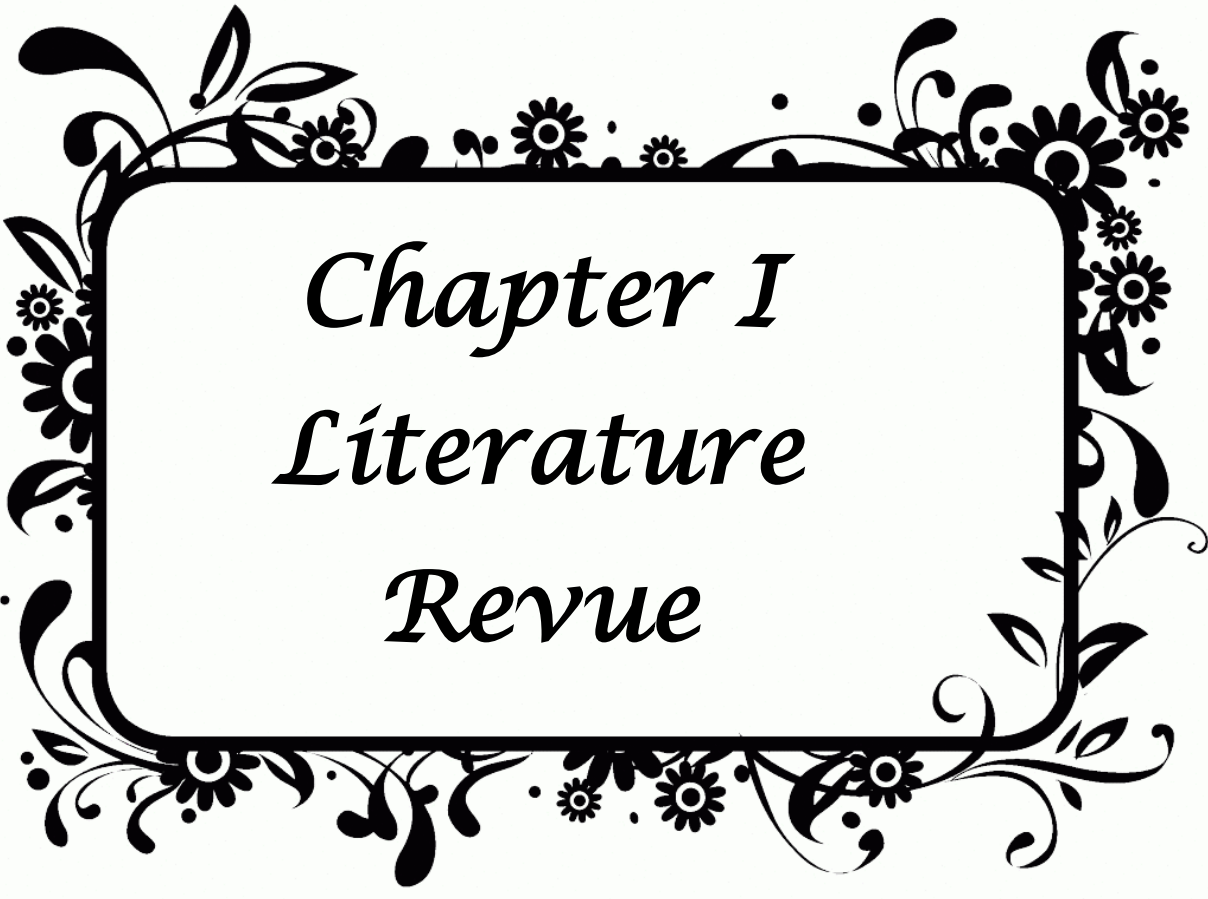
References

- [1] D. Lamb, S. Irvine, Near infrared transparent conducting cadmium oxide deposited by MOCVD, *Thin solid films*, 518 (2009) 1222-1224.
- [2] R. Romero, F. Martin, J. Ramos-Barrado, D. Leinen, Synthesis and characterization of nanostructured nickel oxide thin films prepared with chemical spray pyrolysis, *Thin Solid Films*, 518 (2010) 4499-4502.
- [3] K. Badeker, Concerning the electricity conductivity and the thermoelectric energy of several heavy metal bonds, *Annalen der Physik*, 22 (1907) 749.
- [4] H. Sato, T. Minami, S. Takata, T. Yamada, Transparent conducting p-type NiO thin films prepared by magnetron sputtering, *Thin solid films*, 236 (1993) 27-31.
- [5] Q. Xia, K.S. Hui, K. Hui, D. Hwang, S. Lee, W. Zhou, Y. Cho, S. Kwon, Q. Wang, Y. Son, A facile synthesis method of hierarchically porous NiO nanosheets, *Materials Letters*, 69 (2012) 69-71.
- [6] E.A. Gibson, A.L. Smeigh, L. Le Pleux, J. Fortage, G. Boschloo, E. Blart, Y. Pellegrin, F. Odobel, A. Hagfeldt, L. Hammarström, A p-type NiO-based dye-sensitized solar cell with an open-circuit voltage of 0.35 V, *Angewandte Chemie*, 121 (2009) 4466-4469.
- [7] R.S. Kate, S.A. Khalate, R.J. Deokate, Overview of nanostructured metal oxides and pure nickel oxide (NiO) electrodes for supercapacitors: A review, *Journal of Alloys and Compounds*, 734 (2018) 89-111.
- [8] S. Bulakhe, R. Deokate, Electrochemically prepared Fe: NiO thin film catalysis for oxygen evolution reaction, *Journal of Materials Science: Materials in Electronics*, 33 (2022) 18180-18186.

- [9] I. Sta, M. Jlassi, M. Kandyla, M. Hajji, P. Koralli, R. Allagui, M. Kompitsas, H. Ezzaouia, Hydrogen sensing by sol–gel grown NiO and NiO: Li thin films, *Journal of Alloys and Compounds*, 626 (2015) 87-92.
- [10] R. Amin, R.A. Hameed, K. El-Khatib, H. El-Abd, E.R. Souaya, Effect of preparation conditions on the performance of nano Pt–CuO/C electrocatalysts for methanol electro-oxidation, *international journal of hydrogen energy*, 37 (2012) 18870-18881.
- [11] M. El-Kemary, N. Nagy, I. El-Mehasseb, Nickel oxide nanoparticles: synthesis and spectral studies of interactions with glucose, *Materials Science in Semiconductor Processing*, 16 (2013) 1747-1752.
- [12] A. Nattestad, A.J. Mozer, M.K. Fischer, Y.-B. Cheng, A. Mishra, P. Bäuerle, U. Bach, Highly efficient photocathodes for dye-sensitized tandem solar cells, *Nature materials*, 9 (2010) 31-35.
- [13] K. Oka, T. Yanagida, K. Nagashima, H. Tanaka, T. Kawai, Nonvolatile bipolar resistive memory switching in single crystalline NiO heterostructured nanowires, *Journal of the American Chemical Society*, 131 (2009) 3434-3435.
- [14] A. Farag, I. Yahia, M. Al-Kotb, Nanostructure and enhancement of the optical properties of Tb-doped NiO for photodiode applications, *Chinese Journal of Physics*, 64 (2020) 87-102.
- [15] C. Pisani, R. Dovesi, C. Roetti, Hartree-Fock ab initio treatment of crystalline systems, Springer Science & Business Media 2012.
- [16] G. Shao, Red shift in manganese-and iron-doped TiO₂: a DFT+ U analysis, *The Journal of Physical Chemistry C*, 113 (2009) 6800-6808.
- [17] F. Aryasetiawan, O. Gunnarsson, Electronic structure of NiO in the GW approximation, *Physical review letters*, 74 (1995) 3221.
- [18] M. Towler, N. Allan, N.M. Harrison, V. Saunders, W. Mackrodt, E. Apra, Ab initio study of MnO and NiO, *Physical Review B*, 50 (1994) 5041.
- [19] Z. Szotek, W. Temmerman, H. Winter, Application of the self-interaction correction to transition-metal oxides, *Physical Review B*, 47 (1993) 4029.
- [20] A.D. Becke, A new mixing of Hartree–Fock and local density-functional theories, *The Journal of chemical physics*, 98 (1993) 1372-1377.
- [21] A. Rohrbach, J. Hafner, G. Kresse, Ab initio study of the (0001) surfaces of hematite and chromia: Influence of strong electronic correlations, *Physical Review B—Condensed Matter and Materials Physics*, 70 (2004) 125426.

- [22] K. Tsunoda, K. Kinoshita, H. Noshiro, Y. Yamazaki, T. Iizuka, Y. Ito, A. Takahashi, A. Okano, Y. Sato, T. Fukano, Low power and high speed switching of Ti-doped NiO ReRAM under the unipolar voltage source of less than 3 V, 2007 IEEE International Electron Devices Meeting, IEEE, 2007, pp. 767-770.
- [23] R. Gupta, A. Hendi, M. Cavas, A.A. Al-Ghamdi, O.A. Al-Hartomy, R. Aloraini, F. El-Tantawy, F. Yakuphanoglu, Improvement of photoresponse properties of NiO/p-Si photodiodes by copper dopant, *Physica E: Low-dimensional Systems and Nanostructures*, 56 (2014) 288-295.
- [24] T. Dutta, P. Gupta, A. Gupta, J. Narayan, Effect of Li doping in NiO thin films on its transparent and conducting properties and its application in heteroepitaxial pn junctions, *Journal of Applied Physics*, 108 (2010).
- [25] I. Sta, M. Jlassi, M. Hajji, M. Boujmil, R. Jerbi, M. Kandyla, M. Kompitsas, H. Ezzaouia, Structural and optical properties of TiO₂ thin films prepared by spin coating, *Journal of Sol-Gel Science and Technology*, 72 (2014) 421-427.
- [26] K. Jung, J. Choi, Y. Kim, H. Im, S. Seo, R. Jung, D. Kim, J.-S. Kim, B.H. Park, J.P. Hong, Resistance switching characteristics in Li-doped NiO, *Journal of Applied Physics*, 103 (2008).
- [27] Y.R. Denny, K. Lee, C. Park, S.K. Oh, H.J. Kang, D.-S. Yang, S. Seo, Electronic, electrical and optical properties of undoped and Na-doped NiO thin films, *Thin Solid Films*, 591 (2015) 255-260.
- [28] N. Wang, C. Liu, C.L.B. Wen, H. Wang, S. Liu, W. Jiang, W. Ding, W. Chai, Structural, electrical and optical properties of K-doped NiO films prepared by rapid pyrolysis sol-gel technique, *Thin Solid Films*, 616 (2016) 587-593.
- [29] A. Loukil, A. Boukhachem, M.B. Amor, M. Ghamnia, K. Raouadi, Effects of potassium incorporation on the structural, optical, vibrational and electrical properties of NiO sprayed thin films for p-type optical windows, *Ceramics International*, 42 (2016) 8274-8289.
- [30] J. Jia, F. Luo, C. Gao, C. Suo, X. Wang, H. Song, X. Hu, Synthesis of La-doped NiO nanofibers and their electrochemical properties as electrode for supercapacitors, *Ceramics International*, 40 (2014) 6973-6977.
- [31] D. Han, X. Jing, J. Wang, P. Yang, D. Song, J. Liu, Porous lanthanum doped NiO microspheres for supercapacitor application, *Journal of electroanalytical chemistry*, 682 (2012) 37-44.

- [32] A. Dakhel, Dielectric relaxation behaviour of Li and La co-doped NiO ceramics, *Ceramics International*, 39 (2013) 4263-4268.
- [33] A. Yan, M. Phongaksorn, D. Nativel, E. Croiset, Lanthanum promoted NiO–SDC anode for low temperature solid oxide fuel cells fueled with methane, *Journal of Power Sources*, 210 (2012) 374-380.

A decorative black and white floral border surrounds the text. It features stylized leaves, small flowers, and swirling lines that form a frame around the central text.

Chapter I
Literature
Revue

I.1.Introduction

Semiconductors, a key area of study in material science, have transformed modern technology due to their unique electrical properties. Material scientists have made significant contributions by developing semiconductors with extraordinary chemical, physical, and mechanical characteristics. Thin films, which are extremely thin layers of materials, have emerged as a vital component in various applications. In this chapter, an over view of semiconductors and transparent conduction oxides is provided, then the basic properties of nickel oxide thin films and its applications is presented.

I.2.The Concept of semiconductor

Depending on the external factors they are exposed to, such as temperature, pressure, radiation, magnetic or electric fields, semiconductors can act either as conductors or insulators.

Semiconductors are crystalline materials with average electrical conductivity, allowing them to function as both a conductor and an insulator. 14 semiconductor elements are listed in the periodic table, including silicon, germanium, selenium, cadmium, aluminium, gallium, boron, indium, and carbon.

According to the band theory, the highest energy band allowed (the valence band) is entirely occupied by electrons in semiconductors. However, the height of the forbidden band of a semiconductor is low (1eV), whereas it is remarkable for the true insulators, and is situated between this entire band and the first band upper vacuum in the energy diagram (conduction band).

I.3.Electrical conductivity in semiconductors:

The conductivity of semiconductors is limited at ambient temperature and lies between that of metals and insulators and it behave as insulators at absolute zero, figure (I.1) shows the electrical conductivity at room temperature of some types of materials. Their properties can be modified by changing the temperature or adding impurities by doping them in order to change their electrical properties [1]. According to the principle of construction, at $T=0$, electrons occupy each of the bands' unique molecular orbitals. The lowest orbitals are filled if each atom contributes one electron. The highest occupied orbital at $T=0$ is known as the

Fermi level, and it is positioned around the band's center[1]. At temperatures above $T=0$, the orbital P population is given by the distribution of Fermi-Dirac.

A Boltzmann distribution that recognizes that a level can only have a maximum of two electrons occupying it. This distribution has the following form:

$$P = \frac{1}{e^{(E-\mu)/kT} + 1} \quad (I.1)$$

Where

E: is the energy.

μ : is the chemical potential.

k: Boltzmann constants.

T: Absolute temperature.

At high energies ($E \gg \mu$), the term 1 of the dominator can be neglected from Fermi-Dirac distribution, and the population for $T > 0$ looks like a distribution of Boltzmann to the extent that it decreases exponentially as energy increases[1].

$$P = e^{-(E-\mu)/kT} \quad (I.2)$$

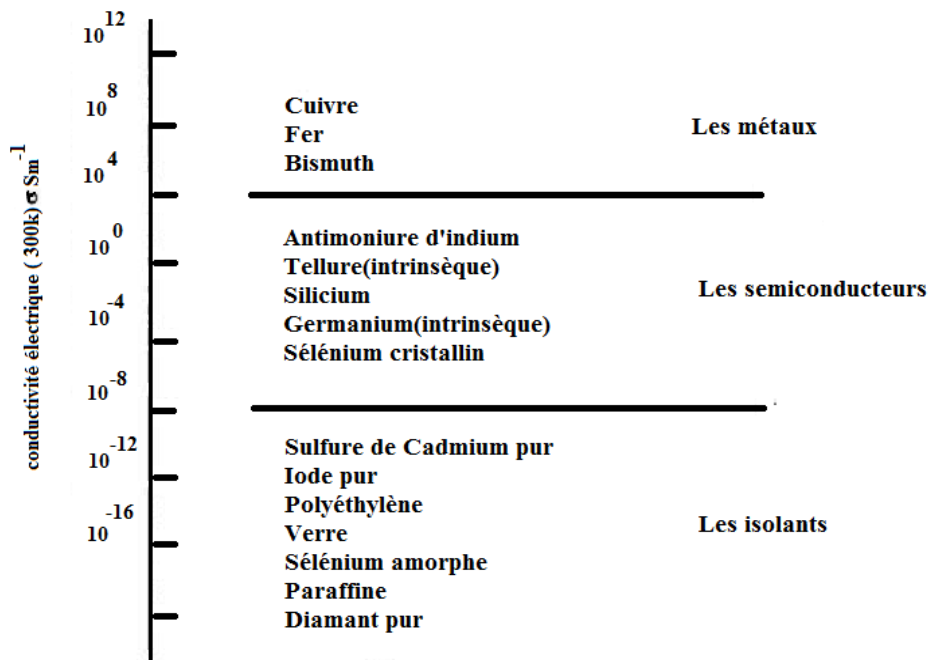


Figure.I.1. Electrical conductivity at room temperature of some types of materials [1]

I.4. Types of semiconductors:

We distinguish between two types of semiconductors: doped extrinsic and perfect intrinsic semiconductors.

I.4.1. Intrinsic semiconductors

They have a very low level of impurities and are extremely pure and well-crystallized semiconductors with a fully periodic crystalline lattice (less than 1 impurity atom for 10^{13} atoms of the semiconductor element). At very low temperatures, they act as insulators and their conductivity increases with the increase of temperature. We call a semiconductor intrinsic if the electrons number n in the conduction band is equal to holes number p in valence band [3].

I.4.2. Extrinsic semiconductors

Doping an intrinsic semiconductor doped by specific impurities makes it extrinsic, while keeping the initial purity level well above the doping rate. Depending on the nature of the atoms introduced, the number of electrons becomes much greater than the number of holes so the semiconductor is called type n, either the number of holes becomes much higher than that of electrons or the semiconductor is called type p.

I.4.2.1.n-type semiconductors

By introducing penta-valent atoms such as phosphorus P, arsenic As into a crystal, some bonds are blocked giving way to these extra atoms which have five valence electrons which fills the bonds by leaving a free electron in the crystal not closely linked to the nucleus ($E \approx 0.01\text{eV}$), and passes easily into the conduction band. Penta-valent or donor atoms become positive ions after the excess electrons pass through the conduction band [4]. This greatly increases the conductivity of the doped material. Negative charges (electrons) are said to be the majority.

I.4.2.2. p-type semiconductors

In this case we introduce trivalent atoms such as Gallium Ga, Indium In, boron B, aluminium Al. The impurity is missing a valence electron to ensure the 4 bonds with the neighboring silicon atoms. A low energy input (0.05eV) is enough for an electron of nearby

silicon to be captured by the impurity: there is formation of a hole that is loosely bound and therefore mobile. The trivalent atoms (acceptors) become negative ions by capturing an electron. Considering the doping rates. These holes are much more numerous than the intrinsic carriers of pure crystal. The extrinsic conduction type p (positive) increases and is ensured by holes, the holes become majority.

I.5. Classification of semiconductors

Semiconductors are classified according to their chemical composition and stoichiometry.

I.5.1. Elementary semiconductors

There are elementary semiconductors such as silicon (Si), the germanium (Ge) and grey tin (α - Sn), which belong to Group IV of the periodic table.

I.5.2. II -VI semiconductors

There are also II -VI semiconductors combining the elements II (Be, Mg, Ca, Sr, Ba) and VI (O, S, Se, Te). The combination of several elements of these two groups also gives a multi-component semiconductor.

I.5.3. Transparent metal oxides (TCOs)

Besides their passive character, transparent metal oxides (TCOs) can act also as an active component. TCOs can be used as a semiconductor material. These materials are competing with existing silicon-based technology [5].

TCOs can be classified into two groups; n-type and p-type

I.5.3.1. n-type TCOs

The majority of the charge carriers in an n-type TCO are negatively charged electrons. Since most TCOs are n-type, practical applications are where one can most frequently find them [6]. The introduction of electron donor atoms causes the appearance of a pseudo energy level located just below the conduction band (BC). Thus, energy necessary for the electrons to migrate into the conduction band is much more easily reached, hence the increase of conduction.

It has been reported that it is possible to achieve very low resistivity values (of the order of $10^{-4}\Omega \cdot \text{cm}$), when doping rates are very high [7].

I.5.3.2. p-type TCOs

The majority of the charge carriers in p-type TCOs are positively charged holes [8]. The introduction of electron-acceptor atoms causes the appearance a pseudo level above the valence band (BV). The energy to be supplied to valence electrons to pass on this acceptor level is low, and the departure of electrons leads to holes in the valence band. P type doping is currently an important challenge and one of the keys to the development of optoelectronic components. This type of doping was carried out only by physical deposition methods [9]. The conductivity type p was first discovered by Aoki et al. in 2001[10]. Since then, more and more doping attempts on different oxides have been tested, such as doping of NiO with lithium (Li) [11], and sodium Na [12], and potassium K [13]

I.6. Nickel oxide (NiO)

Nickel oxide (II) is one of the semiconductors most favored antiferromagnetic transition material and forms the basis of a wide range of applications. As a result, it has been the subject of numerous experimental and theoretical research in recent years. Nickel (II) oxide has the chemical formula NiO and is a chemically stable material. The main commercial forms of refined, comparatively pure nickel are NiO [14]. NiO is typically created artificially because it is actually quite rare in nature. Every year, about countless million kilograms are produced [15]. Black NiO and green NiO are the two main colors of NiO. The green crystal almost perfectly satisfies the stoichiometric ratio of one Ni to one O atom, or $\text{Ni}_{1.00} \text{O}_{1.00}$. The black material has an excess of O i.e., a deficiency of Ni with formula averaging $\text{Ni}_{0.98} \text{O}_{1.00}$ and belongs to the class of non-stoichiometry compounds. NiO is hardly soluble; at 20 °C, its solubility in water is 1.1 mg/L, its density is 6.67 g cm⁻³, and its melting point is 2233 K [14]. NiO is produced using a variety of methods. In addition, when oxygen and nickel powder are heated to temperatures above 400° C, NiO is produced. Additionally, green nickel oxide can be produced by heating a mixture of nickel powder compound and water to a temperature of 1000° C; this technique was employed in a number of industrial processes, and the rate of the reaction can be accelerated by adding NiO [16].

The successful and streamlined method of fabrication uses pyrolysis to create a light green powder from nickel (II) salts like hydroxide, nitrate, and carbonate. Grey to black powders that indicate non-stoichiometry can result from heating the metal in an oxygen or air atmosphere when synthesizing the elements [17].

I.6.1. NiO properties

Nickel oxide has a set of properties (magnetic, optical, electrical and chemical) that allow for use in various applications.

I.6.1.1. NiO crystallographic properties

The mineral form of bunsenite NiO is rare. As a result, it is synthesized. There are many different kinds of ways to create NiO. The most well-known of these is the pyrolysis of Ni^{2+} . The nickel oxide (NiO) crystallizes in a cubic structure with a lattice parameter of $a = 4,176 \text{ \AA}$ (JCPDS, 47-1049) and a type NaCl [18]. The table (I.1) summarizes the main crystallographic characteristics of this oxide.

Table I.1. Crystallographic properties of NiO

NiO	Structure	Cell	Lattice	R	plan	Space group
	Cubic	$a=b=c$	A and B	$(\text{Ni}^{2+}) = 72.0\text{Pm}$	Ni= (0,0,1/2)	Fm3m
	CFC	$\alpha=\beta=\gamma=\pi/2$	Cation (Ni^{2+}) Anion (O^{2-})	$(\text{O}^{2-}) = 140\text{Pm}$	O= (0, 0, 0)	

Figure (I.2) explains the crystal structure of nickel oxide and the literature's description of the DRX of NiO in cubic phase (CFC) [18].

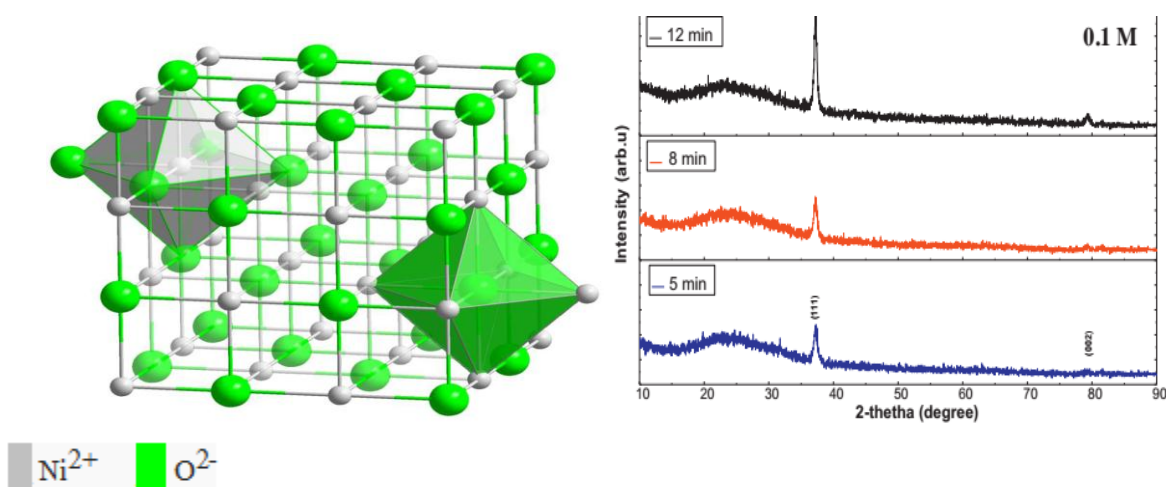


Figure I.2. The crystallographic structure and DRX diffractogram of NiO [19].

I.6.1.2. Electronic properties of NiO

The band structures that distinguish transition metal oxides from other types of oxides determine whether the oxide has an isolating or semi-conducting character. Nickel oxide is one of the transition metals that, through their applications, form a significant family. Their magnetic property is caused by the presence of the "band d" energy band. 3d wave function are nearly located around the atomic nucleus. The band's width is in the range of 5 eV, and it can hold up to 10 electrons in total [20].

The diagram of NiO's molecular orbitals in its ground state is shown in figure (I.3) [21].

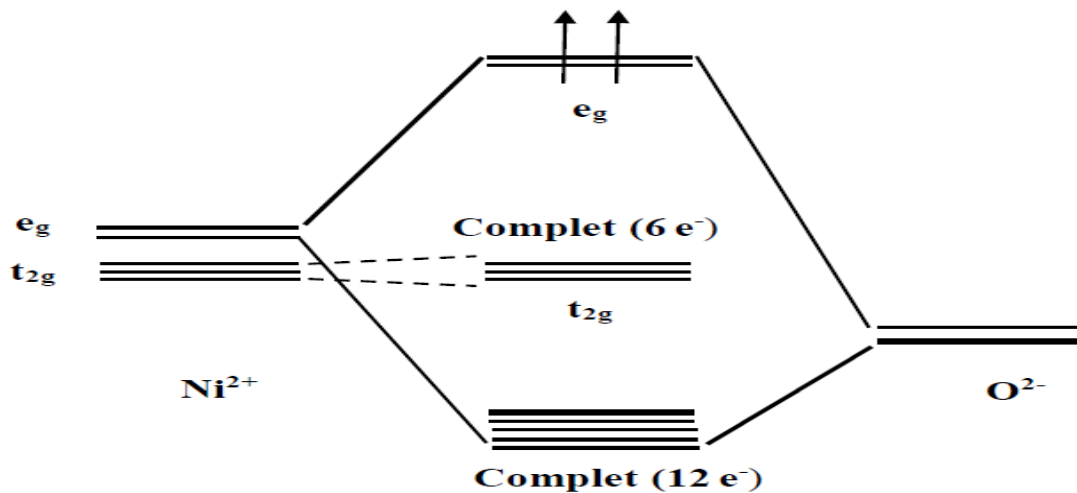


Figure I.3. Representation of the NiO energy levels [21].

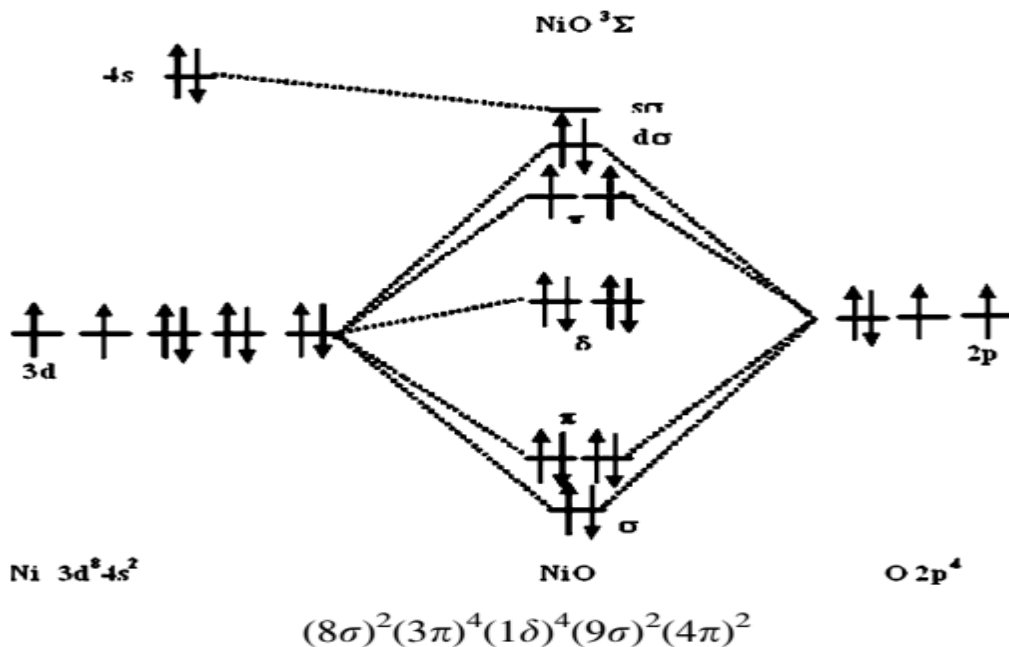


Figure I.4. Schematic representation of the molecular structure of NiO in its ground state (Ni atom and O orbital) [21]

The 3d energy level is responsible for magnetism; it was marginally higher than the 4d energy level in the conduction band [22]. 3d orbitals are composed of two levels which are t_{2g} and e_g, the orbital of ions oxide in recovery with the 3d nickel orbitals constitute the level of low energy, this level and the t_{2g} level are full (figure I.4). Just two electrons make up the anti-latching e_g level. The electronic configuration of nickel and oxygen are: Ni: 3d⁸, O: 2p⁴ [23]. There are two main theories that deal with oxygen-to-nickel p-d transitions (charge transfer) and cationic d-d transitions, respectively, to explain the absorption of NiO. From theoretical point of view, the Ni²⁺ ions have a partially filled d shell in a 3d⁸ ground-state configuration in a completely ionic model of NiO as mentioned above. According to conventional band theory, this should result in metallic behavior, yet NiO is a semiconductor with a wide band gap. Since a long time ago, DFT studies have been successfully used to describe a variety of details of electronic structure, magnetic coupling, and band gap characteristics. however, it incorrectly predicts that the band structure of TM oxides is metallic rather than describing it as an insulator. According to LSDA studies, NiO should have a band gap of about 0.5eV, which is smaller than the outcomes of the experiment. Consequently, a variety of computational techniques have been used to predict the NiO energy band gap, and various outcomes are shown in table (I.2) as a result. A number of researchers have looked into the band structure of NiO's bulk and surface using various techniques, including DFT [24- 27], DFT+U [28- 30, 34-35], and GW [24, 31-32].

Table I.2. NiO energy band gap calculated using various methods.

Method	Ref.	Band gap (eV)	Structure
LDA+U; U=4.6	[29]	2.7	Bulk; Cubic
LSDA+U; U=6.2	[27]	3	Cubic
LDA+U; U=5		2.6	Bulk; Cubic
LDA+U; U=5	[33]	2.1	Surface 001
LDA+U; U=5		0.8	Surface 111 p (2×2)
DFT+U ; U=7	[28]	3.8	Bulk; Rhombohedral
LSDA+U ; U=6.1	[34]	3.7	Bulk
LSDA+U; U=5.4	[35]	4.1	Bulk
MBJLDA	[25]	4.16	Bulk
LSDA+U ; U=6.2		4.04	Cubic; Surface 001
GGA (96)+U ; U=6.2	[30]	4.31	
GG (06)+U ; U=6.2		3.4	
GW	[24]	4.8	Bulk
Hybrid B3LYP	[36]	3.9	Bulk
sX-LDA	[26]	3.85; 4.1	Cubic
GW@LDA	[31]	5.5	Rhombohedral
GoWo@LDA+U;U=5.2	[37]	3.76	Rhombohedral
U+GW; U=4	[32]	3.99	Rhombohedral

From the projected density of states, some studies have predicted the conduction band of NiO and the upper edge of the valence band to be of the same character, i.e Ni 3d, making NiO to become a Mott-Hubbard insulator. Some studies have predicted that the conduction band of NiO and the upper edge of the valence band will be of the same character, i.e. Ni 3d, causing NiO to become a Mott-Hubbard insulator. However, the upper edge of the valence band was correctly predicted by some other authors [27, 29, 31, 34] to be of the O 2p character and that NiO should therefore be classified as a charge-transfer insulator, as opposed to a Mott-Hubbard insulator.

I.6.1.3. Thermal oxidation of nickel

Due to its use in numerous technologies, nickel oxidation has attracted a lot of attention for almost a century. As previously mentioned, one of the most prevalent phases of nickel oxides is known as bunsenite (NiO). There have also been claims of other phases, including Ni₂O₃ and NiO₂ [38]. As was previously demonstrated, the results of these investigations indicated that NiO is a metal with a p-type semiconductor in which nickel vacancies are the predominant defects. Some typical thermodynamic properties for nickel and NiO are listed in table (I.3). For the reaction (I.3), it is also possible to plot G's behaviour in an Ellingham diagram (figure (I.5)).

Table I.3. Standard thermodynamic properties of nickel and NiO [38]

	ΔH_f (Kj mol ⁻¹)	ΔG_f (Kj mol ⁻¹)	ΔS_f (Kj mol ⁻¹)
Ni(s)	0	/	29.9
NiO (s)	-239.701	-211.539	37.991

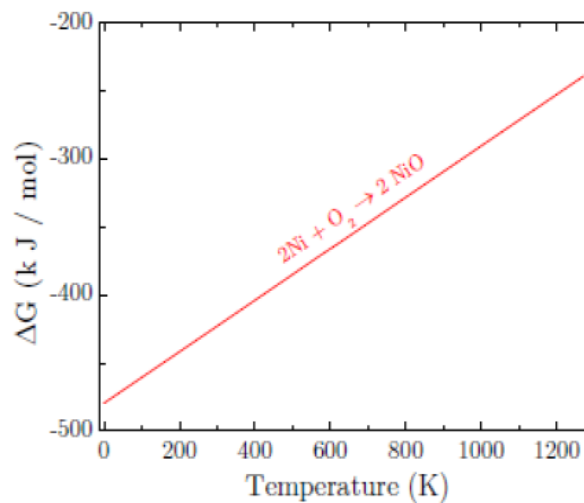


Figure I.5. Gibbs free energy versus temperature in nickel oxidation for the formation of NiO [38].

It is anticipated that the reaction will come after the conversion of nickel that takes place in the oxidation route:



I.6.1.4. Optical properties of NiO

NiO is a semi-conductor that is transparent to ultraviolet (UV), visible, and near-infrared radiation [39]. The optical forbidden band has been estimated to be around 4eV, and the refractive index is 2.33 at 2eV photons [40]. Because Ni^{3+} ions are present inside the oxide lattice, there is a charge transfer transition, which causes an absorption in the visible spectrum [41]. With a width of 4.3–4.4eV, the valence band is made up of localized nickel 3d-bands [42]. Oxygen was coupled with the nickel 3d states at the 2p band, where it had a large energy of 4–8eV. However, the nickel 3d, 4s, and 4p unoccupied states make up the conduction band [43]. The optical absorption gap in NiO is thought to be caused by either a p–d transition in one Ni atom [44] or a d–d transition involving two nearby Ni atoms in the lattice [45]. Figure (I.6) presents nickel oxide transmittance specter in literature [46] and table (I.4) illustrates the optical parameters of NiO thin films obtained by CVD spray method in experimental studies.

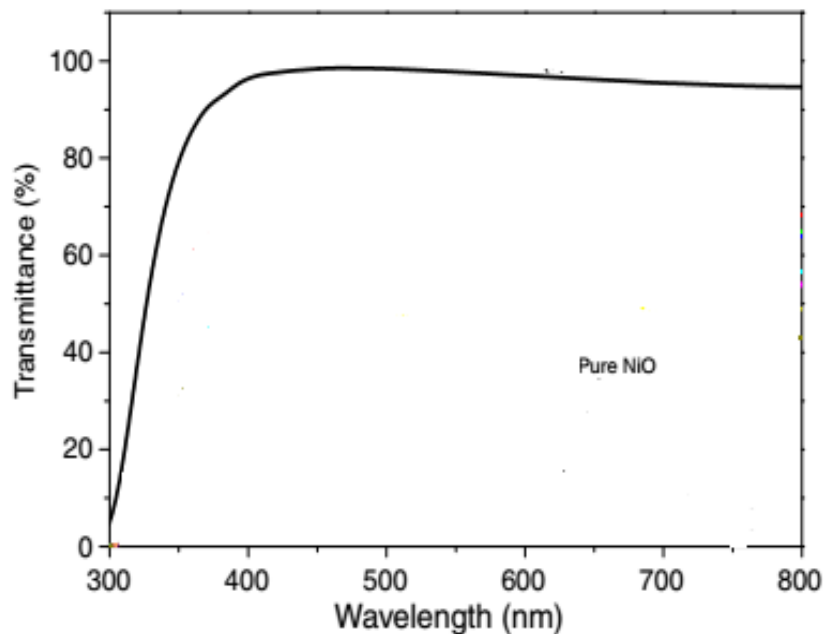


Figure I.6. NiO transmittance spectra [46].

Table I.4. Experimental NiO energy band gap.

Band gap (eV)Ref.	NiO preparation techniques	Method used
3.8	[47] Thermal decomposition	TEM, UV-Vis
3.32	[48] Electron beam evaporation	UV-Vis
3.89 - 3.92	[49] Cationic surfactant (CTAB)	PL, UV-Vis
3.65 - 3.82	[50] DC reactive magnetron sputtering	SEM, UV-Vis-NIR
3.4 - 3.71	[51] RF magnetron sputtering	SEM; UV-VIS-IR
3.47 - 3.86	[52] Sol gel spin coating	SEM, UV-VIS-IR
3.35 - 3.73	[53] Automated Liquid Flow Deposition	SEM, ALFDT
3.744 - 3.867	[54] Sol-gel dip coating	TEM, UV-Vis-NIR
3.6	[56] Thermal oxidation	UV-Vis
2.10 - 3.9	[57] Chemical bath deposition	Absorption, UV-VIS- NIR spectroscopy,
3.87	[58] Verneuil (flame fusion)	SCP
3.17 - 3.83	[60] Spray pyrolysis	UV-Vis-NIR

I.6.1.5. Electrical properties of NiO

NiO has a broadband gap energy and p-type oxide semiconductor characteristics. In theory, stoichiometric purity NiO is a Mott-Hubbard insulator, with a room temperature resistivity of the order of 10^{13} ohm.cm. The insulating properties of NiO have been explained by a number of theories, including cluster theory, localized electron theory, band theory, chemical band approach, and band theory. Pale green is the color of stoichiometric NiO. It has been suggested that the presence of Ni^{3+} ions is related to the black color of NiO.

As charge compensation for the nickel vacancies, these ions are present in NiO [60]. Different samples exhibit varying conductivities, indicating that random impurities or lattice defects dominate the conduction. The appearance of nickel vacancies or an excess of oxygen is suggested as the cause of electronic conduction in undoped NiO. When the active species of nickel and oxygen affect separately on the growth of the film surface in the ionic crystal of NiO, the orientation of the film is typically influenced by the orientation of O_2 . This is due to the fact that NiO lacks the directivity of a mixture of Ni^{2+} and O^{2-} , and that O_2 's radius (0.140 nm) is greater than Ni^{2+} 's (0.069 nm) [61].

A significant concentration of interstitial O atoms in the structure is not possible due to the size of the oxygen atom. Due to the excess O in NiO, the normally occupied Ni sites now have empty spaces, as shown in figure (I.7). To maintain the crystal's overall electrical neutrality, two Ni^{2+} ions should be changed to Ni^{3+} for each empty Ni^{2+} site. It can be suggested that the Ni^{3+} ions introduced into the crystal in this way are positive centers capable of moving between different Ni^{2+} sites. It appears as though a positive hole is moving around the Ni^{2+} sites when an electron jumps from a Ni^{2+} to a Ni^{3+} site. As a result, an excess of oxygen transforms NiO into a p-type semiconductor [62].

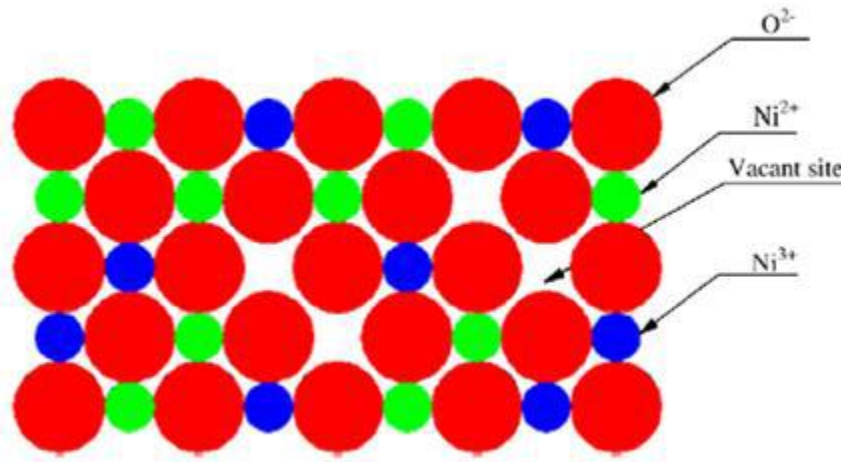


Figure I.7. A schematic of pure non-stoichiometric NiO crystal

Table.I.2. Some electrical properties of NiO

NiO	Element	Unity	range	Ref
	mobility	($\text{Cm}^2/\text{V.S}$)	0.1-1	[63]
	conductivity	($\Omega. \text{Cm}$) ⁻¹	0.1-1	
	Electronic density	(Cm^3)	10^{18} - 10^{19}	

I.6.1.6. Magnetic properties

The magnetic properties of NiO have been studied in both theoretical and experimental contexts. Numerous magnetic orderings, such as ferromagnetic (FM) [26, 70–72] non-magnetic (NM) [73], antiferromagnetic type one (AF1) [26] and antiferromagnetic type two (AF2) [26, 73, 74] have been observed on NiO. The magnetic moments of the Ni ion align ferromagnetically on every (111) plane and antiferromagnetically for adjacent planes in the AF2 case, but the total magnetization is zero [75]. Ni atoms have finite magnetic

moments, but the total magnetization is zero. All spin moments are aligned in one direction in the FM state. According to calculations and experiments, the NiO AF2 ordering is the most stable magnetic configuration, followed by the FM state and the AF1 ordering [73]. The covalent bonding between the Ni and O atoms, or hybridization [35] was found to be stronger than the coupling of the d-d states between nearest neighboring Ni ions. Additionally, the opposite spin next-nearest neighbors of Ni ions are energetically preferred, making the AF spin structure the ground state of NiO. The magnetic moment values of NiO were predicted by some theoretical calculations to be $1.75 \mu_B$ [25], $2.00 \mu_B$ [30], and $1.91 \mu_B$ [35]. According to the experiments, NiO's magnetic moment value varied between 1.7 and 1.9 B [75].

I.6.2. NiO applications

NiO is one of the important P-type classes of semiconducting materials. It has distinctive optical, electrical, and magnetic properties and finds a huge variety of applications such:

I.6.2.1. Photo voltaic cells

The first photovoltaic cell, a new generation of solar cells similar to those developed by Grätzel, was developed on the basis of the color-sensitive n-type semiconductors. A type p (SC-p) semi-conductor was used in these last. Thus, the first color-changing type p semiconductor cell (DSSC-p) was built in the Lindquist team's laboratory in Sweden in 1999 using nickel oxide (NiO), an intrinsic type p semiconductor.

The conversion rate, however, fell short of the first DSSC-n's (7,9%) level and did not exceed 0,0076%. Since then, the study of DSSCs-p has become significantly more intense. As a result, earnings have been able to change over the years, going from 0,0076% in 1999 to 0,4% in 2012 and 1,3% in 2013. The current record for 2015 is 2.5 percent [64].

I.6.2.2. Protective films

The simplest application of the TCO as surface refinishing materials is the direct application of one of their characteristics. In fact, because of free charges, TCO reflect on near and far infrared wavelengths. These materials can be used to create devices such as heated mirrors, an application of HMF with thin ITO couches, a multi-layer heated TiO₂ coating for automobiles, solar cell technology, etc [65]. Utilizing TCO of type-p in this application, metal oxides are used in the field of multi-paned electrochromic windows made of TiO₂, solar cell technology, etc.

I.6.2.3. Antimicrobial activity:

NiO nanotechnologies are very promising for biomedical and bio-sensible applications, for example the brain-implanted NiO nanotechnologies are very promising. It was proved in literature that Ce doped NiO nanomaterial is a superb performance with great sensitivity, selectivity, and stability. Additionally, the antimicrobial activity of NiO doped Ce nanostructures were evaluated [64].

I.6.2.4. Gas sensors:

A component is defined as a gas sensor if at least one of its physical characteristics changes when exposed to a change in the gaseous environment. There are two significant families of metallic oxides that are used as gas sensors. The first is type n (conduction by electrons, for instance SiO₂). They have a conductivity that decreases with an increase in partial pressure of oxygen. They full fill the majority of requirements for gas sensors applications because they are more stable and have characteristics that are more suited to chimi-sorption, the mechanism that predominates in this class of gas sensor. The second family includes all types p (conduction by trench: for instance, NiO). They have a conductivity that increases with an increase in partial pressure of oxygen. They are known to be relatively unstable due to their propensity to exchange lattice oxygen easily with the air. For the time being, P-types are used for specific applications like high-temperature oxygen sensors. For instance, that which is based on NiO [66].

I.6.2.5. Superconductors

Electrochemical supercondensators have developed into key components for energy storage. Their energy and power densities fall in the middle of batteries and condensers, respectively. Although they have a high energy density, batteries and piles have a low power density. Between these two categories of energy storage systems, the supercondensators fit both in terms of energy and power. There are numerous oxidation states in the oxides of transition metals, some of which are conductors. This is the reason they can be prepared with a large, specific surface area. Therefore, metal oxides are good building materials for supercondensators..The way these oxides are synthesized affects their characteristics (specific surface area, crystallinity, conductivity, etc.), which in turn affects their electrochemical characteristics. Nickel oxide is regarded as a promising supercapacitor material, particularly in the case of porous NiO films that have higher capacities due to their unique, significant surface areas.

I.6.2.6. Batteries:

American inventor Thomas Edison created the renowned battery in 1902 using iron-nickel electrodes dipped in an alkaline solution. As a result, numerous projects based on the Edisonian principle on these kinds of batteries have been carried out. Hongjie Dai and his team have created a new Ni-Fe battery, for instance, by including carbon nano-tubes and graphene in the electrodes [67]. The nickel-hydride metal battery has drawn a lot of interest due to its long lifespan and its high levels of specific energy and power [68].

Due to its long lifespan, high specific energy, and specific power, the nickel-hydride metal battery has received a lot of attention. Additionally, nickel oxides are used as the anode in lithium batteries, which are widely used today in a variety of electrical and electronic devices [69]. Nickel hydroxide is widely used as an electrode in alkaline batteries, including those made of nickel-fer (Ni-Fe), nickel-cadmium (Ni-Cd), nickel-hydride metal (Ni-MH), and nickel-zinc (Ni-Zn) [39].

I.7. Earlier works done on alkali doped NiO based thin film: A Review

In (2015) Y.R. Denny, et al employed electron beam evaporation technique to deposit pure and Na-doped nickel oxide (NiO) thin films on glass substrates. They studied the effect of Na doping on the electrical and optical properties and electronic structure of NiO thin films using X-ray photoelectron spectroscopy (XPS), reflection electron energy loss spectroscopy (REELS), X-ray absorption near edge structure, and extended X-ray absorption fine structure. It was established that Na-doped NiO thin films exhibited relatively low resistivity compared to undoped NiO thin films. In addition, the Na-doped NiO thin films deposited at room-temperature have p-type conductivity with a low electrical resistivity of 11.57 Ω cm and high optical transmittance of 80% in the visible light region [11].

In (2016) A. Loukil et al have deposited undoped and 1, 2, 3% molar rates of potassium element (K) doped NiO thin films substrates by a simple mini spray technique at 460 °C. Structural study by means of X-ray diffraction shows that all K-doped NiO thin films crystallized in cubic space group with some noticeable changes in terms of [K]/[Ni] ratio. Raman spectroscopy reveals the principal NiO vibration's mode with the shift related to K incorporation in NiO matrix. For all NiO:K prepared thin films, PL measurements show three large bands located at 405, 420, 485 and 529 nm. Electrical properties were performed using impedance spectroscopy technique in the frequency range 5 Hz–13 MHz at various

temperatures. DC conductivity is thermally activated showing a semiconductor behavior of NiO:K sprayed thin films. This study shows that the electrical conductivity is thermally activated. The calculated values of the activation energy show semiconductor behavior of such films. On the other hand, AC conductivity is investigated through Jonscher law. The imaginary part of the complex impedance has a maximum whose relaxation frequency increases with temperature according to Arrhenius law [13].

Using a rapid pyrolysis sol-gel technique, **Wang et al. (2016)** deposited K-doped NiO films ($\text{Ni}_{1-x}\text{K}_x\text{O}$) on glass substrates. With the aid of X-ray diffraction, scanning electron microscopy, an atomic force microscope, a Hall Effect measurement, and a UV-vis spectrophotometer, the films' structural, morphological, electrical, and optical properties were examined. According to their findings, all elaborated films had cubic structures, and as K doping concentration increased, the residual stress in the films changed from residual compressive stress to residual tensile stress. The K doping concentration significantly influenced the morphologies of the films. They examined the optical band gaps energy of the films and found that it was roughly constant while also confirming that the transmittance generally decreased with increasing K doping concentration [2].

Using the sol-gel spin coating technique, **in 2014Sta et al**, [11] prepared un-doped and lithium (Li) doped NiO thin films on glass slides using nickel acetate and lithium chloride as the sources of nickel and lithium, respectively. AFM and X-ray diffraction (XRD) were used to examine the effects of layer count on the structural, optical, and electrical properties of NiO thin films, respectively. It was explained to them that as the number of layers increased, so did the film's thickness. Four layers of undoped NiO films with high optical transparency were found to be the best appropriate number. This hypothesis was used to create lithium doped NiO films. They demonstrated how the films' morphology changes as the solution's Li concentration rises. The preferred orientations of the films are revealed by XRD to be polycrystalline. It was stated that an increase in Li content causes the optical transmittance of the films to increase in the visible wavelength.

In 2010, Jang et al. [77] used RF magnetron sputtering on glass substrates to create the lithium-doped nickel oxide films. The films' lithium content ranged from 0 to 16 weight percent. Researchers have looked into how characteristics like microstructure, resistivity, and electrical stability are affected by Li concentration. According to reports, the doped Li ions

help to fill crystal defect sites like vacancies or congregate on the film's surface. It was intended to demonstrate two things. First, doped Li filled the Ni vacancies in the film, reducing its electrical conductivity. However, when the Li doping level was further raised, some lithium was insulated on the film's surface and developed bulges. As a result, the electrical aging of the Li-doped NiO films decreased, and their conductivity was more stable.

In 2010 Titas Dutta et al [78] have deposited Li doped NiO thin films on c-sapphire by pulsed laser deposition. From the analysis of the resistivity data, they found that doped Li ions occupy the substitutional sites in the films, thus the p-type conductivity enhanced. The $\text{Li}_{0.07}\text{Ni}_{0.93}\text{O}$ film had a minimum resistivity of 0.15 cm. According to estimates, the activation energy of Li doped NiO films lies between 0.11 and 0.14 eV. A potential electrical transport mechanism is discussed in light of these values. Additionally, a p-n heterojunction has been created for the p-Li doped NiO with n-ZnO that has been optimized. Reduced leakage current was achieved by inserting i-Mg-ZnO between the p and n layers, which improved the current-voltage characteristics. With a turn-on voltage of 2.8 V and a breakdown voltage of 8.0 V, the p-i-n heterojunction demonstrated good rectification behavior.

References

- [1] J.P. Mercier, G. Zambelli, W. Kurz, Introduction à la science des matériaux, EPFL Press 1999.
- [2] D.F. Shriver, P.W. Atkins, Chimie inorganique, Boeck université, (1999) p107.
- [3] Frederic P Miller, Agnes F Vandome, John Mc Brewster, " Semiconducteurs ", VDM Publishing House Ltd., 2010.
- [4] Michel Sauzade, " Introduction à l'électronique analogique ", Paris sud, (1995).
- [5] N. M. Pinto Neves, Al-doped ZnO ceramic sputtering targets based on nanocrystalline powders produced by emulsion detonation synthesis – deposition and application as a transparent conductive oxide material, PhD thesis, university of Nova de Lisboa, (2015).
- [6]. A. Martinson, D. Ginley, Synthesis of Single Phase SrCu₂O₂ from Liquid Precursors, Journal of Young Investigators, 3 (2004) 10
- [7] T.L. Chu, S.S. Chu, Thin film II–VI photovoltaics, Solid-State Electronics, 38 (1995) 533-549.
- [8] A. Banerjee, K. Chattopadhyay, Recent developments in the emerging field of crystalline p-type transparent conducting oxide thin films, Progress in Crystal Growth and Characterization of materials, 50 (2005) 52-105.
- [9] J. P. Monsier, S. Chakrabarti, B. Doggett, E. McGlynn, M. O. Henry, A. Meaney Pro. SPIE. **6474** (2007) 64740I.
- [10] T. Aoki, Y. Shimizu, A. Miyake, A. Nakamura, Y. Nakanishi, Y. Hatanaka, Physica Status Solidi B, **911** (2001) 229.
- [11] I. Sta, M. Jlassi, M. Hajji, H. Ezzaouia, Structural, optical and electrical properties of undoped and Li-doped NiO thin films prepared by sol–gel spin coating method, Thin solid films, 555 (2014) 131-137.
- [12] Y.R. Denny, K. Lee, C. Park, S.K. Oh, H.J. Kang, D.-S. Yang, S. Seo, Electronic, electrical and optical properties of undoped and Na-doped NiO thin films, Thin Solid Films, 591 (2015) 255-260.
- [13] A. Loukil, A. Boukhachem, M.B. Amor, M. Ghamnia, K. Raouadi, Effects of potassium incorporation on the structural, optical, vibrational and electrical properties of NiO sprayed thin films for p-type optical windows, Ceramics International, 42 (2016) 8274-8289.
- [14] H. Abadin, M. Fay, S.B. Wilbur, Toxicological profile for Nickel, (2005).

- [15] F. Ullmann Y. S. Yamamoto, F. T. Campbell, R. Pfefferkorn, J. F. Rounsaville, Ullmann "s encyclopedia of industrial chemistry. VCH (1996).
- [16] P. Pradyot, Handbook of Inorganic Chemicals, McGraw-Hill, Publications, (2002).
- [17] A. J. Hassan, Study of Optical and Electrical Properties of Nickel Oxide (NiO) Thin Films Deposited by Using a Spray Pyrolysis Technique, Journal of Modern Physics, 5 18(2014) 52764.
- [18] J. Wang, P. Yang, X. Wei, Z. Zhou, Preparation of NiO two-dimensional grainy films and their high-performance gas sensors for ammonia detection, Nanoscale research letters, **10**(2015) 119.
- [19] S. Faj, L'oxyde de zinc par dépôt chimique en phase vapeur comme contact électrique transparent et diffuseur de lumière pour les cellules solaires, EPFL, 2003.
- [20] M.Gerl, J.-P. Issi, Physique des matériaux, EPFL-Centre Midi, CH -1015 Lausanne ed., PPUR presses polytechniques, (1997).
- [21] C.W. Bauschlicher, P. Maitre, Theoretical study of the first transition row oxides and sulfides, Theoretical Chemistry Accounts: Theory, Computation, and Modeling (Theoretica Chimica Acta), **90** (1995) 189-203.
- [22] O. Bidault, M. Maglione, M. Actis, M. Kchikech, B. Salce, Polaronic relaxation in perovskites, Physical Review B, **52** (1995) 4191.
- [23] A.K. Ramasami, M. Reddy, G.R. Balakrishna, Combustion synthesis and characterization of NiO nanoparticles, Materials Science in Semiconductor Processing, **40** (2015) 194-202.
- [24] S.V. Faleev, M. Van Schilfgaarde, T. Kotani, All-electron self-consistent GW approximation: Application to Si, MnO, and NiO, Physical review letters, 93 (2004) 126406.
- [25] F. Tran, P. Blaha, Accurate Band Gaps of Semiconductors and Insulators with a Semilocal Exchange-Correlation Potential, Physical review letters, 102 (2009) 226401.
- [26] R. Gillen, J. Robertson, Accurate screened exchange band structures for the transition metal monoxides MnO, FeO, CoO and NiO, Journal of Physics: Condensed Matter, 25 (2013) 165502.
- [27] S.L. Dudarev, G.A. Botton, S.Y. Savrasov, C. Humphreys, A.P. Sutton, Electron-energy-loss spectra and the structural stability of nickel oxide: An LSDA+ U study, Physical Review B, 57 (1998) 1505.

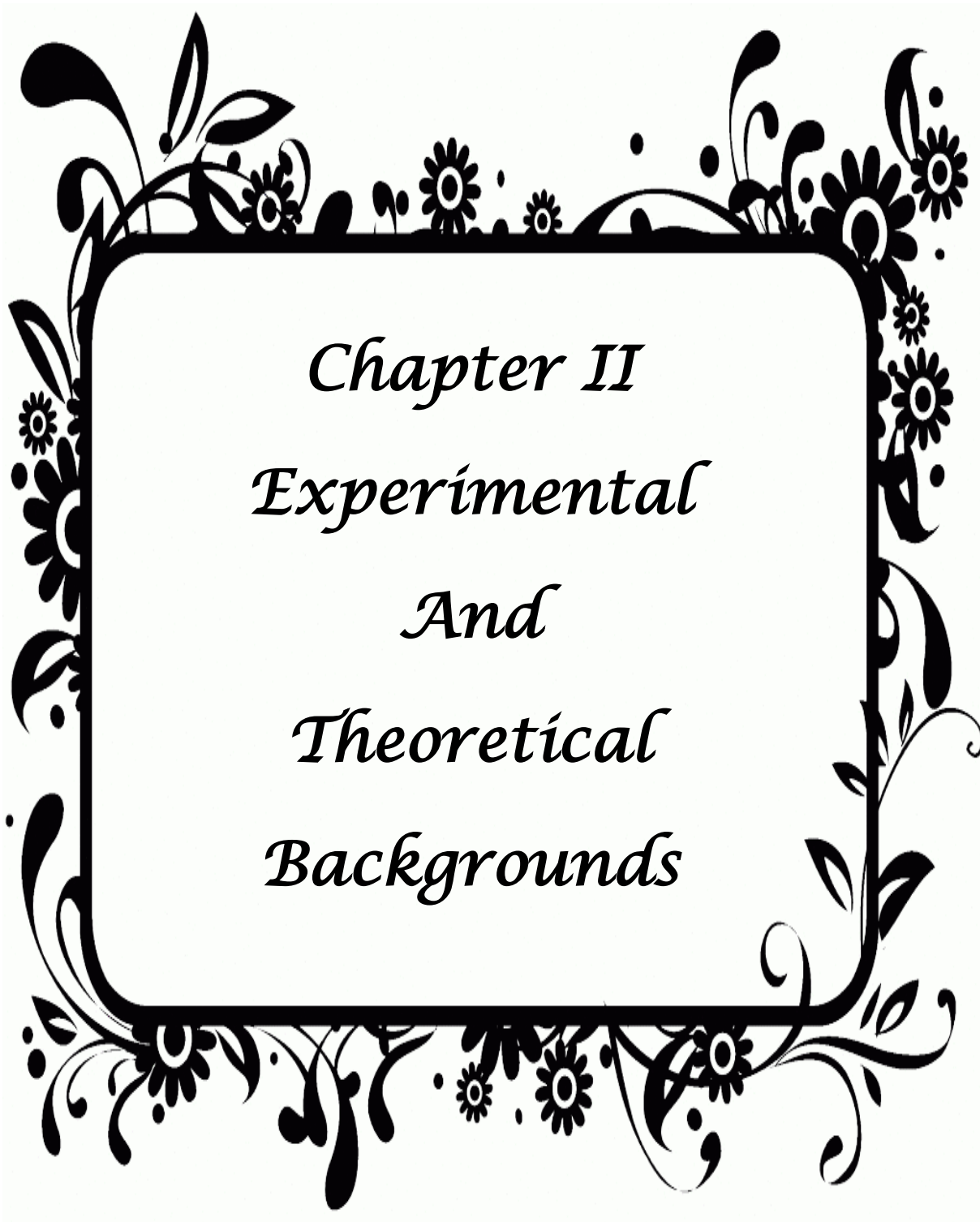
- [28] M. Forti, P. Alonso, P. Gargano, G. Rubiolo, Transition metals monoxides. An LDA+ U study, *Procedia Materials Science*, 1 (2012) 230-234.
- [29] M. Cococcioni, S. De Gironcoli, Linear response approach to the calculation of the effective interaction parameters in the LDA+ U method, *Physical Review B—Condensed Matter and Materials Physics*, 71 (2005) 035105.
- [30] T. Cai, H. Han, Y. Yu, T. Gao, J. Du, L. Hao, Study on the ground state of NiO: The LSDA (GGA)+ U method, *Physica B: Condensed Matter*, 404 (2009) 89-94.
- [31] F. Aryasetiawan, O. Gunnarsson, Electronic structure of NiO in the GW approximation, *Physical review letters*, 74 (1995) 3221.
- [32] S. Kobayashi, Y. Nohara, S. Yamamoto, T. Fujiwara, GW approximation with LSDA+ U method and applications to NiO, MnO, and V₂O₃, *Physical Review B—Condensed Matter and Materials Physics*, 78 (2008) 155112.
- [33] O. Bengone, M. Alouani, J. Hugel, P. Blöchl, LDA+ U calculated electronic and structural properties of NiO (0 0 1) and NiO (1 1 1) p (2× 2) surfaces, *Computational materials science*, 24 (2002) 192-198.
- [34] P. Wei, Z.Q. Qi, Insulating gap in the transition-metal oxides: A calculation using the local-spin-density approximation with the on-site Coulomb U correlation correction, *Physical Review B*, 49 (1994) 10864.
- [35] J. Hugel, M. Kamal, Electronic ground state of MnO, FeO, CoO and NiO within the LSDA+ U approximation, *Solid state communications*, 100 (1996) 457-461.
- [36] J. Muscat, A. Wander, N. Harrison, On the prediction of band gaps from hybrid functional theory, *Chemical Physics Letters*, 342 (2001) 397-401.
- [37] S. Sriram, A. Balu, A. Thayumanavan, Design and development of automated liquid flow deposition method for thin film formation, *Applied Science Research*, 3 (2011) 438-447.
- [38] A. Citra, G.V. Chertihin, L. Andrews, M. Neurock, Reactions of laser-ablated nickel atoms with dioxygen. Infrared spectra and density functional calculations of nickel oxides NiO, ONiO, Ni₂O₂, and Ni₂O₃, superoxide NiOO, peroxide Ni(O₂), and higher complexes in solid argon, *The Journal of Physical Chemistry A*, 101 (1997) 3109-3118.
- [39] Y.-M. Wang, D.-D. Zhao, Y.-Q. Zhao, C.-L. Xu, H.-L. Li, Effect of electrodeposition temperature on the electrochemical performance of a Ni(OH)₂ electrode, *Rsc Advances*, 2 (2012) 1074-1082.

- [40] P. Kofstad, Defects and transport properties of metal oxides, *Oxidation of metals*, 44 (1995) 3-27.
- [41] N. Tsuda, K. Nasu, A. Fujimori, K. Siratori, *Electronic Conduction in Oxides*, second ed., Springer, Berlin, 2000.
- [42] K.S. Lee, H.J. Koo, K.H. Ham, W.S. Ahn, Crystal Molecular Orbital Calculation of the Lanthanum Nickel Oxide by Means of the Micro-Soft Fortran, *Bull. Korean. Chem. Soc.*, 16 (1995) 164.
- [43] S. Hüfner, T. Riserer, Electronic structure of NiO, *Physical Review B*, 33 (1986) 7267.
- [44] A. Williams, J. Kübler, K. Terakura, Williams, Kübler, and Terakura Respond, *Physical Review Letters*, 54 (1985) 2728.
- [45] R. Merlin, Electronic Structure of NiO, *Phys Rev. Lett.*, 54 (1985) 2727.
- [46] S. Chen, T. Kuo, Y. Lin and H. Lin, Preparation and properties of p-type transparent conductive Cu-doped NiO films *Thin Solid Films*, **519** (2011) 4944–4947.
- [47] A. Kalam, A.G. Al-Sehemi, A.S. Al-Shihri, G. Du, T. Ahmad, Synthesis and characterization of NiO nanoparticles by thermal decomposition of nickel linoleate and their optical properties, *Materials characterization*, 68 (2012) 77-81.
- [48] D. Jiang, J. Qin, X. Wang, S. Gao, Q. Liang, J. Zhao, Optical properties of NiO thin films fabricated by electron beam evaporation, *Vacuum*, 86 (2012) 1083-1086.
- [49] K. Anandan, V. Rajendran, Structural, optical and magnetic properties of well-dispersed NiO nanoparticles synthesized by CTAB assisted solvothermal process, *Nanosci. Nanotechnol. Int. J.*, 2 (2012) 24-29.
- [50] A.M. Reddy, A.S. Reddy, K.-S. Lee, P.S. Reddy, Effect of oxygen partial pressure on the structural, optical and electrical properties of sputtered NiO films, *Ceramics International*, 37 (2011) 2837-2843.
- [51] M. Guziewicz, J. Grochowski, M. Borysiewicz, E. Kaminska, J.Z. Domagala, W. Rzdokiewicz, B.S. Witkowski, K. Golaszewska, R. Kruszka, M. Ekielski, Electrical and optical properties of NiO films deposited by magnetron sputtering, *Optica Applicata*, 41 (2011).
- [52] P. Godse, R. Sakhare, S. Pawar, M. Chougule, S. Sen, P. Joshi, V.P. Patil, Effect of annealing on structural, morphological, electrical and optical studies of nickel oxide thin films, *Journal of Surface Engineered Materials and Advanced Technology*, 1 (2011) 35.

- [53] S. Sriram, A. Balu, A. Thayumanavan, Design and development of automated liquid flow deposition method for thin film formation, *Applied Science Research*, 3 (2011) 438-447.
- [54] A. Sawaby, M. Selim, S. Marzouk, M. Mostafa, A. Hosny, Structure, optical and electrochromic properties of NiO thin films, *Physica B: Condensed Matter*, 405 (2010) 3412-3420.
- [56] P. Mohanty, C. Rath, P. Mallick, R. Biswal, N. Mishra, UV-visible studies of nickel oxide thin film grown by thermal oxidation of nickel, *Physica B: Condensed Matter*, 405 (2010) 2711-2714.
- [57] F. Ezema, A. Ekwealor, R. Osuji, Optical properties of chemical bath deposited nickel oxide (NiOx) thin films, *Superficies y vacío*, 21 (2008) 6-10.
- [58] T.D. Kang, H.S. Lee, H. Lee, Optical properties of black NiO and CoO single crystals studied with spectroscopic ellipsometry, *Journal of the Korean Physical Society*, 50 (2007) 632-637.
- [59] S. Mahmoud, A. Akl, H. Kamal, K. Abdel-Hady, Opto-structural, electrical and electrochromic properties of crystalline nickel oxide thin films prepared by spray pyrolysis, *Physica B: Condensed Matter*, 311 (2002) 366-375.
- [60] H. Sato, T. Minami, S. Takata, T. Yamada, Transparent conducting p-type NiO thin films prepared by magnetron sputtering, *Thin Solid Films*, 236 (1993) 27-31.
- [61] H.W. Ryu, G.P. Choi, G.J. Hong, J.S. Park, Growth and Surface Morphology of Textured NiO Thin Films Deposited by Off-Axis RF Magnetron Sputtering, *Jpn. J. Appl. Phys.*, 43 (2004) 5524.
- [62] B. Sasi, Preparation and characterization studies of nanostructured nickel oxide and lithium doped nickel oxide thin films, PhD thesis, University of Kerala, 2007.
- [63] B. Reguig, M. Regragui, M. Morsli, A. Khelil, M. Addou, J. Bernede, Effect of the precursor solution concentration on the NiO thin film properties deposited by spray pyrolysis, *Solar energy materials and solar cells*, **90** (2006) 1381-1392.
- [64] H. Kim, R.C.Y. Auyeung and A. Piqué, Transparent conducting F-doped SnO₂ thin films grown by pulsed laser deposition, *Thin Solid Films*, **516** (2008) 5052-5056.
- [65] F. Ynineb, Contribution à l'élaboration de couches minces d'Oxydes Transparents Conducteurs (TCO), mémoire de Magister en physique, univ-Mentouri-Constantine, (2010).
- [66] C. Natarajan, G. Nogami, Cathodic electrodeposition of nanocrystalline titanium dioxide thin films, *Journal of the Electrochemical Society*, 143 (1996) 1547.

- [67] H. Wang, Y. Liang, M. Gong, Y. Li, W. Chang, T. Mefford, J. Zhou, J. Wang, T. Regier, F. Wei, H. Dai, *Nat. Commun.*, 3 (2012) 917–918.
- [68] W. Zhang, W. Jiang, L. Yu, Z. Fu, W. Xia, M. Yang, *Int. J. Hydrogen Energy*, 34 (2009) 473–480.
- [69] Y. Yuan, X. Xia, J. Wu, J. Yang, Y. Chen, S. Guo, Hierarchically ordered porous nickel oxide array film with enhanced electrochemical properties for lithium ion batteries, *Electrochemistry communications*, 12 (2010) 890-893.
- [70] K. Karthik, G.K. Selvan, M. Kanagaraj, S. Arumugam, N.V. Jaya, Particle size effect on the magnetic properties of NiO nanoparticles prepared by a precipitation method, *Journal of Alloys and compounds*, 509 (2011) 181-184.
- [71] I. Sugiyama, N. Shibata, Z. Wang, S. Kobayashi, T. Yamamoto, Y. Ikuhara, Ferromagnetic dislocations in antiferromagnetic NiO, *Nature nanotechnology*, 8 (2013) 266-270.
- [72] Y. Ichiyanagi, N. Wakabayashi, J. Yamazaki, S. Yamada, Y. Kimishima, E. Komatsu, H. Tajima, Magnetic properties of NiO nanoparticles, *Physica B: Condensed Matter*, 329 (2003) 862-863.
- [73] W.-b. ZHANG, Y.-l. HU, B.-y. TANG, Phase stability and structural distortion of NiO under high pressure, *Transactions of Nonferrous Metals Society of China*, 16 (2006) s52-s58.
- [74] I. Sugiyama, N. Shibata, Z. Wang, S. Kobayashi, T. Yamamoto, Y. Ikuhara, Ferromagnetic dislocations in antiferromagnetic NiO, *Nature nanotechnology*, 8 (2013) 266-270.
- [75] X. Ren, I. Leonov, G. Keller, M. Kollar, I. Nekrasov, D. Vollhardt, LDA+ DMFT computation of the electronic spectrum of NiO, *Physical Review B—Condensed Matter and Materials Physics*, 74 (2006) 195114.
- [76] N. Wang, C. Liu, C.L.B. Wen, H. Wang, S. Liu, W. Jiang, W. Ding, W. Chai, Structural, electrical and optical properties of K-doped NiO films prepared by rapid pyrolysis sol-gel technique, *Thin Solid Films*, 616 (2016) 587-593.
- [77] W.-L. Jang, Y.-M. Lu, W.-S. Hwang, W.-C. Chen, Electrical properties of Li-doped NiO films, *Journal of the European Ceramic Society*, 30 (2010) 503-508.

[78] T. Dutta, P. Gupta, A. Gupta, J. Narayan, Effect of Li doping in NiO thin films on its transparent and conducting properties and its application in heteroepitaxial pn junctions, *Journal of Applied Physics*, 108 (2010) 083715.

A decorative border of black floral and leaf motifs surrounds the central text. The border features stylized flowers, leaves, and swirling lines, creating a frame for the chapter title.

Chapter II
Experimental
And
Theoretical
Backgrounds

II.1. Experimental approach

II.1.1. Introduction

There are many and different thin film deposition techniques. In general, thin film deposition techniques are broadly classified as physical or chemical methods, few of them are discussed in the following sections. In this chapter we will focus specifically on the technique for elaboration nickel oxide thin films using **sol gel spin coating** method. The sol-gel spin coating method was chosen because of its simplicity, safety, low cost, and ability to deposit homogeneous and high-quality thin films [1]. Locally, its implementation is feasible. It also offers the benefit of creating thin films on significant surfaces, such as those of solar cells or flat-screen displays. The basic concepts of the various characterization techniques that we developed and used to analyze the films that we produced will also be covered in this chapter.

II.1.2. Physical deposition methods

To create thin films, physical deposition employs thermodynamic or mechanical methods. These approaches are more expensive, but they provide more dependable and reproducible results. Furthermore, physical procedures require tremendous energy, which are not stored by chemical reactions. To function properly, commercial physical deposition systems requires a low-pressure vapor medium [2].

II.1.2.1. Pulsed Laser Deposition

Pulsed laser deposition (PLD) is a versatile deposition technology for thin film growth that may deposit very large amounts of material. In a high vacuum, a pulsed laser, typically of ultra-violet (UV) wavelength, is used to ablate the material of the target on a regular basis. As a result, the solid material was converted into plasma, resulting in a plume emanating from the direction of the substrates. As it approached the substrate, the plume condensed to produce nano-structured sheets [3].

II.1.2.2. RF Sputtering

The RF sputter gets its name from the use of energy in the radio wave spectrum. This process is frequently utilized in the industry to coat materials used in many technical applications. An RF potential is delivered to the metal electrode placed beneath the dielectric

plate target in this technique. The typical RF frequencies used vary from 5 to 40 MHz. At RF potentials, the electrons oscillating in the alternating field have enough energy to cause ionizing collisions, and the discharge is self-sustaining. Because electrons have significantly higher mobilities than ions, many more electrons will reach the dielectric target surface during the positive half cycle than ions during the negative half cycle, causing the target to become negatively self-biased [4]. The negative dc potential on the insulator target surface repels electrons from its vicinity, forming an ion-rich sheath in front of the target. Ions pummeled the target, resulting in sputtering. The RF sputtering technique has been used to successfully prepare quartz, aluminum oxide, boron nitride thin films, and other glasses. The use of RF sputtering for thin film deposition is critical because it allows for more cost-effective deposition on large-area substrates.

II.1.2.3. Thermal evaporation

Thermal evaporation involves evaporating source materials in a vacuum chamber with a pressure of less than 10^{-6} Torr and condensing the evaporated particles on a substrate. Thermal energy is supplied to a source in this process, from which atoms are evaporated for deposition in the substrate. The source material can be finished heating by any of which the substance to be evaporated is attached [5]. Resistance heating, high-frequency induction heating, or electron beam evaporation can be used to heat larger quantities of source material in crucibles made of refractory metals, oxides, or carbon. The evaporated atoms pass through the evaporation chamber at a lower background pressure and condense on the growth surface. The deposition rate or flux is determined by the distance travelled from the source to the substrate, the angle of impingement into the substrate surface, the substrate temperature T_s , and the base pressure.

II.1.3. Chemical deposition methods

The condensation of chemical substances from the gas phase onto a substrate where the reaction happens to generate a solid deposit is known as chemical vapor deposition (CVD). If not already in the vapor state, the gaseous compound containing the deposited material is generated by volatilization from either a liquid or a solid feed and is induced to flow by a pressure differential or by the diffusion of gas carried into the substrate. The chemical reaction begins near the surface of the substrate and produces the desired substance.

In some processes, the chemical reaction may be triggered by an external agent such as heat, an RF field, light or X-rays, an electric arc or glow discharge, electron bombardment, and so on. The deposit's microstructure, morphology, and adhesion are all strongly tied to the activation process and the nature of the chemical reaction [6]

II.1.3.1. Electro-deposition

Electrolysis is the appearance of chemical changes caused by the passage of an electric current through an electrolyte, and electrodeposition is the deposition of any substance on an electrode as a result of electrolysis. This phenomenon is dominated by two laws, first stated by Faraday in 1833: (i) the magnitude of chemical change occurring is relative to the electric current passed, and (ii) the masses of different kinds deposited at or dissolved from electrodes in the same amount of electricity are in direct proportion to equivalent weights. The two rules can be combined and represented mathematically as follows:

$$w = \frac{IE_t}{F} \quad (II.1)$$

Where W is the deposited material's mass (in g), I is the current (in A), E is the chemical equivalent weight (in g), and t is the reaction time (in s). The Faraday constant, corresponding to 96500 C, is defined as the amount of charge required to deposit one equivalent of any ion from a solution [7].

II.1.3.2. Chemical bath deposition

Chemical bath deposition (CBD) is also known as controlled precipitation, and it has been used to deposit films of many different semiconductors since then. It is currently gaining popularity because it does not require complicated instrumentation such as a vacuum system or other costly equipment. All that is necessary is a vessel to hold the solution (an aqueous solution composed of a few commonly used compounds) and a substrate for deposition [8]. It provides a bottom-up approach to the manufacture of nanocrystalline materials in thin film form with improved particle size control, particle shape, size distribution, particle content, and particle agglomeration.

II.1.3.3. Chemical Vapor Deposition (CVD)

The condensation of chemical substances from the gas phase onto a substrate where the reaction happens to generate a solid deposit is known as chemical vapor deposition (CVD). If not already in the vapor state, the gaseous compound containing the deposited material is generated by volatilization from either a liquid or a solid feed and is induced to flow by a pressure differential or by the diffusion of gas carried into the substrate. The chemical process that produces the desired substance begins near the surface of the substrate that produces the desired material. In some cases, the chemical reaction may be triggered by an external agent, such as the application of heat. Electromagnetic fields, light or X-rays, an electric arc or glow discharge, electron bombardment, and so forth. The deposit's microstructure, morphology, and adhesion are all strongly tied to the activation process and the nature of the chemical reaction. The deposit's microstructure, morphology, and adhesion are all heavily influenced by the activation procedure and the nature of the chemical reaction [6].

II.1.3.4. Spray pyrolysis technique

SPT is a method for creating dense and porous oxide films, ceramic coatings, and powders. This approach has been utilized for dense film deposition, porous film deposition, and powder manufacturing. Using this adaptable process, even multilayer films can be easily created. SPT has been used to deposit electrically conducting electrodes in the glass sector and solar cell manufacturing for decades. The spray pyrolysis method of film deposition necessitates a heated substrate in order to spray the metal salt from the aqueous solution. Droplets were distributed and formed a disk-shaped structure on the substrate's surface before decomposing thermally [9]. The size and form of the disk were related to the temperature of the substrate, the volume, and the momentum of the droplet. As a result, this film was created, which contained overlapping disks of metal salt being transformed to metal oxide.

II.1.3.5. Sol-gel technique

The sol-gel process is named after the abbreviation "solution-gelification." It is a method of "soft chemistry" in solution that allows the creation of numerous inorganic or organic/inorganic hybrids, in a wide range of configurations such as thin films, optical fibers, monolithic glass, and calibrated nano-powders [10], as shown in figure (II.1). The term "soft

chemistry" refers to the fact that chemical reactions in liquid solution occur at significantly lower temperatures than traditional synthetic routes. These conditions also allow for the combination of organic and mineral species, resulting in the formation of new families of organo-mineral compounds with novel properties. This method can be used in a variety of fields, including the production of porous nanomaterials, as well as the fabrication of coatings and encapsulation. This technique was chosen for the creation of the materials studied in this work because it offers several advantages, including the purity and homogeneity of the products created, its ease of implementation, its suitability for the resurfacing of large and/or complex surfaces, its low energy cost and the ability to create materials on the fly thanks to a final control over experimental parameters.

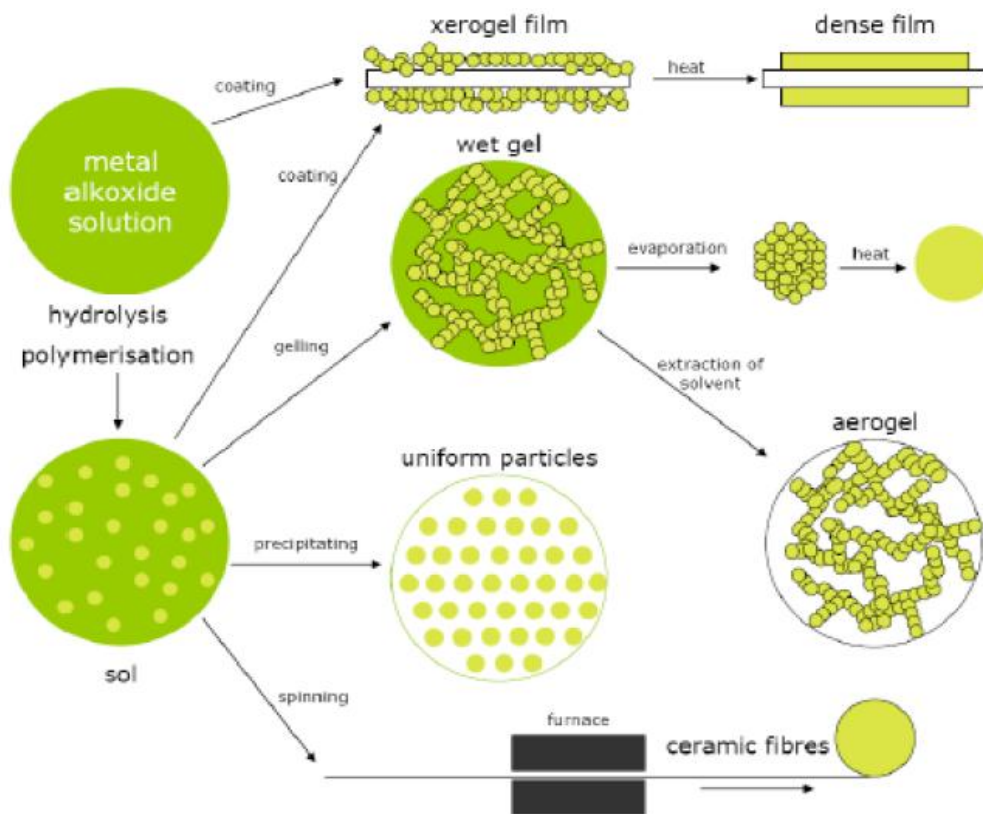


Figure II.1. Schematic summary of the sol-gel process [11].

The formation of a solid via sol-gel results from chemical reactions in liquid phase, which are responsible for the priming of sol-gel reactions and are referred to as "molecular precursor". These reactions occur in two stages: synthesis of "sol" followed by formation of "gel". At this point, it is necessary to define two terms commonly used in sol-gel chemistry: first a sol is a stable dispersion of colloidal particles in a liquid. The size of solid particles (1-1000 nm), which are denser than liquids, must be small enough that the forces responsible for

dispersion are not overcome by gravity. Second, a gel is a three-dimensional lattice of Van-der-Waals connections with infinite viscosity. In which the solvent (water, alcohol) is imprisoned in the pores. When the liquid is water, the term "aqua-gel" or "hydro-gel" is used. And when it comes to alcohol, the term "alcogel" is used. When the lattice is made up of three-dimensional particles, the gel colloidal is formed, and when the network is made up of macromolecules, the gel polymeric is formed. The time required at the surface to transform into gel is referred to as "time of gel" or "point of gel". There are two main routes for sol-gel synthesis, depending on the type of precursor used:

Inorganic or colloidal method: derived from metallic elements (chlorides, nitrates, oxychlorides...) in aqueous solution, it is inexpensive and simple to implement. However, controlling the size and distribution of the powders is difficult. It is for this reason that it is rarely used. However, this is the preferred method for producing ceramic materials.

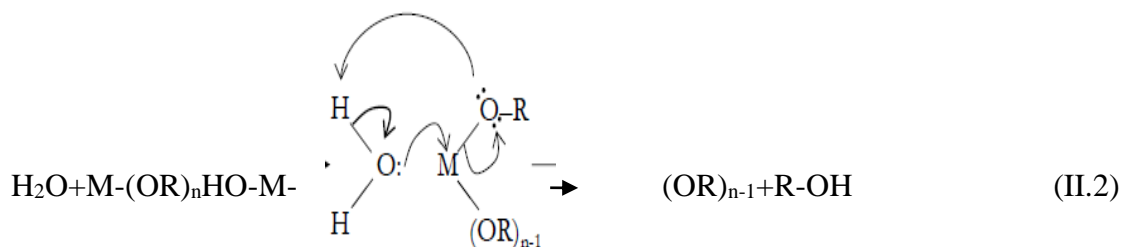
Metal organic (polymeric) method: derived from metallic alkoxides of formula $(MOR)_n$, Where M denotes a valence n metal and R denotes an alkyl radical (formula C_nH_{2n+1}) linked to an oxygen ion via an alkoxide groupement. This route is more expensive than the previous one, but it allows for final granulometry control. It is especially well-suited to irregular layouts, such as the placement of thin sheets of paper. The ML (ICCF) and CLeFS (LMGP) groups have established expertise in this area, and it is this path that has been taken during these research efforts [12].

II.1.3.5. 1. Reaction Mechanisms

To begin, the metallic alkoxide is mixed with a solution made up of an organic solvent (usually alcohol), water, and, in most cases, a catalyze (acid or base). The sol-gel transformation of alkoxides (solution sol gel) occurs via an inorganic polymerisation mechanism in two stages: hydrolysis and (poly-) condensation.

a. The hydrolysis

The hydrolysis reaction initiates the polymerization process and results in the formation of M-OH groups:

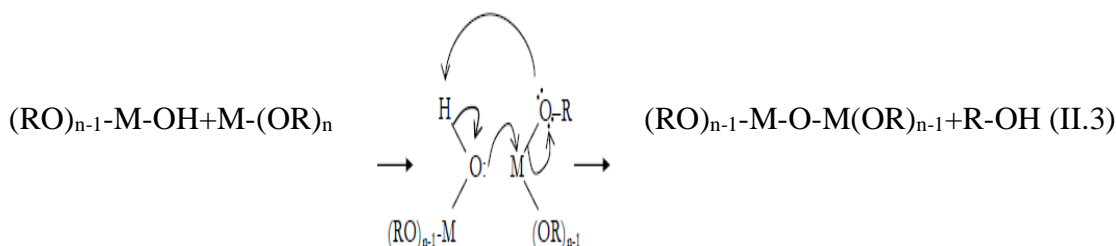


It is based on the substitution of OR groups for OH groups, during which the metal undergoes nucleophilic attack due to the electronegativity of the alkoxy group. As a result, there is a nucleophilic addition of an ice molecule to the metal, followed by a proton transfer to the alcoholic. So there is a nucleophilic addition of a water molecule to the metal, followed by a proton transfer to the alcoholic. This hydroxylation step, which occurs alongside alcohol liberation, can be complete or partial depending on the amount of water present, but the alkoxide is usually only partially hydrolyzed.

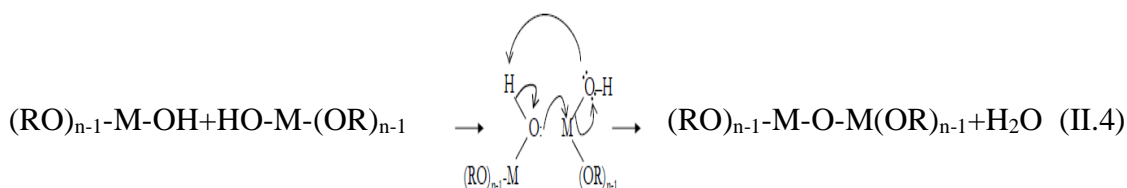
b. Condensation

The reactive species $(RO)_{n-1}-M-OH_n$ formed during hydrolysis are good nucleophiles and can react with a similar or non-hydrolyzed-alkoxide during the subsequent condensation.

- **Alkoxylation** is the formation of an oxygen M-O-M bridge between two metallic atoms while releasing an alcoholic molecule:



- **Oxolation** is the formation of an oxygen M-O-M bridge between two metallic atoms, which results in dehydration.



This reaction has occurred continuously over time, resulting in the formation of polymeric chains of the type $(M-O-M)_n$ (poly-condensation). Condensation, like hydrolysis, modifies the metal's coordination sphere but does not increase its coordination. When these two reactions are completed, a gel is formed. The transformation of a solution into a polymeric solid is known as the "sol-gel" transition or jellification.

II.1.3.5. 2. Sol-gel Transition

This transition consists in the formation of an inorganic network that is piling up the solvent (high viscosity environment), For example an inorganic/solvent composite. The resulting gel phase is distinguished by a 3D "skeleton" solid embedded in a liquid phase. Obviously, the reaction process does not stop at the point of gelation. The ultimate evolution of gel over time is referred to as "aging. "There are several processes that can occur, including: Inorganic polymerization (lattice reinforcement through new bounds).

- The phenomenon of syneresis or phase transformation (reticulation leading to gel reconstitution and solvent expulsion).
- The Ostwald ripening (a particle dissolution and precipitation phenomenon).

The aging of the gel causes structural changes, which manifest as changes in the diameter of the pores and internal capillary forces.

II.1.3.5.3. Drying of the gel

The process for getting a solid material from a gel includes a drying step that results in the evaporation of the solvent outside of the polymeric lattice while the gel solidifies. The evaporation process occurs due to the pores and channels present in porous sol-gel material, which can result in a significant volume change. Using the same solution and depending on the drying mode of the gel, a material can be obtained in two different forms:

a. The xerogel:

Obtainable through conventional drying in atmospheric conditions (normal evaporation), resulting in a significant volume reduction. Residue liquids, in effect, cause capillary forces that lead to the destruction of macro-porosity and, eventually, the formation of a vitreous structure. However, the resulting xerogel, which has a very different texture than the original gel, is still very porous. It is thus possible to subject it to a thermal treatment at varying temperatures depending on the type of material and desired properties. Depending on the temperature, this thermal treatment produces a more packed xerogel, or all-oxide material.

b. Air-gel

Obtained during supercritical drying (in a high-pressure autoclave) with no or little volume reduction. It is a very open structure with a lot of macro porosity. Air-gel, for example, enables the production of controlled-size nano-powders.

II.1.3.5.4. Thin films elaboration via sol-gel method

The obtaining of a stable sol is a critical step in the production of thin films via the sol-gel method. This necessitates monitoring the reaction steps of the sol-gel process, which frequently involves the use of chelating agents (nucleophile molecules, XOH). Organic acids (acetic, citric, malic...), β -dicetones, or poly-hydroxyl ligands are extremely effective at controlling the reactivity of transition metal alkoxides [13,14].

The β -dicetones, in particular, have a highly reactive hydroxy group, allowing these ligands to easily react with metal alcoxides. Various techniques can be used to form thin films using the sol-gel method. The most advanced, such as spin-coating and dip-coating, allow for uniform and controlled film thickness (from a few tens to hundreds of nano metres of thickness per layer). The technique chosen is determined by the properties of the substrate. Such as its geometry or size, as well as specific properties desired for the thin films (transparency, thickness, etc...).

II.1.3.5.4. 1. Dip-coating

This method of forming thin films simply consists of immersing the substrate at a controlled speed in the solution containing the stabilized sol and removing it after a certain immersion time, always at a controlled speed. to obtain a film of regular thickness [16]. During the withdrawal, the liquid will flow on the substrate which will be covered with a uniform layer at the end of the flow. The three steps of this method are illustrated in Figure (II.2).

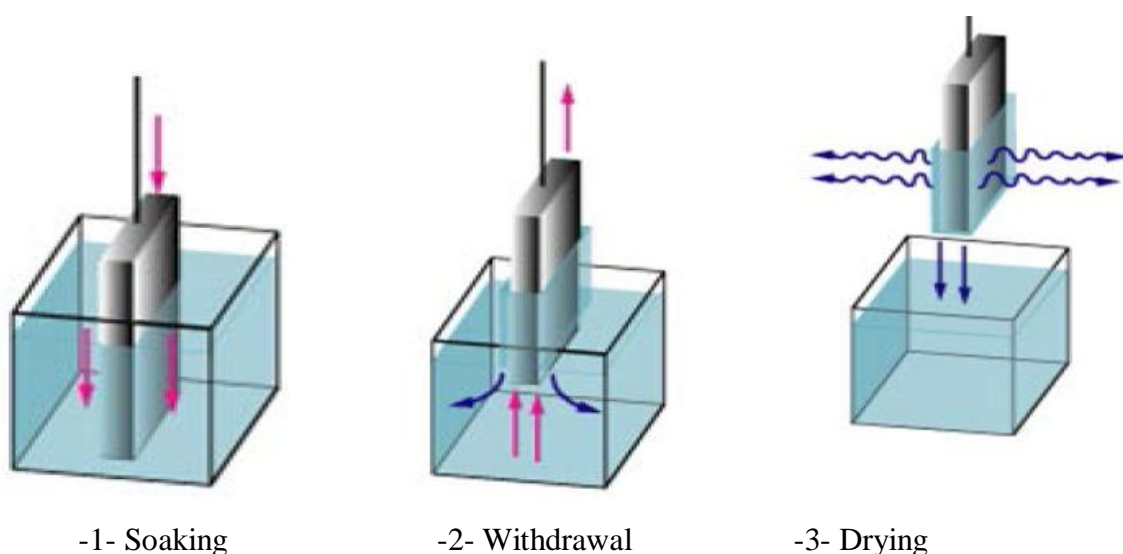


Figure II.2. Dip coating principe [16].

Dip-coating offers many advantages such as inexpensive installation, simplicity of the process, uniformity of the deposit and the possibility of coating complex-shaped substrates (tubes, cylinders, etc.). Viscosity, solution concentration, withdrawal rate, and immersion time affect film thickness. Other technical conditions, such as the regularity of the displacement and the inclination of the substrate, can also influence in more or less significant proportions the thickness of the deposited films.

II.1.3.5.4. 2. Spin-coating

This method is distinguished by four steps [14], which are summarized in figure (II.3):

- (1) The placement of a controlled amount of solution on a substrate.
- (2) High-speed rotation causes liquid to flow to the surface of the substrate under the action of centrifugal force
- (3) Constant-speed rotation results in the ejection of excess liquid in the form of droplets and the uniform reduction of film thickness.
- (4) Evaporation of the most volatile solvents favoring the liquid-solid transformation (sol-gel) and reducing the thickness of the deposited film.

The control of the thickness of the film is possible thanks to the modification of certain parameters related to the spin-coater (speed of rotation, acceleration, etc.) and/or to the deposited solution (volume, concentration and viscosity of the solution in particular). Indeed, the higher the speed, acceleration or rotation time, the thinner the film. On the other hand, the higher the volume, concentration or viscosity of the deposited sol, the thicker the layer.

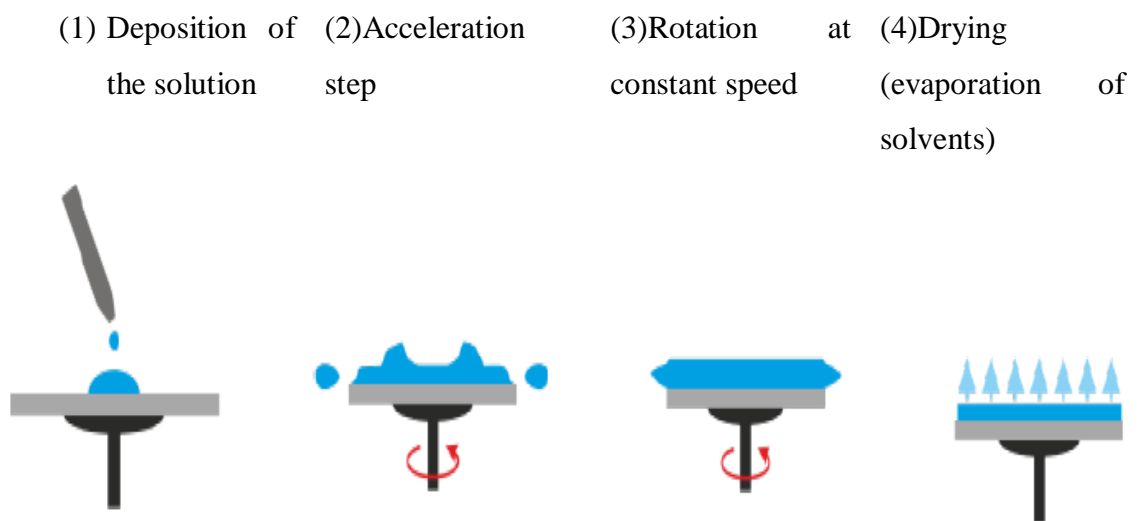


Figure II.3. Spin coating principe [16].

This technique is easy to implement, fast, reproducible and it gives excellent results on flat substrates of small or large size, preferably centro-symmetrical (round, square).

In this thesis, spin-coating method has been adopted to elaborate pure and doped NiO thin films.

II.1.4. NiO thin film characterization techniques

II.1.4.1. Structural characterization

The X-ray diffraction technique is a popular method for characterizing material structure. This technique is only applicable to crystallized materials (poly or mono crystalline).

$$2d_{hkl}\sin\theta = n\lambda \quad (\text{II.5})$$

With n : degree of reflection. In our study, we will limited to the first order, where λ is the length of the X-ray beam's wave, θ is the angle of diffraction, and d_{hkl} is the inter-reticular distance [17].

In this work, we have used a BRUKER-AXS diffractogram of type D8 (University of Biskra), as shown in figure (II.4). The X-ray source was created from $\text{CuK}\alpha$ radiation, with a wavelength of 1.5405\AA and an acceleration tension of 30-40kV and a current of 20-30 mA. The study of the X-ray spectrum allows for the determination of a large number of information about the structural and microstructural properties of the sample to be analyzed, such as: crystalline structures, crystallite size, measuring lattice parameters and the preferred orientation of a texture, and structural defect rates. The ray's angular positions allow us to calculate the distances between plans using Bragg's law (Eq.II.5) and thus arrive at the lattice parameters. The positions and intensities of diffraction rays in the majority of known materials have been studied and are catalogued in data bases in the form of fiches, for example (JCPDS: Joint Committee for Powder Diffraction Standards NiO 47-1049). The comparison of an experimental spectrum with these data allows for the identification of the nature of each phase constitutive of thin films.

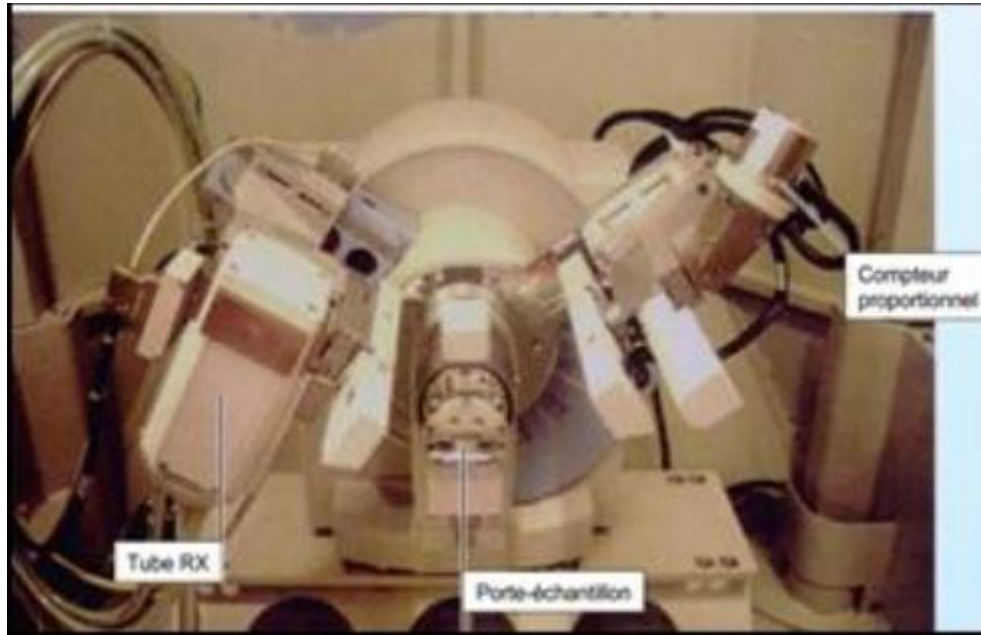


Figure II.4. BRUKER-AXS type D8 Diffractometer

II.1.4.1.1. Crystallite size calculation

The values of the crystallite's sizes G of the various samples have been calculated using the Scherrer equation shown below:

$$G = \frac{0.9\lambda}{\beta \cos\theta} \quad (II.6)$$

Where G : is the crystallite

β : the width at half maximum.

λ : is the X ray wave length ($\lambda=0.15406$ nm).

θ : is the diffraction angle.

II.1.4.1.2. Lattice parameters calculation

It is well known that NiO exhibits a cubic face centered structure (fcc). Thus, nickel oxide lattice parameter are given by the following relationship:

$$a = d_{hkl} \cdot \sqrt{h^2 + k^2 + l^2} \quad (II.7)$$

lattice parameters are affected by macro-strain and the presence of lattice defects such as atomic gaps or substitutional and interstitial atoms [18].

II.1.4.1.3. Stress-Strain calculation:

Stress is the internal forces of matter.

If each crystallite is subjected to a different constraint, the result is a superposition of neighboring peaks. If these forces cause crystalline lattice deformation (elastic deformation), the interarticular distances will change, and the position of the peaks will be altered. If the peaks decay is measured, the stress strain values of the prepared samples can be determined [18].

The equation below explains the relationship between stress σ_{ij} , strain ε_{ij} and the elastic constants C_{ij} of the lattice.

$$\sigma_{ij} = c_{ijkl} \cdot \varepsilon_{kl} \quad (\text{II.8})$$

The effect of lattice strain is manifested on diffractograms by a shift in diffraction peaks. Lattice parameters can be determined by comparing the obtained XRD pattern with the recorded (JCPDS) files. The dislocation density δ ; the dislocation line per volume unit, using the equation below [19].

$$\delta = \frac{1}{D^2} \quad , \quad N = \frac{d}{D^3} \quad (\text{II.9})$$

Where d : is the thickness of the thin film, and D : is the crystallite size.

Also stress is calculated using the following formula [17] :

$$\varepsilon = \frac{\beta \cdot \cos \theta}{4} \quad (\text{II.10})$$

II.1.4.2. Optical Characterization

The Optical characterization allows for the identification of a large number of parameters. They have the advantage, in comparison to electrical methods, of being non-destructive and not requiring completion. Always delicate, with ohmic contacts. They only require a transparent substrate in the range of the wave length to be explored. There are two different optical characterization methods [20].

- a. Methods for analyzing the optical properties of a material, such as transmittance measurements, refraction measurements, allow for the determination of material thickness, optical gap, and refractive index, whereas ellipsometric measurements only determine sample thickness. It's worth noting that a simulation method was used to estimate the thickness of the material, the optical gap, and the refractive index.
- b. Methods that investigate the optical response of a material to an excitation, such as photo and cathode-luminescence, as well as photo-current, which determines the material's gap directly, are not used in this work.

II.1.4.2. 1. UV-visible spectroscopy

The fields of spectroscopy are generally distinguished by the range of the wave length in which measurements are taken. The following fields can be distinguished: UV-visible, UV-visible-near infrared, infrared, and micro-waves. In our case, we used a UV-visible spectrophotometer with dual apertures, the operation of which can be seen in Figure II.5. We were able to trace the curves representing the variation in transmittance using this method vs the wavelength in the range (300-1000nm). It is possible to estimate the thickness of the film and determine its optical properties by using these curves. the optical absorption threshold, the absorption coefficient, the width of the forbidden band, the Urbach energy, and the refractive index.

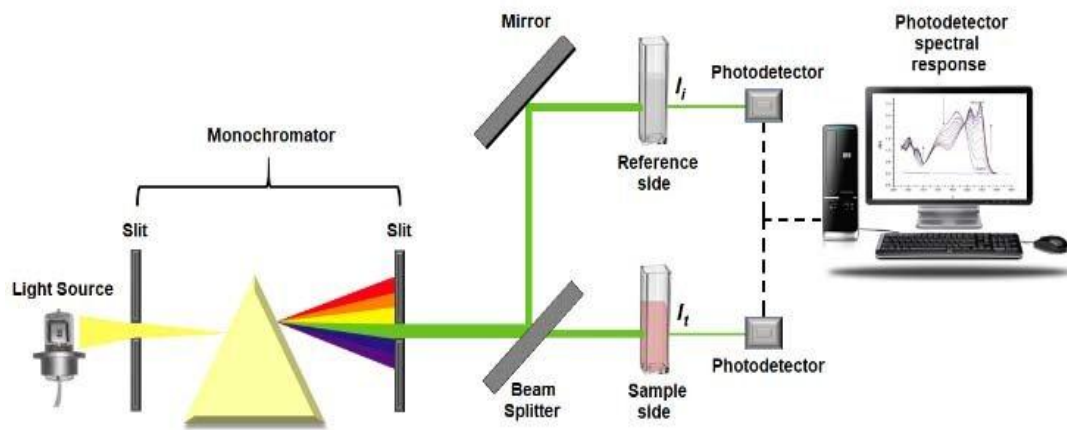


Figure II.5. Schematic representation of UV-Visible spectrophotometer [21]

II.1.4.2. 2. Measurement of optical properties

The optical properties of transparent conductor oxides (TCO) are interesting for a variety of applications. Particularly for photoprotective coating [20]. Also, optical characterisation entails determining the major optical magnitudes: the index of refraction, the coefficients of absorption and extinction, the thickness, the optical gap, and the Urbach energy.

II.1.4.2. 2.3. Measurement of thickness

We used for measuring the thickness of our samples a simulation method that uses a program (Hebal Optic) to determine optical constants based on transmission spectrum data in the ultraviolet and visible ranges. We took the measurements with a spectrophotometer UV-

Vis of type (SHUMATZU 1800) with double beams, one for reference (the glass: because it does not absorb light in the spectral domain), the other for the prepared sample (the glass + the thin layer of NiO); the spectral range ranges from 300 to 1000 nm with an 8 nm resolution. The obtained spectra show the variation in relative transmittance $T(\%)$ of the layer as a function of wavelength (nm). On the figure (II.6), we show a typical appearance of a spectrum obtained in one of our thin films.

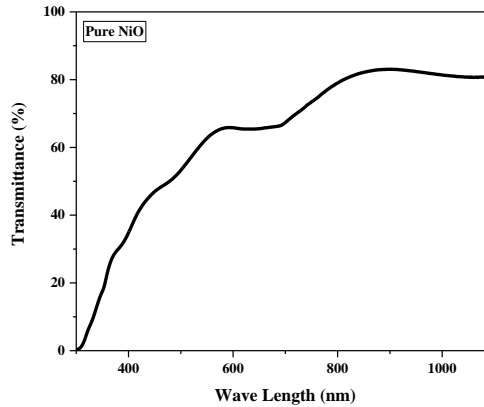


Figure.II.6. Typical transmittance spectra of a pure NiO thin film prepared by spin coating.

The abrupt drop in transmission for shorter wavelengths in the interval (300-370 nm) corresponds to the threshold of absorption energy of our NiO due to the transition between its valence and conduction bands [22]. The value measured between 400 and 700nm gives the average transmittance of the prepared films. There is another method for weigh measurements in which it calculates the thickness (t) is the gravimetric method of weight difference while accounting for the density of NiO, which is 6.7 gm/cm^3 , as defined by the following equation [23]:

$$d = \Delta m / A \cdot \rho \quad (\text{II.11})$$

d : is the thin film thickness, m is the different mass distributions (before and after), ρ is the density, and A is the thin film's surface. There is a third method, which is the method of fringes interferences, but it has not been used due to the lack of interferences in nearly all of our NiO samples.

II.1.4.2. 2.4. Determination of the absorption coefficient

The coefficient of absorption and the coefficient of extinction k of the material that makes up a layer can be calculated using the transmission spectrum. Using the Bouguer-

Lambert-Beer relation, or as it is commonly known, the Beer law, which is given by the following relation [22]

$$T = \exp(-\alpha d) \quad (\text{II.12})$$

d : is the film thickness, T : is the transmittance in (%), α : is the absorption coefficient (cm^{-1}),
 k : is the extinction coefficient (without unity).

$$\alpha = \frac{1}{d} \ln \left(\frac{100}{T(\%)} \right) ; k = \frac{\alpha \lambda}{4\pi} \quad (\text{II.13})$$

It should be noted that this calculation assumes that $(1-T)$ is the absorption of the layer, despite the fact that some incident light is not absorbed, transmitted, but reflected. This approximation is less useful as the thickness of the layer decreases. It is therefore necessary to exercise extreme caution when comparing for very different layer thicknesses.

II.1.4.2. 2.5. Band gap and Urbach energy determination

Many authors are interested in describing the distribution functions of energy states $g(E)$ in energy bands. In the case of crystalline materials, the energy separating the valence band from the conduction band is precisely defined by eV and E_c . The energy $E_c - eV$ corresponds to the energy of the forbidden band. The appearance of the distribution functions of energy states is a metaphor as shown in the illustration figure (II.7). When variations in inter-atomic distances, lengths, or angle of bands appear in a material, this is referred to as "disorder." In this case, the band boundaries described in the case of crystalline lattice and delimited by eV and E_c may disappear. It is observed what is known as localized states, which are formed by a band tail at the borders of the prohibited band in the valence and conduction band figure (II.8). The states extending are found for energies greater than E_c and less than eV . When the disorder becomes too great (for example, the appearance of intermittent connections or impurities in the material), tails may be formed [25].

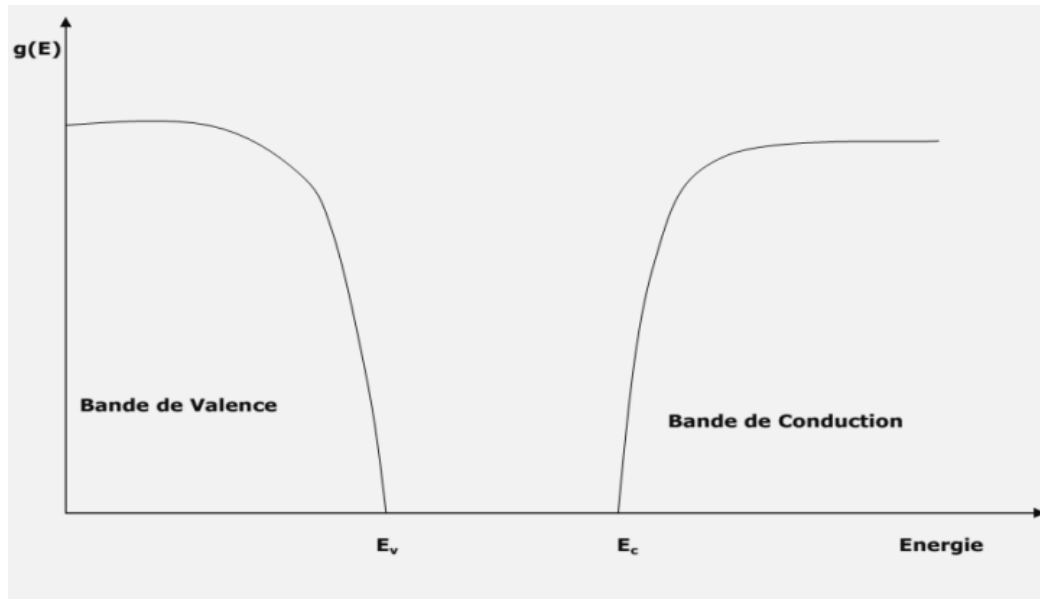


Figure II.7. Energy states distribution function of a crystallized semiconductor [25]

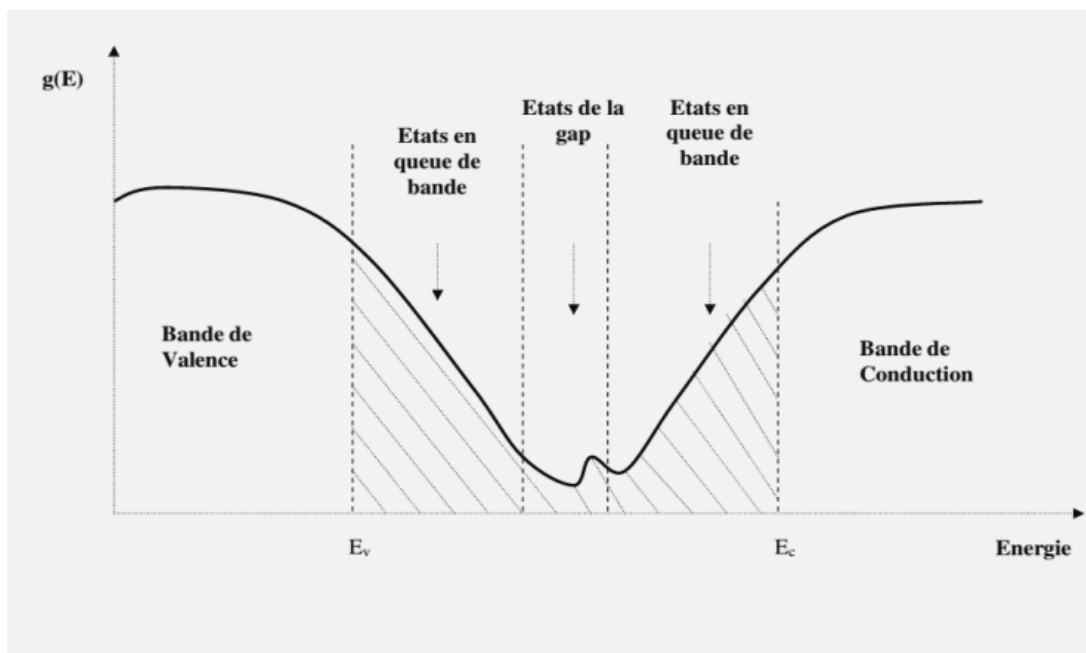


Figure II.8. Function of distribution of energy states in bands: Encroachment of tails in the bands [25]

Urbach parameter (E_u), which corresponds to transitions between the extending states of the valence band and the localized states of the conduction band. The model is used to determine the optical gap [25].

$$(\alpha h\nu)^2 = A(h\nu - E_g) \quad (\text{II.14})$$

A is a constant that reflects the degree of disorder in the amorphous solid structure, E_g is the optical gap expressed in eV, $h\nu$ is the photonic energy in eV. Drawing $(\alpha h\nu)^2$ vs $(h\nu)$ and by extending the linear portion of α^2 until the x-axis ($\alpha^2=0$) the value of E_g is calculated as shown in figure (II.9).

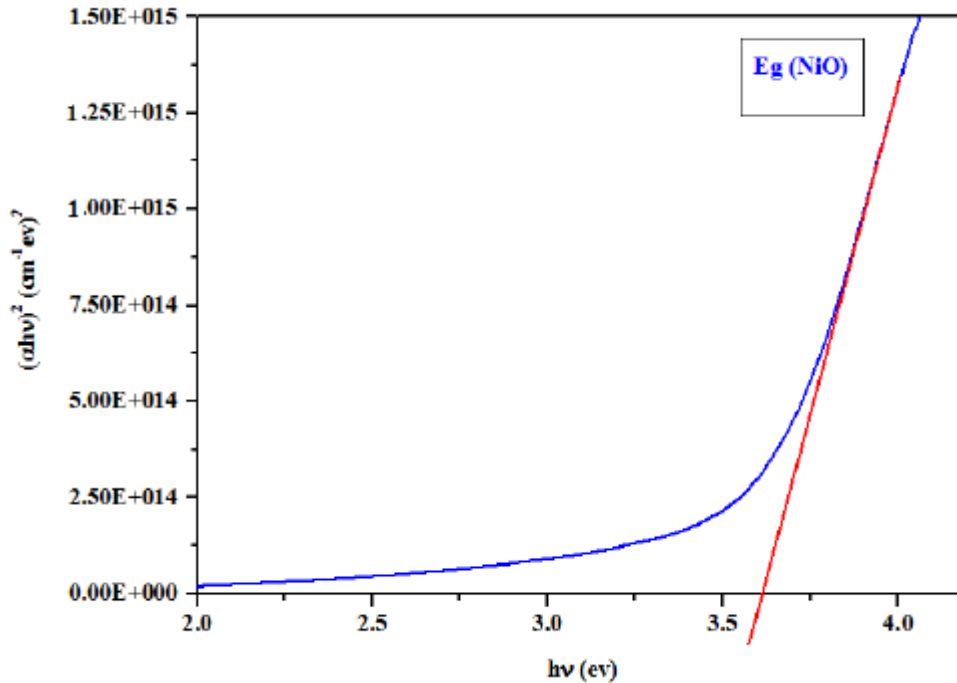


Figure II.9. Energy gap determination of a nickel oxide thin film [26]

Another important parameter that characterizes material disorder is Urbach's energy [26]. The Urbach law states that the absorption coefficient is expressed as [27]

$$\alpha = \alpha_0 \exp\left(\frac{h\nu}{E_U}\right) \quad (\text{II.15})$$

Tracing $\ln(\alpha)$ as a function of $h\nu$. The E_U energy can be obtained using the plotting $\ln(\alpha)$ vs. $h\nu$ and fitting the linear part of the curve with a straight line. The reciprocal of the slope's linear region gives up the E_U value.

$$\ln(\alpha) = \ln(\alpha_0) + \frac{h\nu}{E_U} \quad (\text{II.16})$$

II.1.4.3. Electrical properties measurements

The conductivity of a material σ (or its inverse property, resistivity ρ , where $\rho = 1/\sigma$) corresponds to its ability to conduct electricity. Conductivity in semiconductor materials is ensured by carrier mobilities and the number of available charge carriers (electrons or holes). Different mechanisms for conductivity measurement existed, as did their reliance on

temperature. In semiconductors, it has been reported that as temperatures increase, conductivity increases (more carriers are generated). However, conductivity decreases with increasing temperature in metals (more scattering by the lattice). Furthermore, conductivity is related to crystalline structure. Because the electronic structure is typically attached to the crystal structure, the crystal type and orientation affect conductivity. The size of the crystallites (grains) in polycrystalline materials is also an important parameter because it affects carrier scattering and, at very small sizes, the electronic structure.

II.1.4.3.1. Resistivity measurements

Four-point probe measurements are used to determine the resistivity of a bulk or thin film sample. The use of four contacts instead of two, as in a traditional resistance measurement, allows one to disregard the resistance of the points and only measure the resistance of the sample. Figure (II.10) illustrates the four-point probe measurement setup. As shown in figure (II.10), a current, I , is passed through the sample, and the voltage, V , is measured. The specific resistivity of the sample can then be calculated. When the distance between the limits is significantly greater than the thickness of the thin film ($d \ll a$) The lateral dimensions can be thought of as infinite.

In this case, a bi-dimensional conduction model is considered and provides

$$\frac{U}{I} = K \frac{\rho}{d} \quad (\text{II.17})$$

Where ρ is the resistivity and d : is the thickness of the films. An important surface electrical property in the field of TCOs is the surface resistance R_s defined as the ratio of the resistivity to the thickness of the thin film depending on the relationship were $R_{sq}(a)$.

$$R_{sq} = K \frac{U}{I} = \frac{\rho}{d} \quad (\text{II.18.a})$$

K : is a coefficient and R_{sq} : is the ratio between voltage U and current I . considering a cylindrical propagation of the field lines in the thin film, the coefficient K is $\ln(2)/\pi$ is equal to 4.532. According to the relation (II.18.a) and the previous considerations, we have the formula (II.18.b) to deduce the resistivity ρ (b) from the measurement four points knowing the thickness:

$$\rho = \left(\frac{\ln(2)}{\pi} \cdot \frac{U}{I} \right) \cdot d = R_{sq} \cdot d \quad (\text{II.18.b})$$

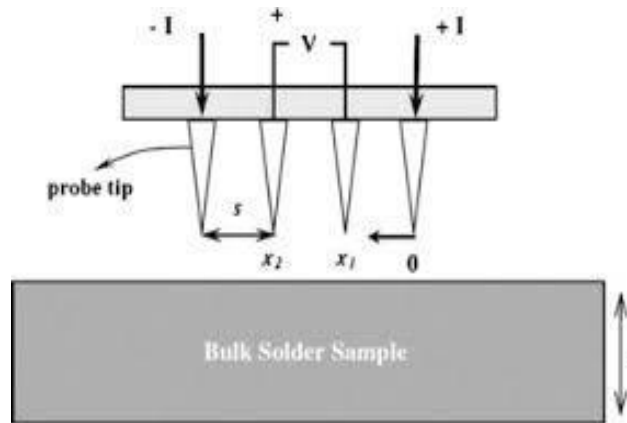


Figure II.10. Schematic of four points probe configuration [28]

II.1.4.3. 2. Conductivity measurements

The electrical measurements that we have taken are mostly about current-tension characteristics $I(V)$. To calculate the resistance of the layer, the calculation of the electrical conductivity depends on the electrical resistance, R of the intrinsic layer, thus even geometric parameters (inter-electrode distance L , the thickness d and the section of the conductive thin film S) [29]. The conductivity σ is related to these parameters by the following relationship

$$\sigma = \left(\frac{L}{S}\right) \left(\frac{1}{R}\right) \quad (\text{II.19})$$

II.2. Theoretical Approach

II.2.1. Introduction

Computational materials science has emerged as a new interdisciplinary field of science and technology as a result of the accessibility of huge advancements in computer technology. Nevertheless, it wouldn't have been as successful without contemporary density functional theory (DFT). However, the electrons and nuclei determine the properties of condensed matter and molecules. The study of electrons reveals important information about matter's electronic, magnetic, optical, and bulk properties. Calculations of electronic structure can be divided into ground state and excited state properties. Elastic properties, charge density and equilibrium volumes, among many other interesting properties of matter, can be derived for the ground state. Electronic excited states, on the other hand, offer beneficial details about optical properties. Although there have been a number of electronic structure methods developed over the years, density functional theory (DFT) is the method most frequently used

for solid systems [30]. DFT is an accurate theory for predicting the properties of new materials, validating experimental data, and explaining new phenomena discovered in experimental work.

II.2.2. The Many Body Problem

In order to determine a material's properties from first principles, a quantum many-body interaction problem must be solved over both the coordinates of the atomic nuclei and the electrons.

$$\hat{H}\psi(\{R_I\}, \{r_i, \sigma_i\}) = E\psi(\{R_I\}, \{r_i, \sigma_i\}) \quad (\text{II.20})$$

whereby for a system containing M nuclei and N electrons the many-body wave-function (ψ) is a function of all the spatial coordinates of nuclei ($\{R_I\}$, $I=1\dots M$) along with the spatial and spin coordinates of electrons ($\{r_i, \sigma_i\}$, $i=1, \dots, N$). The sum of all potential interactions between electrons and nuclei makes up the Hamiltonian (H). In Hartree and Bohr units of length and energy, respectively $e^2 = m_i = \hbar = 1$. where \hbar is the Planck constant, e and m_i are the electric charge and mass of an electron, respectively [31]. \hat{H} is The enlarged form of \hat{h}

$$\hat{H} = -\sum_{i=1}^N \frac{\nabla_i^2}{2} - \sum_{I=1}^M \frac{\nabla_I^2}{2M_I} + \sum_{i=1}^N \sum_{j>i}^N \frac{1}{|r_i - r_j|} + \sum_{I=1}^M \sum_{J>I}^M \frac{Z_I Z_J}{|R_I - R_J|} - \sum_{i=1}^N \sum_{I=1}^M \frac{Z_I}{|r_i - R_I|} \quad (\text{II.21})$$

The kinetic energy of all the electrons and nuclei are represented by the first two terms in Eq. (II.21), and the Coulomb repulsion between electrons and nuclei is represented by the third and fourth terms, respectively. The fifth term represents the Coulomb attraction between electrons and nuclei. The many-electron Schrödinger equation is thought to be able to predict and describe practically every phenomenon encountered in daily life. Although it seems straightforward in form, it is incredibly difficult to solve. Therefore, in order to simplify the situation, it is necessary and preferable to evaluate physical quantities of interest using acceptable approximations. Separation the dynamics of the electrons and the nuclei yields the Born-Oppenheimer approximation, which is the first significant approximation.

II.2.3. Born Oppenheimer approximation

Born and Oppenheimer [32]. made the so-called Born-Oppenheimer (BO) approximation in 1927. Because nuclei are substantially heavier than electrons (the mass of a proton is approximately 1836 times that of an electron), the nuclei move roughly two orders

of magnitude more slowly than the electrons. Consequently, nuclei and electron motion can be separated. Since it is possible to assume that the positions of nuclei are fixed while considering electron motion, the whole wave-function can be expressed as follows [31, 34]

$$\hat{H} = - \sum_{i=1}^N \frac{\nabla_i^2}{2} + \sum_{i=1}^N \sum_{j>i}^N \frac{1}{|r_i - r_j|} - \sum_{i=1}^N \sum_{l=1}^M \frac{Z_l}{|r_i - R_l|} \quad (II.22)$$

The Schrödinger equation involving the electronic Hamiltonian \hat{H}_e becomes

$$\hat{H}_e \psi_e(\{R_l\}, \{r_i, \sigma_i\}) = E_e \psi_e(\{R_l\}, \{r_i, \sigma_i\}) \quad (II.23)$$

Additionally, to make things simpler, the electronic spatial and spin coordinates ($\{r_i; \sigma_i\}$) are combined into a single variable, and Eq. (II.22) is rewritten as

$$\hat{H}_e \psi_e(\{R_l\}, \{X_i\}) = E_e \psi_e(\{R_l\}, \{X_i\}) \quad (II.24)$$

II.2.4. Hartree approximation

The Hartree technique is helpful as a foundation for understanding self-consistency and the self-consistent-field concepts as well as for solving the many-particle problem [35] Kinetic energy and the nucleus-electron interaction terms in Eq. (II.22) are sums of single-particle operators, every one of which affects a single electrical coordinate. While acting on pairs of electrons, the electron-electron interaction term is a pair interaction. The following definition is made to help with the next mathematics.

$$\hat{H}_e = \sum_i \hat{h}_1(\vec{x}_i) + \frac{1}{2} \sum_{i \neq j} \hat{h}_2(\vec{x}_i, \vec{x}_j). \quad (II.25)$$

Because \vec{x}_i is now a generalized coordinate that contains both spatial and spin degrees of freedom. So the Schrodinger equation can now be expressed as follows:

$$\left(\sum_i \hat{h}_1(\vec{x}_i) + \frac{1}{2} \sum_{i \neq j} \hat{h}_2(\vec{x}_i, \vec{x}_j) \right) \psi(r_1, r_2, \dots, r_N) = E \psi(r_1, r_2, \dots, r_N). \quad (II.26)$$

The Hartree method is an approach based on wave-function variation. Despite it is a many-body technique, the approach accompanied is that of a single-particle picture. i.e electrons are seen as filling single-particle orbitals that comprise the wave-function. We suppose that the trial wave-function is generated from these single particle orbitals in order to use the variational principle. Assume there are n random one-particle states $\psi(r_1), \psi(r_2), \dots, \psi(r_N)$. We ought to consider them as an orthonormal set because it will make calculating expectation values easier. Their direct product is the simplest wave-function that may be created.

$$\psi(r_1, r_2, \dots, r_N) = \psi(r_1, r_2, \dots, r_N). \quad (II.27)$$

The variational lowest energy can be calculated using the Hartree approximation. Every function in Eq. (II.27) is normalized to one. In this state, we can determine the expected value of

$$\langle H \rangle = \sum_{i=1}^N \int d\mathbf{r}_i^3 \psi^*(r_i) \left(-\frac{\nabla_i^2}{2} - \frac{Z}{r_i} \right) \psi(r_i) + \sum_{i>j} \sum_j \frac{|\psi_i(r_i)|^2 |\psi_j(r_j)|^2}{|r_i - r_j|} \quad (II.28)$$

The variational principle technique is to choose the $\psi_i(r_i)$ such that $\langle H \rangle$ is a minimum, and then Eq. (II.9) results in the condition that

$$\left[-\frac{\nabla_i^2}{2} - \frac{Z}{r_i} + V_H \right] \psi_i(r_i) = E_j \psi_i(r_i) \quad (II.29)$$

Where V_H represents the Hartree potential

$$V_H(r_i) = \sum_{i \neq j} \int d\mathbf{r}_j^3 \frac{|\psi_j(r_j)|^2}{|r_i - r_j|} \quad (II.30)$$

II.2.5. Hartree-Fock Approximation.

The Hartree-Fock (HF) technique is used to study electron-electron interactions at the mean field level, including Hartree and exchange interactions. The simple sum of the wavefunctions in Eq. (II.27) does not satisfy the indistinguishability principle and does not satisfy antisymmetric which implies that for odd permutations of the electronic variables, a fermion wave-function changes sign. However, an anti-symmetric solution can be constructed by inserting the following determinant, known as the Slater determinant.[37]

$$\psi(r_1, r_2, \dots, r_N) = \frac{1}{\sqrt{N!}} \begin{vmatrix} \psi_1(r_1) & \psi_1(r_2) & \dots & \psi_1(r_N) \\ \psi_2(r_1) & \psi_2(r_2) & \dots & \psi_2(r_N) \\ \vdots & \vdots & \ddots & \vdots \\ \psi_N(r_1) & \psi_N(r_2) & \dots & \psi_N(r_N) \end{vmatrix} \quad (II.32)$$

The exchange of two particles is analogous to the exchange of two columns, which results in a change of sign according to the previously established characteristics of determinants. It is worth noting that if the determinant is zero, two rows are equal. As a result, each ψ_i must be different. This exemplifies Pauli's exclusion principle, which states that two (or more) identical fermions can't be in the same state. The HF potentials can be calculated by

minimizing the total ground-state energy, and Eq (II.31) directly leads to the HF potentials. The HF potentials can be calculated by reducing the total ground-state energy, thus Eq (II.31) leads straight to the HF mean-field, self-consistent field equation

$$\left[-\frac{\nabla_i^2}{2} - \frac{Z}{r_i} + V_H + V_i^x \right] \psi_i(r_i) = E_j \psi_i(r_i) \quad (II.32)$$

where V_i^x is a non-local potential, sometimes known as the exchange potential due to the anti-symmetric aspect of the wavefunction, (Eq. II.33):

$$V_i^x(x_i)\psi_i(r_i) = \left[\sum_{j=1}^N \int \psi_j^*(r_j) \frac{-1}{|r_i - r_j|} \psi_j(r_j) dr_j \right] \psi_i(r_i) \quad (II.33)$$

The HF equation (II.32), which includes the anti-symmetry of the wavefunction or exchange interaction, provides the one-electron approximation with the interacting fermions. This HF technique has been used to periodic systems, such as bulk and surface crystalline materials [38].

The nonlocal potential presents complications in the HF equation. One issue is that it provides an erroneous depiction of the spatial separation of the electrons in a complete many-electron interaction. This missing piece is commonly known as electron correlation. In quantum chemistry, the correlation energy is defined as the difference between the ground state HF energy and the actual ground state energy [31].

Besides the HF formalism, the HF approach is improved by taking electron correlation into consideration.

II.2.6. Density Functional Theory (DFT)

One of the most common computational techniques for exploring and anticipating material properties is density functional theory (DFT). It is a ground-state theory where the charge density is emphasized as an important physical quantity. FT has proven to be extremely useful in establishing structural and electrical properties in a wide range of materials. FT has been widely utilized in first-principles calculations aiming at characterizing and predicting the behavior of molecular and condensed matter systems for these reasons [39,40]

II.2.6.1. The Hohenberg-Kohn Theorem

Consider a system of N interacting (spinless) electrons that is subjected to an external potential $V(r)$, which is commonly the Coulomb potential of the nuclei. If the system possesses a nondegenerate ground state, there can only be one ground-state charge density $n(r)$ for a given $V(r)$. Hohenberg and Kohn established that for a given ground-state charge density $n(r)$, there can be only one external potential $V(r)$:

$$n(r) = N \int |\psi(r_1, r_2, \dots, r_N)|^2 dr_1 dr_2 \dots dr_N \quad (II.34)$$

Ψ is defined as the ground state wave-function. As a result of the Hohenberg and Kohn theorem, the ground-state charge density precisely defines the ground-state energy E . (Eq.II.35):

$$E[n(r)] = F[n(r)] + \int n(r) V(r) dr \quad (II.35)$$

however the internal energy $F[n(r)]$ is a universal functional of $n(r)$ (and not of $V(r)$), which is the charge density. In this approach, the N -body issue is precisely reduced by DFT to a determination of a 3-dimensional function $n(r)$ that minimizes a functional $E[n(r)]$.

II.2.6.2. Kohn-Sham Equations

Kohn and Sham (KS) [41] redefine the problem in a more recognizable form, paving the path for DFT to be used in practical applications. The interacting electron system is transferred onto a non-interacting electron system with the same ground state charge density $n(r)$. The charge density of a system of non-interacting electrons is expressed as a sum over one-electron orbitals (the KS orbitals) $\psi_i(r)$:

$$n(r) = \sum_i^N |\psi_i(r)|^2 \quad (II.36)$$

N represents the electrons number. The Schrödinger equation's solutions are the KS orbitals [42]:

$$\left[-\frac{\nabla^2}{2} + V_H(r) + V_{xc}(r) + V(r) \right] \psi_i(r) = \left(-\frac{\nabla^2}{2} + V_{KS}(r) \right) \psi_i(r) = E_i \psi_i(r) \quad (II.37)$$

where (Eq II.38) determines the energy functional E as follows:

$$E_{tot}[n(r)] = T_0[n(r)] + E_{Coul}[n(r)] + E_{xc}[n(r)] + E_{ext}[n(r)] \quad (II.38)$$

E_{tot} is presumed to be true for any density $n(\mathbf{r})$. $T_0(n)$ represents the anti-symmetrized product wave function kinetic energy (independent electrons), the classical Coulomb energy term is defined by E_{Coul} , $E_{\text{ext}}(n)$ defines the potential energy existed between electrons and ions and $E_{\text{xc}}(n)$ is the exchange correlation energy, which takes into account all adjustments to these values brought on by electron correlation.

II.2.6.3. Exchange-correlation energy

The discrepancy between the exact ground-state energy and the energy calculated using the non-interacting kinetic energy and the HF approximation is explained by the exchange-correlation energy $E_{\text{xc}}(n)$;

$$E_{\text{xc}}(n) = T(n) - T_0(n) + U_{\text{xc}}. \quad (\text{II. 39})$$

The interaction between the electrons and their own exchange-correlation hole is represented by U_{xc} , while $T(n)$ and $T_0(n)$ are exact and non-interacting kinetic energy functionals, respectively. The classical electrostatic interaction between the electron density $n(\mathbf{r})$ and the hole density $n_{\text{xc}}(\mathbf{r}', \mathbf{r})$ can also be used to express the exchange-correlation energy.

$$E_{\text{xc}}[n(\mathbf{r})] = \frac{1}{2} \int \int d\mathbf{r} d\mathbf{r}' \frac{n(\mathbf{r})n_{\text{xc}}(\mathbf{r}, \mathbf{r}')}{|\mathbf{r} - \mathbf{r}'|} \quad (\text{II. 40})$$

Approximations are being investigated for $E'_{\text{xc}}[n]$, which, despite containing contributions from kinetic energy, is commonly referred to as the Exchange-correlation functional and expressed as $E_{\text{xc}}[n]$. The subsections that follow explain some common exchange-correlation functional approximations that are used in practicable DFT codes.

II.2.6.4. Local density approximation (LDA)

All approximate exchange-correlation functionals are based on the local density approximation (LDA). The basic idea of uniform electron gas is at the heart of this model. In this system, the electrons move on a positive background charge distribution, resulting in a neutral ensemble. Exchange and correlation's effects are local in character. Additionally, in LDA, the exchange-correlation energy is presumptively just an integral over the entire space, with the exchange-correlation energy density at each point. and assumed to be identical to that of a homogeneous electron gas at that density [43].

$$E_{xc}^{LDA}[n(r)] = \int dr \epsilon_{xc}[n(r)]n(r) \quad (II.41)$$

The exchange-correlation energy per electron in a homogeneous electron gas $n(r)$ is represented in this case by $\epsilon_{xc}[n(r)]$. Usually, the energy per particle is a representation of the number of electrons per unit volume and is weighted with the possibility that an electron could exist at this position.

The exchange-correlation energy $\epsilon_{xc}[n(r)]$ is made up of two parts: the exchange energy per electron $\epsilon_x[n(r)]$, which represents the exchange energy of an electron in a uniform gas with density $n(r)$, and the correlation energy $\epsilon_c[n(r)]$, which represents the correlation energy of an electron in a uniform gas with density $n(r)$ [31,34].

$$\epsilon_{xc}[n(r)] = \epsilon_x[n(r)] + \epsilon_c[n(r)] \quad (II.42)$$

The exchange-correlation potential is calculated using the exchange-correlation energy functional and is often stated as

$$V_{xc}^{LDA}(r) = \frac{\delta E_{xc}^{LDA}[n(r)]}{\delta n(r)} \quad (II.43)$$

II.2.6.5. Local spin density approximation (LSDA)

The exchange of density functionals to spin-polarized systems is simple, where the actual spin-scaling has been determined, although for correlation further approximations need to be utilized. In DFT, a spin polarized system has two spin densities, up and down n^\uparrow & n^\downarrow however:

$$n(r) = n^\uparrow(r) + n^\downarrow(r) \quad (II.44)$$

and the local-spin-density approximation (LSDA) is denoted as [33,44,45]

$$\begin{aligned} E_{xc}^{LSDA}[n^\uparrow, n^\downarrow] &= \int r \epsilon_{xc}[n^\uparrow(r), n^\downarrow(r)]n(r) \\ &= \int dr n(r) \{ \epsilon_{xc}[n^\uparrow(r), n^\downarrow(r)] + \epsilon_c[n^\uparrow(r), n^\downarrow(r)] \} \\ &= \int dr n(r) \{ \epsilon_{xc}[n, \xi] + \epsilon_c[n, \xi] \} \end{aligned} \quad (II.45)$$

The fractional spin polarization $\xi(r)$ is described as follows [46]

$$\xi(r) = \frac{n^\uparrow(r) - n^\downarrow(r)}{n(r)} \quad (II.46)$$

The local spin-density functional of the total electron spin densities $n^\sigma(r)$ where the spin $\sigma = \uparrow, \downarrow$ in LSDA, is $E_{xc}^{LSDA}[n]$

The $\delta E_{xc}^{LSDA}[n]$ can be expressed as

$$\delta E_{xc}^{LSDA}[n] = \sum_{\sigma} \int dr \left[\epsilon_{xc} + n \frac{\partial \epsilon_{xc}}{\partial n} \right] \delta n(r, \sigma), \quad (II.47)$$

so the exchange correlation potential becomes

$$V_{xc}^{\sigma} = \frac{\delta E_{xc}}{\delta n^{\sigma}(r)} = \left[\epsilon_{xc} + n \frac{\partial \epsilon_{xc}}{\partial n} \right] r, \sigma \quad (II.48)$$

In solids, the broad range of exchange and correlation effects is limited. The fact that the LSDA reproduces the exchange-correlation hole contributes to its success.

II.2.6.6. Generalized Gradient Approximation (GGA)

The use of Generalized Gradient Approximation (GGA) functionals can increase the accuracy offered by the LDA. A functional form is used in GGA to guarantee that the exchange hole and normalization condition are both clearly negative. These depend on the charge density's value as well as its gradient, but they maintain the LDA's exchange-correlation hole's fundamental analytical characteristics [47].

$$E_{xc}^{GGA} = \int dr n(r) \epsilon_{xc} [n(r), \nabla n(r)] \quad (II.49)$$

Because of their reliance on $n(r)$, GGA functionals are frequently referred to as "semi-local" functionals. Those functionals are known to satisfy certain specified conditions, which the precise functional must also satisfy. GGA can produce improved results for several properties, such as geometries and ground state energies of molecules and materials. GGA outperforms LDA, particularly for covalent bonds and weakly bound systems. It produces substantially superior atomic energies and binding energies at a minor computational expense. The LDA, LSDA, and GGA approximations effectively approximate many ground state properties of

systems, including ground state energy, band structure, charge density, and density of states, forces acting on atoms, alongside vibrational properties. Nevertheless, they are not applicable for excited states and unable to model the properties of a number of other materials, particularly transition metal oxides and strongly correlated systems, in which band gaps are always underestimated [48].

II.2.6.7. DFT+U Approximation

DFT+U, additionally termed as LDA+U or GGA+U in, is a method for describing strongly correlated electron systems, particularly in transition metal oxides and transition metals. Anisimov et al. developed the initial expression of the LDA+U method in 1997 [49]. The majority of the generally established exchange-correlation functionals, including the LSDA and GGA functionals, fail to describe the exchange-correlation energy of a system with a high tendency for electron localization and interaction. The failure of the LSDA in strongly correlated oxides (transition metal oxides, rare-earth compounds) has been associated to an imprecise explanation of the strong Coulomb repulsion between 3d and or 4f electrons localized on metal ions. The LDA and its expansions misjudge local magnetic moments and the tendency of such materials to favour high-spin ground states, as well as the insulating gap in circumstances when it is dependent on electron localization.

Due to the absence of the derivative discontinuity with regard to orbital occupancy in the accurate exchange-correlation functional and of the exchange splitting induced by local magnetic moments, the gap in the LSDA and GGA is underestimated. As a result, it is preferable to include the on-site Coulomb interaction term in the exchange-correlation functional. The DFT+U correction term is commonly assumed to be an explicit mean-field treatment of the exchange-correlation energy given by the correlated sites throughout the Hubbard model. DFT+U provides a double-counting correction to account for the contribution previously contained in the LDA term. The Hubbard U parameter characterizes the on-site Coulomb repulsion between 3d electrons. The density matrix can be used to express the LSDA+U functional as [50]

$$E_{xc}^{LSDA+U} = E_{xc}^{LSDA} + \frac{U - I}{2} \sum_{\sigma} \left[\sum_m \sigma_{mm}^{\sigma} - \sum_{mm'} n_{mm}^{\sigma} n_{m'm}^{\sigma} \right] \quad (II.50)$$

in which J denotes the spin-spin exchange interaction parameter, $n_{mm'}^\sigma$ is the (mm') an element of the density matrix of d electrons with the spin configuration σ as well as orbital magnetic quantum numbers m and m' . As a result, Eq. (II.50) can be used to calculate the mm' matrix element of the (one-electron) LSDA+U exchange-correlation potential [51].

$$V_{mm'}^\sigma = \frac{\delta E_{xc}^{LSDA+U}}{\delta n_{m'm}^\sigma} = \frac{\delta E_{xc}^{LSDA}}{\delta n_{m'm}^\sigma} + (U - J) \left[\frac{1}{2} \delta_{mm'} - n_{mm'}^\sigma \right] \quad (II.51)$$

Pickett et al [52] made an important addition in 1998 by slightly modifying the functionals and introducing a linear response technique for obtaining the Hubbard parameters. The relations bellowed fine U and J .

$$U = \epsilon_{3d}^\uparrow \left(\frac{\bar{n}}{2} + \frac{1}{2}, \frac{\bar{n}}{2} \right) - \epsilon_{3d}^\uparrow \left(\frac{\bar{n}}{2} + \frac{1}{2}, \frac{\bar{n}}{2} - 1 \right) \quad (II.52)$$

When the d occupancy varies by one around a mean polarization of unity, and

$$J = \epsilon_{3d}^\uparrow \left(\frac{\bar{n}}{2} + \frac{1}{2}, \frac{\bar{n}}{2} - 1 \right) - \epsilon_{3d}^\downarrow \left(\frac{\bar{n}}{2} + \frac{1}{2}, \frac{\bar{n}}{2} - 1 \right) \quad (II.53)$$

this represents the difference between the up and down eigen values for unit spin polarization. The value of the LDA charge density is termed \bar{n} and the spin-up and spin-down $3d$ eigenvalues are represented by $\epsilon_{3d}^\uparrow (n^\uparrow, n^\downarrow)$ and $\epsilon_{3d}^\downarrow (n^\uparrow, n^\downarrow)$. Usually, the terms U and J are frequently unified by describing U as an effective value, $U_{\text{eff}} = U - J$, and placing $J = 0$ [52]. So, in this investigation, as a result, all U values utilized are regarded as effective values.

II.2.7. CASTEP

Our calculations in this thesis were carried out using the CASTEP numerical modeling code (Cambridge Serial Total Energy Package). It is a prevalent simulation program in solid physics. It allows the execution of the first principles of quantum physics calculations that investigate the properties of crystals and surfaces in materials such as semi-conductors, ceramics,

and metals. It was created in 1988 by Payne et al [53,54]. CASTEP employs DFT to solve the Schrödinger equation. and employs periodic conditions and the Bloch theory, employing the local density approximation (LDA; Local Density Approximation) [55- 57].

For the description of the energy exchange and correlation function, the calculations in this framework are carried out using the pseudo-potential and dual planes (PP-PW) technique.

This code is used to simulate total energy by utilizing special integration of k-points in the first Brillouin zone with a base of planes for the expansion of functions. The symmetry of the system is used to reduce the number of k-points in the primitive cell. The forces exerted on the atoms, the tensile strength of the constraints, and thus the atomic movements and variations in the crystalline cell's parameters, are always symmetric.

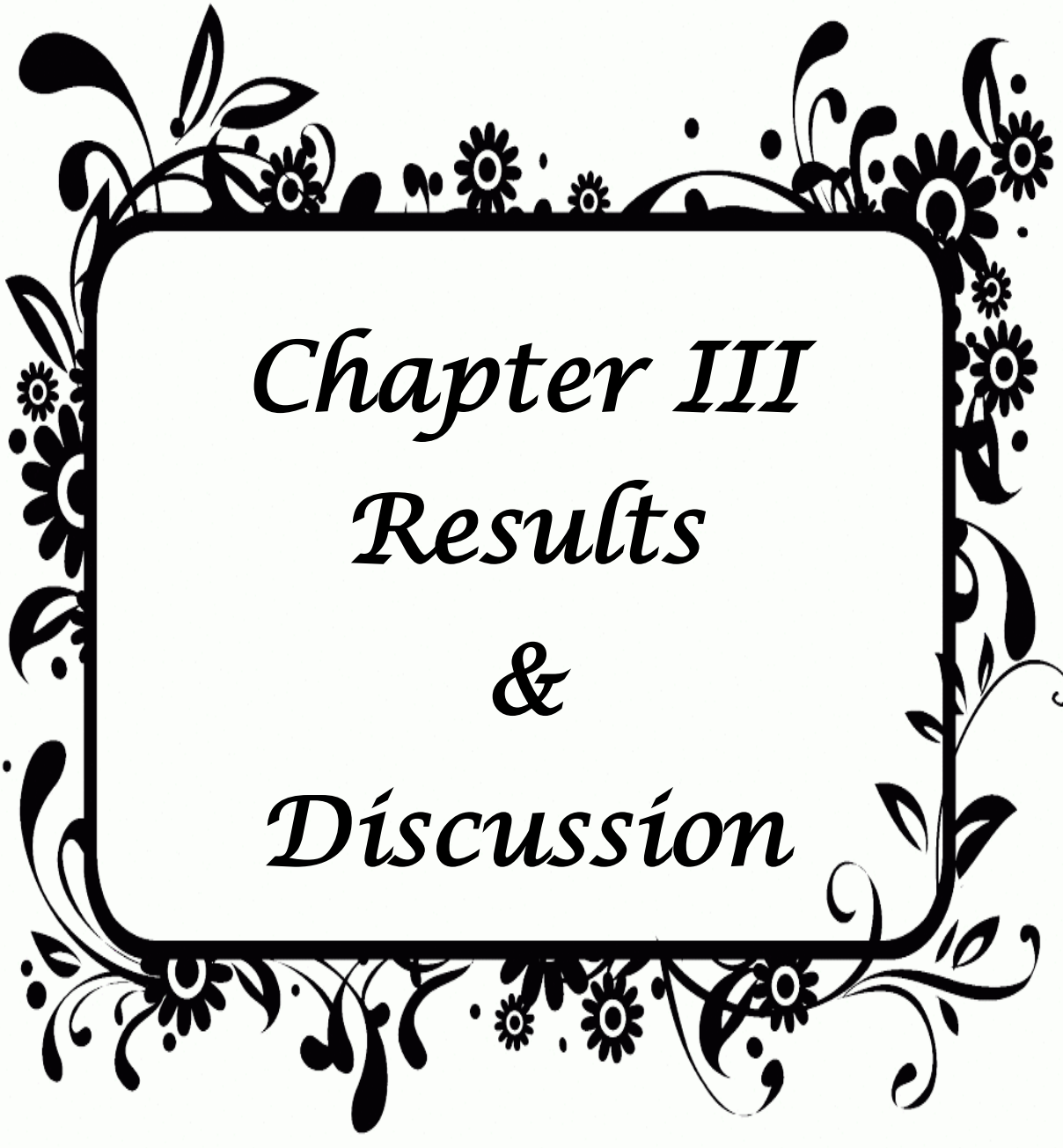
References

- [1] S. Goumri-Said, W. Khan, K. Boubaker, G. Turgut, E. Sönmez, J. Minar, M. Bououdina, M.B. Kanoun, Europium incorporation dynamics within NiO films deposited by sol-gel spin coating: experimental and theoretical studies, *Materials Research Bulletin*, 118 (2019) 110525.
- [2] A. Khan, Synthèse de Cuprates de Strontium (SrCu₂O) par MOCVD comme couche mince d'oxyde transparent conducteur de type P, Grenoble, 2011.
- [3] H.M. Christen, G. Eres, Recent advances in pulsed-laser deposition of complex oxides, *Journal of Physics: Condensed Matter*, 20 (2008) 264005.
- [4] O. Tuna, Y. Selamet, G. Aygun, L. Ozyuzer, High quality ITO thin films grown by dc and RF sputtering without oxygen, *Journal of Physics D: Applied Physics*, 43 (2010) 055402.
- [5] M. Al-Kuhaili, Characterization of thin films produced by the thermal evaporation of silver oxide, *Journal of Physics D: Applied Physics*, 40 (2007) 2847.
- [6] M.H. Yaacob, Investigation of metal oxide nanostructured thin films based optical hydrogen sensors, PhD diss., RMIT University Melbourne, Australia, (2012).
- [7] M. Sharmin, Characterization of boron doped zinc oxide thin films prepared by spray pyrolysis deposition technique, (2015).
- [8] S. Pawar, B. Pawar, J. Kim, O.-S. Joo, C. Lokhande, Recent status of chemical bath deposited metal chalcogenide and metal oxide thin films, *Current Applied Physics*, 11 (2011) 117-161.
- [9] S. Kozhukharov, S. Tchaoushev, Spray pyrolysis equipment for various applications, *Journal of Chemical Technology and Metallurgy*, 48 (2013) 111-118.
- [10] C.J. Brinker, G.W. Scherer, *Sol-gel science: the physics and chemistry of sol-gel processing*, Academic press 2013.
- [11] <http://www.chemat.com/chemattechnology/SolGel.html> (2009).
- [12] J. Livage, C. Sanchez, Sol-gel chemistry, *Journal of Non-Crystalline Solids*, 145 (1992) 11-19.
- [13] P. Judeinstein, C. Sanchez, Hybrid organic-inorganic materials: a land of multidisciplinary, *Journal of Materials Chemistry*, 6 (1996) 511-525.
- [14] C. Sanchez, J. Livage, M. Henry, F. Babonneau, Chemical modification of alkoxide precursors, *Journal of Non-Crystalline Solids*, 100 (1988) 65-76.
- [15] Birnie, D. (2004). *Spin Coating Technique*. pp. 49–55.

- [16] C.J. Brinker, Dip coating, Chemical solution deposition of functional oxide thin films, Springer 2013, pp. 233-261.
- [17] F.G. Keyes, Temperature—Its Measurement and Control in Science and Industry, Journal of the American Chemical Society, 78 (1956) 5707-5708.
- [18] R. Zsigmondy, P. Scherrer, Bestimmung der inneren Struktur und der Größe von Kolloidteilchen mittels Röntgenstrahlen, Kolloidchemie Ein Lehrbuch, (1912) 387-409.
- [19] M. Mekhnache, A. Drici, L.S. Hamideche, H. Benzarouk, A. Amara, L. Cattin, J. Bernede, M. Guerioune, Properties of ZnO thin films deposited on (glass, ITO and ZnO: Al) substrates, Superlattices and Microstructures, 49 (2011) 510-518.
- [20] F. Ynineb, Contribution à l'élaboration de couches minces d'Oxydes Transparents Conducteurs (TCO), mémoire de Magister en physique, univ-Mentouri-Constantine, (2010).
- [21] M.S. Braga, O.F. Gomes, R.F.V.V. Jaimes, E.R. Braga, W. Borysow, W.J. Salcedo, Multispectral colorimetric portable system for detecting metal ions in liquid media, 2019 4th International Symposium on Instrumentation Systems, Circuits and Transducers (INSCIT), IEEE, 2019, pp. 1-6.
- [22] P. Godse, R. Sakhare, S. Pawar, M. Chougule, S. Sen, P. Joshi, V.P. Patil, Effect of annealing on structural, morphological, electrical and optical studies of nickel oxide thin films, Journal of Surface Engineered Materials and Advanced Technology, 1 (2011) 35.
- [23] B. Benhaoua, S. Abbas, A. Rahal, A. Benhaoua, M. Aida, Effect of film thickness on the structural, optical and electrical properties of SnO₂: F thin films prepared by spray ultrasonic for solar cells applications, Superlattices and Microstructures, 83 (2015) 78-88.
- [24] H. Casey, D. Sell, K. Wecht, Concentration dependence of the absorption coefficient for n⁻ and p⁻ type GaAs between 1.3 and 1.6 eV, Journal of Applied Physics, 46 (1975) 250-257.
- [25] J. Tauc, R. Grigorovici, A. Vancu, Optical properties and electronic structure of amorphous germanium, *physica status solidi (b)*, 15 (1966) 627-637.
- [26] A. Moustaghfir, Elaboration et caractérisation de couches minces d'oxyde de zinc. Application à la photoprotection du polycarbonate, Université Blaise Pascal-Clermont-Ferrand II, 2004.
- [27] F. Urbach, The long-wavelength edge of photographic sensitivity and of the electronic absorption of solids, *Physical review*, 92 (1953) 1324.
- [28] M.E. Alnes, Transparent conducting oxides by atomic layer deposition, (2015).

- [29] A. Hafdallah, N. Attaf, Étude du dopage des couches minces de ZnO élaborées par spray ultrasonique, (2007).
- [30] Hohenberg and Kohn, 1964; Kohn and Sham, 1965.
- [31] B. Santra, Density-functional theory exchange-correlation functionals for hydrogen bonds in water, Technische Universität Berlin Berlin, 2010.
- [32] M. Born, J.R. Oppenheimer, Ann. Phys. 87 (1927) 457.
- [33] G. Ortiz, Gradient-corrected pseudopotential calculations in semiconductors, Physical Review B, 45 (1992) 11328.
- [34] M. Cococcioni, A LDA+ U study of selected iron compounds, (2002).
- [35] D.R. Hartree, The wave mechanics of an atom with a non-Coulomb central field. Part I. Theory and methods, Mathematical Proceedings of the Cambridge Philosophical Society, Cambridge university press, 1928, pp. 89-110.
- [36] J. Deslippe, S. Louie, Ab initio theories of the structural, electronic, and optical properties of semiconductors: bulk crystals to nanostructures, (2011).
- [37] V. Fock, Näherungsmethode zur Lösung des quantenmechanischen Mehrkörperproblems, Zeitschrift für Physik, 61 (1930) 126-148.
- [38] D.P. Woodruff, Oxide surfaces, Elsevier 2001.
- [39] E. Baerends, Perspective on “Self-consistent equations including exchange and correlation effects” Kohn W, Sham LJ (1965) Phys Rev A 140: 133–1138, Theoretical Chemistry Accounts: New Century Issue, (2001) 265-269.
- [40] M. Cococcioni, S. De Gironcoli, Linear response approach to the calculation of the effective interaction parameters in the LDA+ U method, Physical Review B—Condensed Matter and Materials Physics, 71 (2005) 035105.
- [41] W. Khon, L.J. Sham, Self-consistent equations including exchange and correlation effects, Phys. Rev, 140 (1965) A1133-A1138.
- [42] X. Hua, X. Chen, W. Goddard, Generalized gradient approximation: An improved density-functional theory for accurate orbital eigenvalues, Physical Review B, 55 (1997) 16103.
- [43] A.S. Foster, Theoretical modelling of non-contact atomic force microscopy on insulators, University of London, University College London (United Kingdom) 2000.
- [44] J.P. Perdew, K. Burke, Y. Wang, Generalized gradient approximation for the exchange-correlation hole of a many-electron system, Physical review B, 54 (1996) 16533.

- [45] C. Bowen, G. Sugiyama, B. Alder, Static dielectric response of the electron gas, *Physical Review B*, 50 (1994) 14838.
- [46] J. Hafner, Ab-initio simulations of materials using VASP: Density-functional theory and beyond, *Journal of computational chemistry*, 29 (2008) 2044-2078.
- [47] X. Ren, LDA+ DMFT investigation of NiO, Citeseer, 2005.
- [48] W. Kohn, Nobel Lecture: Electronic structure of matter—wave functions and density functionals, *Reviews of Modern Physics*, 71 (1999) 1253.
- [49] V.I. Anisimov, F. Aryasetiawan, A. Lichtenstein, First-principles calculations of the electronic structure and spectra of strongly correlated systems: the LDA+ U method, *Journal of Physics: Condensed Matter*, 9 (1997) 767.
- [50] L. Wang, T. Maxisch, G. Ceder, Oxidation energies of transition metal oxides within the GGA+ U framework, *Physical Review B—Condensed Matter and Materials Physics*, 73 (2006) 195107.
- [51] S.L. Dudarev, G.A. Botton, S.Y. Savrasov, C. Humphreys, A.P. Sutton, Electron-energy-loss spectra and the structural stability of nickel oxide: An LSDA+ U study, *Physical Review B*, 57 (1998) 1505.
- [52] W. Pickett, S. Erwin, E. Ethridge, Reformulation of the LDA+ U method for a local-orbital basis, *Physical Review B*, 58 (1998) 1201.
- [53] H. LOUHAB, Etude théorique des propriétés structurales et électroniques des supraconducteurs à basse température: isotopes de ThCr₂Si₂, 2016.
- [54] W. Kohn, L.J. Sham, Self-consistent equations including exchange and correlation effects, *Physical review*, 140 (1965) A1133.
- [55] D.M. Ceperley, B.J. Alder, *Phys. Rev. Lett.* 45, 566, 1980. and generalized gradient approximation (GGA; Generalized Gradient Approximation).
- [56] J.P. Perdew, Y. Wang, Accurate and simple analytic representation of the electron-gas correlation energy, *Physical review B*, 45 (1992) 13244.
- [57] J.P. Perdew, K. Burke and M. Ernzerhof, *Phys. Rev. Lett.*, 77:3865, 1996.

A decorative border of black floral and leaf motifs surrounds the central text. The border features stylized flowers, leaves, and swirling lines, creating a classic and elegant frame.

Chapter III
Results
&
Discussion

III.1. Introduction

This chapter is devoted to present and discuss the obtained results and it is subdivided into two parts: The first section presented results from characterization of pure and A-doped nickel oxide (NiO) (A=Li, Na, K and La) thin films at various concentrations ($x = 3\%$, 6% , 9% , 12% , 25%) using various techniques. The structural, electrical, and optical properties of NiO thin films are next examined. The second section of the chapter presented the results obtained from theoretical calculations using the DFT theory of the structural, optical, electronic and elastic properties of the as studied samples in the experimental part. Then the obtained theoretical results were compared wherever possible with their corresponding measured values.

III.2. Experimental part

III.2.1. Experimental procedure and characterization techniques

Pure, doped and co-doped NiO thin films were prepared by the sol gel spin coating method. 0.2 M of nickel nitrate hexahydrate ($\text{Ni}(\text{NO}_3)_2 \cdot 6\text{H}_2\text{O}$) was dissolved in a mixture of 80% ethanol and 20% distilled water to create the precursor solution. At room temperature, the mixture was agitated for two hours. MEA (Mono Ethanolamine) was added to the mixture as a stabilizer at a molar ratio of 1:1 to the amount of nickel nitrate while the mixture was being stirred. The obtained solution was kept at room temperature for one day in order to age it. To prepare Li-NiO, K-NiO, and Na-NiO samples, doping solutions were prepared by adding lithium, potassium, and sodium nitrates to the mixture mentioned above. Our thin films were grown on glass substrates that had been thoroughly cleaned with distilled water, acetone, and ethanol to get rid of any remaining grasses or contaminants. After dropping the prepared solution onto the substrate, it was spun for 30 seconds at 2500 rpm. To evaporate the solvents, the film was then heated to 220°C for ten minutes. The aforementioned process was carried out eight times. In order to improve their physical characteristics, the prepared films were lastly annealed for two hours at 500°C . To prepare each sample, the same protocol was adhered to. The structural studies were based on XRD characterization using CuK ($\lambda = 1.5418\text{\AA}$) radiation with 2θ values ranging from 20° to 90° in 0.02 steps. Optical properties such as transmittance and band gap were measured using a UV-Visible spectrophotometer

with a wave length range of 300 to 1100 nm. Finally, the resistivity values were measured using the four probes method on a "Jandel RM 3000" apparatus at room temperature.

III.2.2. Results and discussion

III.2.2.1. Structural properties

III.2.2.1.1. Structural properties of Pure and Alkali doped NiO: Ni_{1-x}A_xO (A=Li, Na and K)

III.2.2.1.1.a. Structural properties of Li-doped NiO

Figure (III.1) shows the XRD diffractograms of NiO thin films at different Li concentrations (0%, 3%, 6%, 9%, 12%, and 25% at). These patterns show diffraction peaks at $2\theta = (37.4, 43.4, 63.0, 79.6)$ which corresponds to (111) (200) (220) and (222) crystal planes respectively. The indexed peaks are fully corresponding with NiO cubic phase (JCPDS-00-047-1049). We do not notice the presence of any peaks of impurities, which confirms the purity of the prepared samples. Unlike the intensity of (111) peak, the intensity of (200) peak is generally enhanced, especially at high Li-doping, which leads to the degradation of the (111) preferential orientation of NiO thin films. Similar results have also been reported earlier for Li doped NiO thin films in other reports using various techniques by I.Sta et al [1]; the (111) peak becomes wider (full width at half maximum), suggesting that the doping process leads to a decrease in the grain size. No peaks other than the NiO peaks are observed, which implies that lithium atoms may be incorporated in the NiO lattice. The cubic phase of the NiO matrix remains unaffected by the incorporation of lithium. The inter planar spacing d_{hkl} and lattice parameter; 'a' had been calculated using the following relationship [2, 3]:

$$d_{hkl} = \frac{n\lambda}{2\sin\theta} \quad (\text{III-1})$$

$$a = d_{hkl}\sqrt{(h^2 + k^2 + l^2)} \quad (\text{III-2})$$

Where n is the order of diffraction (usually $n = 1$) and λ is the X-ray wavelength. (hkl): are Miller indices of the crystal planes. The lattice constant of Li-doped NiO samples decreases than slightly increases with increasing dopant concentration which implies that the smaller radius of the embedded Li⁺ (0.076 nm) ions results in this evolution of the lattice constant.

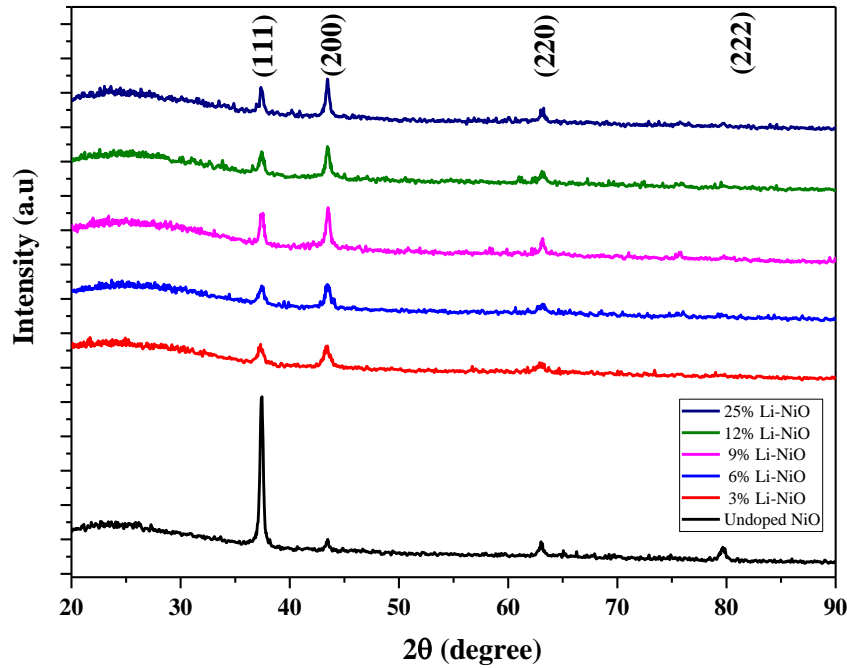


Figure III.1. X-ray diffraction patterns of pure and $\text{Ni}_{1-x}\text{Li}_x\text{O}$ ($x=3\%$, 6% , 9% , 12% , 25%)

Many crystal parameters, including grain size G [4], dislocation density, and micro-strain, can be derived from XRD data, using the following relationships respectively:

$$G = \frac{k\lambda}{\beta_{hkl} \cos \theta_{hkl}} \quad (\text{III.3})$$

$$\delta = 1/D^2 \quad (\text{III.4})$$

$$\varepsilon = \frac{\beta_{1/2}}{4 \tan \theta} \quad (\text{III.5})$$

Where k is the shape factor constant (0.9), θ_{hkl} is Bragg angle, and β_{hkl} is the peak broadening calculated crystallite size, strain and dislocation densities of pure and $\text{Ni}_{1-x}\text{Li}_x\text{O}$ are listed in table (III.1). The values of the average crystallite sizes were found to be 31.56 nm, 20.68 nm, 20.69 nm, 28.97 nm, 36.20 nm, 28.96 nm for the undoped NiO film, the NiO:Li 3%, Li6%, Li9%, Li12% and Li25% respectively table (III.1). We note that the crystallite size decreases than increases with increasing dopant concentration. According to C. Suryanarayana et al [5], the first decrease in crystallite size with Li doping below 9% may be

related to the accumulation of the doped elements at the grain boundaries during the nucleation process which leads to the inhibition of the growth of the grain size, which explains this trend. While the following increase in the grain size could be the result of the close similarity between the ionic radii of Li (0.076 nm) and Ni (0.069 nm); however, a large amount of Li ions are able to substitute Ni ions without causing a significant lattice distortion. The DRX analysis revealed that the 12%Li-doped NiO sample shows the lowest lattice distortion and defects density values.

Table III.1. Values of Bragg angle 2θ , lattice constants a , crystallite size D , mean strain ε and dislocation density δ of NiO thin films as a function to the lithium concentration.

x (at %)	2θ($^{\circ}$)	Lattice constant a (A$^{\circ}$)	Crystallite size G (nm)	Dislocation density δ $\times 10^{15}$ (lines/nm2)	Mean strain ε (%)
0	37.4052	4.160842	31.56631	1.003581	0.10981171
x (at %)	2θ($^{\circ}$)	Lattice constant a (A$^{\circ}$)	Crystallite size G (nm)	Dislocation density δ $\times 10^{15}$ (lines/nm2)	Mean strain ε (%)
3	43.4146	4.165302	20.68874	2.336319	0.16754769
6	43.4109	4.16564	20.68847	2.336379	0.16754984
9	43.5274	4.15503	28.977	1.190949	0.11962418
12	43.4379	4.163176	36.20384	0.762941	0.09574537
25	43.4527	4.161826	28.96947	1.191568	0.11965528

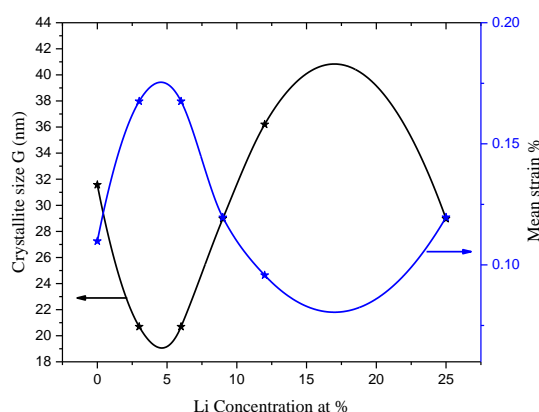


Figure III.2. Variation of crystallite size and mean strain of NiO thin films as a function of Li concentration

III.2.2.1.1.b. Structural properties of Na-doped NiO

Figure (III.2) shows the XRD diffractograms of NiO thin films at different Na concentrations (0%, 3%, 6%, 9%, 12%, and 25%). These patterns show diffraction peaks at $2\theta = (37.34, 43.4, 63.0)$ which corresponds to (111) (200) and (220) crystal planes respectively. The indexed peaks are fully corresponding with NiO cubic phase (JCPDS-00-047-1049). We do not notice the presence of any peaks of impurities, which confirms the purity of the prepared samples. The intensity of the (200) peak is often increased, especially at high Na-doping levels, resulting in a decrease of the (111) preferential orientation intensity of NiO thin films. The doped samples exhibit a decrease in peak intensity and an increase in peak width when compared to the pure sample. This might be interpreted as an indication of deteriorating crystal quality [6]. No peaks other than the NiO peaks are observed, which implies that Sodium atoms may be incorporated in the NiO lattice. The cubic phase of the NiO matrix remains unaffected by the incorporation of Sodium.

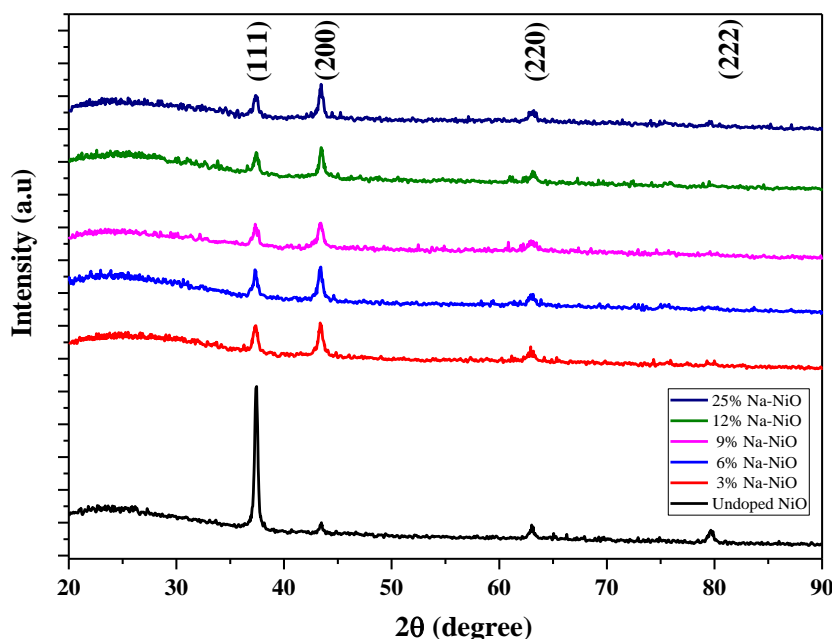


Figure III.3. X-ray diffraction patterns of pure and $\text{Ni}_{1-x}\text{Na}_x\text{O}$ ($x=3\%$, 6% , 9% , 12% , 25%)

The calculated lattice parameter values are given in Table (III.2). It is clear that the lattice parameter first increases significantly from 4.16 nm for pure NiO to 4.173 nm for 9% Na doped NiO representing a lattice expansion, indicating that the Na ions were successfully incorporated into the NiO host lattice by occupying the Ni sites. Then it surprisingly decreases to 4,158nm and 4,160nm for 12% and 25%Na doped NiO respectively. The first increase in lattice parameter could be explained by the ionic radius of Na 0.102 nm (from the precursor) is larger than that of Ni^{2+} , which is 0.069 nm. The smaller lattice parameter may be due to the Ni vacancies that arise from doping the NiO crystal lattice with high amount of Na ions. Calculated crystallite size, strain and dislocation densities of pure and $\text{Ni}_{1-x}\text{Na}_x\text{O}$ are listed in Table (III.2). The values of the average crystallite sizes were found to be 31.56 nm, 24.13 nm, 28.95 nm, 20.68 nm, 20.69 nm, 28.97 nm for the undoped NiO film, the NiO:Na 3% , Na6%, Na9%, Na12% and Na25% respectively Table(III.2). The average crystallite size of 31.56 nm for pure NiO initially decreases to the reach 24.13, 28.9, 20.68 and 20.69nm for 3, 6, 9 and 12% Na, then surprisingly increases to 28.97nm with higher doping levels of 25%Na doping but it remains lower than the undoped one. This trend can be explained as follow: the first decrease in crystallite size with Na doping below 25% may be related to crystallites segregation to have minimum interfacial energy; Additionally, the high

concentration of dopants creates more defects and vacancies, which are defined as the length of a dislocation line per unit [7], help to lower the doped samples' grain size values, which in turn increases strain and dislocation density. The following increase in crystallite size can be associated with the difference in ionic radius as Na^{+1} (0.102 nm) is higher than Ni^{2+} (0.069 nm). The DRX analysis revealed that the 6% and 25% Na-doped NiO sample show the lowest lattice distortion and defects density values.

Table III.2. Values of Bragg angle 2θ , lattice constants a , crystallite size D , mean strain ε and dislocation density δ of NiO thin films as a function of sodium concentration.

x (at %) Na	$2\theta(^{\circ})$ (111)	Lattice constant a (Å)	Crystallite size G (nm)	Dislocation density $\delta \times 10^{15}$ (lines/nm²)	Mean strain ε (%)
0	37.4052	4.160842	31.56631	1.003581	0.10981171
x (at %) Na	$2\theta(^{\circ})$ (200)	Lattice constant a (Å)	Crystallite size G (nm)	Dislocation density $\delta \times 10^{15}$ (lines/nm²)	Mean strain ε (%)
3	43.3983	4.166791	24.13939	0.00171612	0.14359727
6	43.3556	4.170697	28.9597	0.001192372	0.11969564
9	43.321	4.173867	20.68202	0.002337837	0.16760211
12	43.4862	4.158775	20.69389	0.002335156	0.16750598
25	43.4862	4.160451	28.97099	0.001191443	0.119649

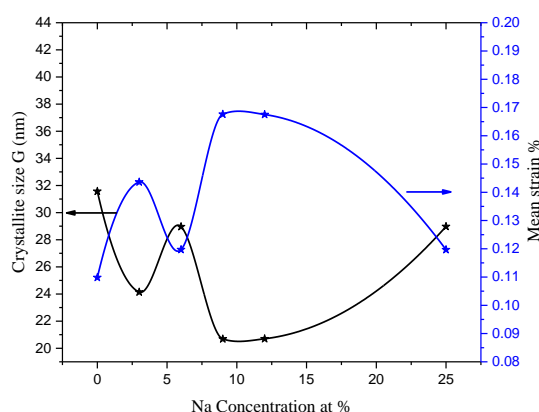


Figure III.4. Variation of crystallite size and mean strain of NiO thin films as a function of Na concentration

III.2.2.1.1.c. Structural properties of K-doped NiO

Figure (III.5) shows the XRD diffractograms of NiO thin films at different K concentrations (0%, 3%, 6%, 9%, 12%, and 25% at). These patterns show diffraction peaks at $2\theta = (37.34, 43.4, 63.0)$ which corresponds to (111) (200) and (220) crystal planes respectively. The indexed peaks are fully corresponding with NiO cubic phase (JCPDS-00-047-1049). We do not notice the presence of any peaks of impurities, which confirms the purity of the prepared samples. Meanwhile, it is seen that the intensity of reflections diminishes with low concentrations of K doping, suggesting that the crystallinity of the films reduces once K is incorporated into the NiO host lattice. We also notice that the crystallinity is enhanced at high concentrations of the K doping (12% and 25%). Pure NiO thin film (111) preferential orientation intensity decreases as a result of higher (200) peak intensity, particularly at high K-doping levels. The observation of no peaks apart from the NiO peaks suggests that Potassium atoms could be well incorporated into the NiO lattice. The addition of Potassium has no effect on the cubic phase of the NiO matrix.

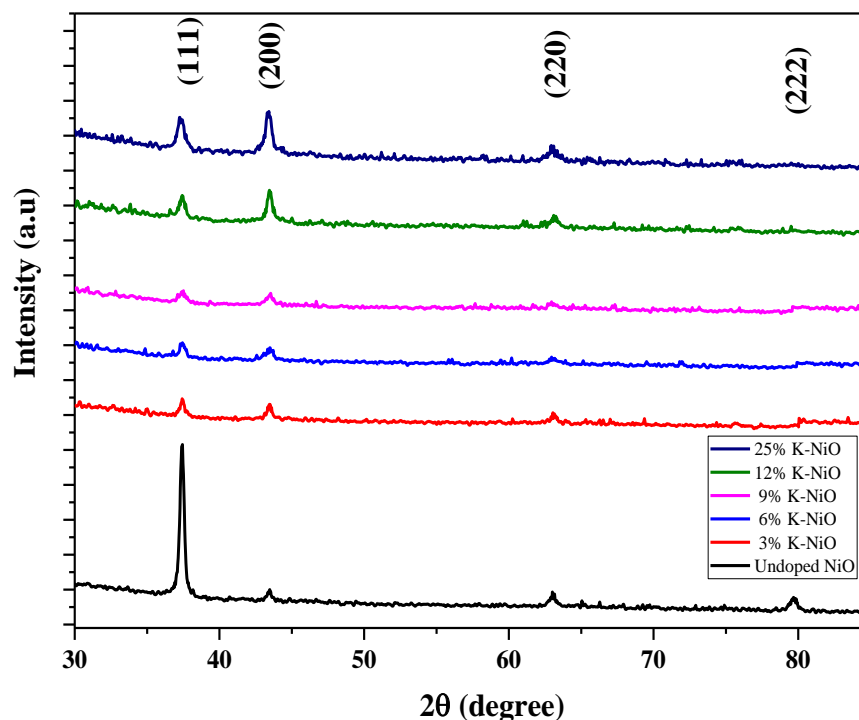


Figure III.5. X-ray diffraction patterns of pure and $\text{Ni}_{1-x}\text{K}_x\text{O}$ ($x=3\%$, 6% , 9% , 12% , 25%)

The calculated lattice parameter values are given in table (III.3). It is clear that the lattice parameter increases significantly from 4.16 nm for pure NiO to 4.17 nm for 25% K doped NiO representing a lattice expansion. The increase in lattice parameter could be explained by the ionic radius of K (0.138 nm) from the precursor) is larger than that of Ni^{2+} , which is 0.069 nm. The lattice parameter is found to have a minimum value (4,15 nm) for a 9% K doping level. According to A. Loukil et al, this occurrence shows that the incorporation of potassium element in NiO can significantly improve the optical, dielectric, and opto-thermal properties of these produced thin films [8]. Additionally, the substantial dependence of these structural characteristics on the potassium level confirmed the incorporation of potassium in the NiO matrix. Calculated crystallite size, strain and dislocation densities of pure and $\text{Ni}_{1-x}\text{K}_x\text{O}$ are listed in table (III.3). The values of the average crystallite sizes were found to be 31.56 nm, 20.68 nm, 20.68 nm, 28.97 nm, 41.38 nm, 24,13 nm for the undoped NiO film, the NiO:K 3% , K6%, K9%, K12% and K25% respectively table (III.3). The average crystallite size of pure NiO 31.56 nm first decreases for low K concentrations than increases along with the increase of K amount in the NiO host lattice to reach a maximum value for 12% K doping. As

mentioned above the decrease in the grain size of the doped samples usually attributed to the accumulation of dopants at the grain boundaries during the nucleation, however the defects and vacancies created by dopants, contribute to the reduction of the grain size of the doped samples. According to Jansons et al. [9] grain size differences due to doping can be attributed to the thermodynamic barrier to development because surface dopants affect crystal surface energy. The DRX analysis revealed that 12% K doping to the NiO host lattice leads to enhancement of the crystallinity by reducing the amount of defects and dislocation densities.

Table III.3. Values of Bragg angle 2θ , lattice constants a , crystallite size D , mean strain ε and dislocation density δ of NiO thin films as a function of potassium concentration.

x (at %)	$2\theta(^{\circ})$	Lattice constant $a(A^{\circ})$	Crystallite size G (nm)	Dislocation density $\delta \times 10^{15}$ (lines/nm²)	Mean strain ε (%)
0	37.405	4.160842	31.56631	1.003581	0.10981171
x (at %) K	$2\theta(^{\circ})$	Lattice constant $a(A^{\circ})$	Crystallite size G (nm)	Dislocation density $\delta \times 10^{15}$ (lines/nm²)	Mean strain ε (%)
	(200)	constant	size G (nm)	density	strain ε
3	43.4146	4.165302	20.68874	2.336319	0.16754769
6	43.4109	4.16564	20.68847	2.336379	0.16754984
9	43.5274	4.15503	28.977	1.190949	0.11962418
12	43.4224	4.16459	41.38861	0.583765	0.08375131
25	43.3419	4.171952	24.13466	1.716791	0.14362538

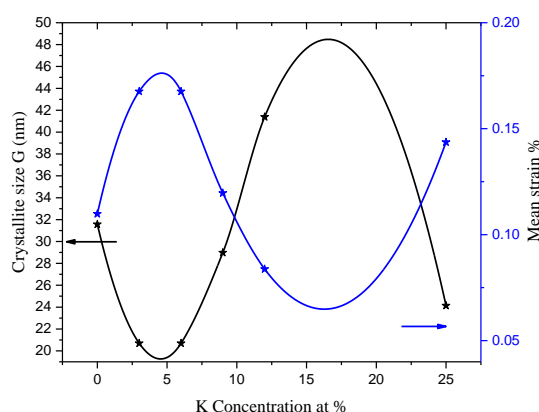


Figure III.6. Variation of crystallite size and mean strain of NiO thin films as a function of K concentration

III.2.2.1.2. Structural properties of co-doped NiO $\text{Ni}_{1-2x}\text{A}_x\text{La}_x\text{O}$ A= (Li, Na, K), ($x=0.03, 0.06$)

Figure (III.6) shows the XRD peak characteristics of co-doped NiO thin films produced under the same conditions. The six samples have characteristic diffraction peaks at angles $2\theta = (37.00, 43.12, 62.72, 75.07, 78.95)$, which correspond to the (111), (200), (220), (311), and (222) crystal planes of the fcc phase structure, respectively. The indexed peaks are fully corresponding with NiO cubic phase (JCPDS-00-047-1049). Also, no La_2O_3 peaks [10, 11] were detected for the doped samples, which indicates the complete solubility of La^{3+} ions at the Ni sites. Compared to the diffraction peaks of the co-doped samples, meanwhile, it can be noticed that the intensity of reflections continuously decreases and the peaks gets broadening with La doping, also, the FWHM of the co-doped samples is extremely large, indicating that the incorporation of La ions within NiO host lattice induces a decline of the crystallinity of the doped films [12]. The lattice parameter of the La co-doped samples with other structural parameters are tabulated in table (III.4). As seen in table (III.4). the grain size of the La co-doped NiO samples is very small in comparison with the alkali doped NiO samples. In addition to what was mentioned above about the accumulation of the dopants in the grain boundaries during the nucleation step which inhibits the crystal growth, the formation of defects, dislocations and strain by dopants would be more induced because of the large ionic radius of La (0.138 nm). Size changes resulting from doping are due to thermodynamic barrier of growth because surface dopants modify surface energy of crystals.

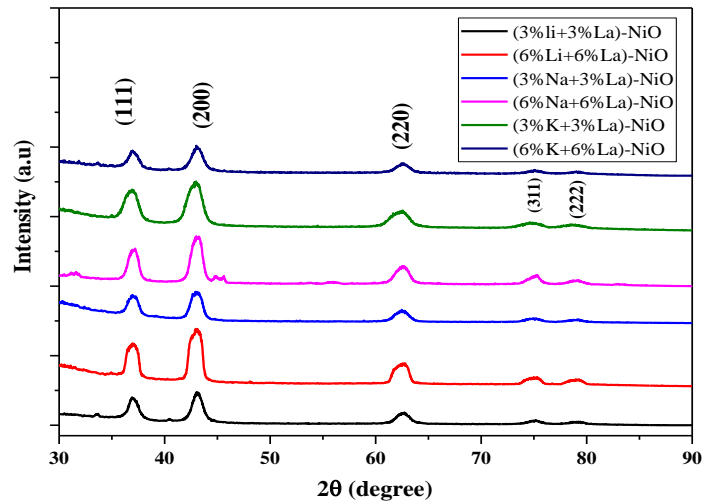


Figure III.7. X-ray diffraction patterns of co-doped NiO $\text{Ni}_{1-2x}\text{A}_x\text{La}_x\text{O}$ A= (Li, Na, K),
($x=0.03, 0.06$)

Table III.4. Values of Bragg angle 2θ , lattice constants a , crystallite size D , mean strain ε and dislocation density δ of co-doped NiO thin films $\text{Ni}_{1-2x}\text{A}_x\text{La}_x\text{O}$ A=(Li, Na, K), ($x=0.03, 0.06$)

material	2θ ($^\circ$) (200)	Lattice constant a (A°)	Crystallite size G (nm)	Dislocation density δ $\times 10^{15}$ (lines/ nm^2)	Mean strain ε (%)
6%La-6%K:NiO	43.1013	4.194122	9.042336	12.230347	0.38334676
3%La-3%Li-NiO	43.1131	4.193029	9.042703	12.229352	0.38333116
3%La-3%Na:NiO	43.4161	4.165165	13.57685	5.425029	0.2553133
6%La-6%Li:NiO	43.5642	4.151691	18.11372	3.047789	0.19136603
3%La-3%K:NiO	43.2764	4.177962	10.85691	8.483747	0.319276
6%La-6%Na:NiO	43.381	4.168372	15.51662	4.153419	0.22339596

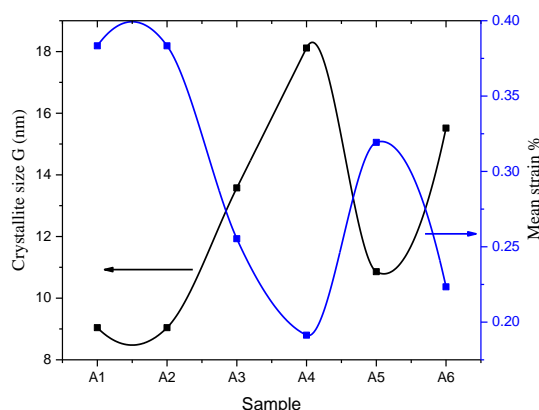


Figure III.8. Variation of crystallite size and mean strain size of co-doped NiO thin films.

III.2.2.2. Optical properties

III.2.2.2.1. Optical properties of Pure and Alkali doped NiO ($\text{Ni}_{1-x}\text{A}_x\text{O}$) (A=Li, Na and K)

III.2.2.2.1.a. Optical properties of Li-doped NiO

Optical transmittance of pure and Li-doped NiO in the wave length range of 300 to 1100 nm is shown in figure (III.9). Pure NiO film exhibits a relatively high transmittance of 85–95% over the visible region; this implies high optical quality due to low scattering or absorption losses. All samples display sharp absorption edges in the wavelength region between 300 and 360 nm, which is related to the transition between valence and conduction bands caused by onset fundamental absorption. The obtained average transmittance of undoped NiO (85%–95%); closely matches with the average transmittance of undoped NiO prepared by sol gel spin coating obtained by Lou et al. [13] and higher than the transmittance of spray pyrolysis-prepared NiO that was obtained by C. Marbet et al. [14]. However, we can see that when the Li concentration increases, the optical transparency decreases gradually, this decrease could be due to the increase of defects, micro strain, and impurities levels in NiO host lattice after doping [15].

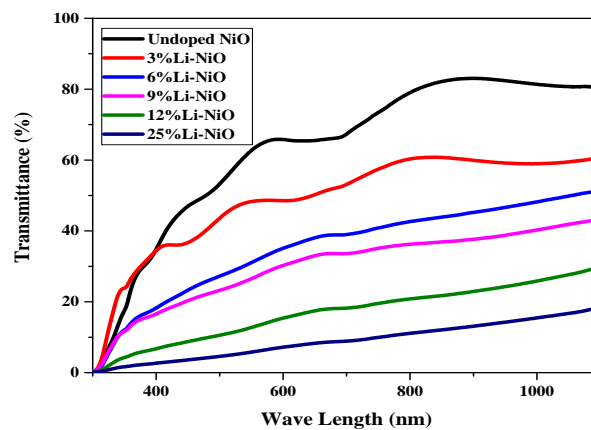


Figure III.9. Transmittance spectra of undoped and Li-doped NiO

As seen in figure (III.9); the absorption edge of Li-doped NiO samples in the near UV switches from this edge to short waves under the Burstein-Moss effect (B-M) [16, 17] or long waves under the Roth effect [18]. The shift in the absorption edge of the films can be explained by the B-M phenomenon, which states that an increase in carrier concentration caused by doping leads in a shift in the Fermi level by reaching the conduction band or the valence band, and to block specific low energy levels at the tail of the conduction band or high energy states at the tail of the valence band. As a result, the band gap widens, expressing the shift of the absorption tail towards the short wave-length (high energy). This broadening of the forbidden band is also responsible for increased transmission in the UV region. The opposing effect, which causes the gap narrowing observed for highly doped semiconductors. When the Fermi level passes in the conduction band, which causes the narrowing of the gap following the fusion of donor bands and conduction and which is called the Roth effect [18]. The reflectance spectra of pure and Li-doped NiO thin films is shown in figure (III.10).

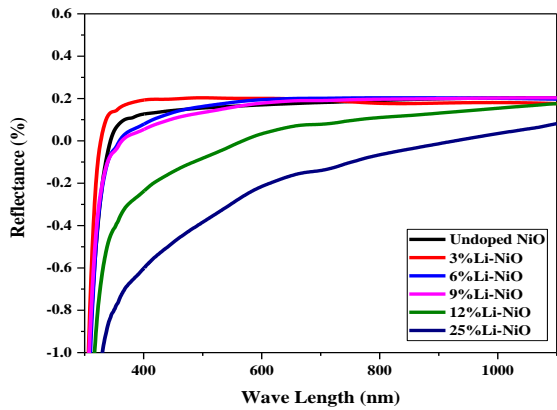


Figure III.10. Reflectance spectra of undoped and Li-doped NiO

The optical band gap (E_g) of the prepared samples was established by the following relationships [3]

$$\alpha = \ln \frac{1}{T} / d \tag{III.6}$$

$$\alpha h\nu = k(h\nu - E_g)^{1/2} \tag{III.7}$$

Where:

α : the absorption coefficient.

T: the transmittance.

d: film thickness

K: proportionality constant

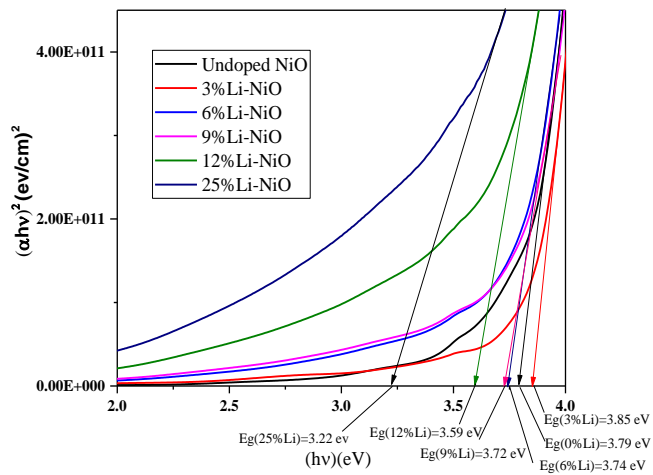


Figure III.11. $(\alpha h\nu)^2$ vs. $(h\nu)$ of undoped and Li doped NiO

Figure (III.11) shows the plots $(\alpha hv)^2$ vs hv . E_g values were calculated by extrapolating the straight-line portion of the plots to the energy axis. Different E_g values are listed in table (III.5). As it can be seen figure (III.11), the obtained band gap values for undoped NiO are in good agreement with reported data [2, 3]. The band gap of Li doped NiO samples was found to increase for 3% Li doping (3.83 eV) than it decreases to reach 3.22 eV for 25% Li. The Structural study based on DRX analysis revealed that doping NiO with Li ions had led to a decrease in the average crystallite size. It is well known the decrease in crystallite size is usually accompanied by an increase in the amount of the defect. These defects create further energy levels, thus the electronic transition which used to occur from the filled valence band to the empty conduction band; is going to happen from the filled valence band to the defect's energy levels, creating more band tail states and leading to band gap narrowing [14]. Our results are comparable by other experimental results [15, 19]. The same thing as the optical gap, the Urbach energy is also related to the disorder in the film lattice, as it is expressed as follows [20]:

$$\alpha = \alpha_0 \exp\left(\frac{hv}{E_u}\right) \quad (\text{III.8})$$

$$\ln\alpha = \ln\alpha_0 + \frac{1}{E_u} hv \quad (\text{III.9})$$

Where α_0 is constant and E_u is the Urbach energy, it was also determined by the curves of $\ln\alpha$ as a function of photon energy hv is used to deduce the Urbach energy $E_u = \frac{\Delta(hv)}{\Delta(\ln(\alpha))}$ of pure and Li doped NiO samples as illustrated in figure (III.12).

Table III.5. Values of optical band gap energy E_g (eV), Urbach energy E_u (meV) and resistivity, of NiO thin films as a function of Li concentration.

x (at%) Li	Band gap energy E_g (eV)	Urbach energy E_u (meV)	Electrical resistivity $*10^4$ Ohm.cm
0	3.79	262.46	5.6625
3	3.83	429.18	0.007
6	3.74	288.18	1.812
9	3.72	2637.36	0.0123
12	3.59	1698.11	0.0303
25	3.22	1360.00	0.0675

According to XRD research, the primary explanation of the higher Urbach energy of doped samples compared to undoped NiO may be lattice distortion and increased micro strain values brought about by the inclusion of dopants in the host lattice of nickel oxide. However, defects generate extra localized defect states that can effectively influence the valence and conduction band edges, and this could be seen as another reason for a smaller band gap in Li doped NiO. More specifically, multiple defect states are formed in the current situation due to increasing impurities and vacancies, which disturb the band structure of the material, resulting in a considerable drop in the optical band-gap and hence increasing the Urbach energy.

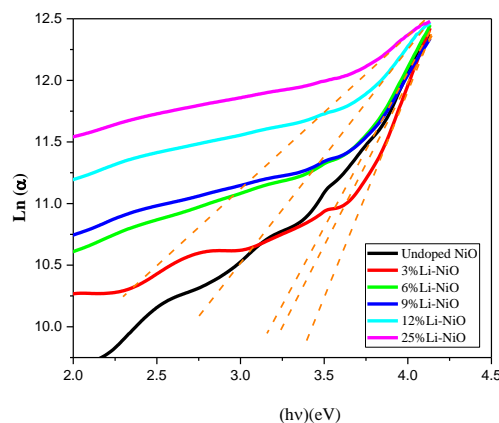


Figure III.12. Estimation of Urbach energy of undoped and Li-doped NiO thin films

III.2.2.2.1.b. Optical properties of Na-doped NiO

Optical transmittance of pure and Na-doped NiO in the wave length range of 300 to 1100 nm is shown in figure (III.13). All samples display sharp absorption edges in the wavelength region between 300 and 360 nm, which is related to the transition between valence and conduction bands caused by the onset fundamental absorption. As shown in figure (III.13), the overall transmittance of the Na doped NiO samples exhibits a relatively low transparency compared to undoped NiO sample and Li doped NiO samples for same concentrations, however the average transmittance of the 3%Na-NiO was determined to be about (39%) while the average transmittance of the 3%Li-NiO was determined to be about (55%) in the visible reason. This decrease in transparency is attributed is related to the development of grain size and the augmentation of impurity levels in the NiO host lattice upon doping [15] which causes an increase in defects, micro-strain, and roughness. Besides this decline in optical transmittance may be also attributed to photon absorption by free carriers generated after alkali doping. [14].

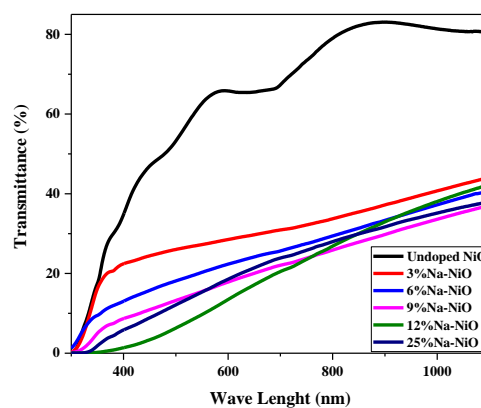


Figure III.13. Transmittance spectra of undoped and Na-doped NiO

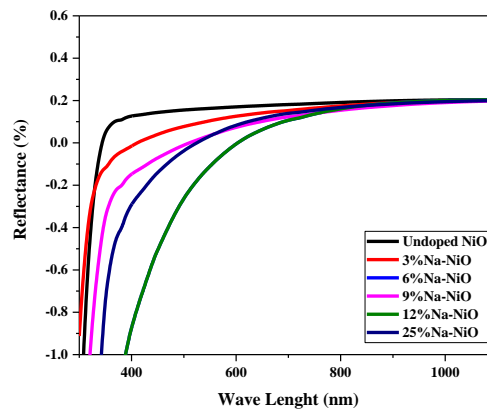


Figure III.14. Reflectance spectra of undoped and Na-doped NiO

We see a red shift in the absorption edge when we compare doped samples to pure ones.

Figure (III.15) shows the plots $(\alpha h\nu)^2$ vs $h\nu$. E_g values of the Na doped NiO samples were calculated by extrapolating the straight-line portion of the plots to the energy axis. Different E_g values are listed in table (III.6). As seen in figure (III.15). The calculated band gap values were found to decrease with the increase of Na concentration in NiO host lattice. Y.R. denny et al [21] has attributed the decrease of the band gap values of the Na doped NiO thin films to the Na 3s states situated over the valence band edge of nickel oxide which results in the lowering of the band gap values of Na-doped NiO sample. The density of impurity energy levels above the valence band edge would be higher, and consequently the band gap became smaller. This decrease in transparency, makes the Na doped NiO samples suitable for optoelectronic devices [22].

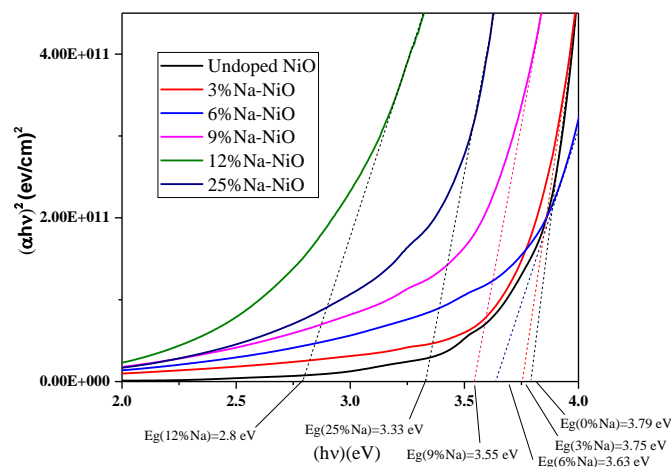


Figure III.15. $(\alpha h\nu)^2$ vs. $(h\nu)$ of undoped and Na doped NiO

Urbach energy of Na doped NiO values are tabulated in table (III.6).

Table III.6. Values of optical band gap energy E_g (eV), Urbach energy E_u (meV) and resistivity, of NiO thin films as a function of Na concentration.

x (at%) Na	Band gap energy E_g (eV)	Urbach energy E_u (meV)	Electrical resistivity* 10^4 Ohm.cm
0	3.79	262.46	5.6625
3	3.67	741.83	0.1425
6	3.63	468.6	0.325
9	3.55	1295.4	0.2925
12	2.08	1022.22	0.4837
25	3.33	787.5	0.0618

As seen in this table, the incorporation of Na ions in NiO host lattice leads to the increase of the Urbach energy. As mentioned above, the created defects and vacancies act as traps for other flaws or impurities that take the shape of platelets or aggregates [23]. These traps contain nano-crystallites and nanoparticles states that could result in high Urbach energy values.

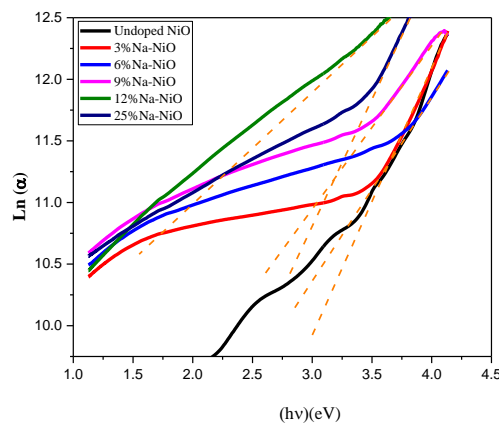


Figure III.16. Estimation of Urbach energy of undoped and Na-doped NiO thin films

III.2.2.2.1.c. Optical properties of K-doped NiO

Optical transmittance of pure and K-doped NiO in the wave length range of 300 to 1100 nm is shown in figure (III.17). All samples display sharp absorption edges in the wavelength region between 300 and 375nm: As shown in figure (III.17), The transmittance for all thin films increases as the wavelength increases in the range of (300-375 nm), and then increases slowly at higher wavelengths. Compared to the undoped sample, all doped samples exhibited a reduced transmittance except the 3%K doped NiO sample which shows a relatively high transmittance in short wave lengths. As mentioned above, introducing of the alkali impurities deteriorates the crystallinity of the films by creating more crystalline defects such dislocations and strain which affects the growth of the crystallite size and increases the roughness of the films thus decreasing the transparency. In addition, the alkali doping leads to create more free carriers and thus more photon absorption which leads to decrease of the transparency.

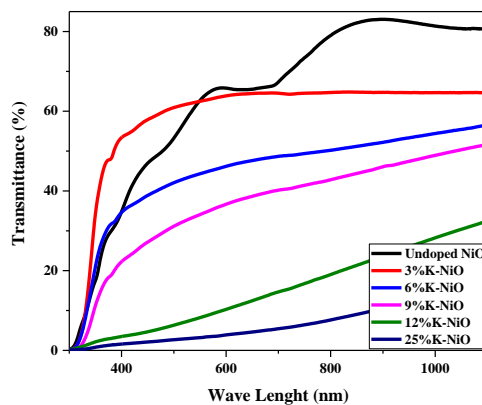


Figure III.17. Transmittance spectra of undoped and K-doped NiO

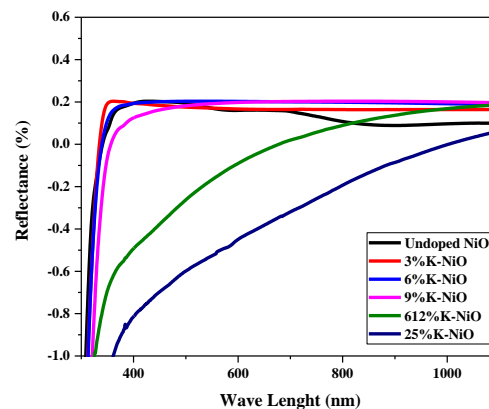


Figure III.18. Reflectance spectra of undoped and K-doped NiO

Figure (III.19) shows the plots $(\alpha h\nu)^2$ vs $h\nu$. E_g values of the K doped NiO samples were calculated by extrapolating the straight-line portion of the plots to the energy axis. Different E_g values are listed in table (III.7). As seen in figure (III.19), the calculated band gap values were found to decrease for 3%K doping (3.63eV) than slightly increase for 6%K doping (3.71eV) but still less than the E_g value of the undoped band gap, than it decreases with the increase of K concentration to reach a minimal value (eV) for 12% K doping. This is associated with the change in transmittance from undoped to K-doped NiO thin films towards the visible range. Due to a red-shift in the optical band gap, which was attributed to the deep states in the band gap, Sharma et al. obtained similar results on Zn doped NiO samples [24]. Furthermore, the influence of a number of variables, including grain size and structural characteristics, may be connected to this phenomenon. Additionally, we observed a band gap shift that increased with K content.

This shift can be attributed to both the existence of defects (oxygen defects or Ni vacancies) caused by the presence of K in NiO thin films as well as the decline in crystallinity. The obtained band gap value of the 6% K-doped NiO (3.71 eV) sample is in good agreement with the band gap value of (6%) of K-doped NiO (3.73 eV) prepared via rapid pyrolysis sol gel technic obtained by C.Q. Liu [15].

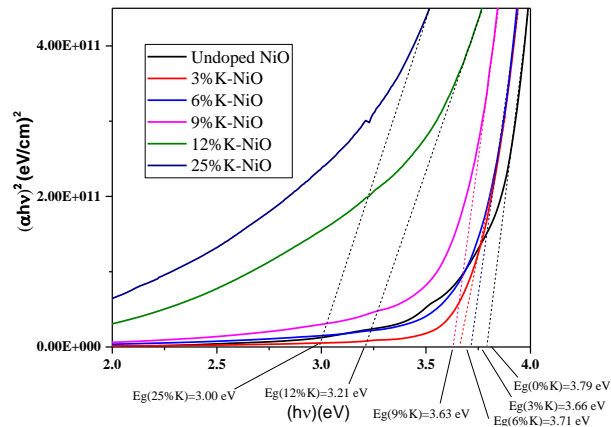


Figure III.19. $(\alpha h\nu)^2$ vs. $(h\nu)$ of undoped and K doped NiO

Urbach energy of K doped NiO values are tabulated in table (III.7). As seen in this table, the incorporation of K ions in NiO host lattice leads to the decrease than increase of the Urbach energy along with the increase of K concentration. That could be attributed to generated structural defects and vacancies which create extra states in the edges of the valence band and conduction band resulting in narrowing the band gap and thus enhancing the Urbach energy values of the doped films.

Table III.7. Values of optical band gap energy E_g (eV), Urbach energy E_u (meV) and resistivity, of NiO thin films as a function of K concentration.

x (at%) K	Band gap energy	Urbach energy	Electrical
	E_g (eV)	E_u (meV)	resistivity* 10^4 Ohm.cm
0	3.79	262.46	5.6625
3	3.74	121.65	0.1665
6	3.71	292.39	1.875
9	3.63	2500.00	1.760
12	3.21	810.3	2.0317
25	3.00	787.5	0.3937

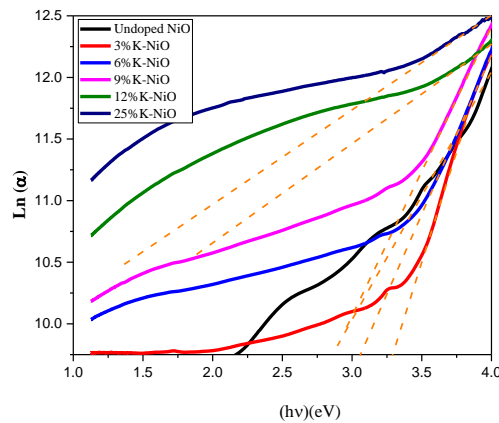


Figure III.20. Estimation of Urbach energy of undoped and K-doped NiO thin films

III.2.2.2.2. Optical properties of co-doped NiO $\text{Ni}_{1-2x}\text{A}_x\text{La}_x\text{O}$ A= (Li, Na, K), ($x=0.03, 0.06$)

The optical transmission T and reflectance R spectra of NiO: La+A (A =Li, Na, K) thin films in the wavelength range 300-1100 nm are shown in Figure (III.21) and Figure (III.22). There are no interference fringes visible. These spectra show that the prepared films exhibit a reflectance less than 20% in the visible range and a transparency coefficient lying between 30 and 60 % in the visible domain. This low transparency can be related to the surface defects (voids, dislocations and pores) already mentioned in the micro-structural study. The transmission of co-doped NiO thin films, on the other hand, is found to be lower than that of alkali doped NiO films for same concentrations. This could be related to these two doping levels, to the raised photon scattering caused by an increase in surface morphological roughness. The decrease in optical transmittance could also be caused by photons' free carrier absorption. Furthermore, it is well known that increased carrier concentrations cause increased scattering, which reduces the transmittance. There is a correlation between the rise in carrier concentration and the decrease in transmittance that occurs with doping.

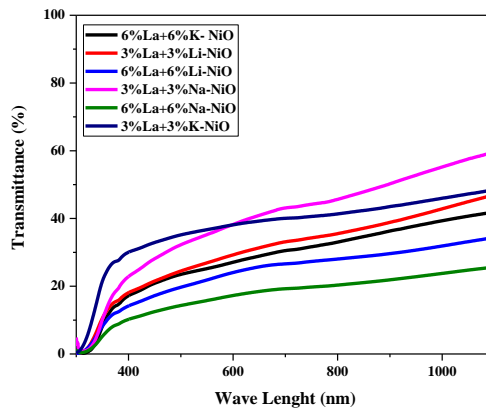


Figure III.21. Transmittance spectra of co-doped NiO

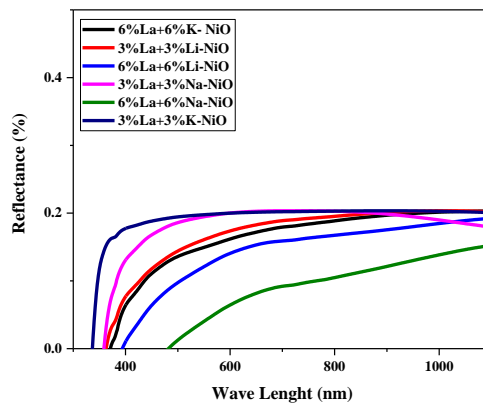


Figure III.22. Reflectance spectra of co-doped NiO

The $(\alpha h\nu)^2$ vs $(h\nu)$ plots of NiO:(La + A) co-doped samples (A=Li, Na and K) are shown in Figure (III.23). The obtained values of the direct energy gap values in terms of La content are listed in table (III.8). They are in good agreement with those reported for NiO films prepared by various techniques [25-27]. Furthermore, variations in E_g and crystallite size D are highly correlated. According to Thota et al. [28], a small variation in the size distribution usually results in a significant broadening of the absorption spectra. We believe that the decrease in average crystallite size caused by La doping may result in an increase in defects. In the presence of defects, the electronic transition occurs from the filled valence band to the energy levels of the defects rather than the usual electronic transition from the filled valence band to the empty conduction band. This phenomenon, which causes an increase in additional band

tail states and shrinkage of the band gap, is usually in competition with another known as the Burstein Moss shift. It does, in fact, cause an increase in the band gap energy value with doping due to the entry of the Fermi level into the conduction band for degenerate semiconductors [29, 30]. NiO that has been doped. This explains E_g 's oscillatory behavior with doping level. NiO that has been doped. This phenomenon, which causes an increase in additional band tail states and shrinkage of the band gap, is usually in competition with another known as the Burstein Moss shift. It does, in fact, cause an increase in the band gap energy value with doping due to the entry of the Fermi level into the conduction band in degenerate semiconductors [29, 30]. This explains E_g 's oscillatory behavior with doping level.

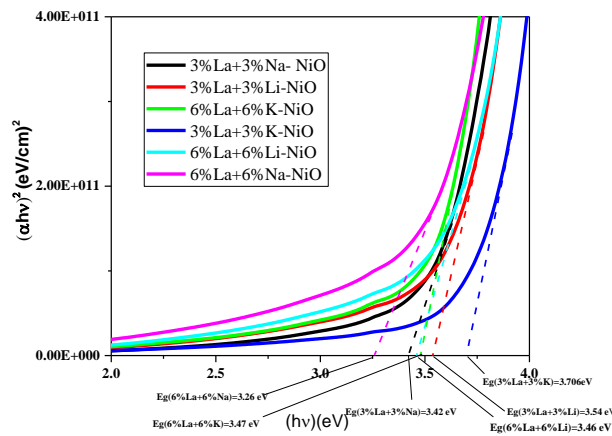


Figure III.23. $(\alpha hv)^2$ vs. (hv) co-doped NiO

The introduction of impurities into semiconductors frequently exposes the band gap's band tailing, which is caused by the creation of localized states. Charge carriers are able to hop from one location to another in these localized states. The band tail energy or Urbach energy (E_u), which characterizes the width of the located states of the co-doped NiO samples were calculated. The band tail energy or Urbach energy (E_u), which characterizes the width of the located states following the empirical Urbach law [31, 32] figure (III.24). The obtained results are shown in table (III.8). The Urbach energy values are extremely high for co-doped samples compared to the alkali doped samples and pure NiO sample. It is possible that the addition of La ions increases the disorder and defects in the NiO:La alkali thin films since this energy is linked to the micro-structural lattice disorder. Indeed, according to the structural study we find a good correlation between the dislocation density δ and the Urbach energy E_u . For these films, the presence of a band tail suggests that the structural disorder and

inhomogeneity are significant. Furthermore, Urbach energy can lead to some explanations of electronic switching between defect states via thermal activation.

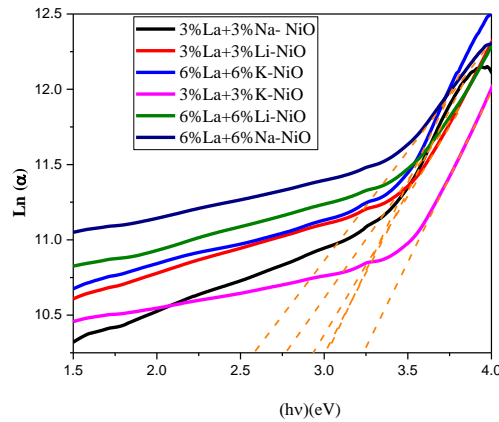


Figure III.24. Estimation of Urbach energy of co-doped NiO thin films

Table III.8. Values of optical band gap energy E_g (eV), Urbach energy E_u (meV), resistivity, and dislocation density of co-doped NiO thin films $\text{Ni}_{1-2x}\text{A}_x\text{La}_x\text{O}$ $\text{A}=(\text{Li}, \text{Na}, \text{K})$, ($x=0.03, 0.06$).

material	Band gap energy E_g (eV)	Urbach energy E_u (meV)	Electrical resistivity* 10^4 Ohm.cm	Dislocation density δ $\times 10^{15}$ (lines/nm ²)
3%La-3%Li-NiO	3.54	1666.66	0.0289	12.229352
6%La-6%Li:NiO	3.46	1700.00	0.048	3.047789
3%La-3%K:NiO	3.706	2291.66	0.009	8.483747
6%La-6%K:NiO	3.47	2650.00	0.0038	12.230347
3%La-3%Na:NiO	3.42	2190.4	0.098	5.425029
6%La-6%Na:NiO	3.26	1440.00	0.0659	4.153419

III.2.2.3. Electrical properties

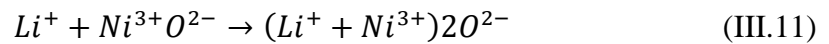
III.2.2.3.1. Electrical properties of Pure and Alkali doped NiO ($\text{Ni}_{1-x}\text{A}_x\text{O}$) (A=Li, Na and K)

III.2.2.3.1.a. Electrical properties of Li-doped NiO

The resistivity of pure and doped NiO films was measured by the four-point probe method using the following relation [33]:

$$\rho = 4.532 \times \left(\frac{V}{I}\right) \times t = \frac{1}{\sigma} \quad (\text{III.10})$$

where ρ is the resistivity, V is the measured voltage, I is the current applied, σ is the conductivity and t is the thickness of the film. The electrical resistivity of undoped and Li doped NiO thin films are summarized in table (III.5) and Figure (III.25) shows the variation of films resistivity and dislocations of NiO films with Li doping concentration. As shown in Figure (III.25), the Li doping has led to lowering in the resistivity values of the NiO samples. Undoped NiO exhibits p-type conductivity, which is caused by nickel vacancies and oxygen atoms that occupy interstitial sites, which leads to the formation of Ni^{3+} [15]. Doping nickel oxide with Alkali atoms such Lithium results in the formation of additional Ni^{3+} ions, as shown in the equation (III.1) [1]:



The incorporation of lithium increases the concentration of Ni^{3+} , which explains why the resistivity of the material decreases after doping. Our samples have lower resistivity values than those reported by I.Sta et al. [1] using the sol gel spin coating technique. Many applications call for transparent conducting films with the highest transmittance achievable in the visible area to improve photo-generated current [14].

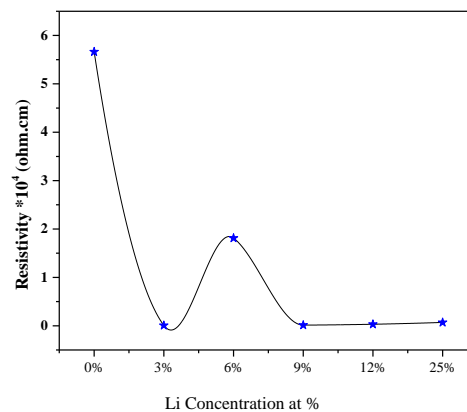


Figure III.25. Variation of the resistivity of NiO thin films as a function of Li concentration

III.2.2.3.1.b. Electrical properties of Na-doped NiO

The resistivity of pure and doped NiO films was measured by the four-probe method. The electrical resistivity of undoped and Na doped NiO thin films are summarized in table (III.6) and figure (III.26) shows the variation of films resistivity and dislocations of NiO films with Na doping concentration. As illustrated in figure (III.26), the incorporation of Na ions in the NiO host lattice has resulted in a decrease in the resistivity values of the NiO samples from $5.66 \times 10^4 \text{ ohm.cm}$ for undoped NiO to $0.327 \times 10^4 \text{ ohm.cm}$ for 3% Na-NiO than it increases slowly to reach $0.0618 \times 10^4 \text{ ohm.cm}$ for 25% Na-NiO. As mentioned above, Pure NiO is known to have p-type conductivity, which occurs from nickel vacancies and oxygen atoms occupying interstitial spaces and generating Ni^{3+} ions [19]. Doping nickel oxide with alkali atoms such sodium (Na) reduces the resistivity of the material because it produces more Ni^{3+} ions. This decrease in electrical resistivity is important for solar cell applications that require lowering cell series resistance.

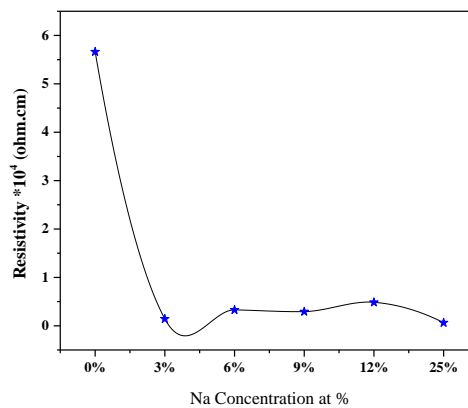


Figure III.26. Variation of the resistivity of NiO thin films as a function of Na concentration

III.2.2.3.1.c. Electrical properties of K-doped NiO

The resistivity of pure and doped NiO films was measured by the four-probe method. The electrical resistivity of undoped and K doped NiO thin films are summarized in table (III.7) and figure (III.27). shows the variation of films resistivity and dislocations of NiO films with K doping concentration. As illustrated in figure (III.27). All of the doped films shows a resistivity values lesser than the undoped NiO film, the incorporation of K ions in the NiO host lattice has resulted in a decrease in the resistivity values of the NiO samples from $5.66 \times 10^4 \text{ ohm.cm}$ for undoped NiO to $0.1665 \times 10^4 \text{ ohm.cm}$ for 3% K-NiO than it increases to reach $2.0317 \times 10^4 \text{ ohm.cm}$ for 12% K-NiO than it decreases again for 25%K-NiO to achieve $0.393 \times 10^4 \text{ ohm.cm}$. This alternative behavior could be explained as follow: When a small amount of K is introduced into the films, the K is ionized into K^+ and replaces Ni^{2+} . Thus one free electron is produced from one NiO atom replacement. Therefore, the carrier concentration increases and the resistivity is decreased with the K concentration at first up to 9% doping. At higher K concentrations (12%), the carrier concentration decreases because of the increasing of the doping atoms and the formation of neutral defects and these neutralized K atoms do not contribute as free electrons. Further increase of the amount of K ions in the NiO lattice creates more structural defects and Ni^{2+} vacancies that can produce two holes which sets free into the valence band and therefore contribute to the conductivity [14].

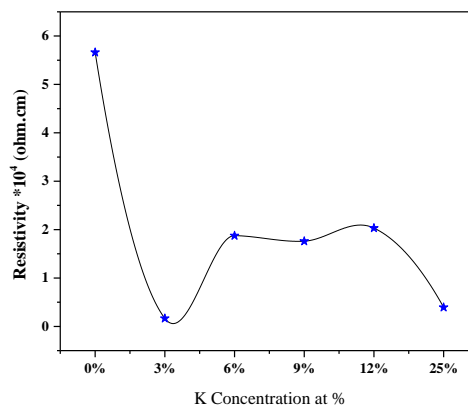


Figure III.27. Variation of the resistivity of NiO thin films as a function of K concentration

III.2.2.3.2. Electrical properties of co-doped NiO $\text{Ni}_{1-2x}\text{A}_x\text{La}_x\text{O}$ A= (Li, Na, K), ($x=0.03, 0.06$)

The resistivity of co-doped NiO $\text{Ni}_{1-2x}\text{A}_x\text{La}_x\text{O}$ A= (Li, Na, K), ($x=0.03, 0.06$) films was measured by the four-probe method. The electrical resistivity of co-doped NiO thin films are summarized in table (III.8) and figure (III.28) shows the variation of films resistivity and dislocations of NiO films with La alkali-doping concentration. This figure reveals clearly that the incorporation of 3%La ions to the 3%alkali doped NiO thin films and 6%La ions to the 6%alkali doped NiO thin films decreases the resistivity of the doped samples. It is well known that stoichiometric NiO is an insulator with conductivity of $10^{-13} \text{ S.cm}^{-1}$ at room temperature, [34]. Its resistivity can be decreased by increasing the number of Ni vacancies and/or interstitial oxygen in NiO crystallites, which results in the production of Ni^{3+} [35]. It is well known that the origin of p-type conduction in nature is also related to the non-stoichiometric form of NiO. In fact, nickel oxide compound has numerous Ni^{2+} vacancies that can produce two holes which sets free into the valence band and therefore contribute to the conductivity. The overall equation of formation of defect and hole can be explained as below [35]:



where h and V_{Ni} represent the hole and the Ni^{2+} vacancies respectively. With lanthanum incorporation into the film, some La^{3+} ions substitute Ni^{2+} in NiO matrix, this may be compensates the deficiencies and therefore decreases considerably the electrical resistivity.

This result shows that extrinsic conduction dominates rather than intrinsic conduction and that the impurities or vacancies present in the material, help to create free carriers in La+A:NiO films (A=Li, Na, K). This decrease in electrical resistivity with La doping can be also correlated with the results of the structural study. A crucial point in the present study is that the addition of 3%La ions to the 3%Li-NiO increases its resistivity from $0.007 \times 10^4 \text{ ohm.cm}$ to $0.0289 \times 10^4 \text{ ohm.cm}$. That could be attributed to the microstructural defects such as dislocations and grain boundaries which affect the mobility of the carriers; in another way they affect the resistivity of the sample since the resistivity is proportional to the reciprocal of the carrier mobility, however, increased dislocation and grain boundaries in the lattice leads to a decrease in the mobility and subsequently to an increase in the resistivity of the thin film.

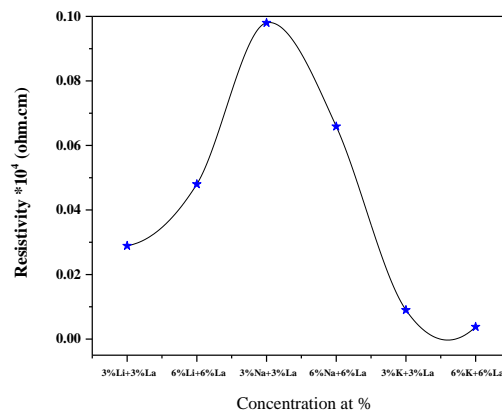


Figure III.28. Variation of the resistivity of co-doped NiO thin films

III.3. Theoretical results

III.3.1. Computational methods

The quantum mechanics program Cambridge Serial Total Energy Package (Castep) [36] was used to investigate the structural, electrical, optical and elastic properties of $\text{Ni}_{1-x}\text{A}_x\text{O}$ for ($x=0.0312, 0.0625, 0.125$ and 0.25) and $\text{Ni}_{1-2x}\text{A}_x\text{La}_x\text{O}$ for ($x=0.0312, 0.0625$) ($\text{A}=\text{Li}, \text{Na}$ and K). Kohn-Sham formation based on the density functional theory (DFT) was used to perform the calculations [37]. Generalized gradient approximation (GGA) in the Perdew Burk-Eruzerhof scheme was used to treat the exchange and correlation potential [38]. Pseudo atomic calculations was applied at Ni 3d8, O 2s2 2p6, Li 1s2, Na 2s2 2p6, K 3s2 3p6, La 5p6 5d1 6s2. The Ultra-soft pseudo potential approach was taken to model the ion electron interactions [39]. Plane wave basis set energy cut-off was taken at 500 eV for all compounds except for $\text{Ni}_{0.968}\text{A}_{0.0312}\text{O}$ and $\text{Ni}_{0.9375}\text{La}_{0.0312}\text{A}_{0.0312}\text{O}$ structures ($\text{A}=\text{Li}, \text{Na}, \text{K}$) however 400 eV energy cut-off was taken. Even with reducing the energy cut-off value for $\text{Ni}_{0.9064}\text{A}_{0.0936}\text{O}$ structures, both electronic and optical properties could not be performed. The Brillouin zone was sampled by employing the monkhort pack method [40] with a separation of $0.05/\text{A}^\circ$. Geometry optimization tolerances were set as follows: the difference of the total energy is within $5 \times 10^{-6} \text{eV/atom}$. The maximum force is $0.01 \text{eV}/\text{A}^\circ$. The maximum stress is 0.02GPa and the maximum displacement was $5 \times 10^{-4} \text{A}^\circ$. Furthermore, more k-points are required to precisely explore electrical and optical properties, and denser k-points are formed. In addition, the number of conduction bands is a significant element in the computation, as it determines the energy range covered and the number of conduction bands. The precision of the Kramers-Kronig transform is determined. There are 15 vacant bands in the current work. To more precisely define the electronic structure, the DFT+U approach was adopted by employing the Hubbard U correction which treats more accurately the strong correlation between the Ni 3d electrons. Hubbard U values were chosen to be 14.0 eV for Ni 3d, 0.0 eV for Ni 2p, and 6.0 eV for O 2p. For the dopant atoms (Li, Na, K and La), Hubbard U was set by the default values.

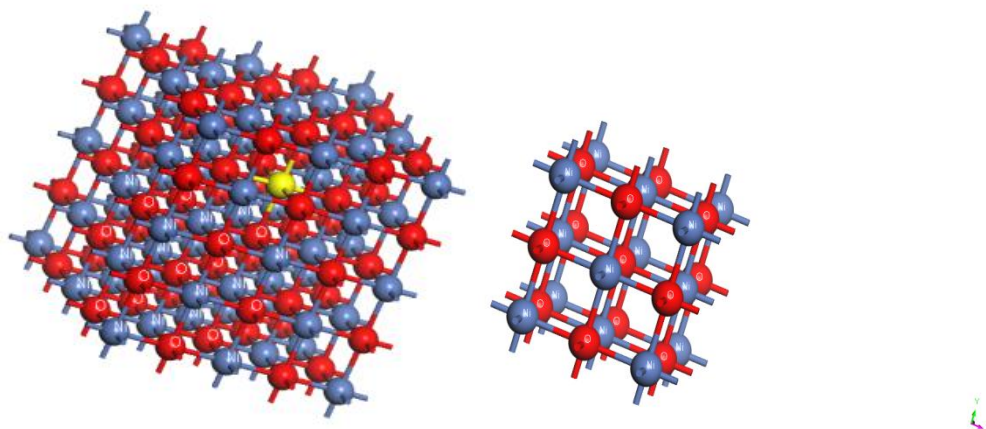


Figure III.29. (a) $1 \times 1 \times 1$ NiO supercell (b) $2 \times 2 \times 2$ NiO supercell ; O atoms are in red, Ni atoms are in blue, Yellow atom represents the dopant atom $x = \text{Li, Na, K, La}$.

III.3.2. Structural properties

III.3.2.1. Structural properties of pure and $\text{Ni}_{1-x}\text{A}_x\text{O}$ ($\text{A} = \text{Li, Na and K}$)

It is necessary to go through structural optimization before computing the elastic, electronic, and optical properties. The structural properties of pure and $\text{Ni}_{1-x}\text{Li}_x\text{O}$, $\text{Ni}_{1-x}\text{Na}_x\text{O}$ and $\text{Ni}_{1-x}\text{K}_x\text{O}$ have been calculated for ($x = 0.0312, 0.0625, 0.0937, 0.125$ and 0.25). The results of the calculation of the lattice parameter a and volume V are listed in the tables (III.9), (III.10) and (III.11) along with the experimental results obtained in this work and the theoretical results available in the literature in order to evaluate our results.

For undoped NiO, it is clear that our calculated results agree with the experimental result obtained in this work and other theoretical data [43]. As no experimental or theoretical results on $\text{Ni}_{1-x}\text{Li}_x\text{O}$ ($x = 0.0312, 0.0625, 0.0937, 0.125$ and 0.25) have been published in the literature, the data tabulated in table (III.9) shows a decrease in the lattice parameter and lattice volume which could be attributed to the difference in the ionic radii between Li^+ and Ni^{2+} ions however the Li radii is much lower than the Ni radii. Lattice parameter (a) and the unit cell volume (V) of $\text{Ni}_{1-x}\text{Na}_x\text{O}$ structures ($x = 0.0312, 0.0625, 0.0937, 0.125$ and 0.25) shows a slight increase in comparison with undoped NiO. The obtained results are illustrated in the table (III.10). A comparison of experimental and theoretical results is made in the same

table. The results of the $\text{Ni}_{1-x}\text{Na}_x\text{O}$ lattice parameter are consistent with experimental measurements.

The results of $\text{Ni}_{1-x}\text{K}_x\text{O}$ illustrated in the table (III.11) show a considerable increase in the lattice parameter and the unit cell volume after K replacement. The reason for this is that the radius of nickel is much lower than that of potassium. When K replaces Ni, the lattice deforms and the residual strain generated during the crystallization process increases the volume. That makes the $\text{Ni}_{1-x}\text{K}_x\text{O}$ superior to the undoped NiO.

Table.III.9. Structural parameters of $\text{Ni}_{1-x}\text{Li}_x\text{O}$ (lattice parameter and cell volume)

material	reference	Calculated (\AA) GGA PBE	Experimental a (\AA)	V (\AA^3)
NiO	Present	4.163	4.165558	72.28
	Other works	4.1632 ^a		
	Other works	4.1888 ^b		
Ni_{0.9687}Li_{0.0312}O	Present	4.1709	4.165302	72.56
Ni_{0.9375}Li_{0.0625}O	Present	4.15	4.16564	70.14
Ni_{0.9063}Li_{0.0937}O	Present	4.1763	4.15503	72.844
Ni_{0.875}Li_{0.125}O	Present	4.147	4.163176	71.3392
Ni_{0.75}Li_{0.25}O	Present	4,068574	4.161826	67.348
Ref	^a [43]	^b [57]		

Table.III.10. Structural parameters of $\text{Ni}_{1-x}\text{Na}_x\text{O}$ (lattice parameter and cell volume)

material	reference	Calculated (\AA) GGA PBE	Experimental a (\AA)	V (\AA^3)
Ni_{0.9687}Na_{0.0312}O	Present	4.1921	4.16679	73.91
Ni_{0.9375}Na_{0.0625}O	Present	4.173	4.1921	72.69
Ni_{0.9063}Na_{0.0937}O	Present	4.179	4.173867	72.982
Ni_{0.875}Na_{0.125}O	Present	4.185	4.158775	73.3
Ni_{0.75}Na_{0.25}O	Present	4,176536	4.160451	72.853

Table.III.11. Structural parameters of $\text{Ni}_{1-x}\text{K}_x\text{O}$ (lattice parameter and cell volume)

material	reference	Calculated (\AA) GGA PBE	Experimental a (\AA)	V (\AA^3)
$\text{Ni}_{0.9687}\text{K}_{0.0312}\text{O}$	Present	4.1367	4.166731	70.28
$\text{Ni}_{0.9375}\text{K}_{0.0625}\text{O}$	Present	4.21	4.165	74.61
$\text{Ni}_{0.9063}\text{K}_{0.0937}\text{O}$	Present	4.29	4.15503	79.05
$\text{Ni}_{0.875}\text{K}_{0.125}\text{O}$	Present	4.28	4.16459	78.623
$\text{Ni}_{0.75}\text{K}_{0.25}\text{O}$	Present	4.39	4.171952	84.60

Figure (III.30) displays the relationship between lattice parameter concentration x and volume.

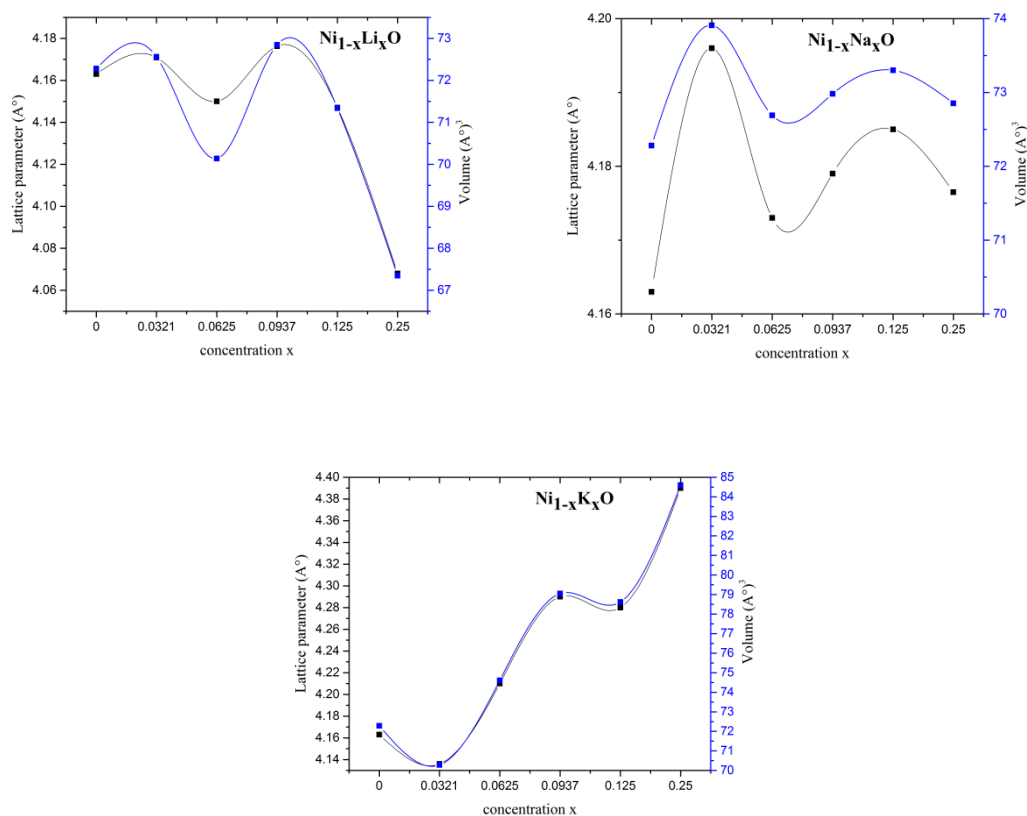


Figure.III.30. Evolution of lattice parameter and volume as a function of concentration x for pure and $\text{Ni}_{1-x}\text{A}_x\text{O}$ ($\text{A}=\text{Li}, \text{Na}$ and K) structures

III.3.2.2. Structural properties of $\text{Ni}_{1-2x}\text{A}_x\text{La}_x\text{O}$ (A=Li, Na and K)

Structural properties as lattice parameter a and unit cell volume of $\text{Ni}_{1-2x}\text{Li}_x\text{La}_x\text{O}$, $\text{Ni}_{1-2x}\text{Na}_x\text{La}_x\text{O}$ and $\text{Ni}_{1-2x}\text{K}_x\text{La}_x\text{O}$ ($x=0.0321, 0.0625$) are illustrated in table (III.12). As seen in this table, the addition of La ions results in the increase of the lattice parameter a and the unit cell volume. This increase is due to the higher mass of the Lanthanum (La) atom than that of the Nickel (Ni) and other alkali ions (Li, Na and K). The comparison of these values (lattice parameter) with the experimental results obtained in the present thesis shows a good concordance for almost all values. To the best of our knowledge, no theoretical or experimental result has been found about $\text{Ni}_{1-2x}\text{Li}_x\text{La}_x\text{O}$, $\text{Ni}_{1-2x}\text{Na}_x\text{La}_x\text{O}$ and $\text{Ni}_{1-2x}\text{K}_x\text{La}_x\text{O}$ for the various concentrations ($x=0.0321, 0.0625$), which allows us to state that our results can be used as a reference.

Table.III.12. Structural parameters of $\text{Ni}_{1-2x}\text{A}_x\text{La}_x\text{O}$ (A=Li, Na and K) ($x=0.0321, 0.0625$) (lattice parameter and cell volume)

material	reference	Calculated (\AA°) GGA PBE	Experimental a (\AA°)	V (\AA°) ³
$\text{Ni}_{0.9375}\text{Li}_{0.0312}\text{La}_{0.0312}\text{O}$	Present	4.166	4.193	72.28
$\text{Ni}_{0.8750}\text{Li}_{0.0625}\text{La}_{0.0625}\text{O}$	Present	4.16	4.151	72.56
$\text{Ni}_{0.9375}\text{Na}_{0.0312}\text{La}_{0.0312}\text{O}$	Present	4.187	4.165	73.42
$\text{Ni}_{0.8750}\text{Na}_{0.0625}\text{La}_{0.0625}\text{O}$	Present	4.27	4.168	77.922
$\text{Ni}_{0.9375}\text{K}_{0.0312}\text{La}_{0.0312}\text{O}$	Present	4.196	4.17	73.90
$\text{Ni}_{0.9375}\text{K}_{0.0312}\text{La}_{0.0312}\text{O}$	Present	4.31	4.17	80.55

In Figure (III.31) we display the relationship between lattice parameter concentration x and volume.

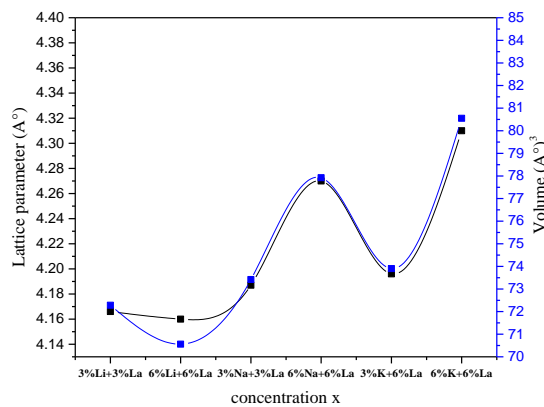


Figure.III.31. Evolution of lattice parameter and volume as a function of concentration x for pure and $Ni_{1-x}A_xO$ ($A=Li, Na$ and K) structures

III.3.3. Electronic properties

III.3.3.1. Introduction

Materials' electronic structures are a major factor in determining their chemical and physical characteristics. It explains how electrons are arranged and behave within atoms. Information regarding atomic composition, bonding, and crystal structure can be found in the electronic structure. Understanding and manipulating the electrical structure of materials in general, and particularly their band structure, is critical for the design and development of electronic devices such as transistors, diodes, and solar cells. Engineers and scientists can manufacture band gaps and adjust the electronic characteristics of materials to produce desired electronic behavior using techniques such as doping, alloying, and heterostructures. In conclusion, the band structure is critical because it affects the electrical conductivity, optical characteristics, and electronic behavior of materials, allowing advances in domains such as electronics, optoelectronics, and material science.

III.3.3.2. Electronic properties of pure and $\text{Ni}_{1-x}\text{A}_x\text{O}$ (A=Li, Na and K)

III.3.3.2.1. Band structures of pure and $\text{Ni}_{1-x}\text{A}_x\text{O}$ (A=Li, Na and K)

The band structure is the arrangement and distribution of energy levels, known as bands, in a material. It indicates the permissible energy levels for electrons. The energy levels are classified into bands that are separated by energy gaps known as band gaps. Lower energy bands, known as valence bands, are often loaded with electrons, whereas higher energy bands, known as conduction bands, are frequently vacant or partially filled. Semiconductors have a lower band gap than insulators, which allows some electrons to pass from the valence band to the conduction band under certain conditions, resulting in moderate conductivity.

Figures (III.32), (III.33), (III.34) and (III.35) show the calculated band structures of pure and Alkali doped NiO structures: $\text{Ni}_{1-x}\text{Li}_x\text{O}$, $\text{Ni}_{1-x}\text{Na}_x\text{O}$, $\text{Ni}_{1-x}\text{K}_x\text{O}$ ($x= 0.0312, 0.0625, 0.125, 0.25$) according to the directions of high-symmetry points in the first Brillion zone. These figures illustrate that the estimated band structures of pure and Alkali doped NiO have indirect band gaps. The predicted band gap of pure NiO is 3.72eV. The estimated value for pure NiO is quite similar to the experimental band gap value found in this work (3.79eV), and it is more accurate than other theoretical data in other DFT simulations [41]. Impurity incorporation in the NiO host lattice has resulted in alterations in band dispersion near the Fermi level. We observed the localization of some bands above the Fermi level, which resulted in the dispersion of the nickel oxide band structure's insulating property. This may be due to the DFT's efficiency in dealing with strongly coupled systems. Also, as it can be seen from figures (III.49), (III.50) and (III.51), the band gap narrowed as a result of impurities being added to the NiO host lattice. It can be clearly seen how close the theoretical and experimental calculated band gaps are. Also these findings demonstrated that the size of the band gap may be modulated by altering the alkali dopants Li, Na, and K. This discovery highlights a major difference between the effects induced by substitutional and interstitial doping. In the previous one, a Ni^{2+} cation is replaced by a A^{+1} (Li^{+1} , Na^{+1} , or K^{+1}) cation, resulting in a hole (i.e. hole doping) and unoccupied levels of Ni above the Fermi level, which minimizes the size of the gap. Interstitial doping involves the addition of electrons to the system (i.e. electron doping), which raises the Fermi level to the CB and creates occupied levels below the Fermi level, so closing the gap. Both experimental and theoretical band gap values obtained in the present work are illustrated in tables (III.13), (III.14) and (III.15)

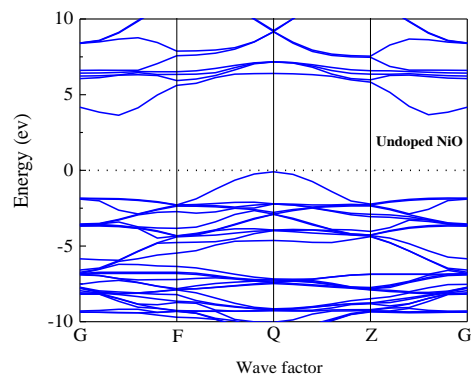


Figure III.32 Electronic Structure of Undoped NiO

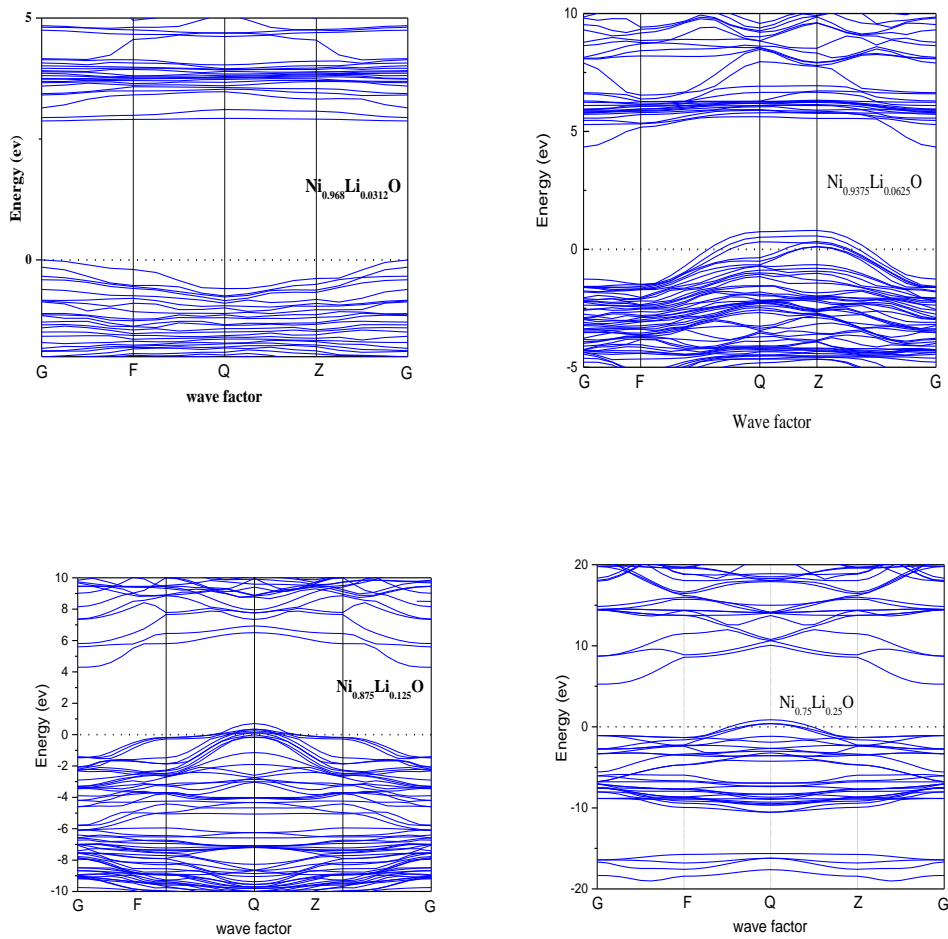


Figure III.33. Electronic band structure of $\text{Ni}_{1-x}\text{Li}_x\text{O}$

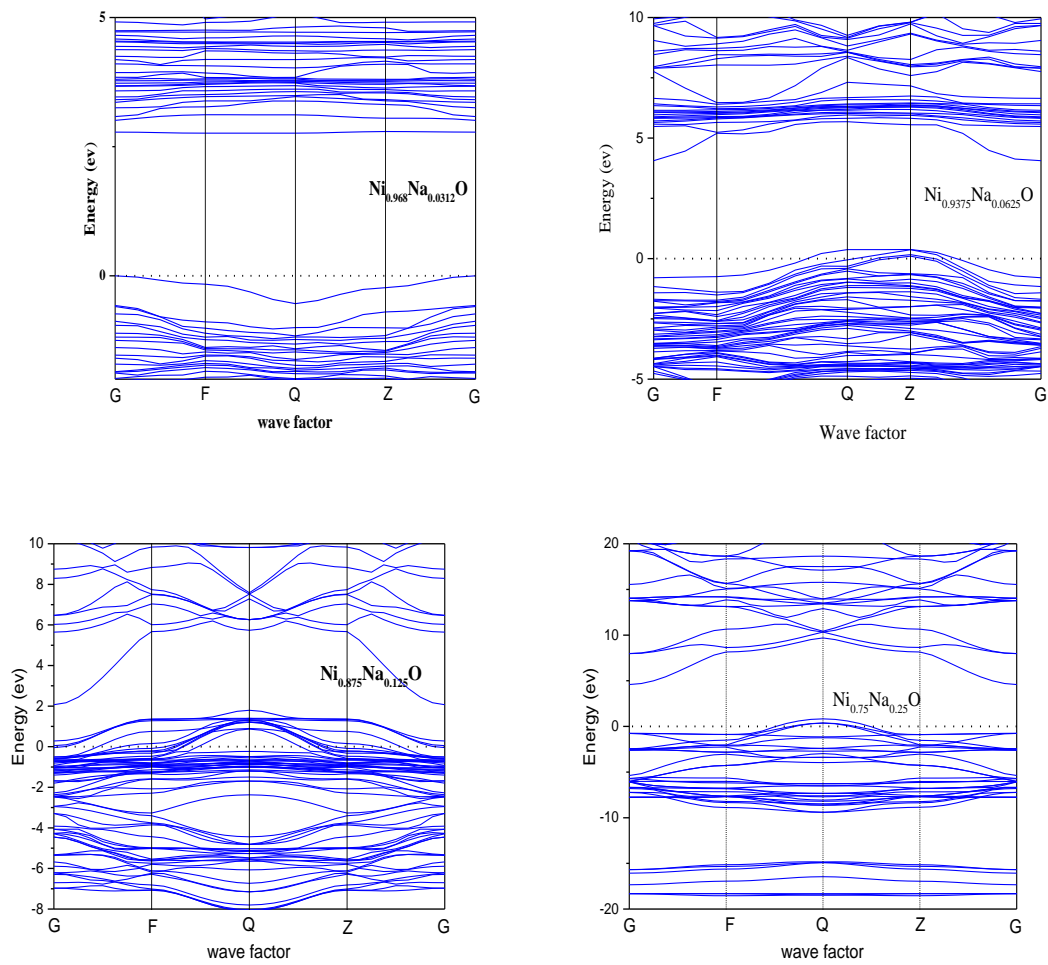
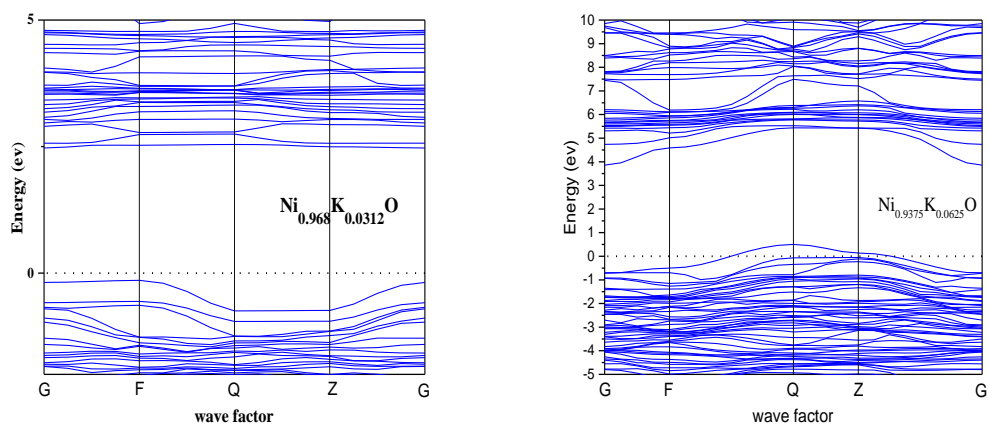


Figure III.34. Electronic band structure of $\text{Ni}_1\text{-Na}_x\text{O}$



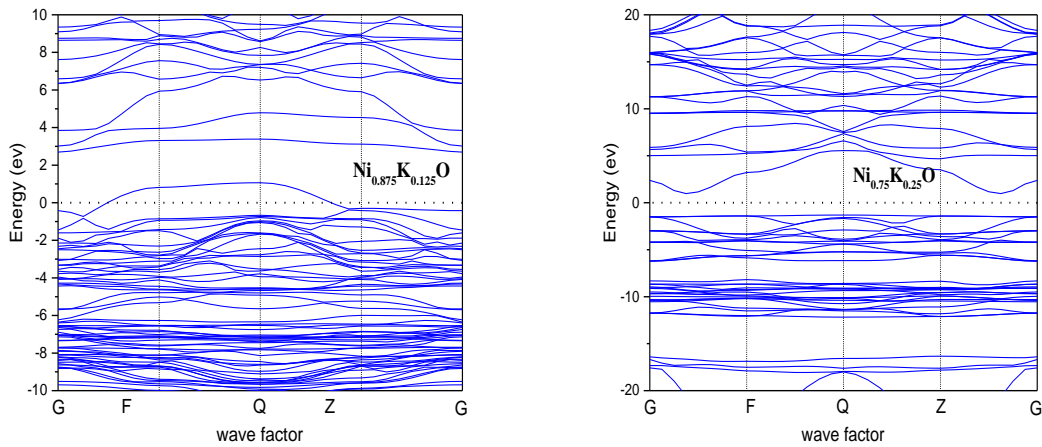


Figure III.35. Electronic band structure of $\text{Ni}_{1-x}\text{K}_x\text{O}$

Table.III.13. Theoretical and experimental band gap energy values of $\text{Ni}_{1-x}\text{Li}_x\text{O}$

material	reference	Calculated band GGA+U (eV)	Eg(eV) gap Visible	Exp./UV- spectrophotometer
NiO	Present	3.73	3.79	
$\text{Ni}_{0.9687}\text{Li}_{0.0312}\text{O}$	Present	2.68	3.83	
$\text{Ni}_{0.9375}\text{Li}_{0.0625}\text{O}$	Present	3.6	3.74	
$\text{Ni}_{0.875}\text{Li}_{0.125}\text{O}$	Present	3.2	3.59	
$\text{Ni}_{0.75}\text{Li}_{0.25}\text{O}$	Present	3.9	3.22	

Table.III.14. Theoretical and experimental band gap energy values of $\text{Ni}_{1-x}\text{Na}_x\text{O}$

material	reference	Calculated band GGA+U (eV)	Eg(eV) gap Visible	Exp./UV- spectrophotometer
NiO	Present	3.73	3.79	
$\text{Ni}_{0.9687}\text{Na}_{0.0312}\text{O}$	Present	2.75	3.67	
$\text{Ni}_{0.9375}\text{Na}_{0.0625}\text{O}$	Present	3.68	3.63	
$\text{Ni}_{0.875}\text{Na}_{0.125}\text{O}$	Present	0.96	2.08	
$\text{Ni}_{0.75}\text{Na}_{0.25}\text{O}$	Present	3.82	3.33	

Table.III.15. Theoretical and experimental band gap energy values of $\text{Ni}_{1-x}\text{K}_x\text{O}$

material	reference	Calculated band gap GGA+U (eV)	$E_g(\text{eV})$ Visible Exp./UV- spectrophotometer
NiO	Present	3.73	3.79
$\text{Ni}_{0.9687}\text{K}_{0.0312}\text{O}$	Present	3.33	3.74
$\text{Ni}_{0.9375}\text{K}_{0.0625}\text{O}$	Present	2.63	3.71
$\text{Ni}_{0.875}\text{K}_{0.125}\text{O}$	Present	1.76	3.21
$\text{Ni}_{0.75}\text{K}_{0.25}\text{O}$	Present	2.1	3.00

III.3.3.2.2. Density of states of pure and $\text{Ni}_{1-x}\text{A}_x\text{O}$ (A=Li, Na and K)

The density of states is a key term in solid-state physics that describes how available energy levels are distributed in a material or system. It can tell us a lot about the behavior and properties of electrons, phonons, and other elementary excitations in a particular energy range. The density of states is commonly expressed as a function of energy, and it is impacted by factors such as the material's crystal structure, band structure, and temperature. It can acquire insights into phenomena such as electrical conductivity, thermal characteristics, and optical behavior by studying the density of states, leading to breakthroughs in materials science, electronics, and energy-related technologies.

Total and partial density of states of pure NiO are illustrated in figure (III.36). The Fermi level separates the valence band (VB) from the conduction band (CB). These materials are an indirect band gap semiconductor, as evidenced by the VB maximum (VBM) and the CB minimum (CBM). The DOS of NiO for both spin channels is symmetric and for this reason the DOS for minority spin is not shown. Accordingly, the band gap (E_g) for NiO is about 3.73 eV slightly lower than the experimental value (3.79eV). For undoped NiO structure, we can see that The whole spectrum is occupied by Ni 3d states, with the exception of the interval from -2 eV to E_F (0eV), where the O 2p states are more prominent. Ni 4s states contribute insignificantly and are not represented.

For Li doping structures ($\text{Ni}_x\text{Li}_{1-x}\text{O}$), The Ni 3d and O 2p states contribute the most to the total DOS. Li 2s states provide a negligible impact. Despite their low occupation, the insertion of Li in the lattice clearly has a substantial impact on the electrical structure. The top of the valence band is dominated by O2p states, while the bottom of the conduction band

is dominated by Ni 3d orbitals. Because of the various p orbitals formed by Na, K, and O atoms, it is possible that Na and K will change the valence band edge (p-type doping) or inject impurity states into the band gap. In the case of Na doping ($\text{Ni}_x\text{Na}_{1-x}\text{O}$), we observe that some bands coming from Na 2p states lie slightly above the VBM of NiO, but a smaller number of Na 2p states equally locate at the CBM. However, these impurity bands are fully occupied and unable to serve as recombination sties due to the Fermi level E_F , which is situated above the Na 2p states. This would greatly lower the photon transition energy for electron transport from these states to the CBM. The band gap narrows with the increase of Na concentration in NiO host lattice as a result of this process, and the resultant value of 3.35 eV is substantially less than that of pure NiO (3.73eV). When it comes to K-doped NiO (figure.III.39), some impurity bands are introduced above the VBM, while others lay in the band gap. A portion of these bands also locate below the CBM. As a result of all of them, the band gap is significantly reduced.

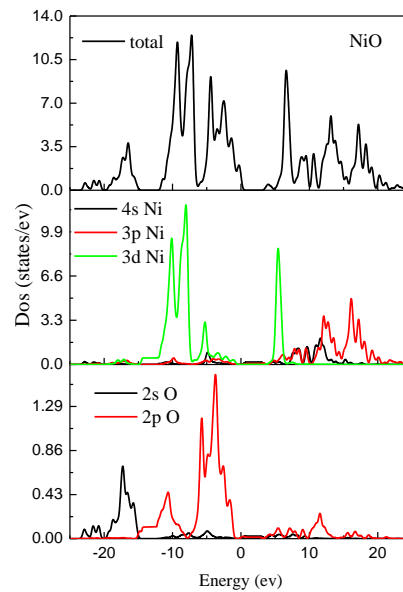


Figure III.36. Total and partial electronic density of states of undoped NiO

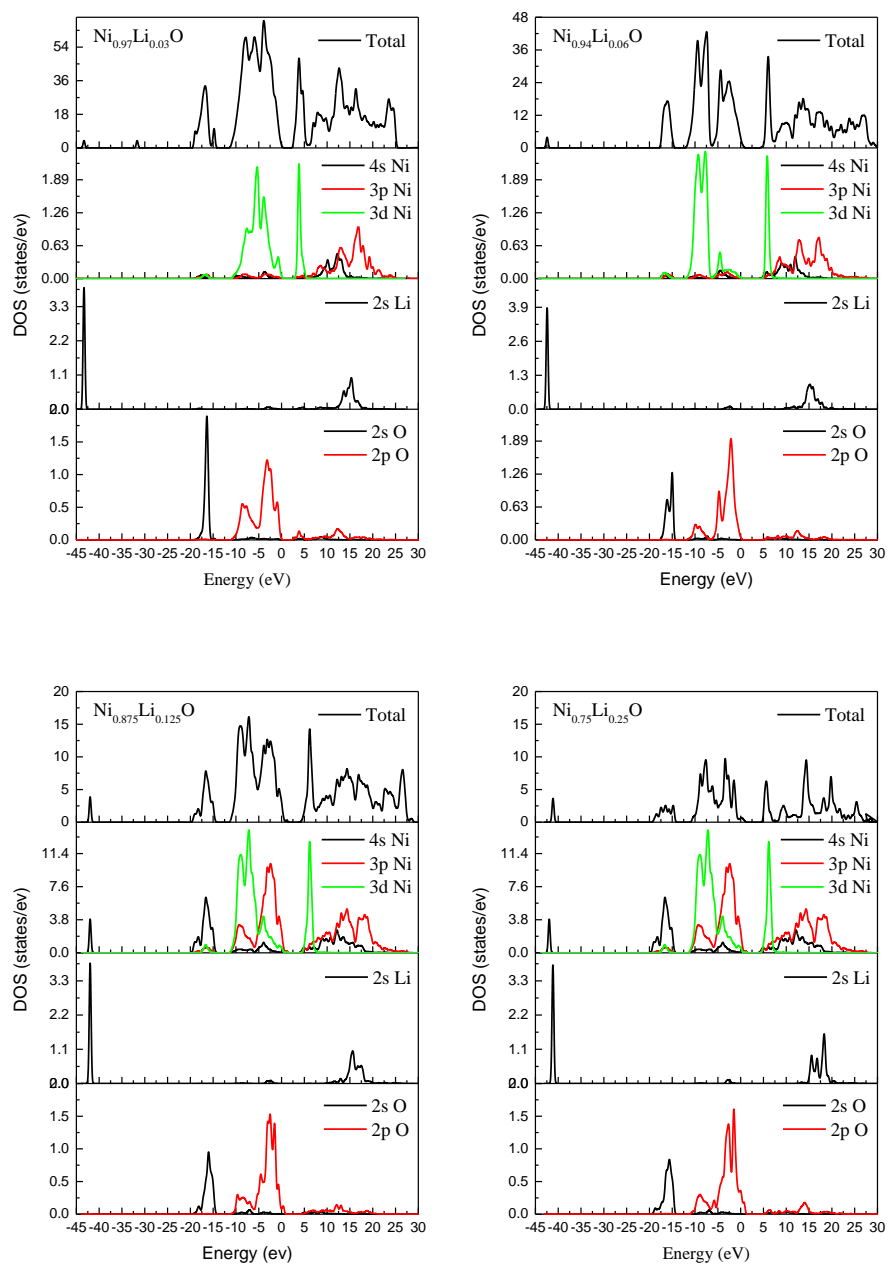


Figure III.37. Total and partial electronic density of states of $\text{Ni}_{1-x}\text{Li}_x\text{O}$

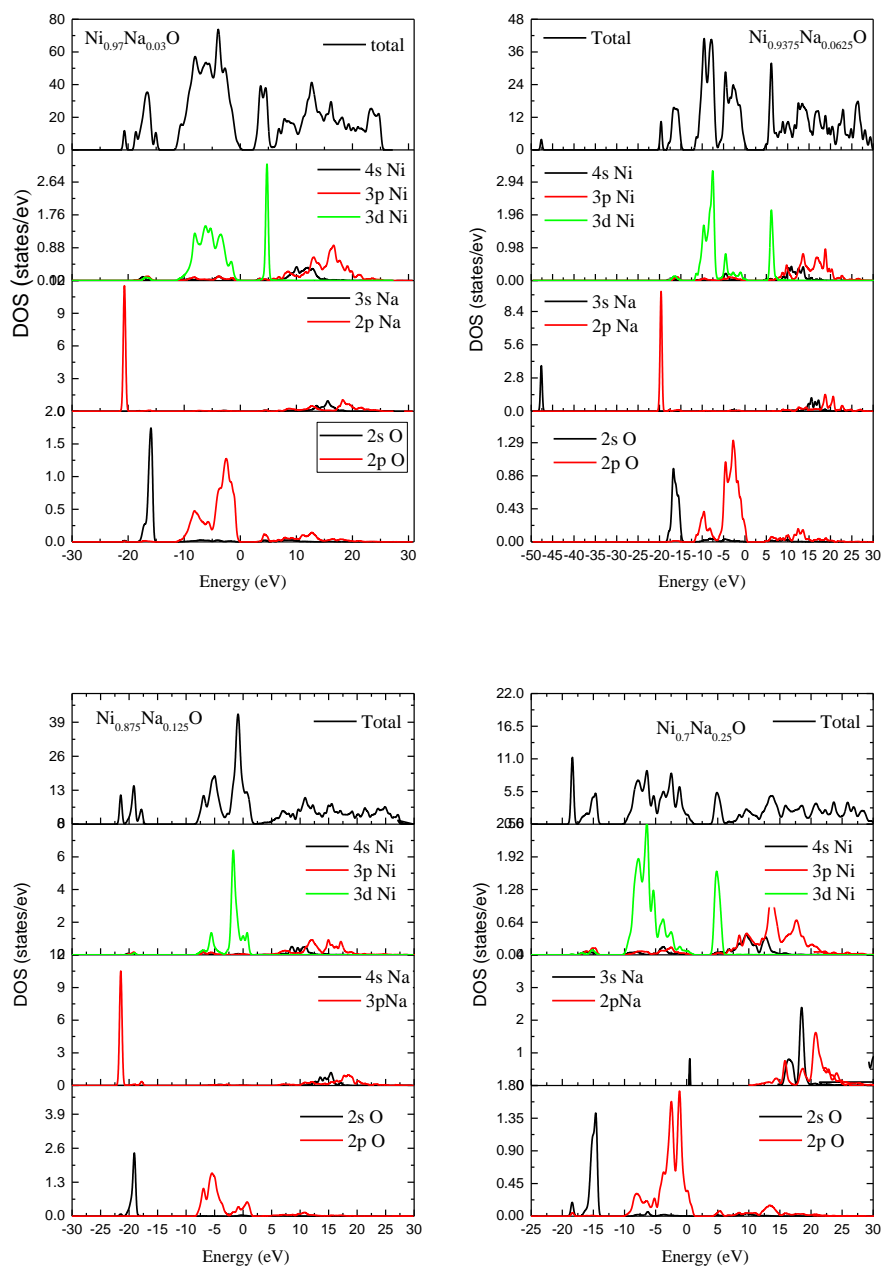


Figure III.38. Total and partial electronic density of states of $\text{Ni}_{1-x}\text{Na}_x\text{O}$

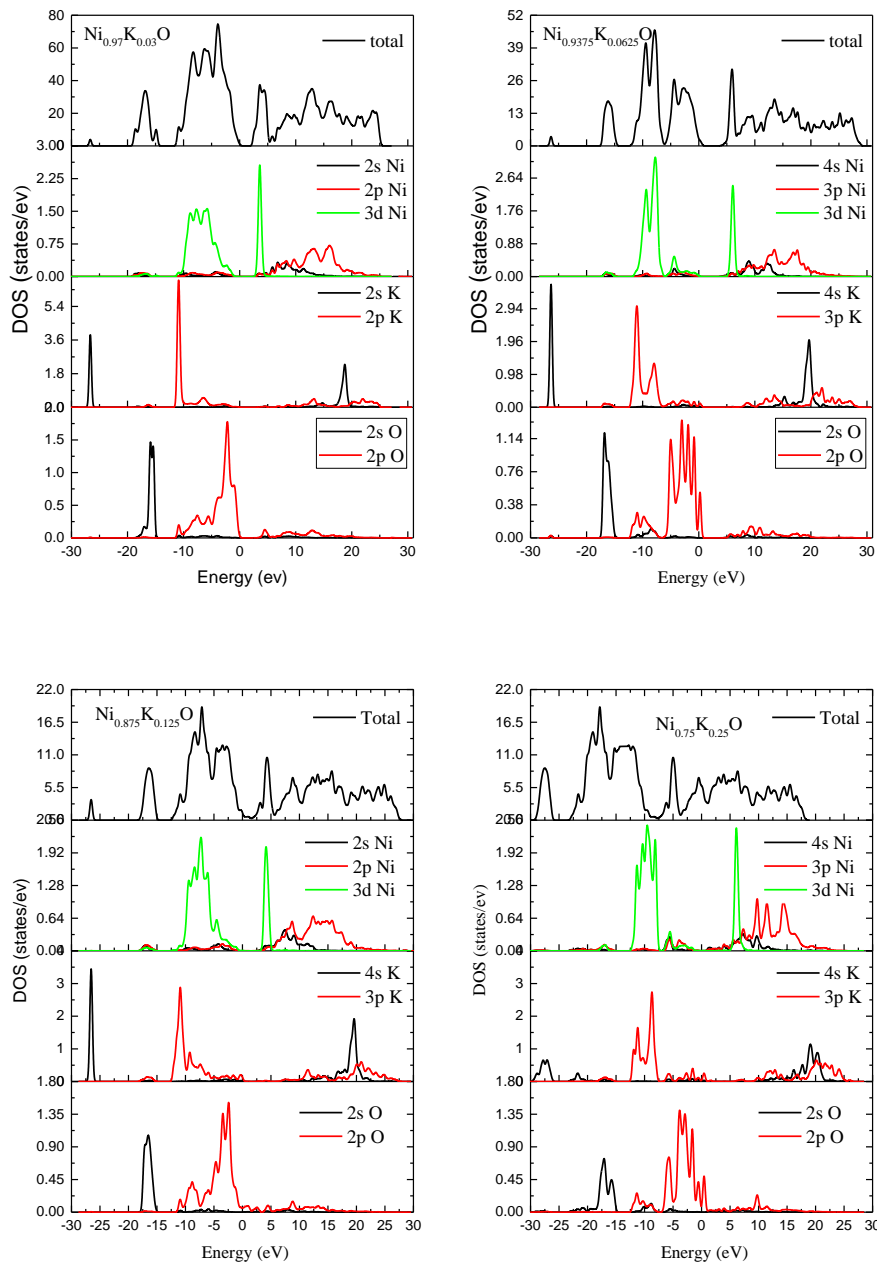


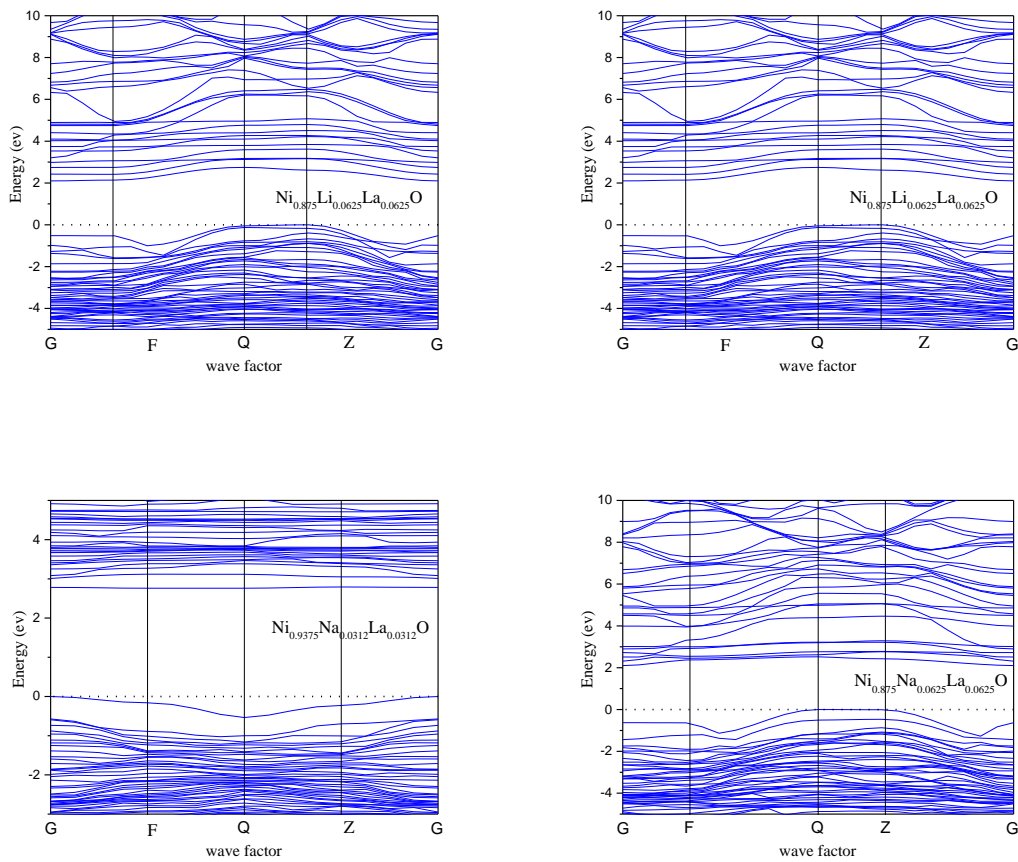
Figure III.39. Total and partial electronic density of states of $\text{Ni}_{1-x}\text{K}_x\text{O}$

III.3.3.3. Electronic properties of $\text{Ni}_{1-2x}\text{A}_x\text{La}_x\text{O}$ (A=Li, Na and K)

III.3.3.3.1. Band structures

The calculated band structures of $\text{Ni}_{1-2x}\text{A}_x\text{La}_x\text{O}$ (A=Li, Na and K) materials are presented in figure (III.40). As shown in figure below, the calculated band structures of $\text{Ni}_{1-2x}\text{Li}_x\text{La}_x\text{O}$, $\text{Ni}_{1-2x}\text{Na}_x\text{La}_x\text{O}$ and $\text{Ni}_{1-2x}\text{K}_x\text{La}_x\text{O}$ ($x=0.0312, 0.0625$), exhibit an indirect band

gaps. The calculated band gap values are close to the experimental band gaps obtained in the present thesis. The addition of La ions to the alkali doped NiO host lattice, led to more band gap shrinking. Unlike the alkali doping, we found that the incorporation of La ions to the alkali doped NiO (Li, Na or even K) led to disappearance of the dispersion around the Fermi level, however, there no bands located above the Fermi level. Both experimental and theoretical band gap values obtained in the present work of the co-doped NiO samples are listed in table (III.16).



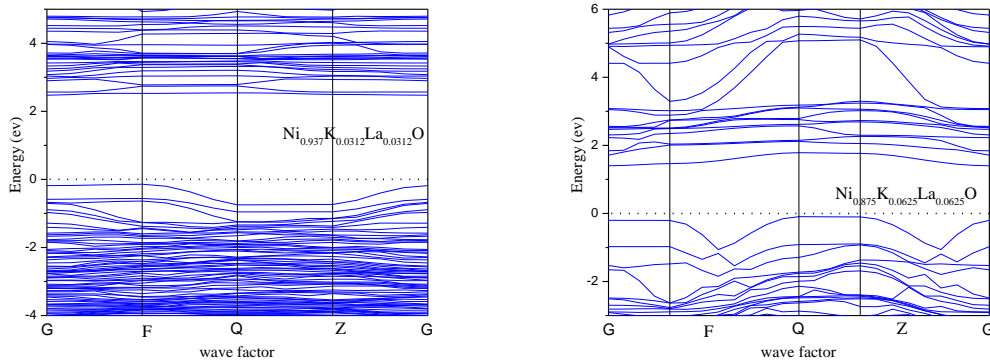


Figure III.40. Electronic band structure of co-doped NiO $\text{Ni}_{1-2x}\text{A}_x\text{La}_x\text{O}$ $\text{A}=(\text{Li}, \text{Na}, \text{K})$, ($x=0.03, 0.06$)

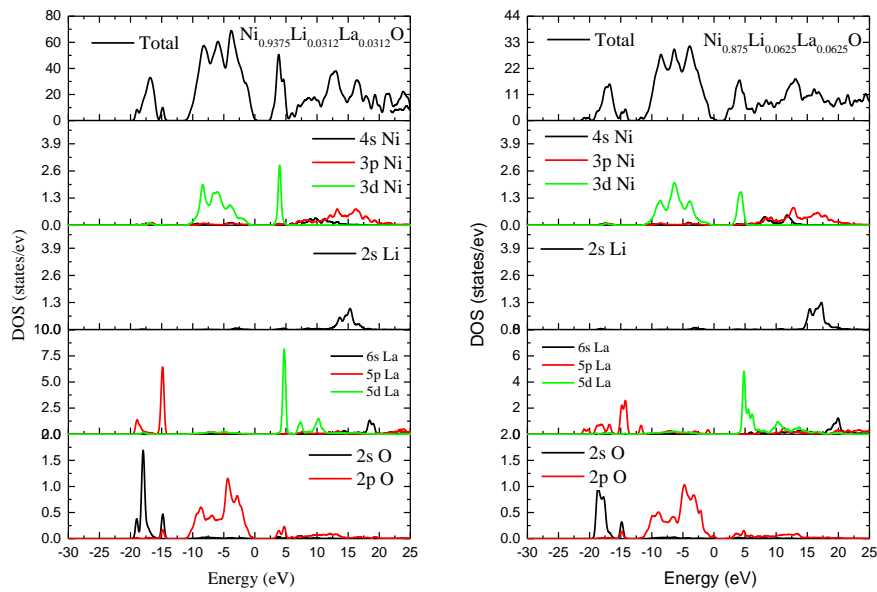
Table.III.16. Theoretical and experimental band gap energy values of co-doped NiO thin films $\text{Ni}_{1-2x}\text{A}_x\text{La}_x\text{O}$ $\text{A}=(\text{Li}, \text{Na}, \text{K})$, ($x=0.03, 0.06$).

material	reference	Calculated band gap GGA+U (eV)	$E_g(\text{eV})$ Exp./UV- Visible spectrophotometer
3%La-3%Li-NiO	Present	2.86	3.54
6%La-6%Li:NiO	Present	2.1	3.46
3%La-3%K:NiO	Present	2.63	3.706
6%La-6%K:NiO	Present	1.5	3.47
3%La-3%Na:NiO	Present	2.75	3.42
6%La-6%Na:NiO	Present	2.0	3.26

III.3.3.3.2. Density of states

Figure (III.41) illustrates the partial and total density of states of $\text{Ni}_{1-2x}\text{Li}_x\text{La}_x\text{O}$ structures ($x=0.0312, 0.0625$). It's clear that La ions has a considerable contribution to the density of states, however the prominent feature observed in the conduction band CB is located around 5 eV above the Fermi level and is dominated by La5d states along Ni3d states. The rest of the conduction band is mainly dominated by Ni3p states with negligible contribution from Li2s and La6s states. Ni4s states have a negligible and are not shown. The states of La5p and O2s from the VBs lying near -15 eV and -20 eV respectively, while the states the states Ni3d with O2p contribute in the VBs ranging from -10 to -3eV. The top of the

valence band is composed mainly of O2p states. Partial and total density of states of $\text{Ni}_{1-2x}\text{Li}_x\text{La}_x\text{O}$ structures is shown in figure (III.57). As seen in this figure, the bands originating from Na2p and La5p states locate just above the VBM of NiO, while less Na2p and La5p states locate at the CBM simultaneously. On the other hand, the Fermi level located above the Na2p states means that these impurity bands are fully occupied and cannot act as recombination sites. This would serve to reduce the photon transition energy significantly for electron transfer from these states to the CBM, consequently this process induces a narrowing of the band gap. For $\text{Ni}_{1-2x}\text{K}_x\text{La}_x\text{O}$ structures, their density of states was shown in figure (III.57). We have found that the incorporation of La atoms to the K doped NiO structures results in the appearance of some impurity bands introduced above the VBM while some lie in the band gap farther some of these states located below the CBM. All of that led to a significant reduction in the band gap to a value around 1.5eV.



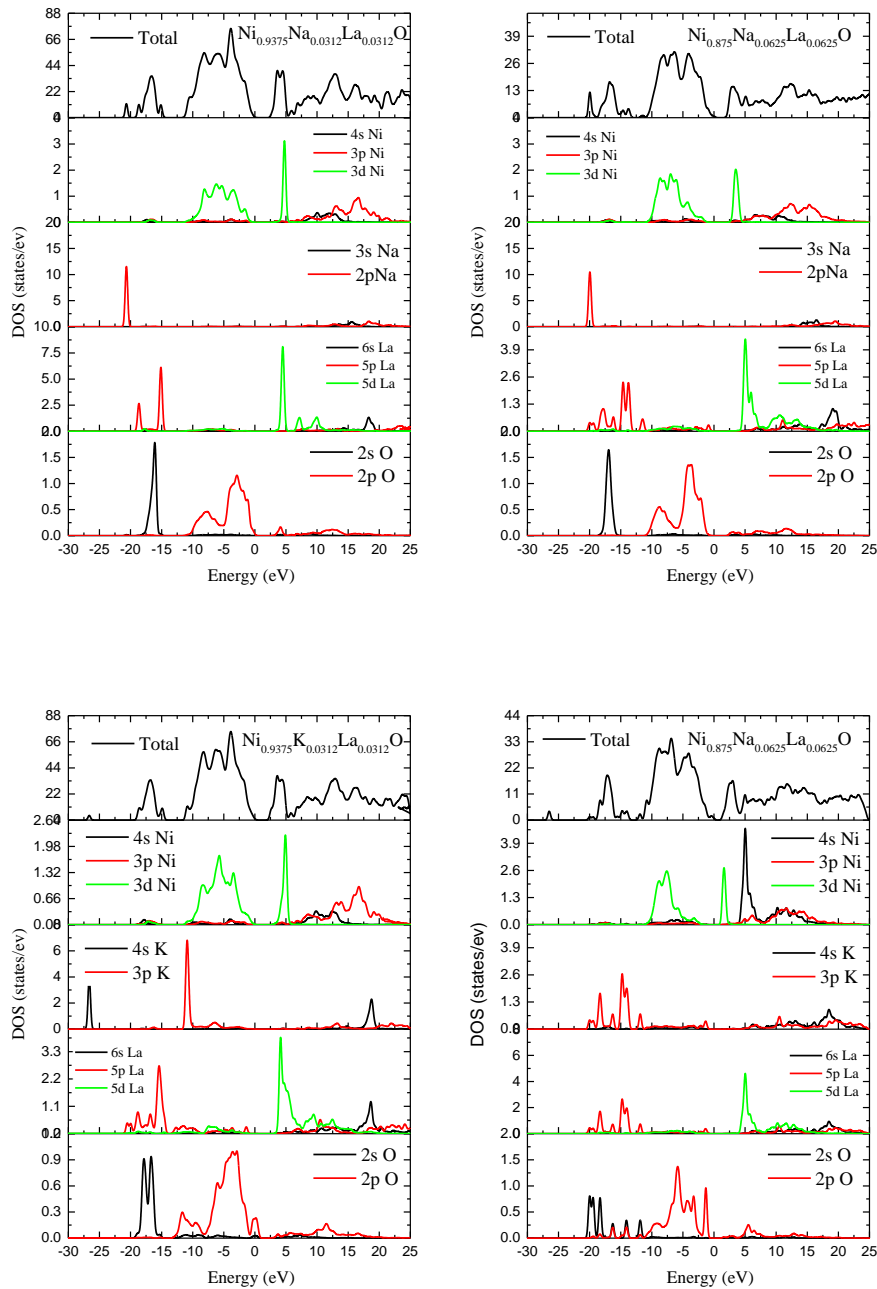


Figure III.41. Total and partial density of states of co-doped $\text{NiO Ni}_{1-2x}\text{A}_x\text{La}_x\text{O}$
 $\text{A}=(\text{Li}, \text{Na}, \text{K}), (x=0.03, 0.06)$

III.3.4. Optical properties

Optical characteristics provide important information about how materials interact with light, allowing researchers to comprehend and control light-matter interactions. A material's optical properties reveal vital information about its electronic structure. Nickel

oxide thin films are semiconductors with a wide band gap. They feature intriguing optical properties that make them extremely attractive for a wide range of applications. In this section, we calculated the optical properties using the dielectric function $\varepsilon(\omega)$ (the dielectric function, the refractive index, the extinction coefficient, absorption, reflectivity, and the loss function) Pure and $\text{Ni}_{1-x}\text{A}_x\text{O}$ (A=Li, Na, K). For different concentrations (x=3%, 6%, 12% and 25%).

III.3.4.1. Optical Constants

The dielectric function is a key feature in the study of different optical and electronic properties of crystals, including light reflection, transmission, and absorption, as well as the behavior of electrons and excitations within the material. Its frequency dependence reveals information on the crystal's behavior across a wide range of electromagnetic frequencies,

from radio waves to x-rays. The dielectric function of the crystals is primarily determined by transitions between the valence and conduction bands; however, optical properties can be calculated using the function written in the form:

$$\varepsilon(\omega) = \varepsilon_1(\omega) + i\varepsilon_2(\omega) \quad (\text{III.13})$$

Where $\varepsilon_1(\omega)$ and $\varepsilon_2(\omega)$ are the real part and imaginary part of the dielectric function respectively.

The imaginary part of the dielectric function can be written as:

$$\varepsilon_2(\omega) = \frac{4\pi e^2}{\Omega \varepsilon_0} \sum_{K,V,C} |\varphi_K^C| u, r |\varphi_K^V|^2 \delta(E_K^C - E_K^V - \omega) \quad (\text{III.14})$$

Where:

e is the electron's charge.

Ω is the volume of a unit cell.

φ_K^C and φ_K^V are proper functions of Bloch type that corresponds to E_K^C, E_K^V respectively.

ω is the frequency.

Indeed, the real and imaginary parts of the dielectric function are given by the Kramers-Kronig relation (III.15) and (III.16)

$$\varepsilon_1(\omega) = 1 + \frac{2}{\pi} P \int_0^{\infty} \frac{\omega' \varepsilon_2(\omega')}{\omega'^2 - \omega^2} d\omega' \quad (\text{III.15})$$

$$\varepsilon_2(\omega) = -\frac{2\omega}{\pi} P \int_0^{\infty} \frac{\varepsilon_1(\omega') - 1}{\omega'^2 - \omega^2} d\omega' \quad (\text{III.16})$$

Where P is the principal part of the Cauchy integral.

With knowledge of the complex dielectric function, other optical constants, such as the refractive index $n(\omega)$, the extinction coefficient $k(\omega)$, and the absorption coefficient $\alpha(\omega)$, The reflectivity $R(\omega)$ and the loss function $L(\omega)$,

can be calculated using the following formulas:

$$n(\omega) = \frac{1}{\sqrt{2}} \left[\sqrt{\varepsilon_1^2(\omega) + \varepsilon_2^2(\omega)} + \varepsilon_1(\omega) \right]^{\frac{1}{2}} \quad (\text{III.17})$$

$$K(\omega) = \frac{1}{\sqrt{2}} \left[\sqrt{\varepsilon_1^2(\omega) + \varepsilon_2^2(\omega)} - \varepsilon_1(\omega) \right]^{\frac{1}{2}} \quad (\text{III.18})$$

$$\alpha(\omega) = \frac{1}{\sqrt{2}\omega} \left[\sqrt{\varepsilon_1^2(\omega) + \varepsilon_2^2(\omega)} + \varepsilon_1(\omega) \right]^{\frac{1}{2}} \quad (\text{III.19})$$

$$R(\omega) = \frac{(n-1)^2 + K^2}{(n+1)^2 + K^2} \quad (\text{III.20})$$

$$L(\omega) = \text{Im} \left(\frac{-1}{\varepsilon(\omega)} \right) = \frac{\varepsilon_2(\omega)}{\varepsilon_1^2(\omega) + \varepsilon_2^2(\omega)} \quad (\text{III.21})$$

III.3.4.2. The dielectric function $\varepsilon(\omega)$

III.3.4.2.1. The dielectric function $\varepsilon(\omega)$ of pure and $\text{Ni}_{1-x}\text{A}_x\text{O}$ (A=Li, Na and K)

Figure (III.42) shows the imaginary part of the dielectric function of pure and Alkali doped NiO structures: $\text{Ni}_{1-x}\text{Li}_x\text{O}$, $\text{Ni}_{1-x}\text{Na}_x\text{O}$, $\text{Ni}_{1-x}\text{K}_x\text{O}$ ($x=0.0312, 0.0625, 0.125, 0.25$). Based on these figures, the curves of $\varepsilon_2(\omega)$ indicate that the first critical points of the dielectric function are produced at 5.1, 1.2, 4.99, 1.98, 2.36 eV for $\text{Ni}_{1-x}\text{Li}_x\text{O}$ structures and 3.14, 4.98, 4.87, 0.89 eV for $\text{Ni}_{1-x}\text{Na}_x\text{O}$ structures and 3.6, 4.87, 4.06, 0.14 eV for $\text{Ni}_{1-x}\text{K}_x\text{O}$ structures for $x=0.0312, 0.0625, 0.125, 0.25$ concentrations respectively. The dielectric

function of the undoped NiO carries three major peaks at 8.3, 11.78, 16.97 eV while in $\text{Ni}_{0.963}\text{Li}_{0.0312}\text{O}$ structure the major transitions appear at 4.5, 9.9, 14.89 eV and 8.44, 12.25, 17.31 eV for $\text{Ni}_{0.937}\text{Li}_{0.0625}\text{O}$ and 8.08, 11.67, 16.16 eV for $\text{Ni}_{0.875}\text{Li}_{0.125}\text{O}$ and 5.56, 9.48, 17.54 eV for $\text{Ni}_{0.75}\text{Li}_{0.25}\text{O}$ structure. The $\text{Ni}_{0.963}\text{Na}_{0.0312}\text{O}$ structure exhibits two major peaks at 6.6, 16.73 eV and at 8.78, 17.2 eV for $\text{Ni}_{0.937}\text{Na}_{0.0625}\text{O}$ and 7.17, 17.3 eV for $\text{Ni}_{0.875}\text{Na}_{0.125}\text{O}$ while the $\text{Ni}_{0.75}\text{Na}_{0.25}\text{O}$ structure carries four major peaks at 0.95, 7.7, 10.5, 17.09 eV. Same for $\text{Ni}_{0.963}\text{K}_{0.0312}\text{O}$ structure which shows major transitions at 6.8, 16.73 eV, and 8.44, 16.7 eV for $\text{Ni}_{0.937}\text{K}_{0.0625}\text{O}$ structure and at 6.94, 12.94, 16.86 eV for $\text{Ni}_{0.875}\text{K}_{0.125}\text{O}$ and at 0.95, 5.45, 15.82 eV for $\text{Ni}_{0.75}\text{K}_{0.25}\text{O}$ structure. The optical transition between the highest valence band and the lowest conduction band is the source of these points, and the critical point values correlate with the optical gaps. For an increase in dopant concentration, the imaginary parts of the differential equation generally decrease.

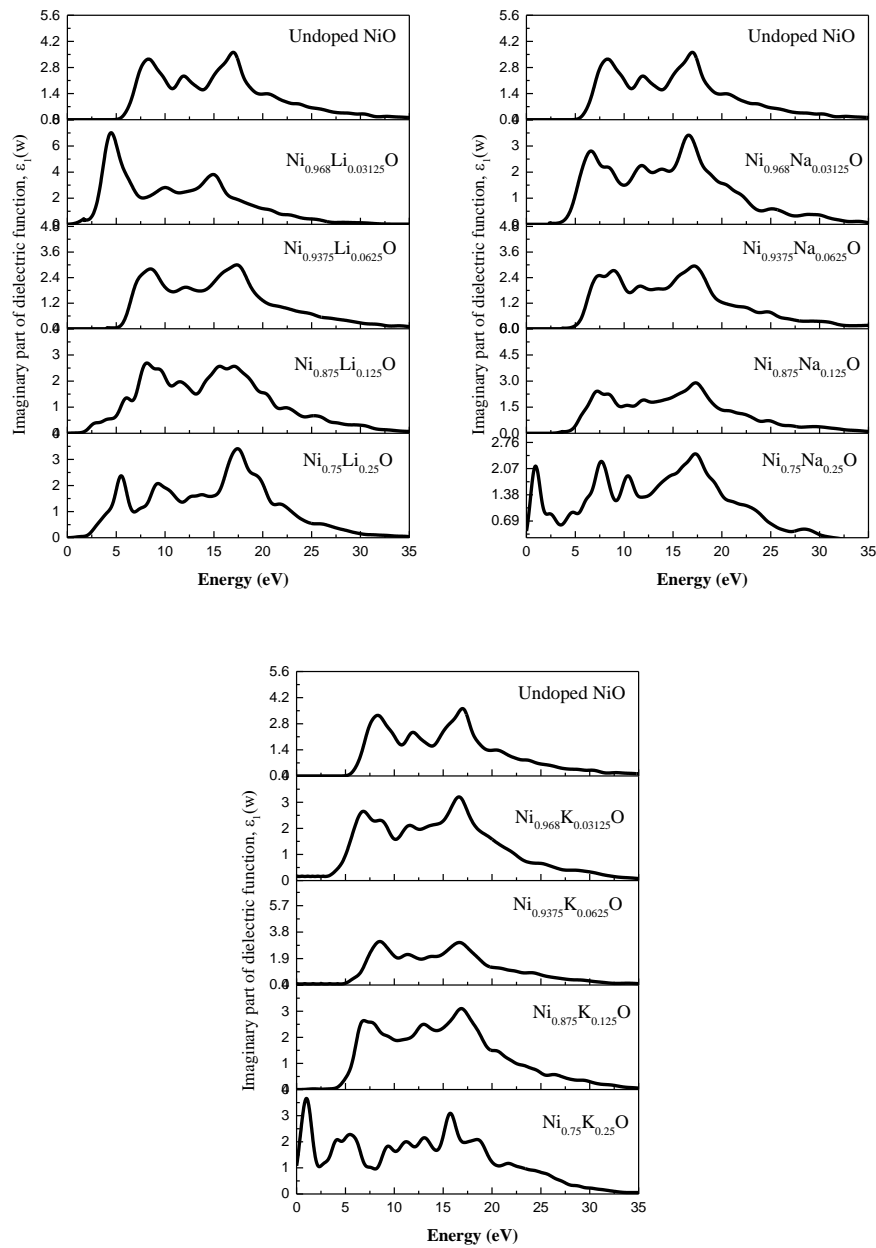


Figure III.42. The imaginary part of the dielectric function of $\text{Ni}_{1-x}\text{A}_x\text{O}$ ($\text{A}=\text{Li}, \text{Na}, \text{K}$).

The real part of the dielectric function of pure and Alkali doped NiO structures: $\text{Ni}_{1-x}\text{Li}_x\text{O}$, $\text{Ni}_{1-x}\text{Na}_x\text{O}$, $\text{Ni}_{1-x}\text{K}_x\text{O}$ ($x=0.0312, 0.0625, 0.125, 0.25$) are illustrated in figure (III.43). It is well known that the frequency zero limit, or $\epsilon_1(0)$, is a significant quantity that represents the electrical response to the static field. According to these figures, the static dielectric constant of $\text{Ni}_{1-x}\text{Li}_x\text{O}$ structures are: 3.03, 9.5, 12.27, 3.1, 3.19eV. And 3.03, 10.01, 4.26, 9.12, 6.19 eV

for $\text{Ni}_{1-x}\text{Na}_x\text{O}$ structures and 3.03, 12.3, 3.4, 8.01 eV for $\text{Ni}_{1-x}\text{K}_x\text{O}$ structures for $x=0, 0.0312, 0.0625, 0.125, 0.25$ respectively.

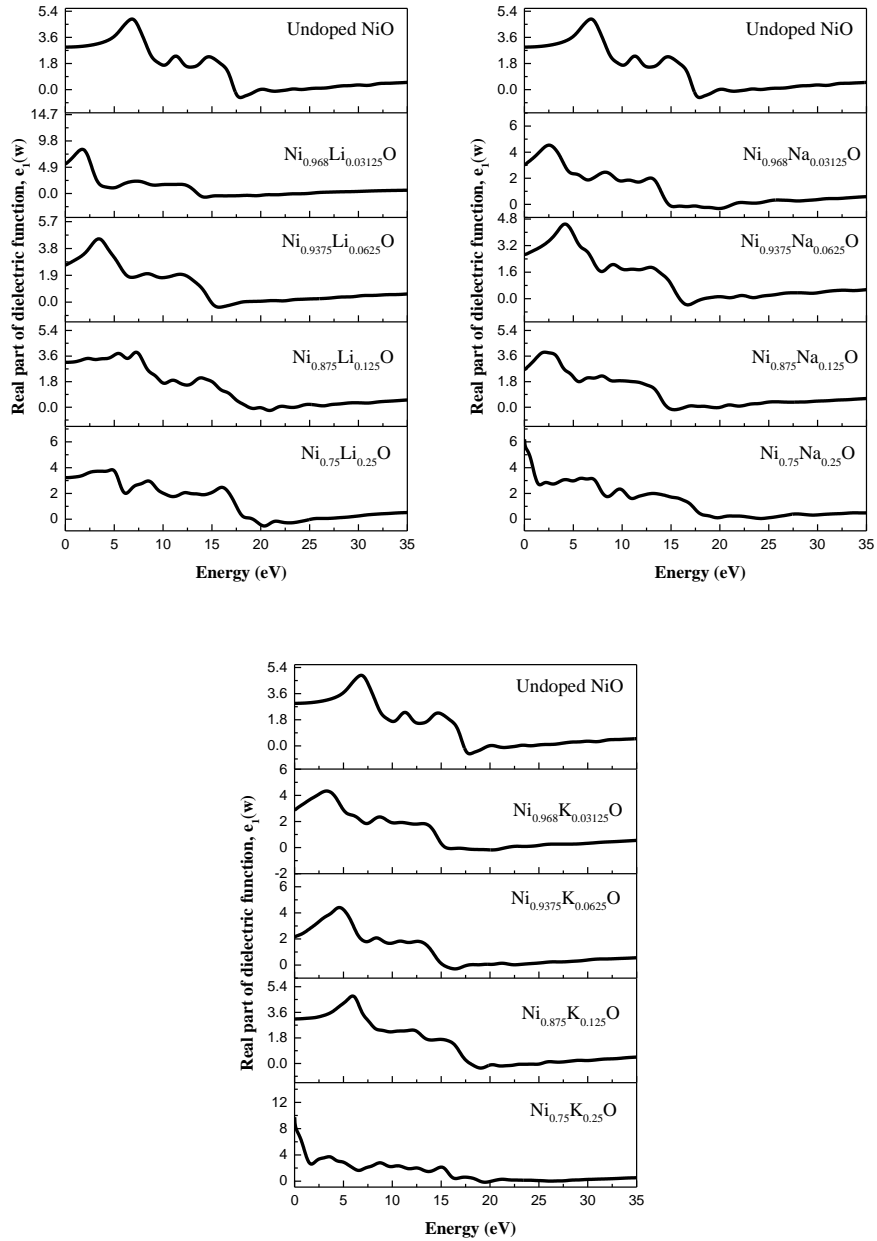


Figure III.43. The real part of the dielectric function of $\text{Ni}_{1-A_x}\text{O}$ ($A=\text{Li}, \text{Na}, \text{K}$).

III.2.4.2.2. The dielectric function $\varepsilon(\omega)$ of $\text{Ni}_{1-2x}\text{A}_x\text{La}_x\text{O}$ (A=Li, Na and K)

The imaginary part of the dielectric function of $\text{Ni}_{1-2x}\text{Li}_x\text{La}_x\text{O}$, $\text{Ni}_{1-2x}\text{Na}_x\text{La}_x\text{O}$ and $\text{Ni}_{1-2x}\text{K}_x\text{La}_x\text{O}$ ($x=0.0312, 0.0625$) structures is presented in figure (III.44). The first transition between the minimum conduction band and the maximum valence band is produced at 1.95, 2.03 eV for $\text{Ni}_{0.937}\text{Li}_{0.0312}\text{La}_{0.0312}\text{O}$ and $\text{Ni}_{0.87}\text{Li}_{0.0625}\text{La}_{0.0625}\text{O}$ respectively. For $\text{Ni}_{0.937}\text{K}_{0.0312}\text{La}_{0.0312}\text{O}$ and $\text{Ni}_{0.87}\text{K}_{0.0625}\text{La}_{0.0625}\text{O}$, the analysis of imaginary part indicates that the first critical point is produced at 3.01 and 3.99 eV respectively, while it is found to be produced at 3.34 and 3.83 eV for $\text{Ni}_{0.937}\text{Na}_{0.0312}\text{La}_{0.0312}\text{O}$ and $\text{Ni}_{0.87}\text{Na}_{0.0625}\text{La}_{0.0625}\text{O}$ respectively. As shown in figure (III.60), the $\text{Ni}_{0.937}\text{Li}_{0.0312}\text{La}_{0.0312}\text{O}$ structure exhibited two major peaks at 5.81 and 16.34 eV. The major peaks of $\text{Ni}_{0.937}\text{K}_{0.0312}\text{La}_{0.0312}\text{O}$ is produced at 5.97, 16.68 eV and at 7.45, 15.85 eV for $\text{Ni}_{0.87}\text{K}_{0.0625}\text{La}_{0.0625}\text{O}$ and at 6.14, 17 eV for $\text{Ni}_{0.937}\text{Na}_{0.0312}\text{La}_{0.0312}\text{O}$. The optical transition between the highest valence band and the lowest conduction band is the source of these points, and the critical point values correlate with the optical gaps.

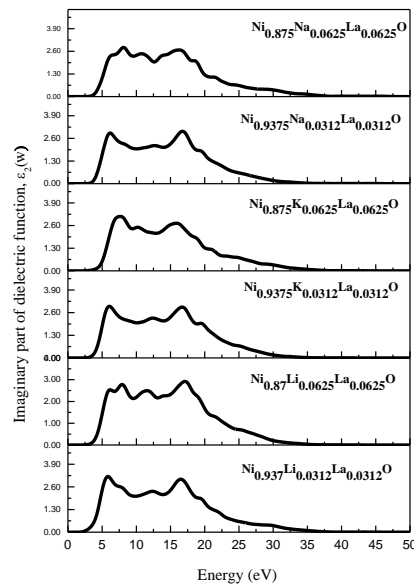


Figure III.44. The imaginary part of the dielectric function of co-doped NiO $\text{Ni}_{1-2x}\text{A}_x\text{La}_x\text{O}$ A=(Li, Na, K)

The variation of the real part $\varepsilon_1(\omega)$ of the differential equation function with energy for the bonds $\text{Ni}_{1-2x}\text{Li}_x\text{La}_x\text{O}$, $\text{Ni}_{1-2x}\text{Na}_x\text{La}_x\text{O}$ and $\text{Ni}_{1-2x}\text{K}_x\text{La}_x\text{O}$ ($x=0.0312, 0.0625$) structures

is shown in figure (III.45). It can be observed that the optical spectra depicted in this figure are similar with only minor variations. According to this figure, the static dielectric constant values are: 3.47, 3.3, 3.34, 3.58, 3.56, 3.66 eV for $\text{Ni}_{0.937}\text{Na}_{0.0312}\text{La}_{0.0312}\text{O}$, $\text{Ni}_{0.87}\text{Na}_{0.0625}\text{La}_{0.0625}\text{O}$, $\text{Ni}_{0.937}\text{K}_{0.0312}\text{La}_{0.0312}\text{O}$, $\text{Ni}_{0.87}\text{K}_{0.0625}\text{La}_{0.0625}\text{O}$, $\text{Ni}_{0.937}\text{Li}_{0.0312}\text{La}_{0.0312}\text{O}$, $\text{Ni}_{0.87}\text{Li}_{0.0625}\text{La}_{0.0625}\text{O}$ respectively.

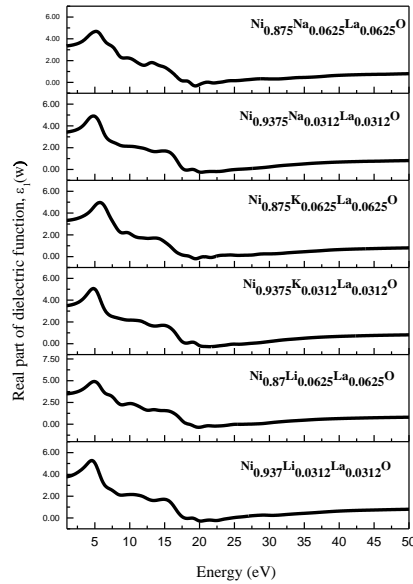


Figure III.45. The real part of the dielectric function of co-doped $\text{NiO Ni}_{1-2x}\text{A}_x\text{La}_x\text{O}$ $\text{A}=(\text{Li}, \text{Na}, \text{K})$

III.2.4.3. Refractive index $n(\omega)$

III.2.4.3.1. Refractive index $n(\omega)$ of pure and $\text{Ni}_{1-x}\text{A}_x\text{O}$ ($\text{A}=\text{Li}, \text{Na}$ and K)

The refractive index, $n(\omega)$ of an optical support is a dimensionless number that indicates how light or any other radiation propagates through the support. The variation of the refractive index $n(\omega)$ with energy is shown in figure (III-46). This figure displays the statistical refractive index, or $n(0)$, for each material. According to the figures below, the statistical refractive index of $\text{Ni}_{1-x}\text{Li}_x\text{O}$ structures are: 1.71, 2.23, 1.68, 1.77, 1.86 eV and for $\text{Ni}_{1-x}\text{Na}_x\text{O}$ are: 1.71, 4.5, 2.07, 3.01, 2.4 eV and for $\text{Ni}_{1-x}\text{K}_x\text{O}$: 1.71, 1.73, 1.6, 1.77, 2.85 eV for $x=0, 0.0312, 0.0625, 0.125, 0.25$ respectively.

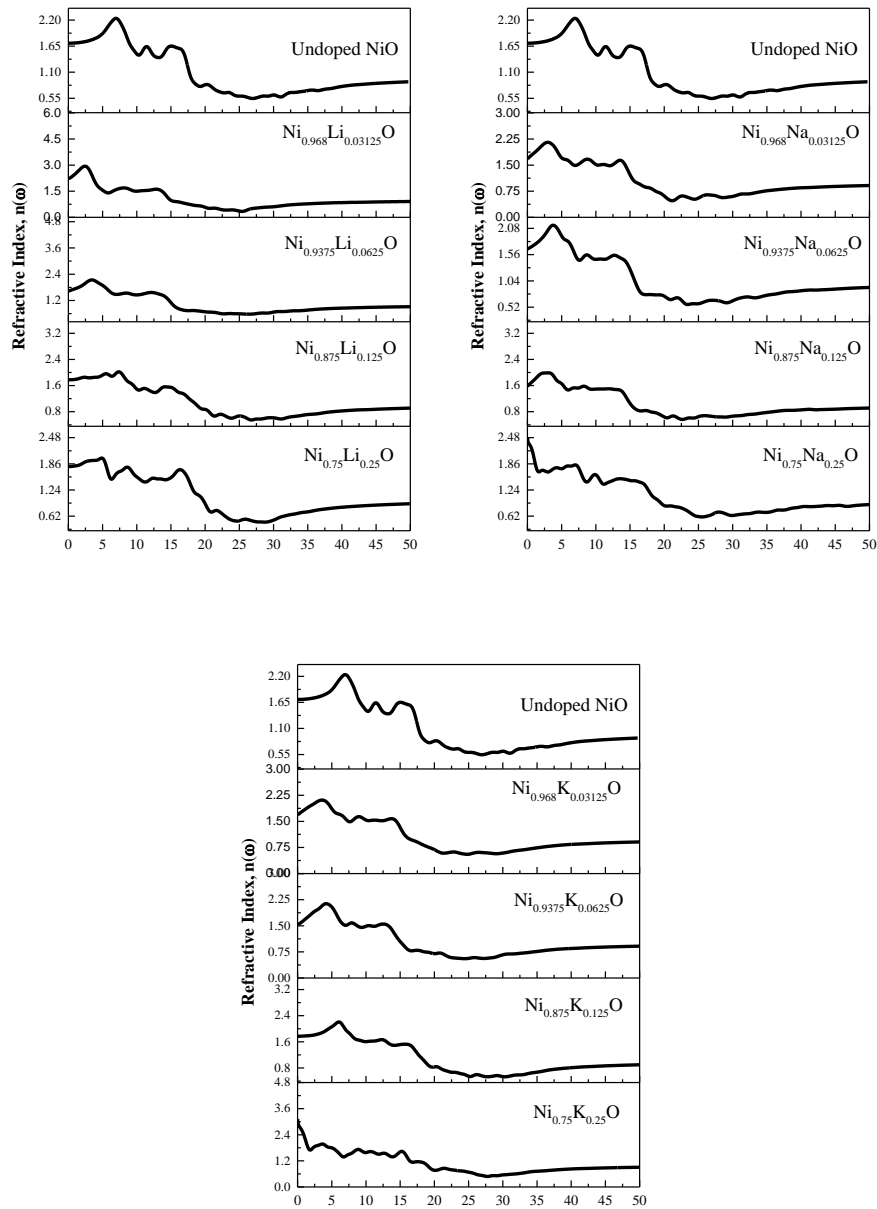


Figure III.46. The refractive index of $\text{Ni}_{1-x}\text{A}_x\text{O}$ ($\text{A}=\text{Li}, \text{Na}, \text{K}$).

III.2.4.3.2. Refractive index $n(\omega)$ of $\text{Ni}_{1-2x}\text{A}_x\text{La}_x\text{O}$ ($\text{A}=\text{Li}, \text{Na}$ and K)

The Refractive index $n(\omega)$ of $\text{Ni}_{1-2x}\text{Li}_x\text{La}_x\text{O}$, $\text{Ni}_{1-2x}\text{Na}_x\text{La}_x\text{O}$ and $\text{Ni}_{1-2x}\text{K}_x\text{La}_x\text{O}$ ($x=0.0312, 0.0625$) structures is presented in figure (III.47). According to this figure(III.47), the

Statistical refractive index of $\text{Ni}_{0.937}\text{Na}_{0.0312}\text{La}_{0.0312}\text{O}$, $\text{Ni}_{0.87}\text{Na}_{0.0625}\text{La}_{0.0625}\text{O}$, $\text{Ni}_{0.937}\text{K}_{0.0312}\text{La}_{0.0312}\text{O}$, $\text{Ni}_{0.87}\text{K}_{0.0625}\text{La}_{0.0625}\text{O}$, $\text{Ni}_{0.937}\text{Li}_{0.0312}\text{La}_{0.0312}\text{O}$, $\text{Ni}_{0.87}\text{Li}_{0.0625}\text{La}_{0.0625}\text{O}$ are :1.91, 1.88, 1.82, 1.91, 1.92 and 2.09 eV respectively. We can notice that the $n(\omega)$ spectres of the co-doped structures are almost similar.

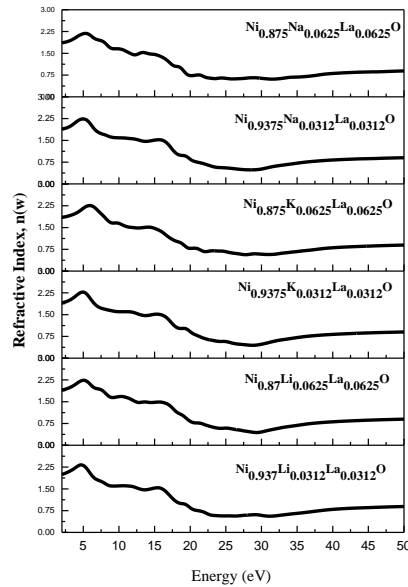


Figure III.47. The refractive index of co-doped NiO $\text{Ni}_{1-2x}\text{A}_x\text{La}_x\text{O}$ $\text{A} = (\text{Li}, \text{Na}, \text{K})$.

III.2.4.4. The extinction coefficient $k(\omega)$

III.2.4.4.1. The extinction coefficient $k(\omega)$ of pure and $\text{Ni}_{1-x}\text{A}_x\text{O}$ ($\text{A} = \text{Li}, \text{Na}$ and K)

The extinction coefficient $k(\omega)$ of pure and Alkali doped NiO structures: $\text{Ni}_{1-x}\text{Li}_x\text{O}$, $\text{Ni}_{1-x}\text{Na}_x\text{O}$, $\text{Ni}_{1-x}\text{K}_x\text{O}$ ($x = 0.0312, 0.0625, 0.125, 0.25$) are illustrated in figure (III.48). We notice multiple peaks, the most intense of which is located at 17.43, 4.76, 18.12, 18.24, 17.78 eV for $\text{Ni}_{1-x}\text{Li}_x\text{O}$ structures and at 17.43, 17.03, 18.53, 17.89, 17.78 eV for $\text{Ni}_{1-x}\text{Na}_x\text{O}$ structures and at 17.43, 16.58, 17.54, 17.78, 16.042 eV for $\text{Ni}_{1-x}\text{K}_x\text{O}$ structures ($x = 0, 0.0312, 0.0625, 0.125, 0.25$ respectively). The extinction coefficient is proportional to the imaginary part of the dielectric function.

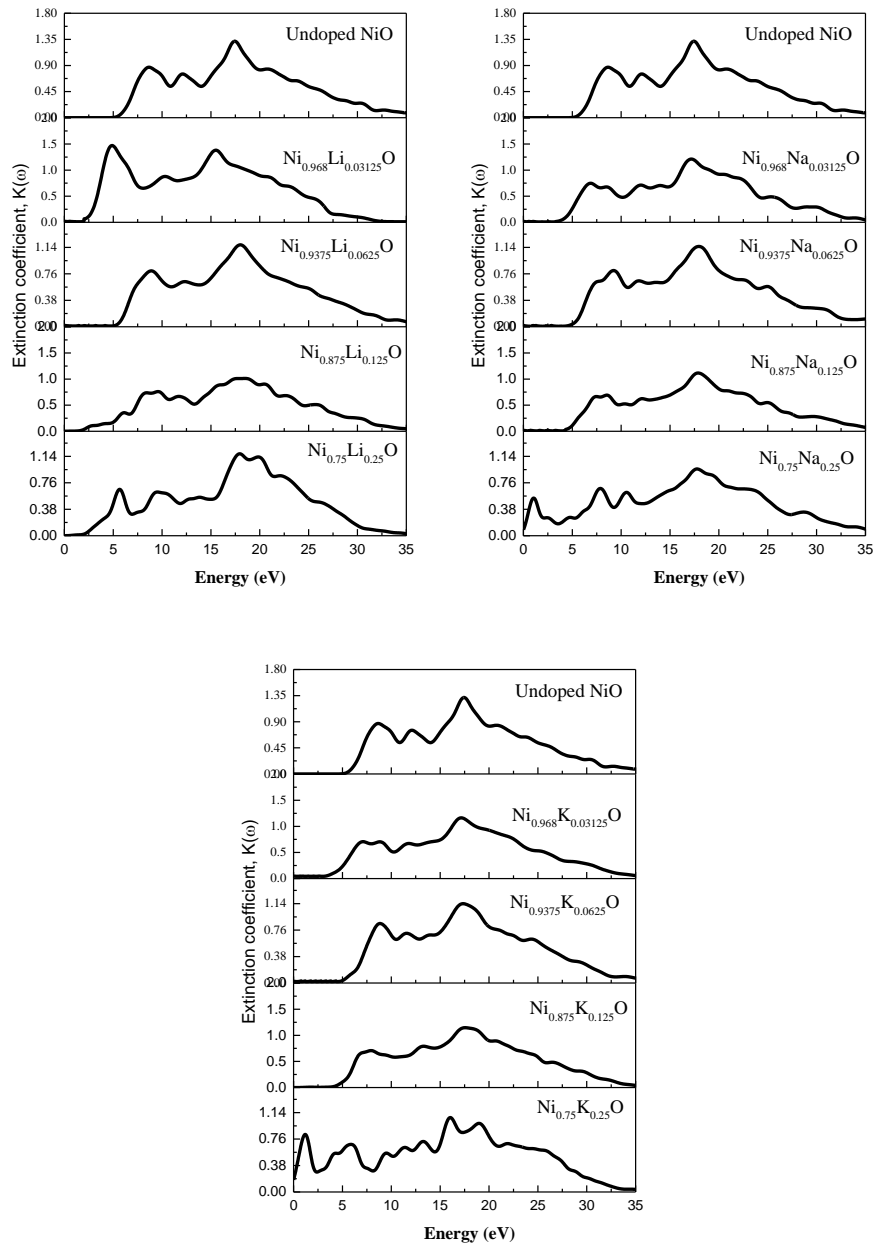


Figure III.48. The extinction coefficient of $\text{Ni}_{1-x}\text{A}_x\text{O}$ ($\text{A}=\text{Li}, \text{Na}, \text{K}$).

III.2.4.4.2. The extinction coefficient $k(\omega)$ of $\text{Ni}_{1-2x}\text{A}_x\text{La}_x\text{O}$ ($\text{A}=\text{Li}, \text{Na}$ and K)

It is evident from figure (III.49) that the extinction coefficient of co-doped structures matches the evolution of the imaginary part of the dielectric function. The extinction coefficient $k(\omega)$ of $\text{Ni}_{1-2x}\text{Li}_x\text{La}_x\text{O}$, $\text{Ni}_{1-2x}\text{Na}_x\text{La}_x\text{O}$ and $\text{Ni}_{1-2x}\text{K}_x\text{La}_x\text{O}$ ($x=0.0312, 0.0625$) structures is presented in the figure (III.49). According to this figure a principal peak situated at 17.5, 17.16, 16.83, 17.50, 17.99, 17.33 eV for $\text{Ni}_{0.937}\text{Na}_{0.0312}\text{La}_{0.0312}\text{O}$,

$\text{Ni}_{0.87}\text{Na}_{0.0625}\text{La}_{0.0625}\text{O}$, $\text{Ni}_{0.937}\text{K}_{0.0312}\text{La}_{0.0312}\text{O}$, $\text{Ni}_{0.87}\text{K}_{0.0625}\text{La}_{0.0625}\text{O}$, $\text{Ni}_{0.937}\text{Li}_{0.0312}\text{La}_{0.0312}\text{O}$, $\text{Ni}_{0.87}\text{Li}_{0.0625}\text{La}_{0.0625}\text{O}$ structures respectively.

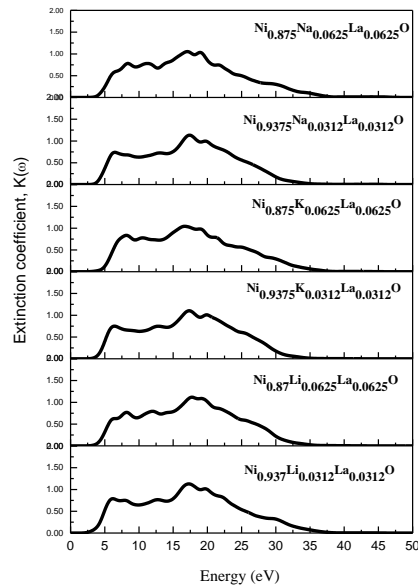


Figure III.49. The extinction coefficient of co-doped NiO $\text{Ni}_{1-2x}\text{A}_x\text{La}_x\text{O}$ $\text{A} = (\text{Li}, \text{Na}, \text{K})$.

III.2.4.5. Absorption coefficient $\alpha(\omega)$

III.2.4.5.1. Absorption coefficient $\alpha(\omega)$ of pure and $\text{Ni}_{1-x}\text{A}_x\text{O}$ ($\text{A} = \text{Li}, \text{Na}$ and K)

The results of the absorption coefficients of pure and alkali doped NiO structures: $\text{Ni}_{1-x}\text{Li}_x\text{O}$, $\text{Ni}_{1-x}\text{Na}_x\text{O}$, $\text{Ni}_{1-x}\text{K}_x\text{O}$ ($x = 0.0312, 0.0625, 0.125, 0.25$) as a function of incident light energy are displayed in figure (III.50). It can be seen that the absorption edge starts from the energy values of 3.86, 2.54, 4.83, 3.33, 2.4 eV corresponding to the energy gaps of $\text{Ni}_{1-x}\text{Li}_x\text{O}$ structures and from 3.86, 3.85, 4.91, 2.67, 2.27 eV corresponding to the energy gaps of $\text{Ni}_{1-x}\text{Na}_x\text{O}$ structures and from 3.86, 3.85, 3.01, 2.93, 1.09 eV corresponding to the energy gaps of $\text{Ni}_{1-x}\text{K}_x\text{O}$ structures for $x = 0, 0.0312, 0.0625, 0.125, 0.25$ respectively. The coefficient of absorption of these alkali doped NiO structures indicates that they have good absorption properties. Also, this figure demonstrates the fact that a progressive change in the absorption edge of the alkali doped NiO structures occurs with an increase in the concentration of dopants. The absorption region of the alkali doped NiO materials are located in the near-ultraviolet.

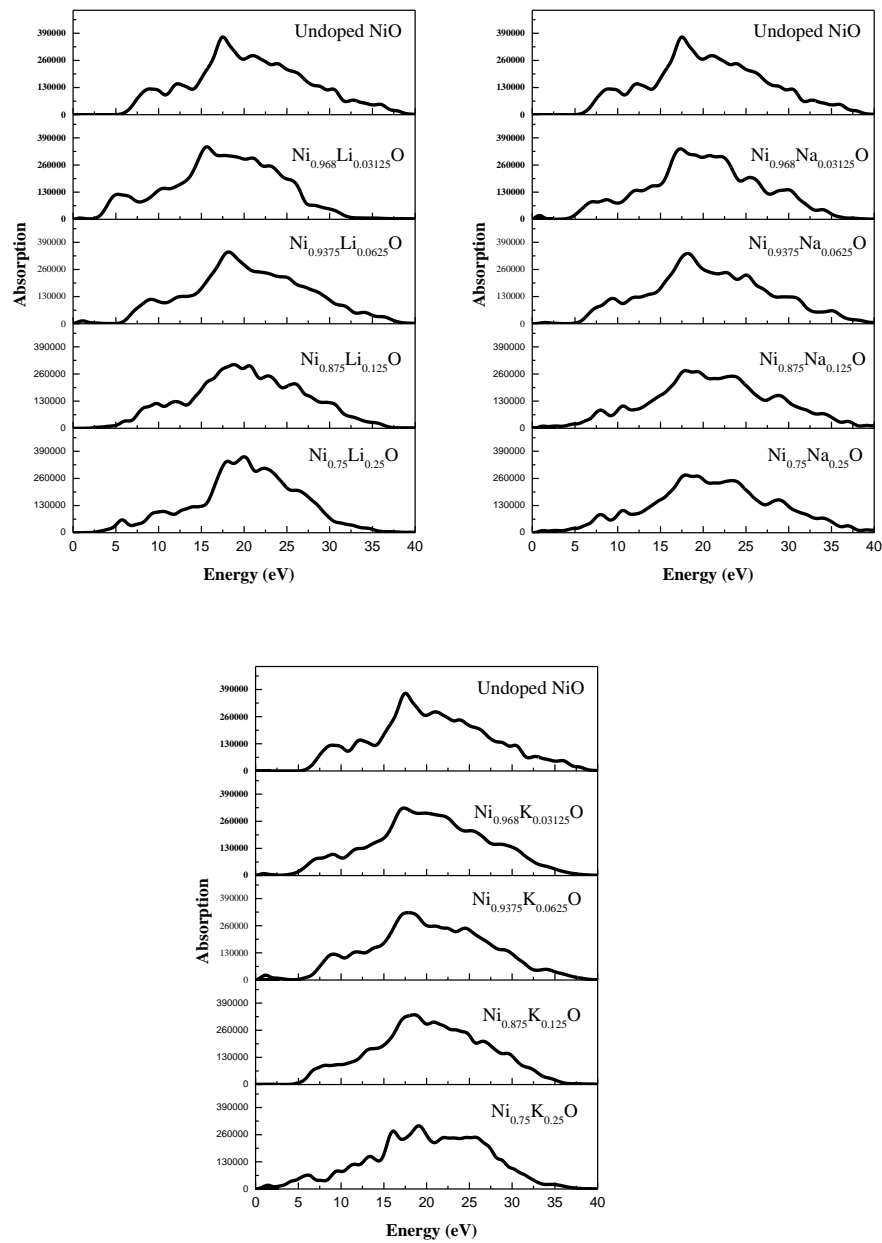


Figure III.50. The absorption coefficient of $\text{Ni}_{1-x}\text{A}_x\text{O}$ ($\text{A}=\text{Li}, \text{Na}, \text{K}$).

III.2.4.5.2. Absorption coefficient $\alpha(\omega)$ of $\text{Ni}_{1-2x}\text{A}_x\text{La}_x\text{O}$ ($\text{A}=\text{Li}, \text{Na}$ and K)

The results of the absorption coefficients of co-doped NiO structures $\text{Ni}_{1-2x}\text{Li}_x\text{La}_x\text{O}$, $\text{Ni}_{1-2x}\text{Na}_x\text{La}_x\text{O}$ and $\text{Ni}_{1-2x}\text{K}_x\text{La}_x\text{O}$ ($x = 0.0312, 0.0625$) as a function of incident light energy are presented in figure (III.51). It can be seen that the absorption edge starts from the energy values of 2.85, 3.59, 3.75, 3.55, 3.29, 3.012 eV corresponding to the energy gaps for $\text{Ni}_{0.937}\text{Na}_{0.0312}\text{La}_{0.0312}\text{O}$, $\text{Ni}_{0.87}\text{Na}_{0.0625}\text{La}_{0.0625}\text{O}$, $\text{Ni}_{0.937}\text{K}_{0.0312}\text{La}_{0.0312}\text{O}$, $\text{Ni}_{0.87}\text{K}_{0.0625}\text{La}_{0.0625}\text{O}$,

$\text{Ni}_{0.937}\text{Li}_{0.0312}\text{La}_{0.0312}\text{O}$, $\text{Ni}_{0.87}\text{Li}_{0.0625}\text{La}_{0.0625}\text{O}$ structures respectively. According to figure (III.67), the absorption of co-doped NiO structures is similar, which is consistent with the extinction coefficient curves. The highest peak of the co-doped NiO curves belongs to $\text{Ni}_{0.87}\text{Li}_{0.0625}\text{La}_{0.0625}\text{O}$ structure is located at 19.30eV, where the absorption is 3.32×10^5 /cm.

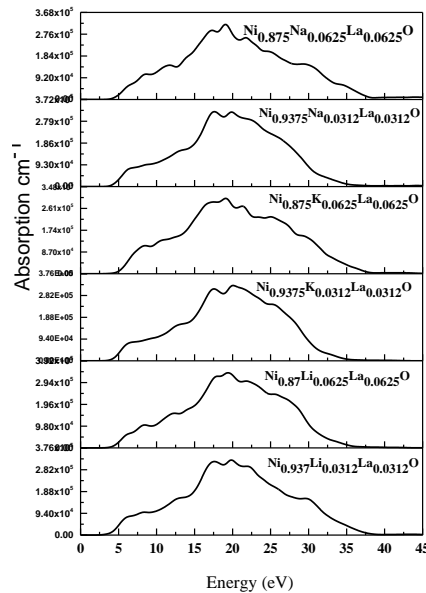


Figure III.51. The absorption coefficient of co-doped NiO $\text{Ni}_{1-2x}\text{A}_x\text{La}_x\text{O}$ A= (Li, Na, K).

III.2.4.6. Reflectivity $R(\omega)$

III.2.4.6.1. Reflectivity $R(\omega)$ of pure and $\text{Ni}_{1-x}\text{A}_x\text{O}$ (A=Li, Na and K)

The calculated reflectivity of pure and Alkali doped NiO structures: $\text{Ni}_{1-x}\text{Li}_x\text{O}$, $\text{Ni}_{1-x}\text{Na}_x\text{O}$, $\text{Ni}_{1-x}\text{K}_x\text{O}$ ($x=0.0312, 0.0625, 0.125, 0.25$) is laid out in the equation (III-8) and illustrated in the figure (III.52). Maximum reflectivity is produced by energy values at 17.82, 16.01, 18.81, 20.97, 20.82 eV for $\text{Ni}_{1-x}\text{Li}_x\text{O}$ and at 17.82, 19.96, 15.52, 15.35, 15.18 eV for $\text{Ni}_{1-x}\text{Na}_x\text{O}$ and at 17.82, 17.33, 18.64, 18.81, 19.31 eV for $\text{Ni}_{1-x}\text{K}_x\text{O}$. These values are in the ultraviolet range. As a result, the current findings suggest that the Alkali doped NiO materials could be used in optical devices such as ultraviolet radiation screens.

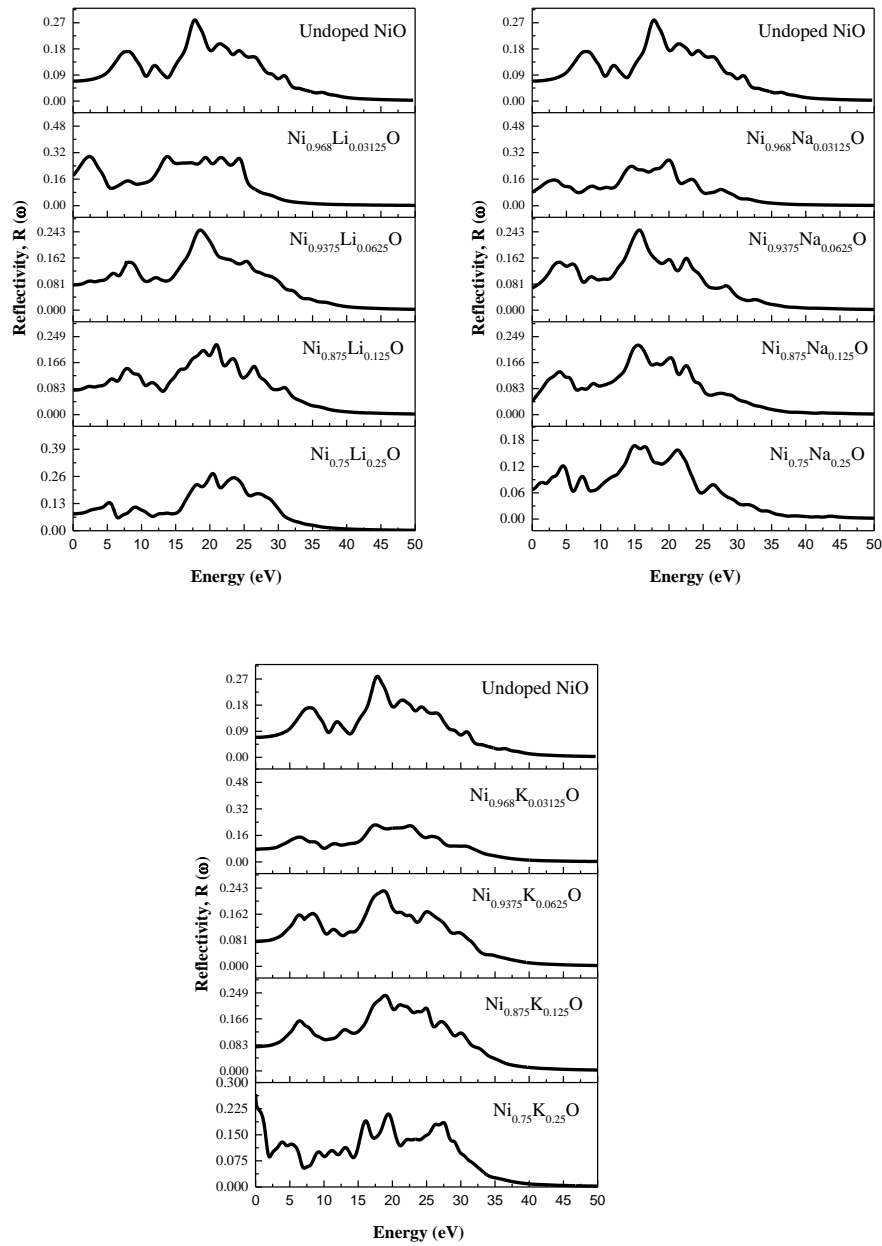


Figure III.52. Reflectivity of $\text{Ni}_{1-x}\text{A}_x\text{O}$ ($\text{A}=\text{Li}, \text{Na}, \text{K}$).

III.2.4.6. Reflectivity $R(\omega)$ of $\text{Ni}_{1-2x}\text{A}_x\text{La}_x\text{O}$ ($\text{A}=\text{Li}, \text{Na}$ and K)

The results of the reflectivity coefficients of co-doped NiO structures $\text{Ni}_{1-2x}\text{Li}_x\text{La}_x\text{O}$, $\text{Ni}_{1-2x}\text{Na}_x\text{La}_x\text{O}$ and $\text{Ni}_{1-2x}\text{K}_x\text{La}_x\text{O}$ ($x=0.0312, 0.0625$) as a function of incident light energy are presented in figure (III.53). It can be seen that the Maximum reflectivity is produced by energy values at 19.45, 20.19, 19.45, 21.52, 19.75, 22.7eV. These energy values are in the

ultraviolet region. Therefore, the present results suggest that the co-doped NiO Materials can be used in optical devices such as ultraviolet radiation shields.

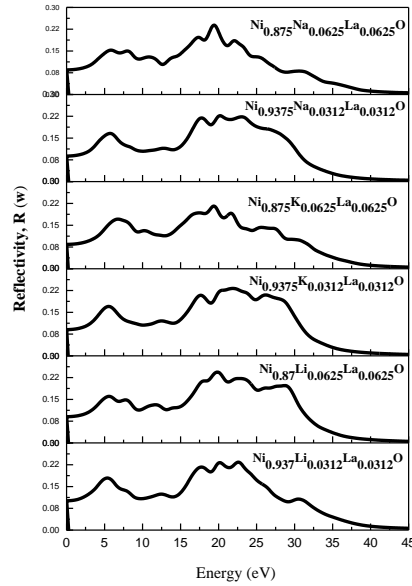


Figure III.53. Reflectivity of co-doped NiO $\text{Ni}_{1-2x}\text{A}_x\text{La}_x\text{O}$ A= (Li, Na, K).

III.2.4.6. Energy loss function $L(\omega)$

III.2.4.6.1. Energy loss function $L(\omega)$ of pure and $\text{Ni}_{1-x}\text{A}_x\text{O}$ (A=Li, Na and K)

The function of loss of energy of electrons $L(\omega)$ is an optical parameter that describes the loss of energy of an electron moving rapidly through a material. The peaks in the spectral lines $L(\omega)$ represent the properties associated with plasma resonance, and the corresponding frequency is the plasma frequency above which the material is a dielectric $\epsilon_1(\omega) > 0$ and below which the material behaves as a metallic compound in some sense $\epsilon_1(\omega) < 0$. In addition, the peaks of the spectra $L(\omega)$ overlaps the trailing edges in the reflection spectra. The $L(\omega)$ peaks of pure and Alkali doped NiO structures: $\text{Ni}_{1-x}\text{Li}_x\text{O}$, $\text{Ni}_{1-x}\text{Na}_x\text{O}$, $\text{Ni}_{1-x}\text{K}_x\text{O}$ ($x = 0.0312, 0.0625, 0.125, 0.25$) is laid out in the equation (III-8) and illustrated in the figure (III.54).

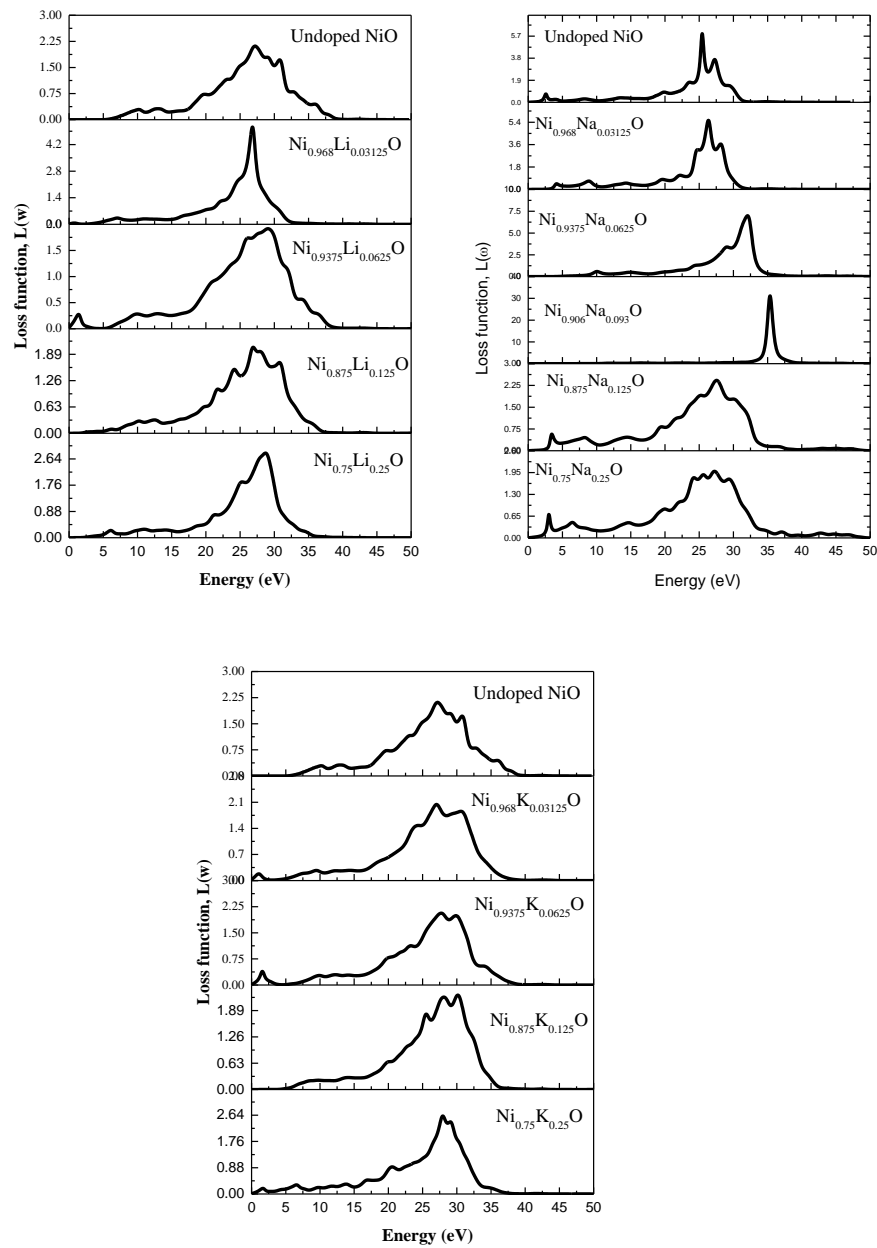


Figure III.54. Loss functions of $\text{Ni}_{1-x}\text{A}_x\text{O}$ ($\text{A}=\text{Li}, \text{Na}, \text{K}$).

III.2.4.6.2. Energy loss function $L(\omega)$ of $\text{Ni}_{1-2x}\text{A}_x\text{La}_x\text{O}$ ($\text{A}=\text{Li}, \text{Na}$ and K)

The energy loss function $L(\omega)$, which describes the energy loss of a semiconductor when electrons pass through a homogeneous dielectric medium, can be obtained from the dielectric function according to equation (III.21). The $L(\omega)$ peaks of co-doped NiO structures $\text{Ni}_{1-2x}\text{Li}_x\text{La}_x\text{O}$, $\text{Ni}_{1-2x}\text{Na}_x\text{La}_x\text{O}$ and $\text{Ni}_{1-2x}\text{K}_x\text{La}_x\text{O}$ ($x=0.0312, 0.0625$) are shown the figure (III.55).

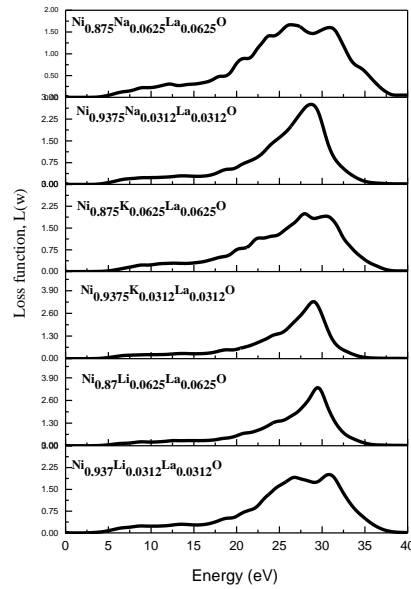


Figure III.55. Loss functions of co-doped NiO $\text{Ni}_{1-2x}\text{A}_x\text{La}_x\text{O}$ A= (Li, Na, K).

III.2.5. Elastic properties

III.2.5.1. Introduction

The Elastic properties of materials describe their mechanical behavior; their study is very essential in the field of engineering [42]. The elastic properties of solid materials have an important scientific and technological significance. Their measurement provides information about the forces that connect the atoms or ions that make up a solid, which is critical for interpreting and comprehending the nature of chemical bonds in solids. The elasticity of solids is the material's response to applied forces; these forces can cause reversible deformations (return to the initial state). Hooke's law only applies to small deformations and establishes that in an elastic solid, deformation is proportional to constraint. Tensors of constraints describe the forces. The responses are known as deformations, and they are also provided by tensors. Because the deformation occurs in the linear domain, the relationship between constraint and deformation is constant for small constraints. The tensor constraint and deformation symmetries allow us to write Hooke's law as follows.

$$\sigma_{ij} = \sum_{K,L} C_{ijkl} \varepsilon_{kl} \quad (\text{III.22})$$

Where σ_{ij} , ε_{kl} and C_{ijkl} are the tensors of constraint, deformation, and elasticity respectively. In cubic symmetry, this is simplified into a 6 x 6 matrix of elastic constants C_{ij} . In the case of cubic symmetry, this matrix has just three non-zero independent elements: C_{11} , C_{12} , and C_{44} . The elasticity constant C_{11} represents the resistance to constraint (compression or traction). The value C_{44} represents the resistance to shear. The elastic constant C_{12} does not have a straightforward physical meaning, but its combination with other constants provides additional information on the elastic behavior of cubic materials. The relationship between tension, elasticity, and deformation becomes:

$$\bar{\sigma} = \begin{pmatrix} C_{11} & C_{12} & C_{12} & 0 & 0 & 0 \\ C_{12} & C_{11} & C_{12} & 0 & 0 & 0 \\ C_{12} & C_{12} & C_{11} & 0 & 0 & 0 \\ 0 & 0 & 0 & C_{44} & 0 & 0 \\ 0 & 0 & 0 & 0 & C_{44} & 0 \\ 0 & 0 & 0 & 0 & 0 & C_{44} \end{pmatrix} \quad (\text{III.23})$$

Numerical results obtained for the elastic constants (C_{ij}) of the pure and $\text{Ni}_{1-x}\text{A}_x\text{O}$ ($\text{A}=\text{Li}$, Na and K) are reported in tables (III.17), (III.18) and (III.19) with the results compared to other experimental and theoretical calculations. All C_{ij} values are in GPa. In a cubic structure, mechanical stability necessitates the following constraints on elastic constants [41].

$$C_{11} + 2C_{12} > 0, C_{44} > 0 \quad \text{and} \quad C_{11} - C_{12} > 0 \quad (\text{III.24})$$

III.2.5.2. Elastic constants calculation

The obtained results are listed in the tables (III.17), (III.18) and (III.19) for the pure and alkali (Li , Na , K) doped NiO structures, respectively. And, in order to make a comparison, we compared previously published experimental and theoretical data.

III.2.5.2.1. Elastic constants calculation of pure and $\text{Ni}_{1-x}\text{A}_x\text{O}$ ($\text{A}=\text{Li}$, Na and K)

The estimated C_{ij} values above clearly show that restrictions are satisfied, meaning that both undoped and A -doped NiO ($\text{A}=\text{Li}$, Na , K) are mechanically stable for all concentrations. The results obtained in this study correspond well with earlier theoretical and experimental [43, 44] reports for undoped NiO with a minor discrepancy within the calculated C_{11} values and the experimental data. The complex explanation of the correlation between the

Mott type insulator's 3d electrons is the cause of the discrepancy [45]. As far as we know, there is no reference in the literature to these constants. As a result, the findings in this research offer predictive data for future studies. It is clear from the computed C_{ij} values above that constraints have been satisfied, suggesting that both doped and undoped NiO exhibit mechanical stability. For both pure and alkali doped NiO, it was discovered that C_{11} is greater than C_{44} . This leads us to assume that in these materials, compression resistance is greater than shear resistance. Being aware that C_{11} measures the resistance to linear compression in a direction. From tables below (III.17), (III.18), (III.19) we notice that C_{11} increases than decreases along with the concentration x for all doped NiO structures. When the values of the elastic constants obtained for $Ni_{1-x}Li_xO$, $Ni_{1-x}Na_xO$ and $Ni_{1-x}K_xO$ are compared, we can see that the elastic constants obtained for $Ni_{1-x}Li_xO$ materials have a high value in comparison to the results obtained for Na and K-doped NiO for low concentrations, while $Ni_{1-x}Na_xO$ materials exhibit the highest values for the higher concentrations. The most significant factor directly controlling a material's identification hardness is its C_{44} . Strong resistance to monoclinic shear distortion is indicated by a significant value of C_{44} . In the present case Li and Na doping showed a higher C_{44} values especially for low concentrations unlike K doping. The variation of elastic constants of $Ni_{1-x}A_xO$ ($A=Li, Na, K$) as function of the concentration x is illustrated in the figure (III.56).

Table III.17. Elastic constants of $\text{Ni}_{1-x}\text{Li}_x\text{O}$ as a function of the concentration x .

	Reference	C_{11}	C_{12}	C_{44}
NiO	Present	247.84	183.53	39.54
	Other works	342.7 ^a	141.3 ^a	41.2 ^a
		342.5 ^a	136.5 ^a	42.1 ^a
		360 ^b	250 ^b	36 ^b
		389 ^b	131 ^b	43 ^b
		415 ^b	117 ^b	91.69 ^b
Ni_{0.9687}Li_{0.0312}O		260.5	180.07	81.008
Ni_{0.9375}Li_{0.0625}O		277.23	148.05	49.25
Ni_{0.9063}Li_{0.0937}O		288.26	147.56	81.15
Ni_{0.875}Li_{0.125}O		303.61	147.15	64
Ni_{0.75}Li_{0.25}O		372.37	183.61	63.32
	^a Ref [43]		^b Ref [44]	

Table III.18. Elastic constants of $\text{Ni}_{1-x}\text{Na}_x\text{O}$ as a function of the concentration x .

material	Reference	C_{11}	C_{12}	C_{44}
Ni_{0.9687}Na_{0.0312}O		236.27	176	79.47
Ni_{0.9375}Na_{0.0625}O		221.52	148.19	42
Ni_{0.9063}Na_{0.0937}O		211.87	171.12	78.25
Ni_{0.875}Na_{0.125}O		198.41	178.05	20.75
Ni_{0.75}Na_{0.25}O		174.63	110.63	94.63

Table III.19. Elastic constants of $\text{Ni}_{1-x}\text{K}_x\text{O}$ as a function of the concentration x .

	Reference	C_{11}	C_{12}	C_{44}
Ni_{0.9687}K_{0.0312}O		246	148.45	63.98
Ni_{0.9375}K_{0.0625}O		246.03	163.63	31.98
Ni_{0.9063}K_{0.0937}O		245.89	190.34	43.95
Ni_{0.875}K_{0.125}O		245.09	133.76	17.47
Ni_{0.75}K_{0.25}O		220.97	124.88	23.11

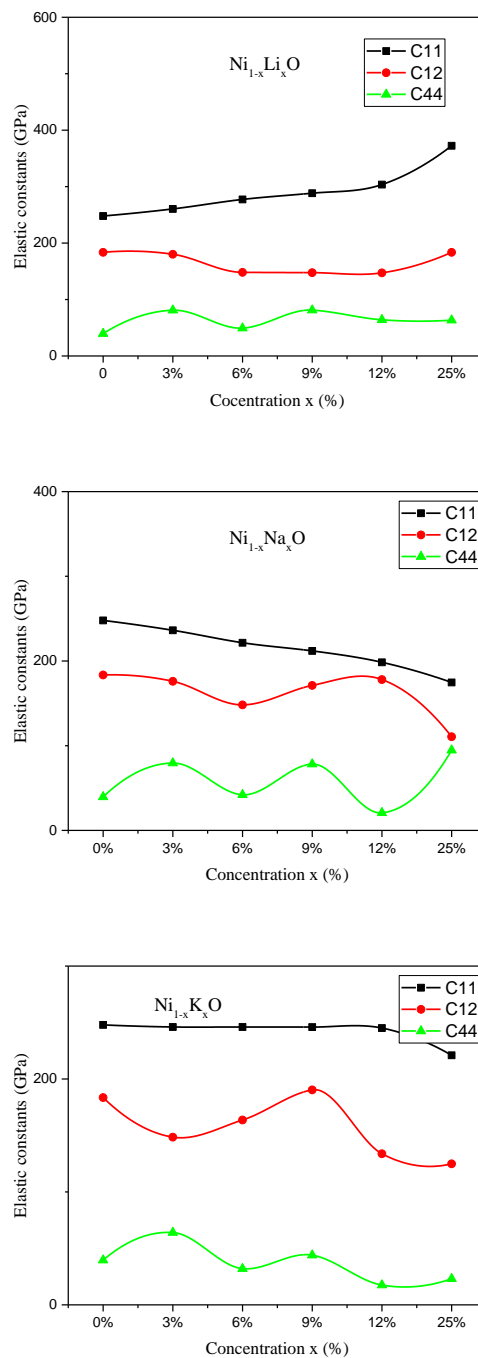


Figure III.56. Variation of elastic constants of $\text{Ni}_{1-x}\text{A}_x\text{O}$ ($\text{A} = \text{Li}, \text{Na}, \text{K}$) as function of the concentration x .

III.2.5.2.2. Elastic constants calculation of $\text{Ni}_{1-2x}\text{A}_x\text{La}_x\text{O}$ ($\text{A} = \text{Li}, \text{Na}$ and K)

Our results for the elasticity modules C_{11} , C_{12} , and C_{44} are shown in table (III.20). The above predicted C_{ij} values unequivocally demonstrate that constraints are met, indicating that

at for all concentrations $\text{Ni}_{1-2x}\text{A}_x\text{La}_x\text{O}$ ($\text{A}=\text{Li}, \text{Na}, \text{and K}$) for ($x=0.0312, 0.0625$) exhibit mechanical stability. To the best of our knowledge, our results can serve as a reference in the lack of experimental and theoretical data on the elastic constants of $\text{Ni}_{1-2x}\text{A}_x\text{La}_x\text{O}$ ($\text{A}=\text{Li}, \text{Na}, \text{and K}$) materials. As shown in the table below, introducing La atoms in the doped NiO structure leads to increase the elastic constants value. Same in the previous investigation of pure and doped NiO structures, the C_{11} elastic constants exhibits higher values than other elastic constants C_{12} and C_{44} which means a resistance to compression higher than the resistance to shear. The computed C_{44} values of undoped, alkali doped and co-doped NiO were discovered to be relatively low. Kube et al. claim that this low value of C_{44} is indicative of d-band filling in transition metal alloys [46]. Variation of elastic constants co-doped NiO $\text{Ni}_{1-2x}\text{A}_x\text{La}_x\text{O}$ $\text{A}=(\text{Li}, \text{Na}, \text{K})$ as function of the concentration x is presented in figure (III.57).

Table III.20. Elastic constants of $\text{Ni}_{1-2x}\text{A}_x\text{La}_x\text{O}$ ($\text{A}=\text{Li}, \text{Na}$ and K) as a function of the concentration x .

material	Reference	C_{11}	C_{12}	C_{44}
$\text{Ni}_{0.9375}\text{Li}_{0.0312}\text{La}_{0.0312}\text{O}$		586.91	213	72
$\text{Ni}_{0.8750}\text{Li}_{0.0625}\text{La}_{0.0625}\text{O}$		378.4	138	24
$\text{Ni}_{0.9375}\text{Na}_{0.0312}\text{La}_{0.0312}\text{O}$		378.2	163.34	52.2
$\text{Ni}_{0.8750}\text{Na}_{0.0625}\text{La}_{0.0625}\text{O}$		289.64	104.57	49.371
$\text{Ni}_{0.9375}\text{K}_{0.0312}\text{La}_{0.0312}\text{O}$		415.13	169.86	37.78
$\text{Ni}_{0.9375}\text{K}_{0.0312}\text{La}_{0.0312}\text{O}$		523.38	184.07	40.46

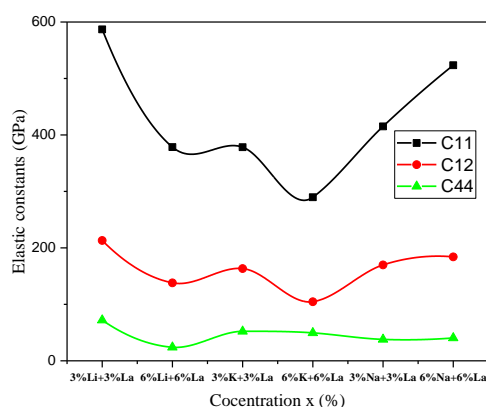


Figure III.57. Variation of elastic constants co-doped NiO $\text{Ni}_{1-2x}\text{A}_x\text{La}_x\text{O}$ $\text{A}=(\text{Li}, \text{Na}, \text{K})$ as function of the concentration x .

III.2.5.3. Elasticity modulus

III.2.5.3.1. Elasticity modulus of pure and $\text{Ni}_{1-x}\text{A}_x\text{O}$ (A=Li, Na and K)

III.2.5.3.1.1. Bulk modulus

The Bulk module of a material is defined as the relative fluctuation of its volume V per unit of applied hydrostatic pressure P [47]:

$$B = -V \frac{dP}{dV} \quad (\text{III.25})$$

Where P presents pressure and V presents volume. T is considered constant, it's also known as a module of rigidity isotherm or a modulus of volume. The Bulk module measures the response of a solid to a change in pressure; it is a Key of the material that enters its state equation. However, the derivation from V is not well defined because it can be done in a variety of ways. Furthermore, each Bulk modulus B can be calculated using the Voigt-Reuss-Hille approximations [47-51], as shown in the following equation:

$$B = \frac{(C_{11}+2C_{12})}{3} \quad (\text{III.26})$$

III.2.5.3.1.2. Shear modulus

The shear modulus G is the relationship between the applied shea constraint and the resulting angle of deformation. The shear module, also known as the slip modulus, the Coulomb module, or the second coefficient of Lamy. is unique to each material and plays a role in the classification of deformations caused by shear attempts [52]. It can be calculated using the following formula:

$$G = \frac{(C_{11}-C_{12}+2C_{12})}{5} \quad (\text{III.27})$$

III.2.5.3.1.3. Young's modulus

The Young's modulus or elasticity E is given by the following relation [51]:

$$E = \frac{9BG}{3B+G} \quad (\text{III.28})$$

III.2.5.3.1.4. Poisson's ratio

The Poisson coefficient characterizes the traction of a solid perpendicular to the direction of the applied effort. The Poisson coefficient is defined as follows [52]:

$$\nu = \frac{3B-2G}{2(3B+G)} \quad (\text{III.29})$$

III.2.5.3.1.5. Debye temperature

The Debye temperature characterizes the behavior of a material's thermal capacity. This parameter is affected by the specific heat and the fusion temperature of the material. The temperature of Debye is calculated as a function of the average speed of sound using the equation [53]:

$$\theta_D = \frac{h}{k_B} \left[\frac{3n}{4\pi} \left(\frac{N_A \rho}{M} \right) \right]^{1/3} V_m \quad (\text{III.30})$$

Where : h is the Plank constants (h = 6.6262 J.s)

K_B : is the Boltzman $K_B = 1.38 \times 10^{-23} \text{ J. deg}^{-1}$

N_A : Avogadro's Number

ρ : is the volumic mass

n: number of atoms par formula unit.

M: the molecular mass per formula unit.

The average wave velocity V_m can be achieved by using the following equation [54]

$$V_m = \left[\frac{1}{3} \left(\frac{2}{V_t^3} + \frac{1}{V_l^3} \right) \right]^{-1/3} \quad (\text{III.31})$$

Where V_l and V_t are Where V_l and V_t are the longitudinal and transversal sound speeds obtained from Navier's equation [42]:

$$V_l = \sqrt{\frac{3B+4G}{3\rho}} \quad (\text{III.32})$$

$$V_t = \sqrt{\frac{G}{\rho}} \quad (\text{III.33})$$

Where ρ , B and G are density, Bulk modulus and shear modulus.

Bulk B and Shear G modulus are calculated using the elastic constants C_{ij} . Bulk modulus B is thought to be the resistance to rupture, while the shear modulus G is thought to be the resistance to deformation. The calculated modules of shear and Bulk are shown in the tables (III-21), (III-22) and (III-23). According to equations (III.28) the Young's modulus, which measures material rigidity, is related to the Bulk and shear modulus. In order to classify the compounds as either fragile or ductile, the B/G ratio was calculated. If B/G is less than the critical value of 1.75, a material is considered fragile; otherwise, it is ductile if it is greater than 1.75 means (fragile < 1.75 < ductile) [56], as a result, both pure and alkali doped NiO are ductile composites. The Debye temperature (θ_D) of materials is an important parameter that is related to several physical properties such as specific heat, elastic constants, and fusion temperature. It is also directly related to the thermal vibration of atoms. Furthermore, it reflects structural stability and the strength of solid-solid bonds. According to our knowledge, the literature contains no information on the shear modulus, longitudinal voice velocity, or Debye (θ_D) temperatures of $\text{Ni}_{1-x}\text{A}_x\text{O}$ ($A=\text{Li}, \text{Na}, \text{K}$); so, our results are predictions and may serve as a reference for future experimental research. The evolution of bulk modulus (B), shear modulus (G) and Young modulus of $\text{Ni}_{1-x}\text{A}_x\text{O}$ ($A=\text{Li}, \text{Na}, \text{K}$) as function of the concentration x is presented in figure (III.58).

Table III.21. Variation of the elastic modules and the Debye temperature θ_D of $\text{Ni}_{1-x}\text{Li}_x\text{O}$ as a function of the concentration x .

Material	B(GPa)	G(Gpa)	B/G	E(GPa)	ν	$V_l(\text{m/s})$	$V_t(\text{m/s})$	V_m (m/s)	Θ_D (K°)
NiO	204.9667	36.5875	5.6020	103.598	0.415	2589.70	6820.0	2937.9	386.
	199 ^a						4266	0537	86
	186 ^b								
	191 ^c								
	208 ^d								
	187 ^e								
	210 ^f								
	236 ^g								
$\text{Ni}_{0.9687}\text{Li}_{0.0312}\text{O}$	206.88	64.6908	3.1979	175.753	0.358	3315.43	7057.5	3731.8	532.
			82	2	41	155	2132	2361	76
$\text{Ni}_{0.9375}\text{Li}_{0.0625}\text{O}$	191.11	55.386	3.4505	151.520	0.367	3047.93	6666.4	3435.1	495.
			11	5	859	744	4909	4875	98
$\text{Ni}_{0.9063}\text{Li}_{0.0937}\text{O}$	194.52	76.812	2.5324	203.632	0.325	3993.90	6948.5	4435.7	632.
			17	5	526	077	7052	1356	43
$\text{Ni}_{0.875}\text{Li}_{0.125}\text{O}$	199.3033	69.692	2.8597	187.250	0.343	3523.55	7215.2	3958.0	516.
			73	2	413	905	1899	8329	31
$\text{Ni}_{0.75}\text{Li}_{0.25}\text{O}$	246.53	75.744	3.2547	206.122	0.360	3738.39	8007.6	4209.1	616.
			79	3	651	679	0106	903	03

Table III.22. Variation of the elastic modules and the Debye temperature θ_D of $Ni_{1-x}Na_xO$ as a function of the concentration x .

Material	B(GPa)	G(Gpa)	B/G	E(GPa)	ν	V_t (m/s)	V_l (m/s)	V_m (m/s)	Θ_D (K°)
$Ni_{0.9687}Na_{0.0312}O$	196.09	59.736	3.28261	162.687	0.361	2876.43	6179.	3239.	459.59
				8	724	95	95745	15487	
$Ni_{0.9375}Na_{0.0625}O$	172.63	39.866	4.33034	111.049	0.392	2349.95	5592.	2657.	379.17
	33			8	788	831	542	56753	
$Ni_{0.9063}Na_{0.0937}O$	184.70	55.1	3.35214	150.349	0.364	2670.45	5780.	3008.	441.54
	33		8	4	332	84	46671	26765	
$Ni_{0.875}Na_{0.125}O$	184.83	16.522	11.1873	48.1318	0.456	1545.48	5468.	1762.	227.84
	67		1	8	6	405	62037	53189	
$Ni_{0.75}Na_{0.25}O$	131.96	69.578	1.89662	177.532	0.275	3278.50	5892.	3651.	520.52
	33		4	5	781	777	16144	00278	

Table III.23. Variation of the elastic modules and the Debye temperature θ_D of $Ni_{1-x}K_xO$ as a function of the concentration x .

material	B(GPa)	G(Gpa)	B/G	E(GPa)	ν	V_t (m/s)	V_l (m/s)	V_m (m/s)	Θ_D (K°)
$Ni_{0.9687}K_{0.0312}O$	180.96	57.898	3.12561	156.955	0.35	2523.3	5328.4	2839.1	409.34
	67		2	4	5447	6942	0093	4512	
$Ni_{0.9375}K_{0.0625}O$	191.09	35.668	5.35765	100.736	0.41	2063.2	5336.9	2339.4	329.76
	67			5	2142	3187	4857	9574	
$Ni_{0.9063}K_{0.0937}O$	208.85	37.48	5.57248	106.093	0.41	2181.0	5731.6	2474.1	343.28
	67		3	7	5338	7189	214	8697	
$Ni_{0.875}K_{0.125}O$	170.87	32.748	5.21772	92.3445	0.40	2047.8	5241.4	2321.3	293.15
			3	8	9927	487	7527	532	
$Ni_{0.75}K_{0.25}O$	156.91	33.084	4.74277	92.7344	0.40	2199.5	5421.8	2490.4	337.81
			6	1	1499	6344	7225	6097	

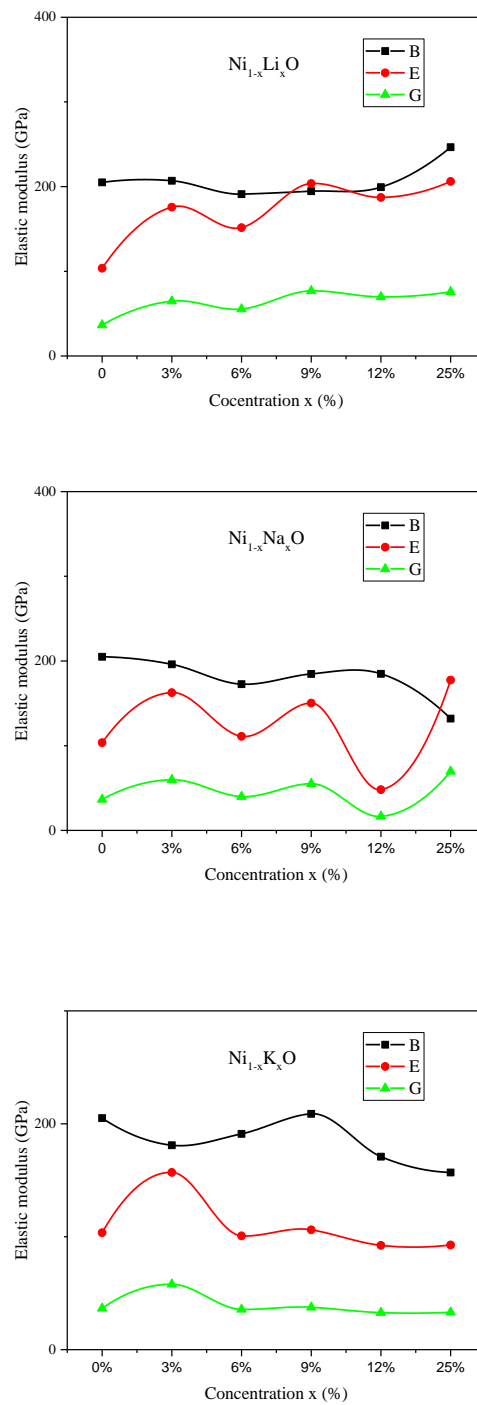


Figure III.58. Evolution of bulk modulus (B), shear modulus (G) and Young modulus of $Ni_{1-x}A_xO$ (A=Li, Na, K) as function of the concentration x.

III.2.5.3.2. Elasticity modulus of $\text{Ni}_{1-2x}\text{A}_x\text{La}_x\text{O}$ (A=Li, Na and K)

The results of elastic modulus calculations for $\text{Ni}_{1-2x}\text{A}_x\text{La}_x\text{O}$ (A=Li, Na and K) ($x=0.0321, 0.0625$) are presented in the table (III.24). There are no experimental or theoretical values for the rigidity module, for $\text{Ni}_{1-2x}\text{Li}_x\text{La}_x\text{O}$, $\text{Ni}_{1-2x}\text{Na}_x\text{La}_x\text{O}$ or $\text{Ni}_{1-2x}\text{K}_x\text{La}_x\text{O}$ materials, thus, our results are predictions and can serve as a reference for future experimental research. As seen in table (III.24), the introduction of La ions in doped NiO structure led to increase the resistance to fracture and resistance to plastic deformation. The Young' modulus E, defined as the relationship between constraint and deformation, is commonly used to provide a measure of solid rigidity. Because the B/G value for all of the compounds was greater than 1.75, co-doped NiO are ductile compounds. The formulas (III.32) and (III.33) were used to calculate the propagation speeds of elastic longitudinal and transversals of the co-doped NiO structures. Figure (III.59) illustrates the Evolution of bulk modulus (B), shear modulus (G) and Young modulus of $\text{Ni}_{1-2x}\text{A}_x\text{La}_x\text{O}$ (A=Li, Na and K) as function of the concentration x.

Table III.24. Variation of the elastic modules and the Debye temperature θ_D of $Ni_{1-2x}A_xLa_xO$ (A=Li, Na and K) as a function of the concentration x.

material	Ref	B(GPa)	G(Gpa)	B/G	E(GPa)	ν	V_l (m/s)	V_t (m/s)	V_m (m/s)	Θ_D (K $^\circ$)
$Ni_{0.93}Li_{0.031}La_{0.0312}O$		337.63	117.98	2.86176	317.020	0.343	4123.75	8446.	4632.353	661.9
O	67		2	4	1	51	338	24583	89	6
$Ni_{0.87}Li_{0.062}La_{0.062}O$		218.13	62.48	3.49125	171.103	0.369	2975.99	6536.	3354.713	480.1
O	33			1	6	267	647	75703	1	9
$Ni_{0.937}Na_{0.031}La_{0.03}O$		234.96	74.292	3.16265	201.625	0.356	3285.42	6966.	3697.330	524.6
O				5	4	979	413	33015	38	3
$Ni_{0.875}Na_{0.062}La_{0.06}O$		166.26	66.636	2.49502	176.349	0.323	3209.09	6278.	3595.224	495.7
O			6	5	6	219	876	98416	01	0
$Ni_{0.937}K_{0.031}La_{0.031}O$		251.61	71.722	3.50822	196.496	0.369	3228.21	7103.	3639.318	517.5
O	67			2		844	757	21936	27	2
$Ni_{0.937}K_{0.031}La_{0.031}O$		297.17	92.138	3.22530	250.522	0.359	3735.42	7975.	4205.184	586.2
O	33			7	7	497	419	49393	27	5

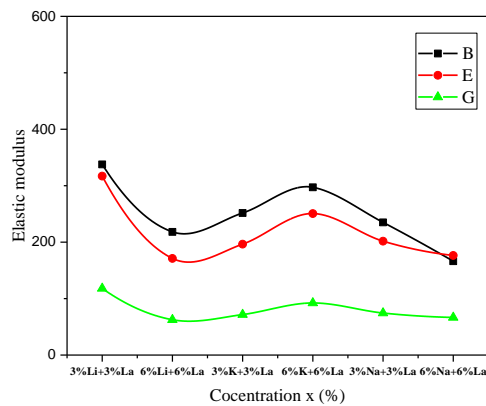


Figure III.59. Evolution of bulk modulus (B), shear modulus (G) and Young modulus of $Ni_{1-2x}A_xLa_xO$ (A=Li, Na and K) as function of the concentration x.

References

- [1] I. Sta, M. Jlassi, M. Kandyla, M. Hajji, P. Koralli, R. Allagui, M. Kompitsas and H. Ezzaouia, *Journal of Alloys and Compounds* **626** (2015), 87–92.
- [2] M.B. Amor, A. Boukehchem, K. Boubaker and M. Amlouk, *Materials Science in Semiconductor Processing* **27** (2014), 994–1006.
- [3] S. Benramache, Y. Aoun, S. Lakel, B. Benhaoua and C. Torchi, The calculate of optical gap energy and urbach energy of Ni_{1-x}CoxO thin films.
- [4] N.N. Jandow, M.S. Othman, N.F. Habubi, S.S. Chiad, Khudheir A. Mishjil and I.A. Al-Baidhany, *Mater Res Express* **6**(2019), 116434.
- [5] C. Suryanarayana, *International Materials Reviews* **40** (1995), 41–64.
- [6] A.C. Gandhi, J. Pant, S.D. Pandit, S.K. Dalimbkar, T.-S. Chan, C.-L. Cheng, Y.-R. Ma and S.Y. Wu, *The Journal of Physical Chemistry C* **117** (2013), 18666–18674.
- [7] Z. He, Z. Li, Q. Xiang, W. Yan and H. Zhang, *International Journal of Applied Ceramic Technology* **16** (2019), 160–169.
- [8] A. Loukil, A. Boukhachem, M.B. Amor, M. Ghamnia and K. Raouadi, *Ceramics International* **42** (2016), 8274–8289.
- [9] A.W. Jansons, K.M. Koskela, B.M. Crockett and J.E. Hutchison, *Chemistry of Materials* **29** (2017), 8167–8176.
- [10] G. Baldinozzi, J.F. Berar, G. Calvarin, Rietveld refinement of two-phase Zr-doped Y₂O₃, in: *Materials Science Forum*, Aedermannsdorf, Switzerland: Trans Tech Publications, 1984-, 1998: pp. 680–685.
- [11] W. Zachariassen, The crystal structure of the modification C of the sesquioxides of the rare earth metals, and of indium and thallium, *Norsk Geologisk Tidsskrift*. 9 (1927) 82.
- [12] V. Đoridjević, B. Milićević, M.D. Dramićanin, Rare Earth-Doped Anatase TiO₂ Nanoparticles, *IntechOpen*. Copyright. 2 (2017) 25–52.
- [13] X. Lou, X. Zhao, J. Feng and X. Zhou, *Progress in Organic Coatings* **64** (2009), 300–303.
- [14] C. Mrabet, M.B. Amor, A. Boukhachem, M. Amlouk, T. Manoubi, *Ceram. Int.* **42**, 5963 (2016).
- [15] N. Wang, C. Liu, C.L.B. Wen, H. Wang, S. Liu, W. Jiang, W. Ding and W. Chai, *Thin Solid Films* **616** (2016), 587–593.
- [16] T. S. Moss, "The interpretation of the properties of indium antimonide", *Proceedings of*

the Physical Society. Section B, Vol. 67, No. 10, (1954), 775-782.

[17] E. Burstein, "Anomalous optical absorption limit in InSb", *Physical Review*, Vol. 93, No. 3, (1954), 632-633.

[18] A. P. Roth and D. F. Williams, "Properties of zinc oxide films prepared by the oxidation of diethyl zinc", *Journal of Applied Physics*, Vol. 52, No. 11, (1981), 6685-6692.

[19] Victor Hugo Lopez-Lugo, Manuel Garcia-Hipolito, Arturo Rodriguez-Gomez, and Juan Carlos Alonso-Huitron, *Nanomaterials* **13**, 197 (2023).

[20] S. Benramache, S. Lakel, O. Belahssen and B. Benhaoua, *Optik* **126** (2015), 2946–2949.

[21] Y.R. Denny, K. Lee, C. Park, S.K. Oh, H.J. Kang, D.-S. Yang and S. Seo, *Thin Solid Films* **591** (2015), 255–260.

[22] V. Ganesh, L. Haritha, M. Anis, M. Shkir, I. Yahia, A. Singh and S. AlFaify, *Solid State Sciences* **86** (2018),98–106.

[23] Y.-S. Kim and K.-J. Chang, *Phys. Rev. Lett.* **86**, 1773 (2001).

[24] Ratnesh Sharma, A.D. Acharya, S.B. Shrivastava, Manju Mishra Patidar, MohanGangrade, T. Shripathi, V. Ganesan, *Optik - International Journal for Light and Electron Optics*, 127, Issue 11(2016)4661.

[25] H. Kamal, E.K. Elmaghraby, S.A. Ali, K. Abdel-Hady, Characterization of nickel oxide films deposited at different substrate temperatures using spray pyrolysis, *J. Crys. Gro.* 262 (2004) 424-434.

[26] A. Mendoza-Galván, M.A. Vidales-Hurtado, A.M. López-Beltrán, Comparison of the optical and structural properties of nickel oxide-based thin films obtained by chemical bath and sputtering, *Thin Solid Films*, 517 (2009) 3115-3120.

[27] S.A. Makhlof, M.A. Kassem, M.A. Abdel-Rahim, Crystallite size dependent optical properties of nanostructured NiO films, *Optoelectronics and Advanced Materials* 4-10 (2010) 1562.

[28] S. Thota, A. Mallick, S.K. Singh, The role of surface effects on the optical behavior of nanocrystalline NiO, *AIP Conf. Proc.* 1536 (2013), 521-522.

[29] K. Anandan, V. Rajendran, Structural, optical and magnetic properties of well-dispersed NiO nanoparticles synthesized by CTAB assisted solvothermal process, *Nonoscience and Nanotechnology* 2(4), (2012) 24-29.

- [30] R. Boughalmi, A. Boukhachem, I. Gaided, K. Boubaker, M. Bouhafs, M. Amlouk, Effect of tin content on the electrical and optical properties of sprayed silver sulfide semiconductor thin films, *Materials Science in Semiconductor Processing* 16 (2013) 1584-1591.
- [31] F. Urbach, The Long-Wavelength Edge of Photographic Sensitivity and of the Electronic Absorption of Solids, *Phys. Rev.* 92 (1953) 1324.
- [32] W. Martienssen, Über die excitonenbanden der alkalihalogenidkristalle, *J. Phys. Chem. Solids* 2(1957) 257-267.
- [33] CR. Bamford, Colour generation and control in glass, *Glass science & technology*, Amsterdam, the Netherlands, Elsevier, 1977.
- [34] W. Guo, K.N. Hui, K.S. Hui, High conductivity nickel oxide thin films by a facile sol-gel method, *Mater. Lett* 92 (2013) 291-295.
- [35] W.L. Jang, Y.M Lu, W.S Hwang, W.C Chen, Electrical properties of Li-doped NiO films, *Journal of the European Ceramic Society* 30 (2010) 503-508
- [36] M. Segall, P.J. Lindan, M.A. Probert, C.J. Pickard, P.J. Hasnip, S. Clark and M. Payne, *Journal of Physics: Condensed Matter* 14 (2002), 2717.
- [37] P. Hohenberg and W. Kohn, *Phys R eV* 136 (1964), B864.
- [38] J.P. Perdew, K. Burke and M. Ernzerhof, Errata:(1997) *Phys R eV Lett* 78 (1996), 1396.
- [39] D. Vanderbilt, *Physical Review B* 41 (1990), 7892.
- [40] H.J. Monkhorst and J.D. Pack, *Physical Review B* 13 (1976), 5188.
- [41] S. Goumri-Said, W. Khan, K. Boubaker, G. Turgut, E. S'önmez, J. Minar, M. Bououdina and M.B. Kanoun, *Materials Research Bulletin* 118 (2019), 110525.
- [42] E. Schreiber, O. L. Anderson et N. Soga, *Elastic constants and their measurement* (McGraw-Hill, Inc. 1973 USA).
- [43] W. Jifang, E. Fisher and M. Manghnzmi, *Chinese Physics Letters* 8 (1991), 153.
- [44] K.C. Pitike, A.E. Marquez-Rossy, A. Flores-Betancourt, D.X. Chen, K. Santosh, V.R. Cooper and E. Lara-Curzio, *Journal of Applied Physics* 128 (2020), 015101.
- [45] T. Eto, S. Endo, M. Imai, Y. Katayama and T. Kikegawa, *Physical Review B* 61 (2000), 14984.
- [46] H. Ikehata, N. Nagasako, T. Furuta, A. Fukumoto, K. Miwa and T. Saito, *Physical Review B* 70 (2004), 174113.

- [47] P. Germain ,*Mécanique des milieux continus, Cours à l'usage de la licence*, Masson et Cie. 1962.
- [48] H.C. Chen, L.J. Yang, *Physica B* 406, 4489. 2011.
- [49] Z.M. Sun, S. Li, R. Ahuja, J.M. Schneider, *Solid State Commun.* 129, 589. 2004.
- [50] Z.J. Lin, Y.C. Zhou, M.S. Li, *J. Mater. Sci. Technol.* 23, 721. 2007.
- [51] M.W. Barsoum, T. El-Raghi, W.D. Porter, H. Wang, S. Chakraborty, *J. Appl. Phys.* 88. 6313. 2000.
- [52] B. Mayer, H. Anton, E. Bott, M. Methfessel, J. Sticht, P. C. Schmidt, *Intermetallics* 11 23. 2003.
- [53] CRC Handbook of Chemistry and Physics, 56th Edition (1975-1976).
- [54] KS Kim, W.Lambrecht, and B. Segall. *Phys. Rev. B*, 53(24) :16310_16326, 1996.
- [55] E. Schreiber, O.L. Anderson, N. Soga, *Elastic Constants and Their Measurements*, McGraw-Hill, New York, 1973.
- [56] S. Pugh, "XCII. Relations between the elastic moduli and the plastic properties of polycrystalline pure metals," *The London, Edinburgh, and Dublin Philosophical Magazine and Journal of Science*, vol. 45, pp. 823-843, 1954.
- [57] I. Garduño, J. Alonso, M. Bizarro, R. Ortega, L. Rodríguez-Fernández and A. Ortiz, *Journal of Crystal Growth* **312**(2010), 3276–3281.
- [58] R. Clendenen and H. Drickamer, *The Journal of Chemical Physics* **44** (1966), 4223–4228.
- [59] I. Wakabayashi, H. Kobayashi, H. Nagasaki and S. Minomura, *Journal of the Physical Society of Japan* **25** (1968),227–233.
- [60] Y. Noguchi, M. Uchino, H. Hikosaka, T. Atou, K. Kusaba, K. Fukuoka, T. Mashimo and Y. Syono, *Journal of Physics and Chemistry of Solids* **60** (1999), 509–514.
- [61] L. Ming, M. Madon, M. Manghnani and L.J. Wang, *High-Pressure Research: Application to Earth and Planetary Sciences* **67** (1992), 245–255.
- [62] E. Huang, *International Journal of High Pressure Research* **13** (1995), 307–319.
- [63] T. Sasaki, *Physical Review B* **54** (1996), R9581.

A decorative black floral border with various flowers and leaves surrounds a central white rectangular area. The border is symmetrical and ornate, featuring several different flower designs and leaf shapes.

*General
Conclusion*

General Conclusion

This thesis focused on developing pure, alkali-doped NiO and alkali-la co-doped NiO thin films with low thickness and slightly higher alkali contents (x) ($x = 3\%$, 6% , 9% , 12% and 25% at%) using the sol-gel method. The preparation protocol for undoped and alkali-doped NiO and alkali-la co-doped NiO thin films on glass substrates was developed using spin coating technique, starting with Nickel nitrate hexa-hydrate, and Mono Ethanolamine) MEA as a starting material, and stabilizer.

Ideal experimental conditions were chosen in order to guarantee that the prepared thin films crystallized well. These conditions were chosen based on our review of the experimental literature. such as molar ratio of the solvent to metal ions, stirring, aging, cleaning and drying of substrates, spinning, preheating and annealing. The synthesized samples were examined using a variety of methods, including X-ray diffraction, ultraviolet-visible UV-vis spectrophotometry, and the four points method.

On the other hand, first-principles calculations of structural, electronic, optical and elastic properties of pure and alkali-doped NiO and alkali-la co-doped NiO cubic materials ($x = 3\%$, 6% , 12% and 25% at%) were performed by DFT as implemented in CASTEP code. The generalized gradient approximation (GGA) in the scheme of Perdew–Burke–Ernzerhof (PBE) was employed to describe the exchange-correlation function. To ensure calculation convergence, we used ideal input criteria for computer code, based on theoretical literature reviews. such as the valence-electron configurations for the O, Ni, Li, Na, K and La atoms, the energy cut-off, pseudopotential, the sampling of the Brillouin zone by k-point meshes, the optimization convergence for maximum force, energy change, maximum displacement, maximum stress and the SCF convergence threshold.

We summarize our findings from previous chapters and draw the following conclusions:

Experimental investigations indicates that for Li doped NiO:

- The XRD analyses indicate that the deposited films are polycrystalline structure and (200) plane is preferential orientation
- No impurity peaks are identified from the XRD pattern.

- The crystallite size decreases than increases with increasing dopant concentration. And it varies between 24.13 and 28.97 nm was affected by Li concentration.
- All films exhibit a high optical transparency and transmittance is found to decrease with the increase in Li concentration.
- The band gap of Li doped NiO samples was found to increase for 3% Li doping (3.83 eV) than it decreases to reach 3.22 eV for 25% Li.
- The resistivity has been found to decrease with the increase in Li concentration, giving the lowest value in case of 3% Li doping.

For Na-doped NiO

- The XRD analyses indicate that the deposited films are polycrystalline structure The intensity of the (200) peak is often increased, especially at high Na-doping levels and the doped samples show a decrease in peak intensity and an increase in peak width when compared to the pure sample.
- No impurity peaks are identified from the XRD pattern.
- The average crystallite size of 31.56 nm for pure NiO initially decreases to the reach 24.13, 28.9, 20.68 and 20.69nm for 3, 6, 9 and 12% Na, then surprisingly increases to 28.97nm with higher doping levels of 25%Na doping
- the overall transmittance of the Na doped NiO samples exhibits a relatively low transparency compared to undoped NiO sample and Li doped NiO samples for same concentrations
- The calculated band gap values were found to decrease with the increase of Na concentration in NiO host (3.67 to 3.33ev)
- The resistivity has been found to decrease with the increase of Na concentration giving the lowest value in case of 25% Na doping.

For K-doped NiO

- For low K concentration the (111) presents the preferential peak intensity while the (200) peak is the preferred growth orientation for 12% and 25% K concentration.
- The lattice parameter increases significantly from 4.16 nm for pure NiO to 4.17 nm for 25% K doped NiO representing a lattice expansion.

- The average crystallite size of for pure NiO 31.56 nm first decreases for low K concentrations than increases along with the increase of K amount in the NiO host lattice to reach a maximum value for 12% K doping.
- The transmittance for all thin films increases as the wavelength increases in the range of (300-375 nm), and then increases slowly at higher wavelengths
- the calculated band gap values were found to decrease for 3%K doping (3.63eV) than slightly increase for 6%K doping (3.71eV) but still less than the E_g value of the undoped band gap, than it decreases with the increase of K concentration to reach a minimal value (eV) for 12% K doping
- K doping has resulted in a decrease in the resistivity values of the NiO samples from $5.66 \times 10^4 \text{ohm.cm}$ for undoped NiO to $0.1665 \times 10^4 \text{ohm.cm}$ for 3% K-NiO than it increases to reach $2.0317 \times 10^4 \text{ohm.cm}$ for 12% K-NiO than it decreases again for 25%K-NiO to achieve $0.393 \times 10^4 \text{ohm.cm}$

For alkali-La co-doped NiO

- The XRD analyses indicated that the deposited films are polycrystalline structure and (200) plane is preferential orientation with no La_2O_3 or other impurity peaks.
- The intensity of the peaks continuously decreases and the peaks gets broadening with La doping.
- the FWHM of the co-doped samples is extremely large, indicating that the incorporation of La ions within NiO host lattice induces a decline of the crystallinity of the doped films
- The grain size of the La co-doped NiO samples is very small in comparison with the alkali doped NiO samples.
- The transparency of the co-doped samples is lying between 30 and 60 % in the visible region.
- The incorporation of La ions in the NiO structure decreased the resistivity of the films and it varies between 0.009 and $0.0659 \times 10^4 \text{ Ohm.cm}$.

Theoretical investigations revealed that:

Our findings concerning the structural characteristics of the equilibrium state (the mass (V) and lattice parameter (a)) of undoped, alkali-doped, and La-alkali co-doped NiO

structures agree well with the experimental values obtained in this work and those calculated using other ab-initio methods. Based on our findings, we note that the lattice parameters increase as the concentrations of sodium and potassium increase because the atomic radius of sodium and potassium is larger than that of nickel (Ni) atoms. Conversely, the lattice parameter decreases as the lithium concentration increases. The addition of La ions results in an extreme increase of the lattice parameter.

Convenient effective Hubbard U values are found to enhance the band gap according to DFT+U calculations. However, the band gap values of the calculated band structures agree well with the experimental values acquired for this work.

In addition, we computed the density of total and partial states of undoped, alkali-doped, and La-alkali co-doped NiO structures.

The optical properties allowed us to determine the dielectric constant, the refractive index, the reflectivity, the absorption coefficient, and the energy loss function of undoped, alkali-doped, and La-alkali co-doped NiO structures. Our findings are in excellent agreement with other theoretical and experimental works that are available in the literature. The three main peaks that make up the imaginary part have slightly different intensities due to impurity doping. It is discovered that the static refractive index changes as alkali doping rises.

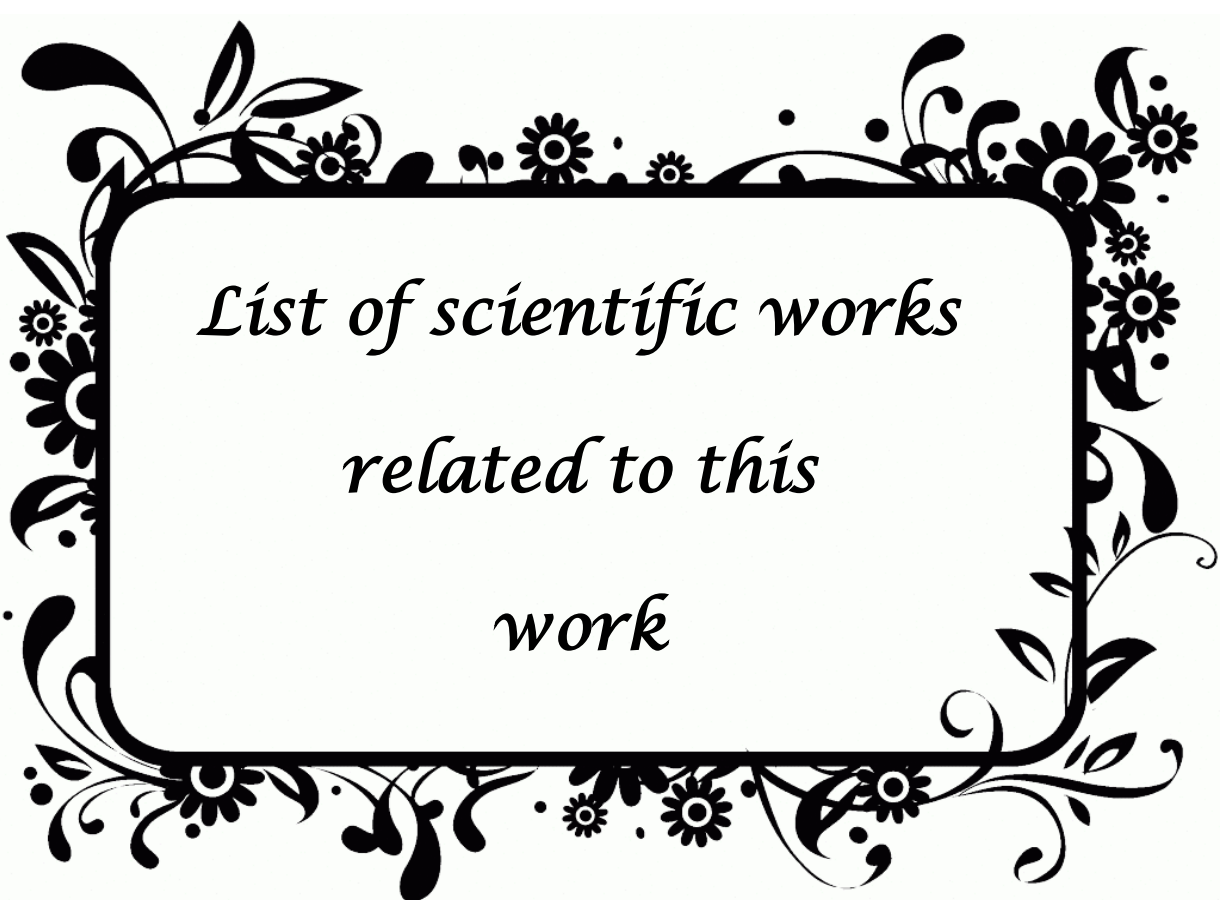
The strong absorption region gradually becomes more elongated as the concentration of alkali doping increases. The absorption threshold of $\text{Ni}_{1-x}\text{A}_x\text{O}$ and $\text{Ni}_{1-2x}\text{A}_x\text{La}_x\text{O}$ (A=Li, Na and K) follows in the near-ultraviolet. The electronic and optical properties show that $\text{Ni}_{1-x}\text{A}_x\text{O}$ (A=Li, Na, K) is a good candidate for optoelectronic applications.

We have determined the Debye temperature for $\text{Ni}_{1-x}\text{A}_x\text{O}$ and $\text{Ni}_{1-2x}\text{A}_x\text{La}_x\text{O}$ (A=Li, Na and K), as well as the constants and elastic modules (C11, C12, C44, B, G, E, and ν), as well as the longitudinal and transversal velocities (V_l , V_s). The obtained results are predictable given the lack of theoretical and experimental data pertaining to these properties in the literature. The obtained numerical results regarding the structural, electrical, optical, and elastic properties of $\text{Ni}_{1-x}\text{A}_x\text{O}$ and $\text{Ni}_{1-2x}\text{A}_x\text{La}_x\text{O}$ (A=Li, Na and K), are under no pressure.

In conclusion, it is noteworthy that the current study yields two significant outcomes.

Experimentally, the transparency and band gap energy of alkali doped NiO thin films were found to be influenced by alkali content in the visible region, indicating that the doping process with alkali makes these films suitable for use in opto-electronic devices, wherein alkali doped NiO thin films are transparent to visible light and have the ability to absorb the ultra violet wave range in the spectrum. The resistivity of alkali doped NiO thin films can be reduced by alkali content, but increasing the alkali content in NiO thin films decreases the transparency. We found that the addition of small amounts of La to the same concentration of alkali doping decreases effectively the resistivity of NiO thin films without reducing their transparency, so the result would be a p-type thin film with a high transparency and very low resistivity.

From a theoretical perspective, incorporating DFT+U correction into standard DFT shows that the band gap energy and its associated electronic and optical properties are greatly enhanced by convenient effective Hubbard U values. On the other hand, NiO thin film properties are significantly impacted by alkali-doping and alkali-La co-doping which allows us to thinking about widening the range of their potential applications especially for thermoelectric applications. So, the issue is still left open.

A decorative border of black floral and leaf motifs surrounds the text. The border features stylized flowers, leaves, and swirling lines, creating a classic, elegant frame.

*List of scientific works
related to this
work*

Publications:

1) Alkali Doping Nickel Oxide Thin Films Using Sol-Gel Spin Coated and Density Functional Theory: Structural and Physical Properties

H. Touhami, K. Almi, Said Lakel and M. N. E. Boumerzag

Russian Journal of Physical Chemistry B, 2023, Vol. 17, No. 5, pp. 1057–1068

<https://doi.org/10.1134/S1990793123050287>

2) Experimental and theoretical investigation of the effect of alkali (Li, Na and K) doping on the properties of nickel oxide thin films: Comparative study

Hanna Touhami, Kenza Almi and Said Lakel

Main Group Chemistry (2023)

<https://content.iospress.com/articles/main-group-chemistry/mgc220130>

International Communications:

1) DFT and Experimental study on the physical properties of p semiconductors oxides $\text{Ni}_{1-x}\text{K}_x\text{O}$ for thermoelectric and sensor applications

Hanna Touhami, Maria Harzeli, Kenza Almi, Said Lakel.

13JCTC (13th International Days of theoretical and Computational Days of Chemistry), 02nd and 03rd February, 2020 at the university of Biskra, Algeria.

2) Structural, Optical and electrical Properties of Undoped and K-doped NiO Thin Films Prepared by Sol-Gel Spin Coating Method.

Hanna Touhami.

ICONN2021(International Conference en Nano-science and nano-technology), 01stto 03rd February, 2021, organized by department of physics and nano-technology, SRMIST, India.

3) Structural, Optical and electrical Properties of Undoped and Li-doped NiO Thin Films Prepared by Sol-Gel Spin-Coating Method For Thermoelectric Applications.

Hanna Touhami, Kenza, Almi, Maria Nor Elyakin, Boumerzag, Said Lakel.

IC-SEAM (1stInternational Conference on Sustainable Energy and Advanced Materials. 21th and 22th April 2021, Ouargla, Algeria.

National Communications

4) Experimental and DFT study on the physical properties of p semiconductors oxides $\text{Ni}_{1-x}\text{Li}_x\text{O}$

Hanna Touhami, Kenza, Almi, Said Lakel.

NVCCPEE (First National Virtual Conference on Chemical Process and Environmental Engineering), 15th and 16th December 2021 at the university of Biskra. Algeria

Abstract

In the present work, pure and alkali doped NiO ($\text{Ni}_{1-x}\text{A}_x\text{O}$) and La-alkali co-doped ($\text{Ni}_{1-2y}\text{A}_y\text{La}_y\text{O}$) NiO thin films where (A=Li, Na and K) and ($x=0.03, 0.06, 0.09, 0.125$ and 0.25) and ($y=0.03, 0.06$) were synthesized by sol-gel spin coating method and deposited on glass substrates. XRD analysis showed that the prepared films belongs to a cubic structure with (100) plane wave as preferential growth orientation for pure and K doped NiO for small K contents and the (200) for higher K contents along with Li, Na, and La-alkali co-doped NiO thin films. The grain size decreased with the increase of the concentration of doping elements in the NiO lattice. Optical properties of the prepared films were investigated. As x increased the transparency of the prepared films decreased. Also the optical study revealed that the optical band gap tends to decrease with alkali doping and achieves minimal values with Na doping. The Urbach energy increases systematically with the decrease of the optical band gap. The resistivity measurements showed that the alkali doping and La-alkali co-doping led to a significant decrease in the resistivity values. Structural, electronic, optical and elastic properties of pure and alkali doped NiO ($\text{Ni}_{1-x}\text{A}_x\text{O}$) and La-alkali co-doped ($\text{Ni}_{1-2y}\text{A}_y\text{La}_y\text{O}$) NiO thin films where (A=Li, Na and K) and ($x=0.03, 0.06, 0.125$ and 0.25) and ($y=0.03, 0.06$) were performed using the first principle method based on density functional theory. The optimization of the geometry of the studied samples revealed that lattice parameter is affected with alkali doping and La-alkali co-doping. The band structure and density of states calculations showed that doped and co-doped samples exhibited an indirect band gaps. The optical parameters: $\varepsilon_1(\omega), \varepsilon_2(\omega), n(\omega), k(\omega), \alpha(\omega), R(\omega), L(\omega)$ and elastic constants: (C_{ij}, B, G, E, ν and B/G), the longitudinal and shear wave velocities (V_l, V_s), and Debye temperature θ_D were further investigated.

Both experimental and theoretical results obtained in this work are in good agreement.

Key words: Alkali doped NiO, Spin coating, DFT, electrical properties, Gap energy, Elastic properties.

ملخص

قمنا في هذا العمل بتحضير الشرائح الرقيقة لأكسيد النيكل أحادية التطعيم ($Ni_{1-x}A_xO$) وثنائية التطعيم ($Ni_{1-2y}A_yLa_yO$) و المطعم بالذرات القلوية ($A=Li, Na \text{ and } K$) مضافا إليها ذرة اللانثانيوم في التطعيم الثنائي مع قيم مختلفة للتركيز هي كالآتي: ($y=0.03, 0.06$) and ($x=0.03, 0.06, 0.09, 0.125 \text{ and } 0.25$) باستخدام طريقة الطلاء بالتدوير محلول-هلام و المرسبة على شرائح من الزجاج. أظهر تحليل الأشعة السينية أن جميع العينات المحضرة ذات تبلور متعدد و بنية مكعبة و أن شرائح أكسيد النيكل النقي بالإضافة إلى شرائح أكسيد النيكل المطعم بتركيز منخفضة من البوتاسيوم لها توجه مفضل نحو المستوى البلوري (111) بينما بقية الشرائح المطعم بالليثيوم و الصوديوم و البوتاسيوم بتركيز عالية و ثنائية التطعيم تمتلك جميعا توجه مفضل نحو المستوى البلوري (200). كما أوضحت الدراسة البنيوية أن حجم الحبيبات يتناقص بزيادة تركيز الشوائب. كما بينت دراسة الخصائص البصرية للشرائح المحضرة أن زيادة تركيز التطعيم تؤدي إلى تناقص في الشفافية. تتناقص قيم طاقة العصابة الممنوعة بزيادة تركيز التطعيم. تزداد قيم طاقة ايرباخ تلقائيا بتناقص قيم طاقة العصابة الممنوعة. أظهرت قياسات المقاومة الكهربائية أن التطعيم الأحادي بالذرات القلوية يؤدي إلى تناقص في قيم المقاومة الكهربائية بشكل ملحوظ. كما أن اضافة ذرات اللانثانيوم إلى أكسيد النيكل المطعم بالذرات القلوية بنسب متساوية و قليلة يؤدي إلى انخفاض كبير في قيم المقاومة مع الاحتفاظ بناقلية مرتفعة نسبيا. قمنا أيضا بدراسة نظرية للخصائص البنيوية و الالكترونية و الضوئية و المرونية للمركبات ($Ni_{1-x}A_xO$) و ($Ni_{1-2y}A_yLa_yO$) من أجل ($x=0.03, 0.06, 0.09, 0.125 \text{ and } 0.25$) and ($y=0.03, 0.06$) حيث ($A=Li, Na \text{ and } K$) باستخدام طريقة المبادئ الأولية المعتمدة على نظرية دالية الكثافة DFT. كشف تحسين هندسة العينات المدروسة أن ثابت الشبكة يتأثر بالتطعيم كما أظهرت دراسة كثافة الحالات الالكترونية الكلية و الجزئية (DOS and PDOS) أن العينات المدروسة تمتلك نطاق ممنوع غير مباشر. كما تم حساب الخصائص الضوئية ($C_{ij}, B, G, E, \nu \text{ and } B/G$) و الثوابت المرونية ($\epsilon_1(\omega), \epsilon_2(\omega), n(\omega), k(\omega), \alpha(\omega), R(\omega), L(\omega)$) و سرعات الموجبة الطولية و العرضية V_L, V_S و درجة الحرارة ديبياي θ_D .

النتائج التجريبية المتحصل عليها من خلال تحليل العينات المعدة مخبريا على توافق تام مع النتائج المتحصل عليها من خلال الدراسة النظرية.

الكلمات المفتاحية: أكسيد النيكل المطعم بالذرات القلوية، الطلاء بالتدوير، نظرية دالية الكثافة، الخصائص الكهربائية، العصابة الطاقية، الخصائص المرونية.